Transport in III-Nitride Devices

by

Ahmed Mohamed

M.S., University of Illinois at Chicago, 2019

B.S., University of Khartoum, 2014

Thesis

Submitted as partial fulfillment of the requirements for the degree of Doctor of Philosophy in Electrical and Computer Engineering in the Graduate College of the

University of Illinois at Chicago, 2021

Chicago, IL

Defense Committee

Michael A. Stroscio, Chair and Advisor
Mitra Dutta
Junxia (Lucy) Shi
Vitali Metlushko
Carmen Lilley, Mechanical and Industrial Engineering

Improving the Understanding of Carrier and Thermal Transport in Electronic Heterostructure Devices by Proper Treatment of Boundary Effects in Wide Bandgap Semiconductors

Short title: Transport in III-Nitride Devices

Abstract

Carrier and thermal transport in semiconductors – both important parameters for the operation of electronic and optoelectronic devices – are primarily dependent on the thermal conductivity of the crystal lattice. Dominant anharmonic coupling processes, such as electron-phonon and phonon-phonon coupling, provide helpful insights into the thermal characteristics of wide bandgap semiconductors. Investigation on phonon coupling mechanisms will expand our understanding of their effects on electron transport and thermal conductivity of semiconductor devices, whereby mitigate the associated device problems and finally improve the performance of electronic and optoelectronic devices.

More specifically, in high electron mobility transistors (HEMTs), the fast emission of longitudinal optical (LO) phonons can result in the formation of hot spots near the gate region where high electric fields produce hot electrons. In this thesis, we investigate the probability of phonon emission as a function of electron energy for confined and interface phonon modes for different wurtzite heterostructures. Novel phonon engineering concepts are introduced which facilitate thermal management through the production of polar optical phonons and acoustic phonons. This work offers a wide range of theoretical modeling and experimental studies of the carrier and thermal transport dynamics in structures including those in GaN- and AlN-based devices.

“I see a beautiful city and a brilliant people rising from this abyss. I see the lives for which I lay down my life, peaceful, useful, prosperous and happy. I see that I hold a sanctuary in their hearts, and in the hearts of their descendants, generations hence. It is a far, far better thing that I do, than I have ever done; it is a far, far better rest that I go to than I have ever known.”

— Charles Dickens, A Tale of Two Cities.

Acknowledgements

To my mom, the strongest person I have ever known and the most empathetic. She never developed a thick skin to protect herself from hurt. She wants to feel and share everyone's pain. She trusts too freely and too completely. She suffered great losses, but she always persevered, worked day and night, always believed the best was yet to come. While many spend time and money to counter anxiety and depression, her remarkable faith retains within her heart the strongest inner peace I have ever seen in a person. Her optimism has guided me and made me believe that anything was possible. We test her patience, I know I did, but she always responds with unparallel love.

To my dad. Dad is always busy but never too busy to share his love and passion with us and those around him. Dad could relate to anyone in distress, he is a sympathetic man who looks for the good in each person and he usually finds it. He loves to laugh, and he values a great joke, always enjoys teasing his children but never out of malice. Dad honors and nurtures his family and his friendships with a generous and a selfless soul.

Mom, dad, your decency, candor and kind soul will inspire me forever. Thank you for being the best parents anyone could ever have.

To my best friends Mohannad Ibrahim (NC State) and Mohammed Awadallah (McGill). Mohannad is an amazing person. It never fails to astound me how generous, giving and intelligent he is. In the grand scheme of things, he was almost behind every positive adjustment into my personality and how I think about life. Whenever I feel challenged – something I encounter frequently – he is always faithful to convince me that I do know a few things and just need to press on. His excitement for science and career was infectious and inspired me through my darkest and most doubt-filled moments in 2015.

Mohammed has an unusual combination of a determined, relentless and fun spirit. He is the kind of humorous person who gets you laughing just being in the room. He is also a man who listens, and it often surprises me how well he knows me. Mohammed represents the values I truly cherish; acknowledging there are areas within us that can be stronger, always treating people with dignity and always remembering to have modesty.

Thank you my friends! There are many things I could say about you two but the one thing I *should* say is that I could not joyfully spend a single day without having you in my life. May I never have to!

To professor Michael A. Stroscio, a man – while sharp and perceptive – is always receptive to feedback and recommendations. He always strives to let me develop my abilities as an independent researcher. He aspires to build trusting relationships with us in the research group and with the students in his classes in order to create a safe, positive and inclusive learning environment. And during the challenging times in the middle of the COVID-19 pandemic, he gave me the support I needed to move ahead.

Professor Stroscio, thank you for shaping me into the researcher that I am today! Your humor and your humble nature combine with your academic brilliance have made working with you easy and empowering. For all the hours we spent in your office while you were guiding me through the topics, for all the times I showed up unannounced at your office, yet you still welcomed me with a smile, I am forever grateful!

This thesis represents not only my work at the Nanoengineering Research Laboratory, but it is also a milestone in more than 4 years of hard work at the University of Illinois at Chicago. Students at a large university can easily feel as though their presence no longer matters. On the contrary at UIC, I feel a moment of relief when I step into its campus. I know and feel that I am valued, not just inside the classroom or the lab, but outside of the university context as well. Thank you, UIC, for always being committed to

providing an environment in which research and learning prosper and in which our endeavors are driven by academic integrity and professional development.

The Air Force Office of Scientific Research (AFOSR) and the Army Research Lab (ARO), your contributions could be taken for granted but not by me! You are a solid proof of why this country is the greatest country on earth. Thank you for making my work at UIC possible.

Author contributions

All studies, data analysis and writing in this thesis were completed by Ahmed Mohamed as the primary contributor unless otherwise stated. Chapter 3 describes research conducted in collaboration with professor Can Bayram and Kihoon Park with the Innovative Compound Semiconductor Laboratory at the University of Illinois at Urbana Champaign (UIUC). Chapter 3 was also co-authored with Giorgio Bonomo (ETH Zurich), with contributions by Sidra Farid with the Nanoengineering Research Laboratory at the University of Illinois at Chicago (UIC). Studies in Chapter 4 were conducted with substantial help from Shreya Gosh (now with UIUC) in collaboration with Marcos Araque and Debopam Datta (Caltech). Chapter 6 presents a summer collaboration with the Laboratory of Life Sciences Electronics at Ecole Polytechnique Fédérale de Lausanne (EPFL) under supervision of Professor Carlotta Guiducci and with help from Saurabh Tomar.

Professors Michael A. Stroscio and Mitra Dutta contributed substantially to this thesis in different aspects ranging from projects supervision, work validation, writing and editing revised documents and providing resources.

Contents

List of Tables

List of Figures

Chapter 1

Introduction

1.1 Advances in III-V devices

The advantages of III-V compound semiconductors over silicon for use in devices capable of operating in high-frequency and high-power applications were investigated early in the semiconductor development [1]. Many of the famous compound semiconductors, such as AlGaAs, InGaN, AlGaN and AlInGaP, are available as direct band gap materials in which no phonon interaction is required. These materials surpass silicon in their potential efficiency in light emission [2].

III–V semiconductors have wide applications in high-performance electronic and optoelectronic devices due to their excellent electronic properties including high electron mobility and low exciton binding energy [3]. For instance, similar to CdSe, InP has bulk bandgap and exciton Bohr radius, therefore, size-dependent band-edge emission of InP nanocrystals can also be tunable across the entire visible range [4]. InSb is another example of III–V semiconductor materials that showed a well-resolved excitonic transition of Bohr radius of 54 nm [5].

Compound semiconductors are extremely useful in high-speed electronic applications [6]–[8]. The speed of each transistor is largely dependent on the velocity of the hot carriers in the operating device [9]. Compared to Si, GaAs transistors are able to operate at much higher frequencies since their electron drift velocity is considerably higher [10]. The electron velocity in InAs is notably higher than both GaAs and Si [11]. Furthermore, in analogy to preferring silicon over germanium, devices manufactured using III-V semiconductor devices such as GaN, which possess much larger electronic bandgaps (3.4 eV) than silicon (1.12 eV), are capable of operating in much higher temperature ranges [12], [13].

Earlier in the semiconductor revolution, compared for silicon, compound semiconductors' use in the extensive commercial applications and high production volumes was limited; their structures were more difficult to grow than silicon [14] since their crystals have many crystal defects [15] accompanied by the expensive fabrication costs [16]. Compound semiconductors also tend to be more fragile which limits their growth abilities [17].

In recent years, however, the high price of compound semiconductors has shrunk. Compared to Silicon, collectively, the excellent electrical and optical properties of these materials have become more valuable for certain applications including the ongoing research on high-speed data transfer in 5G, 3D sensors and further extending the range of electric vehicles. Silicon's limited qualities such as frequency range, light detection efficiency and power have rendered these applications unresolved.

1.2 Wide bandgap nitride-based III-V devices and complications of wurtzite structures

III-nitride semiconductors have great potential in tolerating high electric fields and elevated temperatures. This clearly demonstrates that their full potential is not exploited yet, albeit the impressive industrial revolution that took place over the past two decades in their performance. From the AlInGaAs and AlInGaN alloy systems, there is, in principle, a continuous spectrum of direct bandgaps from deep in the infrared ($\lambda = 3.5$ nm in InAs) to far into the ultraviolet ($\lambda = 200$ nm in AlN) [18]. Although they offer this wide range of bandgaps from the infrared to the deep UV, several challenges still need to be overcome to extend the lasing wavelength region of group-III nitrides. For example, the thermal stability of the InGaN active region is severely influenced, along with the lattice mismatch, in long-wavelength (λ > 500 nm) laser diodes [19]. Also, quantum wells (QWs) with high indium content (In > 25%) have been shown to have worsening optical properties as a result of the formation of misfit dislocations [20]. For this reason,

the growth temperature in recent studies were drastically decreased to avoid QW degradation, which is associated with a deteriorating quantum efficiency [21], [22]. Thanks to the high vacuum environment, it is possible to grow QW layers at a much lower temperature through molecular beam epitaxy (MBE) compared to metalorganic vapor phase epitaxy (MOVPE) and could be used to reduce the thermal budget on the active region and, consequently, obtaining longer wavelength range [23].

Throughout this thesis, we focus on the III-nitride devices, such as GaN, InGaN and AlInN. These devices have been the main focus of extensive research and development among all electronic materials over the last two decades. The development of III-nitride materials and devices has much in common with the early research of other III–V systems. For example, metalorganic chemical vapor deposition (MOCVD) and MBE growth technologies were both successfully used for III-nitride device growth [24], [25]; both electronic and photonic applications were studied early in the revolution; yet achieving sufficiently high p-type carrier densities remained a primary complication limiting the device development [26]. Many obstacles were presented by III-nitride devices: Although III–V semiconductors share the same cubic crystallographic structure, the nitrides possess strong polar and piezoelectric properties in their allotropic hexagonal form [27], [28]; conventionally, III-nitride devices were grown hetero-epitaxially on highly lattice-mismatched substrates which led to devices with very high defect densities [29], in contrast to employing homoepitaxial growth or closely lattice-matched substrates in previous III–V structures where much lower defect densities are achieved [30]; and many III-nitride devices have been found to show surprisingly strong tolerance to the presence of these crystalline defects than other III–V materials [31].

Given their tight relatedness, the wurtzite (WZ) structure of III–V semiconductors and those of the III–V zinc-blendes (ZB) can essentially coexist into crystal form during their phase transformation [32]. Similarly, as in the diamond and zinc-blende nanostructures, the wurtzite phase can be formed by

considering two interpenetrating lattices. In this case, they are described as “hexagonal close packed lattices.” The nearest neighbors and next nearest neighbors are the same in the ideal wurtzite and zinc-blende structures. The wurtzite phase is considered both a complication and a potential feature to be utilized, such is the case for nanowire homo-structures where both wurtzite and zinc-blende phases alternate to attain band gap engineering. Despite well-regarded efforts, many fundamental electronic and optoelectronic properties of wurtzite III–V compound semiconductors are not fully evaluated yet.

1.3 Thermal generation in HEMTs

The development of semiconductors, a key component in modern electronics, has followed a continuous size reduction process in recent years, and thermal management has become one of its most thrilling problems with respect to their applications.

Nitride based high electron mobility transistors are strong candidates for the future high-power and high-frequency applications. But the formation of hot spots and high temperature in these localized regions can limit their applications due to performance degradation and break-down. Understanding the underlying thermal transport processes will be an important step towards solving heat dissipation challenges in these devices. Furthermore, self-heating effect can degrade the drain saturation current, transconductance and causes reliability problem [33]. The self-heating effect, which has been subject to widespread research [33] –[35], increases the channel temperature due to the transfer of energy from the electrons to the lattice. Transistors such as GaN have high drive voltages which causes rapid increase in the lattice temperature due to dissipation of Joule power, consequently, phonon scattering increases thus deteriorating the carrier mobility and electron saturation velocity [36]. In addition, at very high-power levels, there is a spike in the junction temperature, which critically increases the meantime to failure (MTTF) of GaN transistors [37]. Several studies have been proposed to improve thermal management by realizing substrates such as

diamond and silicon carbide with high thermal conductivity. Yet, thermal conductivity is found to decrease with the rise of temperature due to optical phonon scattering caused by free carriers from dopants such as Al and N in SiC and the presence of N impurity in the diamond [38]. Additionally, these substrates are expensive and have a wide range of diameter scalability challenges. GaN-diamond composite substrates [39] and AlGaN-GaN flip-chip underfill technology [40] methods have been implemented to improve the thermal interfaces on the whole wafer; however, the problem of hot spots in the device channel region continues to occur. In other studies, particularly in AlGaN-GaN HEMTs, numerous attempts towards the dissipation of self-heating effect have been investigated, such as substrate transfer [41] and hot spot extension using nanocrystalline diamond films on top of the device [42]. However, devices using these approaches have shown moderate performance.

As an overview, self-heating in the transistor is generated when hot electrons transfer energy to the lattice vibrations (namely phonons) via crystal lattice scattering. Since scattering inside the device is not uniform, this process can generate localized hot spots [35], [43]–[45]. Attempting to provide more accurate heat extraction mechanisms and trying to capture the essential physics of the hot electron effect and comparing with experimentations may enable lower peak temperatures, consequent enhanced life span and enhanced reliability of different solid-state devices.

Inside a semiconductor device, heat is generated due to collisions between hot electrons with the atoms of the crystal i.e., the lattice. This happens when the phonon emission rate exceeds the phonon absorption rate as the energy coming from the electrons is transmitted to the lattice [46]–[48]. These hot phonons that were launched by energetic hot electrons remain localized in the regions where electrons flow. Since longitudinal optical (LO) phonons have small group velocity, they tend to accumulate and store energy, and as consequence heat is generated [35], [49]. This thesis discusses the idea of removing this heat through the hot phonons' decay through a variety of vibration modes. For GaN it was proposed that LO

modes change into longitudinal acoustic (LA) and transverse optical (TO) modes after 5 ps following the Ridley process [50], that is similar to the value reported for GaAs [51]. The calculated time of electron-LO phonon interaction for GaN is approximately 9 fs, meaning that in GaN, hot electrons are emitted nearly 12 times more than in GaAs [52]. For GaN-based HEMTs, the hot phonon lifetime in the two-dimensional electron gas channel is close to 350 fs, that is 35 times greater than the lifetime of the spontaneous LO phonons (~ 10 fs) [53]. This difference in their lifetime causes an accumulation of heat in the channel.

Efforts have been made to approach the understanding of the thermal behavior of nitride-based high-electron-mobility transistors (HEMTs) experimentally and numerically under bias conditions. These efforts include the recent work reported by Mohanty, Chen, Yeh and Horng (2019) which indicated that by using a micro-trench structure fabricated on the silicon substrate of an AlGaN/GaN HEMT via deep reactive ion etching, the temperature near the drain edge of the channel can be lowered by ~ 22 °C [36]. Furthermore, the thermal performance of the AlGaN/GaN HEMT was investigated by Vallabhaneni, Gupta and Kumar (2017) using Boltzmann Transport Equation (BTE) based model which can provide a description of the non-equilibrium nature of the phonon transport in the hot spot [54]. Hiroki et al., 2014 (2017) modified the I_D versus V_{DS} behavior due to self-heating effect in HEMT grown on SiC by substrate-transfer technique using hexagonal boron nitride [41], [55].

On the other hand, electron and phonon temperature profiles along the 2DEG channel were provided by different researchers [56]–[59]. Studies have also investigated various experiments and theories on the transport of heat in transistor structures such as GaN field effect transistors (FET) [60], silicon-on-insulator (SOI) bipolar junction transistors (BJT) [61] and AlGaN-GaN heterostructure field effect transistors (FETs) grown on sapphire and SiC substrates [62]. Thermal transport between two different materials including microfabricated and synthetic low-dimensional nanostructures [63], [64], heat

transport in nanostructured thin film materials, including superlattices [65]–[67] and examination of issues associated with metrology and measurement science [68].

1.4 This thesis

In this thesis, we present research findings of a detailed investigation of lattice vibrations in low-dimensional heterostructures of wurtzite materials with strong polarization coupling. The purpose of this research is to advance the theory of phonons for technologically important materials such as GaN and AlN as well as to introduce new phonon-related effects which can be used in pseudomorphic heterostructures. Indeed, by considering the possibilities for applications of phonon-related effects, we always expand the borders of our knowledge about the fundamental properties of the material. On the other hand, research on fundamental subjects often leads to unexpected discovery of technologically important phenomena.

The thesis is organized as follows:

Chapter 2 summarizes the key theories of phonons in nanocrystals including the dielectric continuum model for optical phonons and the elastic continuum mode for acoustic phonons. The chapter proceeds to discuss the different decay channels of optical modes into acoustic modes. We discuss and analyze the momentum relaxation and the matrix element in bulk wurtzite GaN.

Chapter 3 introduces the development of the theory of phonon confinement in heterostructures made of optically anisotropic materials. We obtain dispersion relations for polar optical phonon modes in wurtzite within the context of the dielectric model. We develop a formalism for the calculation of the scattering rate in wurtzite crystals and quantum wells considering features of the optical phonon spectra in optically anisotropic medium. We proceed to derive the average group velocity of the emitted phonons to explore the possibility of exploiting the interface mode phonons as an additional heat dissipation channel. Given the energy distribution of electrons, we report that the quantum well thickness can be engineered to exploit

the interface phonon modes, which can propagate a distance of few tens of nanometers before decaying into heat-carrying acoustic phonons.

Chapter 4 deals with the quantization of the acoustic modes in nanomechanical systems with coupled acoustic and electromagnetic modes in piezoelectric structures. We second-quantize the Bleustein-Gulyaev (BG) modes in the theory of surface acoustic wave devices to conveniently describe and analyze the relationship between the acoustic modes and the electromagnetic modes in the nanoscale regime.

Chapter 5 offers a new source of understanding of heat transport in the superlattices via the description of the effective medium model as an additional and a faster heat transport mechanism. We explore the piezoelectric stiffening effect on GaN and AlN elastic layers and the possibility of using the stiffened elastic constants to increase the rate of heat transport away from the hot spot.

Chapter 6 describes a TCAD simulation approach of silicon nanowire-based ion sensitive field effect transistor (ISFETs). We employ a site-binding model along with a quantum corrected model for electron transport to provide prospects for the fabricated devices.

In Chapter 7, we offer perspectives on future directions, summarize the major results and give concluding remarks.

[1]Chapter 2

Phonon kinematics

2.1 Introduction

Self-heating in electronic and optoelectronic devices is a substantial problem in situations with high current density [69], [70]. This is particularly important where nonuniform distribution of current density occurs through miniaturization or in devices based on two-dimensional electron gases (2DEG) [71]. Self-heating is difficult to remove in most devices and therefore detrimental to their performance. It seems fitting to perceive electron-phonon interactions and self-heating phenomena to further understand the transport properties aimed at using III-nitride materials in high-power and high-frequency applications.

In this chapter, we demonstrate that phonons are confined in nanostructures and their corresponding wavevectors can be well-described by continuum models of phonons. We shall also see that the dielectric and elastic continuum models in nanostructures may be applied to describe the Fröhlich and piezoelectric interactions and deformation potential in a variety of nanostructures including quantum wells.

In polar materials – particularly of interest nitride-based – electron-phonon scattering (also known as Fröhlich scattering) governs the dissipation channels of hot electron energy. This interaction manifests itself upon application of an electric field, at which electrons are accelerated until their energy is sufficient to emit optical phonons. Due to the form of the Fröhlich interaction, phonons produced by this carrier relaxation process are mainly zone-center longitudinal optical (LO) phonons [72]. Because the LO phonons behave like standing waves, they must decay into traveling acoustic waves to dissipate energy

[1] This chapter is partially published in IOP Journal of Physics: Condensed Matter, [295].

from the self-heating region [73]. Investigation of the intrinsic phonon decay of optical phonons into heat-carrying acoustic phonons is critical to understand the hot phonon bottleneck issue and to mitigate the associated device problems. Therefore, we investigate the most popular decay channels in this chapter.

2.2 Dielectric continuum model

The dielectric continuum model of optical phonons in polar materials is based on the concept that the electric polarization $\vec{P}(\vec{r})$ is created primarily due to the lattice vibrations in the crystal. For a medium of dielectric constant $\epsilon(\omega)$, the polarization $\vec{P}(\vec{r})$ is described in terms of the equations of electrostatics [74]–[76]. The potential $\Phi(\vec{r})$ associated with $\vec{P}(\vec{r})$ is given by Kim and Stroscio (1990) [77]

$$\nabla^2\Phi(\vec{r}) = 4\pi\nabla.\vec{P}(\vec{r}) \tag{2.1}$$

and the electric field $\vec{E}(\vec{r})$ is given by

$$\vec{E}(\vec{r}) = -\nabla\Phi(\vec{r}) \tag{2.2}$$

Moreover, $\vec{E}(\vec{r})$ and $\vec{P}(\vec{r})$, in medium n are related through the dielectric susceptibility, $\nu_n(\omega)$:

$$\vec{P}(\vec{r}) = \nu_n(\omega)\vec{E}(\vec{r}) \tag{2.3}$$

where

$$\nu_n(\omega) = \frac{\epsilon_n(\omega) - 1}{4\pi} \tag{2.4}$$

with

$$\epsilon_n(\omega) = \epsilon_n(\infty)\frac{\omega^2 - \omega_{LO,n}^2}{\omega^2 - \omega_{TO,n}^2} \tag{2.5}$$

The dielectric continuum model has been applied to describe the properties of dimensionally confined optical phonons in many electronic and optoelectronics devices fabricated from semiconductor

nanostructures [78], [79]. These include quantum wells, superlattices, quantum wires, and quantum dots. To illustrate the basic features of the dielectric continuum model of optical phonons, the case of confinement in just one dimension as in a quantum well or superlattice is considered first. Atoms vibrate with different modes within the crystal, and as a result, different types of phonons will be produced.

The dielectric continuum model predicts a set of confined optical phonon modes commonly referred to as the slab modes [80]. These slab modes may be determined by applying the dielectric continuum model and by imposing electrostatic boundary conditions at each heterointerface [81]. The normal-mode frequencies and orthogonal confined phonon modes are obtained through the simultaneous solution of the equations arising from the dielectric continuum model, subject to the boundary conditions that the potential, $\Phi(\vec{r})$ and the normal component of $D(\vec{r})$ are continuous at each heterointerface [82]. Taking the heterointerfaces to be normal to the z-direction, the electrostatic potential $\Phi_i(\vec{r})$ in the region $\vec{R}_i = (z_i, z_{i+1})$ and its two-dimensional Fourier transform $\Phi_i(\vec{q}, z)$ are related by

$$\Phi_i(\vec{r}) = \sum_q \Phi_i(\vec{q}, z) e^{-i\vec{q}.\vec{r}} \qquad 2.6$$

where $\vec{q}$ is the two-dimensional wavevector in the ($x - y$)-plane.

2.3 Elastic continuum model

The acoustic phonons are described using the elastic continuum model of phonons. The model describes adequately the acoustic phonons of confined nanostructures of two atomic monolayers [83], [84]. From Hooke's law $T = Ye$ where e is the strain and Y is the proportionality constant or Young's modulus.

Consider an element dx between x and $x + dx$ along a structure. The essential equations of elastic deformation are strain-displacement equation and equation of motion of particle (force equation) [85]. In

In 1-D structure, the strain is written as $e = \frac{\partial u}{\partial x}$, where $u(x,t)$ is the elastic displacement along the x axis. The force is given by Newton's second law as

$$\rho(x)Adx\frac{\partial^2 u(x,t)}{\partial t^2} = [T(x+dx) - T(x)]A \tag{2.7}$$

$$T(x+dx) - T(x) = \left(\frac{\partial T}{\partial x}\right)dx = \left(\frac{Y\partial e}{\partial x}\right)dx = \left(Y\frac{\partial^2 u}{\partial x^2}\right)dx \tag{2.8}$$

where S_j is given by

$$S_1 = S_{xx} = \frac{\partial u}{\partial x}, \qquad S_2 = S_{yy} = \frac{\partial v}{\partial y}, \qquad S_3 = S_{zz} = \frac{\partial \omega}{\partial z} \tag{2.9}$$

$$S_4 = S_{yz} = S_{zy} = \frac{1}{2}\left(\frac{\partial \omega}{\partial y} + \frac{\partial v}{\partial z}\right),$$

$$S_5 = S_{xz} = S_{zx} = \frac{1}{2}\left(\frac{\partial u}{\partial z} + \frac{\partial \omega}{\partial x}\right),$$

$$S_6 = S_{xy} = S_{yx} = \frac{1}{2}\left(\frac{\partial u}{\partial y} + \frac{\partial v}{\partial x}\right),$$

and T_i are of

$$T_1 = T_{xx}, \qquad T_2 = T_{yy}, \qquad T_3 = T_{zz}, \qquad T_4 = T_{yz} = T_{zy}, \tag{2.10}$$

$$T_5 = T_{xz} = T_{zx}, \qquad T_6 = T_{xy} = T_{yx}$$

for $c_{ij} = c_{ji,}$ only 21 distinct elements are needed to construct the 6×6 matrix of c_{ij}. In cubic crystal, c_{ij} matrix is given as [80]

$$\begin{pmatrix} c_{11} & c_{12} & c_{12} & 0 & 0 & 0 \\ c_{12} & c_{11} & c_{12} & 0 & 0 & 0 \\ c_{12} & c_{12} & c_{11} & 0 & 0 & 0 \\ 0 & 0 & 0 & c_{44} & 0 & 0 \\ 0 & 0 & 0 & 0 & c_{44} & 0 \\ 0 & 0 & 0 & 0 & 0 & c_{44} \end{pmatrix} \tag{2.11}$$

whereas in wurtzite crystal, c_{ij} is of the form [80]

$$\begin{pmatrix} c_{11} & c_{12} & c_{13} & 0 & 0 & 0 \\ c_{12} & c_{11} & c_{13} & 0 & 0 & 0 \\ c_{13} & c_{13} & c_{33} & 0 & 0 & 0 \\ 0 & 0 & 0 & c_{44} & 0 & 0 \\ 0 & 0 & 0 & 0 & c_{44} & 0 \\ 0 & 0 & 0 & 0 & 0 & (c_{11-}c_{12})/2 \end{pmatrix} \quad 2.12$$

However, for zinc-blende crystal, only 3 distinct elements are needed c_{11}, c_{22} and c_{44}. For isotropic cubic medium, c_{ij} can be represented using two constants λ and μ which are known as Lame's constants [86]

$$\lambda = c_{12} = c_{13} = c_{21} = c_{23} = c_{31} = c_{32}$$

$$\mu = c_{44} = c_{55} = c_{66} = \frac{1}{2}(c_{11} - c_{12})$$

$$\lambda + 2\mu = c_{11} = c_{22} = c_{33} \quad 2.13$$

Therefore, for an isotropic case we can write

$$T_{xx} = \lambda(S_{xx} + S_{yy} + S_{zz}) + 2\mu S_{xx} = \lambda\nabla + 2\mu S_{xx,}$$

$$T_{yy} = \lambda(S_{xx} + S_{yy} + S_{zz}) + 2\mu S_{yy} = \lambda\nabla + 2\mu S_{yy,}$$

$$T_{zz} = \lambda(S_{xx} + S_{yy} + S_{zz}) + 2\mu S_{zz} = \lambda\nabla + 2\mu S_{zz,}$$

$$T_{yz} = \mu S_{yz,} \quad T_{zx} = \mu S_{zx}, \quad T_{xy} = \mu S_{xy} \quad 2.14$$

three dimensional generalizations are given by

$$\rho\frac{\partial^2 u}{\partial t^2} = \frac{\partial T_{xx}}{\partial x} + \frac{\partial T_{yx}}{\partial y} + \frac{\partial T_{zx}}{\partial z} = (\lambda + \mu)\frac{\partial \Delta}{\partial x} + \mu\nabla^2 u$$

$$\rho\frac{\partial^2 v}{\partial t^2} = \frac{\partial T_{xy}}{\partial x} + \frac{\partial T_{yy}}{\partial y} + \frac{\partial T_{zy}}{\partial z} = (\lambda + \mu)\frac{\partial \Delta}{\partial y} + \mu\nabla^2 v$$

$$\rho\frac{\partial^2 \omega}{\partial t^2} = \frac{\partial T_{xz}}{\partial x} + \frac{\partial T_{yz}}{\partial y} + \frac{\partial T_{zz}}{\partial z} = (\lambda + \mu)\frac{\partial \Delta}{\partial z} + \mu\nabla^2 w \quad 2.15$$

The three-force equation is also given as

$$\rho \frac{\partial^2 u_\propto}{\partial t^2} = \frac{\partial T_{\alpha\beta}}{\partial r_\beta} \tag{2.16}$$

where

$$T_{\alpha\beta} = \lambda S_{\alpha\alpha}\delta_{\alpha\beta} + 2\mu S_{\alpha\beta} \tag{2.17}$$

The solutions for the displacement between particles are described as

$$u = \frac{\partial \phi}{\partial x} + \frac{\partial \Psi_x}{\partial x} - \frac{\partial \Psi_y}{\partial z}$$

$$v = \frac{\partial \phi}{\partial y} + \frac{\partial \Psi_x}{\partial z} - \frac{\partial \Psi_y}{\partial x}$$

$$w = \frac{\partial \phi}{\partial z} + \frac{\partial \Psi_y}{\partial x} - \frac{\partial \Psi_x}{\partial y} \tag{2.18}$$

where

$$\nabla^2 \phi = \frac{1}{c_l^2}\frac{\partial^2 \phi}{\partial t^2}$$

$$\nabla^2 \Psi_i = \frac{1}{c_t^2}\frac{\partial^2 \Psi_i}{\partial t^2};\ \ i = x, y, z$$

$$c_l^2 = (\lambda + 2\mu)/\rho$$

$$c_t^2 = \lambda/\rho \tag{2.19}$$

The linear solution denotes the longitudinal acoustic modes and the spherical solution denotes the transverse acoustic modes [87].

2.4 Momentum relaxation of bulk wurtzite GaN

Both energy and momentum relaxation processes are considered in this thesis upon studying the scattering of electron through phonons considering the effects of temperature and electric field. It can be found that under different electric fields the relaxation mechanisms are much different. The energy and momentum

relaxation processes are different for each nitride structures [88]. In low frequency fields, the dominant mechanism is the scattering by polar optical phonon for energy relaxation and the scattering by ionized impurity, acoustic phonon and polar optical phonon for momentum relaxation. Meanwhile, in high electric fields, the inter-valley scattering is purported to be the primary mechanism for energy relaxation, while the polar optical phonon and inter-valley scattering are claimed to be the primary mechanisms for momentum relaxation [89]–[92]. The momentum relaxation is time consuming compared to the energy relaxation, this has been attributed to the approximate correction method [93] and to the fact that nearly all scattering mechanisms cause momentum relaxation, but only polar optical phonon and inter-valley scattering cause energy relaxation [94]. Both energy and momentum relaxation processes are temperature-dependent [91], [95], [96]. Finally, the energy and momentum relaxation rates as a function of electron temperature are given as in Eqn. 2.20 [97], which will be used to model the relaxation time and heat transport in the following chapter.

$$W(\mathbf{k}) \tag{2.20}$$

$$= \frac{e^2\sqrt{m^*}}{2\sqrt{2}\pi\hbar}\int_0^{2\pi} d\phi \int_0^{\pi} \sin\theta \, d\theta \left(n_{ph} + \frac{1}{2} \pm \frac{1}{2}\right)$$

$$\times \frac{\sigma}{\sqrt{E_k cos^2\phi' \mp \hbar\omega}} \frac{1}{\omega} \frac{(\omega_\perp^2 - \omega^2)^2(\omega_z^2 - \omega^2)^2}{(\varepsilon_\perp^0 - \varepsilon_\perp^\infty)\omega_\perp^2(\omega_z^2 - \omega^2)^2 \sin^2\theta + (\varepsilon_z^0 - \varepsilon_z^\infty)\omega_z^2(\omega_\perp^2 - \omega^2)^2 \cos^2\theta}$$

$$\sigma = \begin{cases} 0 & for\ \cos(\phi') < \sqrt{\hbar\omega/E_k} \\ 2 & otherwise \end{cases},$$

Here, n_{ph} is the phonon occupation number, $\cos(\phi') = \sin\theta \sin\theta_k \cos\phi + \cos\theta \cos\theta_k$, where θ_k represents the angle between the initial electron wave vector and the c-axis, θ is the angle between the wave vector and the c-axis, ϕ is the azimuthal angle between the electron wave vector and the phonon wave vector, E_k is the electron energy and $\hbar\omega$ is the phonon energy (transition energy), $\varepsilon_\perp^0$ is the dielectric

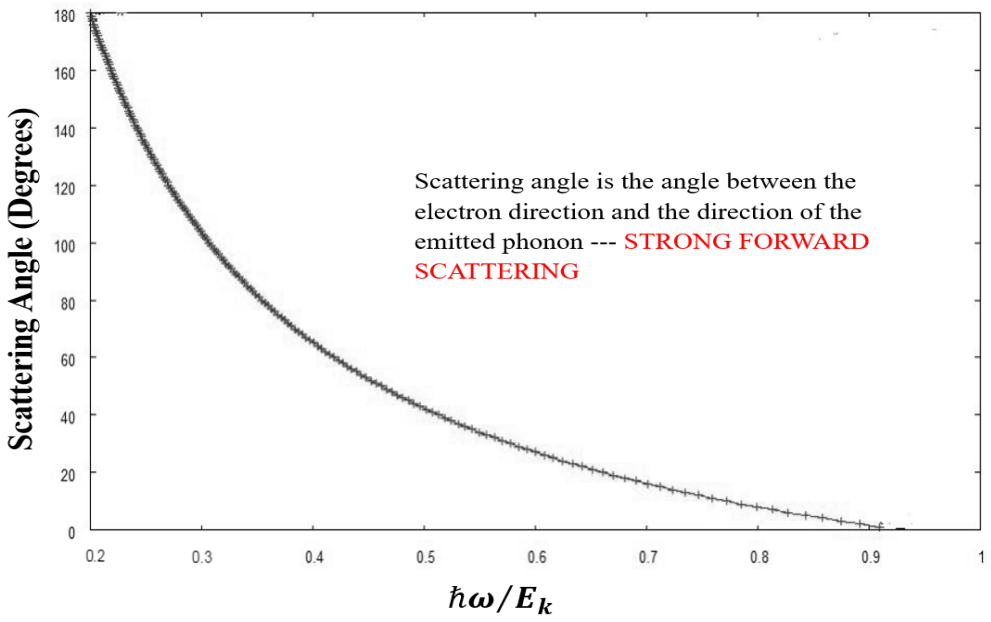

Fig. 1. Scattering angle versus the rate of phonon emission with respect to the hot electron.

---

constant associated with the direction perpendicular to the c-axis and ε_z^0 is the dielectric constant associated with the direction parallel to the c-axis.

2.5 Matrix element of bulk phonons

To describe the probability of a transition of an electron with wavevector k in the subband by a phonon of wavevector q, the matrix element for wurtzite can be defined as [97]

$$|M_q|^2 = \frac{2\pi e^2\hbar}{V\omega}\cdot\frac{1}{q^2}\cdot\left(n_{ph}+\frac{1}{2}\pm\frac{1}{2}\right) \cdot \frac{(\omega_\perp^2-\omega^2)^2(\omega_z^2-\omega^2)^2}{(\varepsilon_\perp^0-\varepsilon_\perp^\infty)\omega_\perp^2(\omega_z^2-\omega^2)^2\sin^2\theta+(\varepsilon_z^0-\varepsilon_z^\infty)\omega_z^2(\omega_\perp^2-\omega^2)^2\cos^2\theta} \quad 2.21$$

The largest scattering probability for small q can be justified by the $1/q$ dependence in Eqn. 2.21. We are interested in small q values as they contribute significantly to the electron-phonon coupling above the

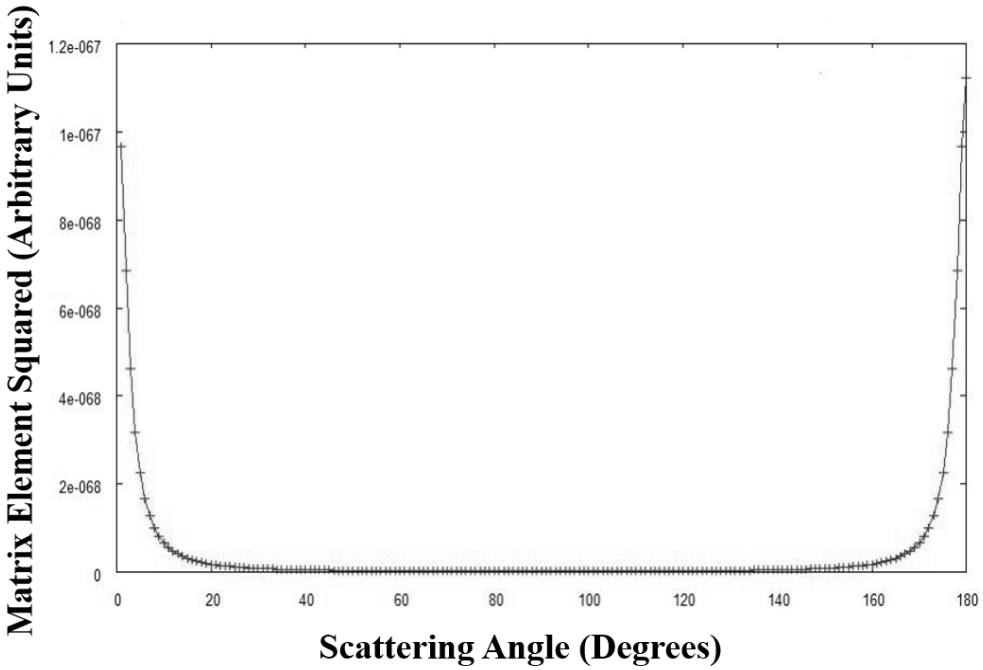

Fig. 2. Absolute square of the matrix element for bulk optical phonons in GaN versus the scattering angle for an electron having an energy of 1 eV.

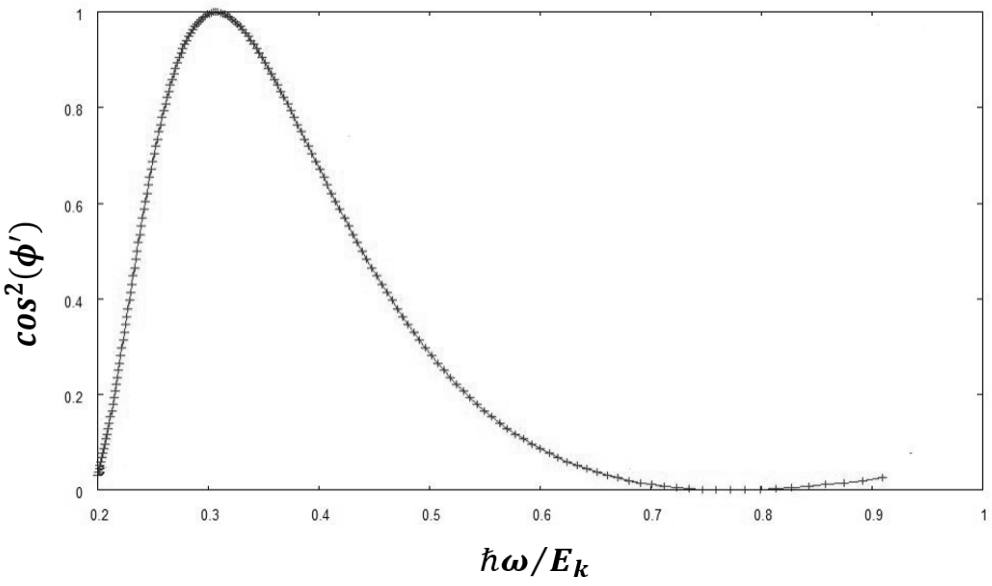

Fig. 3. Angular probability function and variation of the step function (σ) for phonons with energies smaller than the electron energy in bulk GaN.

phonon emission threshold when phonons strongly interact with electrons in the GaN structure, thus creating phonons along the heterointerface which combine mixing of LO and TO modes.

Since the matrix element follow the boundary conditions $q_y = \pm\frac{m\pi}{L_y} and\ q_z = \pm\frac{n\pi}{L_z}$ which results in $M_{avg}^2 = \frac{1}{a}\int_{-\frac{a}{2}}^{\frac{a}{2}} cos^2(q_z z)dz$, therefore, it has been illustrated that the lifetime of optical phonon confined in the quantum well is half of the mean lifetime of the unconstrained phonon [98].

2.6 Phonon decay channels

Investigations have suggested that hot electrons that possess densities greater than 10^{17} cm^{-3} can emit a nonequilibrium supply of hot phonons, which slow down the energy relaxation process [99], [100]. As has been discussed briefly in chapter 1, the phonon generation time is about 9 fs for GaN, compared to about 115 fs in GaAs, but decay time is strongly density dependent [52], [101]–[103].

Based on the group theory, phonon modes that coexist in the hexagonal wurtzite structure are E_2(high), E_2(low), A_1(LO), A_1(TO), E_1(LO), E_1(TO) and $2B_1$ [104]. The phonon dispersion curves along several high-symmetry directions along with the decay mechanisms for different modes including the dominant A_1(LO) phonon are depicted in different research studies [104]–[107]. It turns out that the electron-TO scattering rate is more than two orders of magnitude lower than the electron–LO scattering rate, and therefore, the LO phonon modes are most important when considering electron scattering mechanisms at moderate to high fields in GaN. Also, the Ridley process occurs in a much longer characteristic timescales than those associated with electron–phonon scattering or LO phonon emission [108]. As such, the density of LO phonons can build up and cause even more scattering between the electrons and these phonons. The

Table 1. Decay channels and lifetimes of optical phonon modes in GaN and AlN [104].

	Channel	**Lifetime (ps)**		**Energy (meV)**
		GaN	**AlN**	
A_1(LO)	(a) E_1(TO) + TA(LA)	1.44	0.8	69.34 + 22.30
	(b) E_1(TO) + E_2^1			
E_1(LO)	E_2^2 + LA(TA)	0.94	0.7	75.01 + 17.36
E_2^2	LA + LA + LA	1.3	1.7	23.56
	B_1^1 + LA			
	E_2^1 + TA			
A_1(TO)	E_2^2 + E_2^2	0.91	1.2	33.10
	LA + TA			
E_1(TO)	B_1^1 + B_1^1	1.55	1.8	34.72

TO phonon lifetime is known to be shorter than the LO mode [109], [110]. Furthermore, TO exhibits weak temperature dependence which implies a small anharmonic coupling for this mode [111]–[113].

As phonons build up and exceed the equilibrium concentration of phonons, we refer to them as "hot." The time associated with the disintegration of these hot phonons into the short lifetime TO and more mobile LA phonons can be referred to as the hot phonon lifetime [114]. Clearly, this lifetime is responsible for the density of the phonons that are built up in the channel. In GaN, phonon lifetime measurements deduced by time-resolved Raman technique versus the carrier concentration between 10^{16} and 2×10^{19} cm^{-3} indicate decreasing lifetime with increasing carrier concentration, which also include the fluctuation technique [115]. Essentially, for the A_1(LO), the lifetime decreases from 2.5 ps for 10^{16} cm^{-3} to about 0.35 ps for

10^{19} cm^{-3}, the latter being consistent with that deduced from the 2DEG [116]. Also, as the bulk electron density is increased further, the LO phonon lifetime goes through a minimum, corresponding to the resonance with plasmons, and then increases again because of the slower response [116].

Different important decay channels in nitride based III-V semiconductors, which are being considered in this thesis, are summarized as shown in Table 1. In GaN, process $A_1(LO) \rightarrow E_2^2$ + TA is reported to have the main contribution providing 60% of the decay [25]. In AlN, the dominant processes are $A_1(LO) \rightarrow A_1(TO)$ + TA (35%), $A_1(LO) \rightarrow E_2^2$ + LA (23%), $A_1(LO) \rightarrow B_1^2$ + TA (15%) and $A_1(LO) \rightarrow E_2^2 + E_1^2$ (16%) over the entire temperature range. In InN, $A_1(LO) \rightarrow E_1(TO) + E_1^2$ and $A_1(LO) \rightarrow A_1(TO) + E_1^2$ are the dominant processes accounting for about 60% toward the decay with channel $A_1(LO) \rightarrow E_2^2 + E_1^2$ providing a 20% contribution.

2.6.1 LO phonon decay

In the simplest geometry, Raman scattering is produced and measured in backscattering configuration [117], [118]. For example, for the $A_1(LO)$ mode, the scattering configuration can be denoted by the notation $z(xx)\bar{z}$, where z represents the incident laser propagation direction in the [0001] direction, where z represents the scattered light propagation direction post the energy relaxation process in the [0001] direction, x represents the polarizations of the electric field of the incident and scattered photons, respectively [119].

The zone-center optical phonons decay to acoustic phonons due to lattice anharmonicity via Klemens channel primarily in GaAs [120] and Ridley channel in GaN [50] depending on the energy level of acoustic phonons. In polar materials, collective excitation of energetic electrons can interact with LO phonons via longitudinal electric field. LO modes can be considered for estimation of bulk carrier concentration [121].

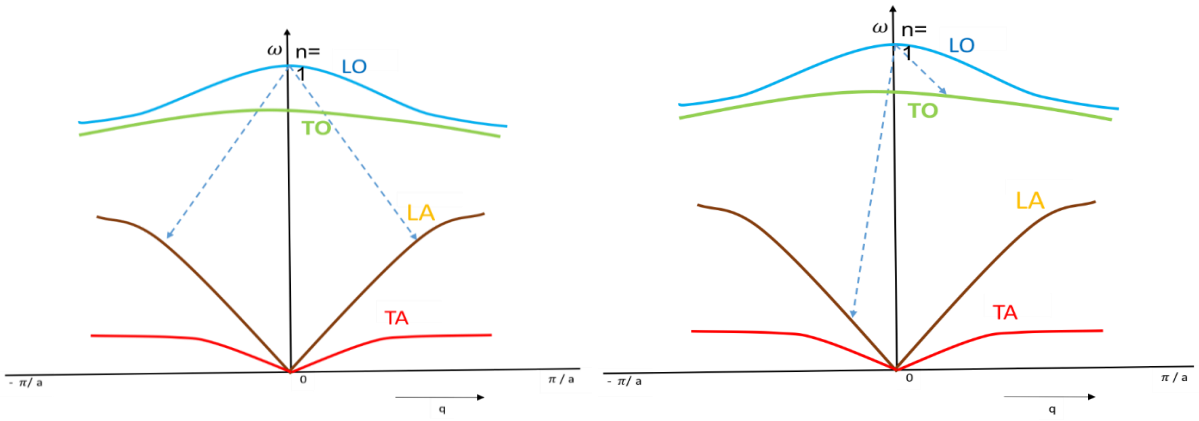

Fig. 4. Dispersion curves of phonons for optical and acoustic branches in linear diatomic chain. (a) depicts the decay of LO mode into two LA modes while (b) depicts the decay of LO mode into TO and LA modes.

Based on the perturbation theory, anharmonic three (four) phonon coupling denotes to these important processes: either one single phonon decays into two (three) phonons, or two (three) phonons combine to form a single phonon [122]–[124]. The decay mechanism of a phonon can be obtained from the temperature dependent frequencies and linewidths of phonon modes [125]. Therefore, Raman spectroscopy is considered as an important tool that has been used by many researchers to obtain the frequencies and linewidth of different phonon modes in a variety of structures [111], [112], [117]–[128].

2.6.2 Dominant decay Mechanisms

The presence of population in the final phonon modes gives rise to the temperature dependence of the lowest order anharmonic decay process. This process is defined according to [129]

$$\Gamma_{ph-ph}(T) = \Gamma_0[1 + n(\hbar\omega_1, T) + n(\hbar\omega_2, T)] \qquad 2.22$$

where Γ_0 is the decay time of LO phonon at $T = 0$ K and $n(\hbar\omega_1, T)$ and $n(\hbar\omega_2, T)$ are the occupation numbers of the lower energy phonons. This expression works for a single dominant decay mode but can be generalized to incorporate additional decay channels. From Eqn. 2.22, phonon lifetimes can be

calculated as $\tau = \hbar/\Gamma$, since the analysis of the temperature dependence of the phonon lifetime provides information about the dominant decay channels.

Now, since the lifetime of LO phonons has a larger temperature dependence than what has been reported experimentally, Tsen et al. (2007) have concluded that the decay of A1(LO) phonons into small wave vector LO and small wave vector LA or TA modes is not a likely mechanism [115]. On the other hand, it has been suggested that the decay channel of zone-center A_1(LO) phonons in wurtzite structures into a large wave vector TO phonon (E_1(TO)), assuming that the TO phonon dispersion curve is relatively flat across the Brillouin zone, and a large wave vector LA or TA phonon, as shown in Table 1, fits many experimental data [105], [130]. Moreover, it was reported that high energy A_1(LO) and E_1(LO) lifetimes cannot be modeled by using a symmetric phonon decay process [131]. For the A_1(LO) mode, it was suggested, both theoretically [50] and experimentally [115] that an asymmetric three-phonon process is the dominant decay pathway, by which the LO phonon deconstructs into a TO and a LA mode.

E_2^2 decays through the symmetric decay channel of the E_2^2 phonon into two phonons of half the father phonon energy with opposite wave vectors. But Kuball, Hayes, Shi and Edgar (2001) reported with a good accuracy that a symmetric decay is not the dominant decay channel for the E_2^2 phonons [132]. On the other hand, the decay of the E_2^2 phonon into a high-energy and a low-energy phonon, i.e., an asymmetric phonon decay, agree with the experimental data very well [131].

Studies on Raman spectra show the likely production of A_1(TO) and E_1(TO) phonon modes when the backscattering geometry is considered [133]. It was also shown that A_1(LO) and E_1(LO) modes may produce the forbidden E_1(LO) mode via mode mixing when the backscattering is not parallel or perpendicular to an optical axis [134]. In AlN, a decay channel into two phonons of about equal energy and an additional three-phonon decay channel were introduced for A_1(TO) and E_1(TO) [52], however, the

lack of experimental verification suggests that the symmetric phonon decay is not the dominant decay channel for the TO phonon [132].

LA has a higher probability of decaying into TA modes as was suggested in the calculations by Bovensiepen, Petek and Wolf (2010) that the dominant decay mechanism in cubic crystals is that LA decays into two equal energy TA modes [135]. Likewise, Klemens' prediction was verified by Tamura (1984) that LA primarily decays into two TA modes in isotropic mediums [136]. The calculations were obtained for various crystals including Si, Ge, GaAs, LiF and NaF. Nevertheless, in 2017, Liu et al. validated Herring's theory [137] that the anharmonic up-conversion scattering process TA → LA + TA is responsible for the decay in a sample of InGaN/GaN quantum well grown on GaN wurtzite buffer [138]. Therefore, while it is established in isotropic crystals that TA phonons cannot decay through splitting into a pair of low-frequency phonons [139], there still seem to be disagreements on the magnitude and the dominant decay channel of the acoustic phonons.

2.7 Summary

We have presented the nonequilibrium distribution of the longitudinal optical (LO) and the rates of the decay and the mechanisms by which it occurs as they are of primal importance to the development of next generation devices. Evidently, the lifetime of the emitted phonons is over an order of magnitude longer than the characteristic emission time, which leads to a nonequilibrium distribution of these polar LO phonons. Only through efficient decay of these hot phonons into other phonon modes is this effect minimized and performance then maximized.

[2]Chapter 3

Electron-optical phonon interaction in III-V nitride structures

3.1 Introduction

Here, we present a detailed theoretical analysis of the interaction between electrons and optical phonons of interface and confined modes in wurtzite quantum well heterostructures based on the uniaxial dielectric continuum model. We start by examining the concepts of confinement of the optical and acoustic phonons within a quantum well of nanostructured materials on the vibrational spectra. We numerically calculate the formalism describing the interface and confined mode optical phonon dispersion relation, electron–phonon scattering rates, and average group velocity of emitted optical phonons. The dispersion relation of the interface phonons shows a convergence to the resonant phonon frequencies with a steep slope around the zone center indicating a large group velocity. At the onset of interface phonon emission, the average group velocity is small due to the large contribution of interface and confined mode phonons with close-to-zero group velocity, but eventually increases up to larger values than the bulk acoustic phonon velocity along the wurtzite crystal *c*-axis (8 nm/ps). By adjusting the thickness in the double heterostructure, the average group velocity can be engineered to become larger than the velocity of acoustic phonons at a specific electron energy. This suggests that the high group velocity interface mode optical phonons can be exploited to remove heat more effectively and reduce junction temperatures in GaN-based heterostructures [140].

[2] This chapter is partially published in *Nature Scientific Reports*, [140], *PLOS One*, [186], *Diamond and Related Materials*, [217] and *IOP Journal of Physics D: Applied Physics*, [204].

3.2 Phonon confinement

Phonon modes in QWs can be classified as confined and interface modes according to the dielectric continuum model. The independent electron and phonon confinement changes qualitatively the contribution of interface phonons to electron-phonon scattering [141]. In QWs such as GaAs/AlAs, the contribution of GaAs-like and AlAs-like interface phonon modes to the electron scattering depends on their penetration depth into a GaAs layer. In low-dimensional structures the interface modes are joint modes of both materials as well as the half-space modes in the barriers.

Considering the theory of electron-phonon interactions in a dielectric slab given by Licari and Evrard (1977) [142]. In this theory, a single dielectric slab of infinite extent in the x- and y-directions is situated with its faces at $-a$ and $+a$ and with its surface bounded by a vacuum in the regions with $|Z| \geq a$. Within this dielectric slab $\nabla.\vec{D}(\vec{r}) = 0$, where, as usual, $\vec{D}(\vec{r}) = \epsilon(\omega)\vec{E}(\vec{r}) = \vec{E}(\vec{r}) + 4\pi\vec{P}(\vec{r})$. Defining a scalar potential through $\vec{E}(\vec{r}) = -\nabla\phi(\vec{r})$ and, since the system is translationally invariant in the (x, y)-plane, taking $\phi(\vec{r})$ to be of the form of $\phi(\vec{r}) = \phi(z)e^{i\vec{q}_{||}\vec{r}_{||}}$, where $\vec{r}_{||} = (x, y)$ and $\vec{q}_{||} = \left(q_x, q_y\right)$, it follows that

$$\epsilon(\omega)\left(\frac{\partial^2}{\partial z^2} - q_{||}^2\right)\phi(z) = 0 \tag{3.1}$$

where $q_{||} = q_x^2 + q_y^2$. This equation is satisfied when $\epsilon(\omega) = 0$ or when $\left(\frac{\partial^2}{\partial z^2} - q_{||}^2\right)\phi(z) = 0$, $\phi(z)$ is a solution of the wave equation. In the case of $\epsilon(\omega) = 0$, Licari and Evrard took this solution (as did Fuchs and Kliewer, 1965, and Kliewer and Fuchs, 1966a, b) to be of the form [74]–[76]

$$\phi(z) = \sum_{q_z}(\phi_1 sinq_z z + \phi_2 cosq_z z), \tag{3.2}$$

inside the slab i.e., in the range $(-a, +a)$. Outside the slab, where $\epsilon = 1$, the solutions have the form $\phi(z) = \emptyset_{\pm} exp\left(\pm\sqrt{q_x^2 + q_y^2}z\right)$, where the positive sign applies for $z \leq -a$ and the negative sign applies

for $z \geq +a$. The constants $\emptyset_1$, $\emptyset_2$, $\emptyset_+$ and $\emptyset_-$ are determined by the usual boundary conditions that the tangential component of $\vec{E}$ and the normal component of $\vec{D}$ are continuous at $z = \pm a$. From these conditions it is seen that $\emptyset_\pm = 0$ and it is thus clear that for this mode $\phi(z)$, $\vec{E}(\vec{r})$ and $\vec{D}(\vec{r})$ are zero in the regions surrounding the slab; in particular $\phi(z)$ vanishes at the surfaces of the layer, where $z = \pm a$. For z in the range $(-a, +a)$, the boundary conditions may be satisfied by taking either $\emptyset_1 = 0$ or $\emptyset_2 = 0$, so that there are two solutions corresponding to the two polarization vectors

$$\overrightarrow{P_+^{\mathcal{J}}}(\vec{r}) = \frac{\phi_2}{4\pi a} e^{i\vec{q}_{||}\cdot\vec{r}_{||}} i\left(i\vec{q}_{||} a \cos\frac{\mathcal{J}\pi}{2a}\mathcal{Z} - \hat{\vec{z}}\frac{\mathcal{J}\pi}{2a}\sin\frac{\mathcal{J}\pi}{2a}\mathcal{Z}\right), \qquad 3.3$$

$$\mathcal{J} = 1,3,5, \ldots,$$

$$\overrightarrow{P_-^{\mathcal{J}}}(\vec{r}) = \frac{\phi_1}{4\pi a} e^{i\vec{q}_{||}\cdot\vec{r}_{||}} i\left(i\vec{q}_{||} a \sin\frac{\mathcal{J}\pi}{2a}\mathcal{Z} - \hat{\vec{z}}\frac{\mathcal{J}\pi}{2a}\cos\frac{\mathcal{J}\pi}{2a}\mathcal{Z}\right), \qquad 3.4$$

$$\mathcal{J} = 2,4,6, \ldots,$$

where $\hat{\vec{z}}$ is the unit vector in the z-direction. Of course, $\nabla.\vec{D}(\vec{r}) = 0$ implies that $\nabla^2\Phi(\vec{r}) = -\nabla.\vec{E}(\vec{r}) = +4\pi\nabla.\vec{P}(\vec{r})$. These standing modes are now widely known as the confined optical phonon modes in a slab.

According to Pozela et al. (1994) [141], "[t]he physical nature of the confinement of optical phonons and electrons is different. Electrons are confined due to electron wave reflections at electric potential barriers. The electron QW is the well between potential barriers. Phonons are confined due to multiple reflections of optical phonon waves at the heterointerfaces between semiconductor layers having a large difference of optical phonon frequencies, and the optical phonon QW is formed in the layer sandwiched between two semiconductors. Independent electron and phonon confinement allows interface phonon scattering to be reduced by shifting the electron QW with respect to the phonon one." The confined modes obtained from

the dielectric continuum model are found to give a reasonably good representation of these modes in quantum wells and superlattices.

Phonon confinement is important for the description of electron-phonon interaction mechanisms [143] as it increases electron-phonon scattering rates [144]–[146], causes substantial nonlinearities in the dispersion relations of acoustic phonon modes and modifies the phonon density of states [147]. Phonon confinement significance is clearly implied when the transverse dimensions of a quantum well are smaller than the phonon coherence length [143] and should be considered to obtain accurate estimates for electron-phonon scattering in low-dimensional nanostructures [148]–[150].

3.3 Confined and interface optical phonon dispersion in wurtzite quantum wells

Dispersion relations for polar optical phonon modes in multiple wurtzite quantum wells (QW's) are obtained within the framework of the dielectric continuum model which was presented in chapter 2. Three QWs will be considered: (a) AlN/GaN/AlN; (b) GaN/InGaN/GaN; and (c) AlN/AlInN/AlN.

It is well established that the anisotropy of the dielectric medium causes a number of qualitative irregularities in the phonon spectrum [78], [151]–[154]. There are many types of modes in the double heterostructure system under study such as [153]–[155]: (1) Interface modes whose amplitude is at its maximum at the interface and decreases exponentially away from the interface. (2) Half-space modes of bulk phonons and no polarization in the opposite layer and whose polarization parallel to the interface is very small or vanishes at the interface. (3) Propagating modes which are created by the overlapping of the characteristic phonon frequencies. (4) Confined modes which are characterized by the leakage of the potential through the interface and their finite dispersion leads to the formation of bands of allowed frequencies. Among these four optical phonon modes, the electrons that are confined in the Nitride based

quantum well mostly interact with the interface and confined phonons; the effect of the half-space and propagating modes on the electrons is negligible in this system [156]. Here, therefore, we only consider the electron scattering with interface and confined mode optical phonons.

3.3.1 AlN/GaN/AlN QWs

GaN-based semiconductors are of great interest in the electronics and optoelectronics groups because they possess large electronic bandgaps (3.4 eV) suitable for fabricating semiconductor lasers with wavelengths in blue and ultraviolet [157] and electronic devices designed to withstand high electric fields (3.3 MV/cm) and elevated temperatures (700°C) [158]. In particular, AlGaN/GaN high electron mobility transistors (HEMTs) are among the most promising devices for high-power applications [159]. The spontaneous and piezoelectric polarization fields of this heterostructure allow the GaN layer to form a high-density electron channel through which electrons can flow with high saturation velocity (2.5×10^7 cm/s); this is partly due to the optical phonons with high energy ($\hbar\omega_{LO} = 92$ meV) in GaN [160]. The electron velocity saturation occurs with the onset of emission of these optical phonons and therefore their energy roughly determines the electron saturation velocity according to $v_0 \approx [\hbar\omega_{LO}/m]^{1/2}$, where m is the effective electron mass. Taking a closer look into the material, the large mismatch between the cation and anion masses causes a large splitting between the energies of the optical and acoustic phonon branches which raises the energy of optical phonons [161]. The drawback associated with these high energy optical phonons is their short interaction time with electrons compared to the long decay time into acoustic phonons.

In the double heterostructure of interest in this subsection, which is a GaN quantum well sandwiched by two AlN layers (AlN/GaN/AlN), there exists four distinct classes of optical phonon modes [153]: the interface, confined, half-space, and propagating modes. Among these four optical phonon modes, the electrons that are confined in the GaN quantum well mostly interact with the interface and confined

Table 2. Properties of prominent III-V nitride materials

	GaN	**AlN**	**BN**	**InP**	**InN**
$A_1(LO)(cm^{-1})$	734 [105]	890 [105]	1258 [162]	346 [164]	586 [166]
$A_1(TO)(cm^{-1})$	531 [105]	611 [105]	1006 [162]	305 [164]	447 [166]
$E_1(LO)(cm^{-1})$	741 [105]	912 [105]	1286 [162]	347 [164]	593 [166]
$E_1(TO)(cm^{-1})$	559 [105]	671 [105]	1053 [162]	306 [164]	476 [166]
ϵ^{∞}	5.35 [133]	4.77 [133]	4.50 [163]	9.99 [165]	8.40 [167]

phonons; the effect of the half-space and propagating modes on the electrons is negligible in this system [156]. Here, therefore, we only consider the electron scattering with interface and confined mode optical phonons.

In this configuration, the available optical phonon modes and the phonon frequencies for each mode are determined by the relation between the dielectric constant functions. The frequency-dependent dielectric functions parallel ϵ_z and perpendicular ϵ_t to the *z*-axis are given as [80]

$$\epsilon_{1,2z}(\omega) = \epsilon_z^{\infty} \frac{\omega^2 - \omega_{Lz}^2}{\omega^2 - \omega_z^2} \tag{3.5}$$

$$\epsilon_{1,2t}(\omega) = \epsilon_t^{\infty} \frac{\omega^2 - \omega_{Lt}^2}{\omega^2 - \omega_t^2} \tag{3.6}$$

Where ω is the phonon frequency, ω_{Lz}, ω_z, ω_{Lz}, ω_{Lt} and ω_t are the characteristic frequencies of A_1(LO: longitudinal-optical), A_1(TO: transverse-optical), E_1(LO) and E_1(TO) optical phonon modes, respectively. For the AlN/GaN/AlN quantum well, two sets of material parameters are required such that we obtain four dielectric functions, namely ϵ_{1z}, ϵ_{1t}, ϵ_{2z} and ϵ_{2t}, where the subscripts 1 and 2 indicate the GaN and

AlN, respectively. With $\omega = 0$, the Lyddane-Sachs-Teller relation is recovered, and the static dielectric constants are obtained. Throughout this chapter, we take the *z*-axis along the *c*-axis of the wurtzite crystal [0001] and perpendicular to the heterointerfaces. The phonon frequencies and dielectric constants for bulk GaN and AlN used in the calculations are listed in Table 2. Using these frequency-dependent dielectric functions of bulk GaN and AlN, the phonon frequencies and available phonon modes of the AlN/GaN/AlN quantum well are deduced by the dielectric continuum model. Notice that the phonon frequencies are listed in units of cm^{-1}. We assume that the two high-frequency dielectric constants are identical, i.e., $\epsilon_z^\infty = \epsilon_t^\infty = \epsilon^\infty$ [151].

The conditions imposed on the available interface mode optical phonon frequency are

$$\epsilon_{1,z}(\omega)\epsilon_{1,t}(\omega) > 0,\ \epsilon_{2,z}(\omega)\epsilon_{2,t}(\omega) > 0 \text{ and } \epsilon_{1,z}(\omega)\epsilon_{2,z}(\omega) < 0 \tag{3.7}$$

For confined modes, the conditions are

$$\epsilon_{1,z}(\omega)\epsilon_{1,t}(\omega) < 0 \text{ and } \epsilon_{2,z}(\omega)\epsilon_{2,t}(\omega) > 0 \tag{3.8}$$

To clearly illustrate the available range of phonon frequencies for each mode, the four dielectric constants as a function of phonon frequency are shown in Fig. 5. The characteristic frequencies of the dielectric functions which define the phonon frequency ranges are indicated by vertical dashed lines. According to the conditions in Eqn. 3.7, the interface phonons are allowed in two phonon frequency intervals, $(\omega_{1t}, \omega_{2z})$ and $(\omega_{1Lt}, \omega_{2Lz})$. Since the former (latter) interval corresponds to the TO (LO) phonon frequencies of GaN and AlN, we label the phonon modes that lie in this frequency range as TO (LO) interface phonons. These intervals are indicated in the figure as red and blue shaded regions, respectively. Similarly, according to the conditions in Eqn. 3.8, the confined phonons are allowed in two phonon frequency intervals, $(\omega_{1z}, \omega_{1t})$ and $(\omega_{1Lz}, \omega_{1Lt})$.

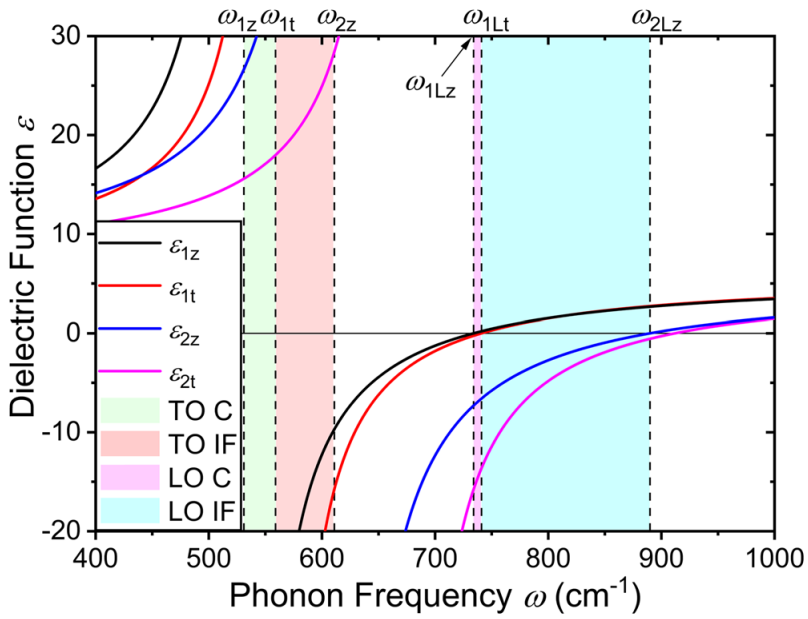

Fig. 5. The dielectric constants as a function of phonon frequency. The characteristic frequencies of the dielectric functions which define the range of available interface (IF) and confined (C) mode phonon frequencies are indicated by vertical dashed lines. The region shaded in red (ω_{1t}, ω_{2z}) is where the interface phonons associated with the TO phonon modes of bulk GaN and AlN are defined. The region shaded in blue ($\omega_{1Lt}, \omega_{2Lz}$) is where the interface phonons associated with the LO phonon modes of bulk GaN and AlN are defined. The regions shaded in green (ω_{1z}, ω_{1t}) and magenta ($\omega_{1Lz}, \omega_{1Lt}$) are where the confined phonons are defined.

The dispersion relations for the IF and confined modes are given by [168]

$$q = \frac{1}{2}\ln\left[\frac{\xi_1 + \xi_2}{\pm(\xi_1 - \xi_2)}\right]/(\alpha d) \qquad 3.9$$

and

$$q_n = [n\pi + \mu \arctan(\xi_2/\xi_1)]/(\alpha d)$$

$$n = 1, 2, 3, \ldots \quad \text{and } 0 \quad \text{if} \quad \mu = 1 \tag{3.10}$$

$$q_n = [n\pi - \mu \arctan(\xi_1/\xi_2)]/(\alpha d)$$

$$n = 1, 2, 3, \ldots \quad \text{and } 0 \quad \text{if} \quad \mu = -1 \tag{3.11}$$

Here, q is the phonon wave vector, n labels the different eigenmodes of the confined modes with $n = 1$ corresponding to the lowest order mode, $n = 2$ corresponding to the second order mode, etc.

Also, $\alpha = \frac{1}{2}\sqrt{|\epsilon_{1t}/\epsilon_{1z}|}$, $\beta = \frac{1}{2}\sqrt{|\epsilon_{2t}/\epsilon_{2z}|}$, $\xi_1 = \sqrt{|\epsilon_{1t}\epsilon_{1z}|}$, $\xi_2 = \sqrt{|\epsilon_{2t}\epsilon_{2z}|}$, $\mu = \text{sign}(\epsilon_{1z}\epsilon_{2z})$.

The interface and confined mode phonon dispersion relations in Eqs. 3.1 & 3.11 are shown in Fig. 6. The subscripts *A* and *S* indicate asymmetric and symmetric modes, and superscripts *IF* and *C* indicate interface and confined modes, respectively. The low frequency modes that are associated with the TO phonon frequencies of GaN and AlN are plotted in (a) and the high frequency modes that are associated with the LO phonon frequencies are plotted in (b). The symmetric modes are shown in dashed lines and asymmetric modes are shown in solid lines for both interface and confined phonons. The characteristic phonon frequencies, which separate the interface modes from the confined modes, and resonant interface phonon frequencies are indicated with horizontal lines. In terms of phonon energy, the LO interface phonon modes ($91.9 < \hbar\omega_{LO}^{IF} < 110.3$ eV) are higher in energy compared to the TO phonon modes ($69.3 < \hbar\omega_{TO}^{IF} < 75.8$ eV). The TO and LO resonant interface phonon energies are 71.7 and 103.2 meV, respectively. Compared to interface phonon modes, more than a pair of symmetric and asymmetric confined modes exist in each phonon frequency interval. Here, we only plot two of each symmetric and asymmetric confined modes that mostly contribute to the electron-phonon scattering process. However, in principle, there are an infinite amount of modes available. It should be noted that for the confined modes, the

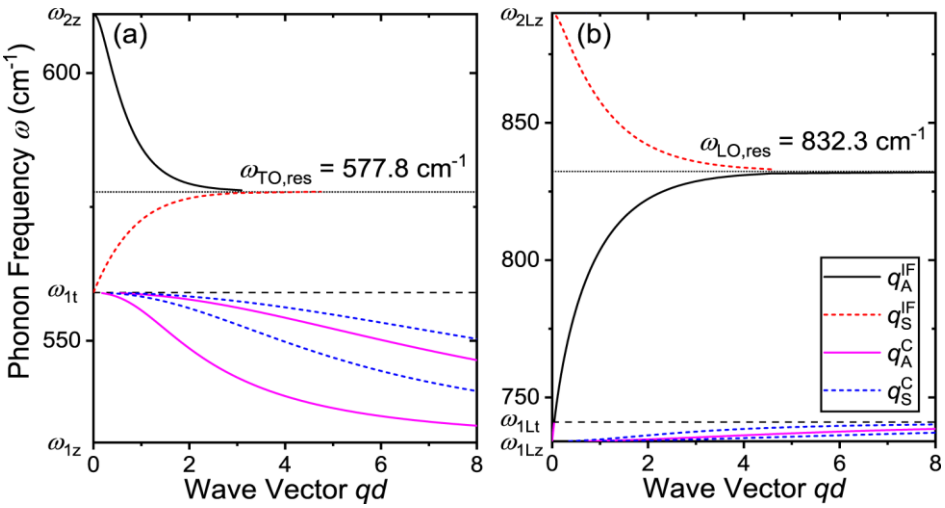

Fig. 6. Dispersion relation of asymmetric interface (black), symmetric interface (dashed orange), asymmetric confined (magenta) and symmetric confined (dashed blue) mode phonons of the AlN/GaN/AlN quantum well in the (a) low-frequency and (b) high-frequency region. Only a few of the confined mode phonons are plotted. Phonon modes associated with TO phonon modes of AlN and GaN are shown in the lower-frequency region whereas those associated with LO phonon modes are in the higher-frequency region. The interface phonon resonant frequencies are shown in dotted horizontal lines and the other characteristic frequencies are shown in dashed horizontal lines. The *x*-axis is shown in the dimensionless wave vector qd.

---

dispersion curves asymptotically approach a characteristic phonon frequency of GaN (i.e., ω_{1z} for TO confined modes and ω_{1Lt} for LO confined modes), whereas for the interface modes the curves approach the resonant frequency with increasing wave vector. This interface phonon dispersion relation gives rise to a phonon emission threshold energy in the electron-phonon scattering process that does not correspond to an energy of the characteristic phonons of either AlN or GaN. Another important feature in the dispersion relation is that these interface phonon modes have a nonzero slope at the zone center. This indicates that the group velocity $v_g = \frac{d\omega}{dq}$ is nonzero and that optical phonons generated at the interface

will not stay where they were generated (as bulk optical phonons do) but will propagate along the interface. Notice that the x-axis is set to the dimensionless product of phonon wave vector q and the quantum well thickness d. Therefore, the group velocity will increase with increasing quantum well thickness due to the stronger dispersion.

3.3.2 GaN/InGaN/GaN QWs

GaN/InGaN multiple quantum wells (MQWs), with low In-content, offers tunable band gaps ranging from 2.9 – 3.4 eV for In content (0 – 0.4) [169]. They also have been well-regarded for their applications in quantum well infrared photodetectors (QWIPs), quantum cascade infrared photodetectors (QCIPs), and blue and white light emitting diodes [170]. They are strong favorites for artificial lighting to replace the present fluorescent and incandescent lighting [170]. However, and as discussed in chapters 1 and 2 extensively, as nitride devices, and semiconductors in general, are being scaled down to operate in nanometer regions, reliability issues appear due to the heat generation and increase in junction temperature which contribute significantly to the degradation of device's performance. In view of the advantages and applications of InGaN QWs, it is fitting to investigate the possibility of enhancing their reliability via optical phonon emission as phonon engineering emerges as an important tool in nanoscale regimes [161]. Studies have shown the importance of investigating the interaction between electrons and polar-optical-phonons, as polar optical phonon emission is known as the primary energy relaxation process of hot electrons in GaN [50], [171]. The importance of carrier-phonon interactions and phonon-assisted processes are now well known and is illustrated in a number of different nanostructures [172]–[174]. Polar optical electron-phonon scattering through the Frohlich interaction is the dominant scattering process in

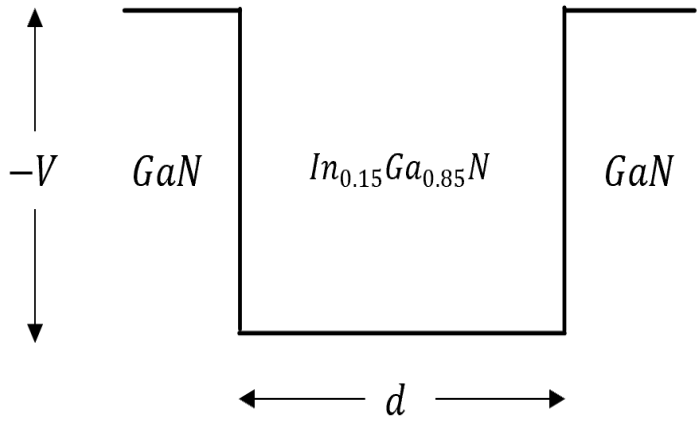

Fig. 7. Schematic diagram of a typical GaN/InGaN/GaN double barrier quantum well structure. The width *d* of the InGaN layer is set initially to 5 nm for the scattering rates numerical calculations. The well depth *v* of 0.5 eV represents the discontinuity between the conduction bands of InGaN and GaN. The values reported for E_C are -2.8 eV and -2.3 eV for GaN and InGaN based on DFT calculations [175].

---

low-defect GaN/InGaN QWs over a wide range of temperatures; moreover, the optical phonon production dominates over the acoustic phonons production via the deformation potential [80].

Polar optical electron-phonon scattering through the Frohlich interaction is the dominant scattering process in low-defect GaN/InGaN QWs over a wide range of temperatures; moreover, the optical phonon production dominates over the acoustic phonons production via the deformation potential [80].

Fig. 7 introduces a schematic for the case of a simplified layered structure of GaN/$In_{0.15}Ga_{0.85}N$/GaN QW. The difference between the dielectric constants between GaN and InGaN leads to the production of polar interface and confined optical phonon modes. In this chapter, we calculate the scattering rates $\frac{1}{\tau}$ for these

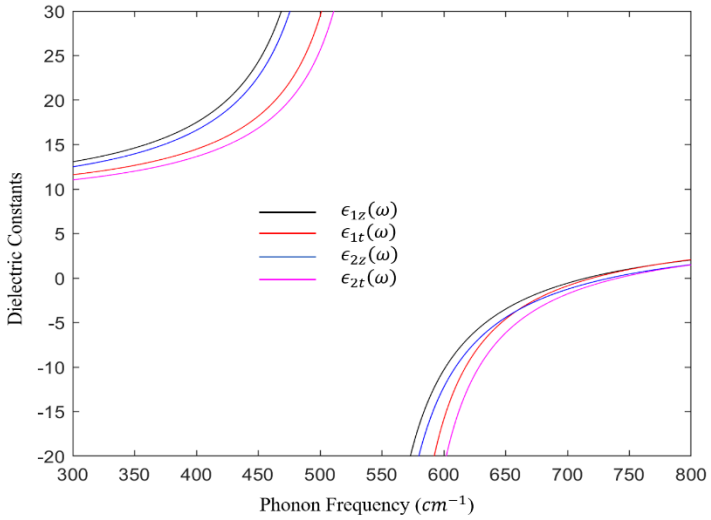

Fig. 8. The frequency-dependent dielectric functions of GaN/InGaN/GaN QW. $\epsilon_{1z}(\omega)$ and $\epsilon_{1t}(\omega)$ for InGaN are designated in black and red and $\epsilon_{2z}(\omega)$ and $\epsilon_{2t}(\omega)$ for GaN are designated in blue and magenta.

---

two phonon modes as functions of the electron energy E_k for GaN/$In_{0.15}Ga_{0.85}$N/GaN QWs, which are based on the analysis and the formalism of Ref. [156]. It is shown that through phonon engineering, it is possible to preferentially channel the phonon emission into interface modes propagating with high optical phonon velocities which lead to elongated, lower-temperature hot spots in the region where the interface optical phonons decay into acoustic phonons.

Phonons of confined and interface modes coexist in certain regions in GaN/InGaN wurtzite heterostructures. Confined modes exist within two frequency intervals: $C_I = [\omega_{1z}, \omega_{1t}]$ and $C_{II} = [\omega_{1Lz}, \omega_{1Lt}]$, while interface modes exist between $[\omega_{2z}, \omega_{1t}]$ and $[\omega_{1Lt}, \omega_{2Lz}]$ [168], [176], [81]. The range of the allowed frequencies is illustrated by the frequency-dependent dielectric constants [176], [177] given in Eqs. 3.5 and 3.6.

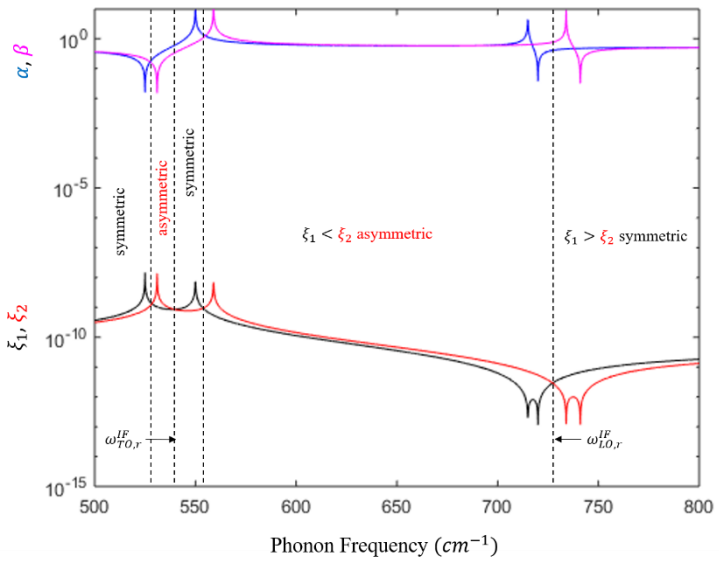

Fig. 9. Parameters of the phonon wave function. $\xi_1$and ξ_2 are indicated by black and red and α and β are indicated by blue and magenta. The vertical black dotted lines separate each symmetric and asymmetric region.

In this subsection, subscript 1 is assigned for InGaN and 2 is assigned for GaN. For GaN/InGaN with indium content of 15%, $\epsilon_{1,2z}(\omega)$ and $\epsilon_{1,2t}(\omega)$ are plotted in Fig. 8. The dielectric constants $\epsilon_{1z}(\omega)$ and $\epsilon_{1t}(\omega)$ in Fig. 8 converge at large values near their TO frequencies of ω_z and ω_t for both materials. The dielectric constants switch to negative values outside the range of the allowed frequencies > 741 cm^{-1} and remain positive at values < 525 cm^{-1}, which indicate that $\epsilon_{1,2z}(\omega)\epsilon_{1,2t}(\omega) < 0$ always holds for GaN/InGaN structure. In that case, no overlap of the characteristic frequencies will occur, and the boundary conditions will satisfy neither the oscillating solution nor the decaying solution for the existence of IF and confined modes.

Eqs. 3.19–3.11 represent the case for IF modes. The upper sign in the denominator is for symmetric modes and the lower sign is for asymmetric modes. Eqn. 3.10 is defined for even confined modes and Eqn. 3.11

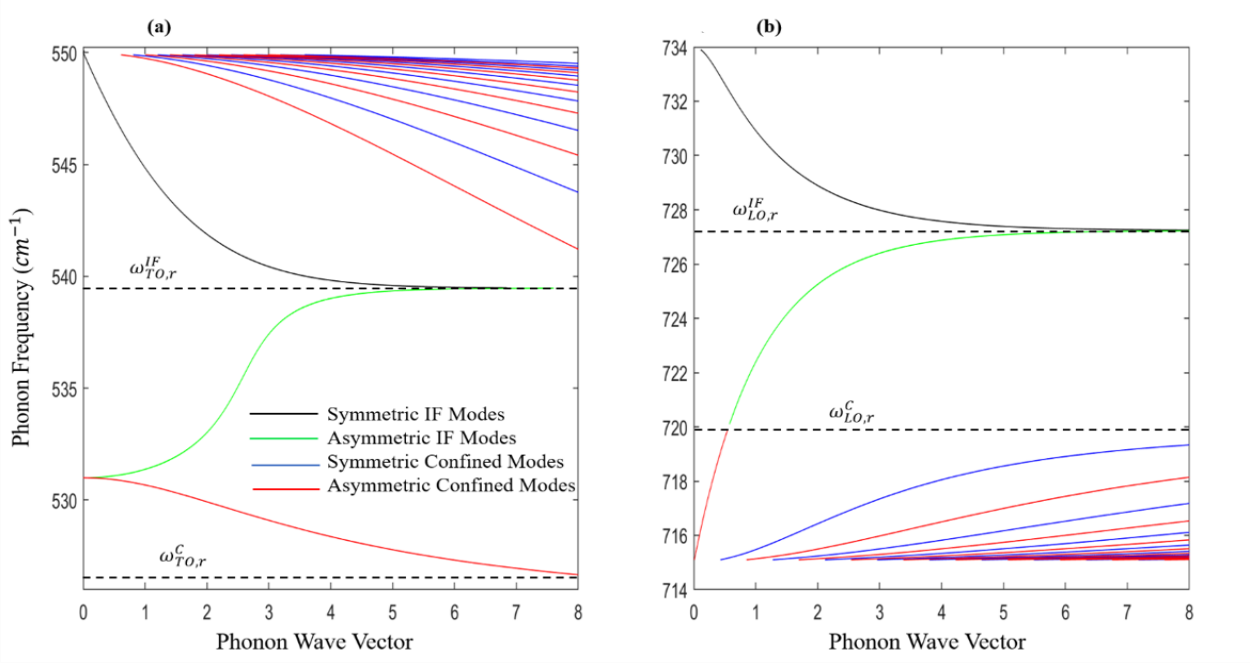

Fig. 10. Dispersion relation of frequencies $\hbar\omega$ in a wurtzite GaN/$In_{0.15}Ga_{0.85}$N/GaN quantum well as a function of free phonon wave number when $n = 0$. The resonant frequency for IF and confined are indicated by the black dotted lines. The modes depicted are symmetric IF in black, asymmetric IF in green, even confined in blue and odd confined in red. The low-order energy intervals $\hbar\omega_{TO}$ are shown in (a) and the high-order energy intervals $\hbar\omega_{LO}$ are shown in (b).

---

is defined for odd confined modes. The symmetric and asymmetric phonons satisfy the relations $\xi_1 > \xi_2$ and $\xi_1 < \xi_2$, respectively. Indeed, these relations are illustrated in Fig. 9. The characteristic frequencies can be obtained from the peaks of ξ_1 and ξ_2 while their intersections denote the resonant frequencies. Fig. 10 (a) and (b) depict the dispersion of polar optical phonons for interface and confined modes for low and high energy regions. The symmetric IF modes are shown in black and the asymmetric modes are shown in green. Also, the even confined modes are plotted in blue and the odd confined modes are plotted in red. The dispersive behavior of Eqs. 3.10 and 3.11 shows that the confined modes usually have infinite solutions for given n and q in the intervals $[\omega_{1z}, \omega_{1t}]$ and $[\omega_{1lz}, \omega_{1lt}]$, however, only a certain number of

confined modes are considered at given n and q. It is evident from the dispersion curves that the scattering rates increase due the strong presence of the confined phonons.

From Fig. 10, one can see that only the first few confined modes for any odd and even modes are considered. The higher order modes are normally ignored because $\langle f|v|i\rangle \approx 0$, when the potential v has many oscillations. The IF modes of lower frequencies associated with TO modes propagate around a resonant frequency of 539.5 cm^{-1}, defined as $\omega_{TO,r}^{IF}$ in Fig. 10 (a), whereas the higher frequencies (LO modes) have a resonant frequency of 727.2 cm^{-1}, defined as $\omega_{LO,r}^{IF}$ in Fig. 10 (b). As q approaches ∞, the confined modes saturate at 525.1 cm^{-1} (~ω_{1z}) and 719.9 cm^{-1} (~ω_{1Lt}), which are labeled as $\omega_{TO,r}^{C}$ and $\omega_{LO,r}^{C}$ to show that they denote the emission thresholds for confined modes at the low and high frequency regions, respectively. The confined modes asymptotically reduce to the characteristic frequencies ω_{1t} for TO modes and ω_{1lz} for LO modes. The trend verifies that the confined modes exist between $[\omega_{1t}, \omega_{1z}]$ and $[\omega_{1Lt}, \omega_{1Lz}]$. The strong dependence of the scattering rates on the dispersion relation and the values of the above resonance frequencies help us predict the energy required to emit TO-like and LO-like phonons. In Fig. 10, the slopes of the optical branches indicate which modes have higher group velocity. Nonetheless, the slopes of these optical phonons (including IF) are still slower than the acoustic phonons.

3.3.3 AlN/AlInN/AlN QWs

Aluminum and indium nitride ternaries have attracted much interest because of their excellent physical and chemical properties, such as ultra-hardness, high thermal conductivity, and chemical inertness that withstand high temperatures. AlInN based high-electron-mobility transistors (HEMTs) have been investigated to provide graded and improved polarization charges with minimal effects of strain [178]–[180]. Several researchers have introduced devices based on AlInN with maximum current capabilities greater than those of AlGaN/GaN structures [181]. Furthermore, optimization of quantum well structures

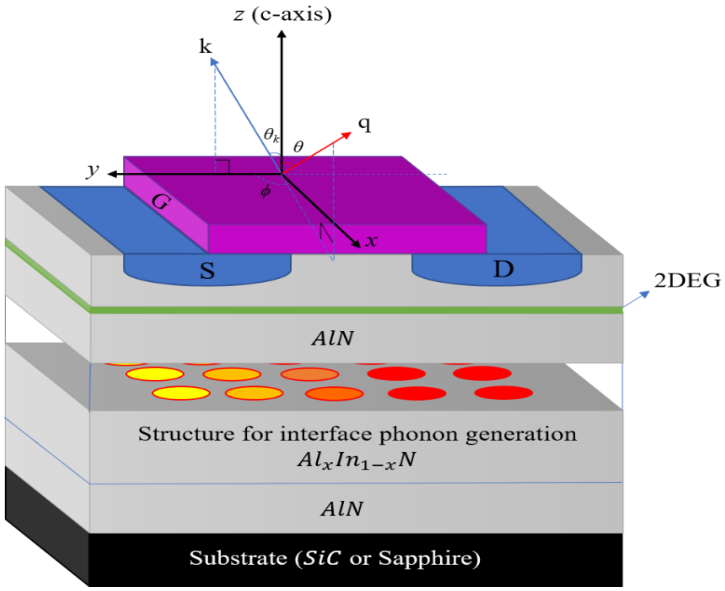

Fig. 11. Aluminum nitride-based high electron mobility transistor (HEMT) including a structure for interface (IF) phonon generation.

---

based on AlInN has been carried out by using theoretical analysis dependent on compressive strain and well thicknesses [182].

Recent advances in synthesis and processing are enabling the production of AlInN structures for various applications. Examples include the realization of AlInN compounds for large optical gain for deep-UV LED [183], lattice matched GaN/AlInN superlattices for the near-infrared based on intersubband transitions [184] and reduced dislocation densities [185].

This subsection deals with the use of phonon engineering to reduce peak temperatures in hot spots in AlInN-based electronic compounds. This application was not anticipated in the original formulation of the dielectric continuum for optical phonons in wurtzites or in a large number of papers based on the original formulation [80]. Specifically, hot-electron-generated phonons – which lead to the elevated temperatures in hot spots – are engineered by the use of heterostructures so that a large fraction of the

phonons are interface phonons which have group velocities much higher than those of bulk optical phonons. As in the case of bulk optical phonons, these interface phonons decay into heat carrying acoustic phonons. But because of their high group velocities the interface optical phonons' decay into acoustic phonons occurs over an elongated hot spot region with the consequence that the hot spot temperature is reduced. In the following segment, generation rates of interface optical phonons from hot electrons in the hot spot region are calculated from first principles and estimates are made for the fraction of phonons that are interface phonons. We have focused on wurtzite materials instead of cubic materials since the wurtzite materials are more readily available as a result of the advanced growth technologies for wurtzites. These results, together with the group velocities, for interface optical phonons, are used to estimate the dimensional elongation of the hot spots and, thus, the temperature reduction of the hot spots.

In previous studies, the phonon total scattering rate was formulated for a GaN free-standing quantum well (QW), and for a GaN quantum well (QW) embedded between two AlN layers [156]. These scattering processes involve a variety of modes including confined and interface modes, which can be used as a means of controlling heat transport and temperature profiles since the different modes have different propagation speeds [161], [186].

The application of epitaxially grown quantum wells (QW) was discussed as a possible approach to deal with the temperature profiles near the transistor gate. Fig. 11 depicts a general schematic to produce fast moving interface phonons in AlInN ternaries.

In a nitride based HEMT with a two-dimensional electron gas (2DEG) between the source and the drain, the formation of the 2DEG at the interface has led to the fabrication of high-performance electronic heterostructures, and also, the reduction of the impact of the interfacial roughness and the alloy scattering and the confinement of electrons in a quantum well. For operational ranges of gate, source, and drain voltages, there are regimes where electrons are very energetic and the balance of LO phonon emission and

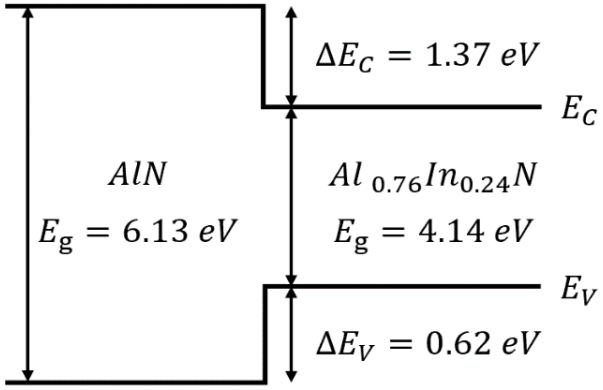

Fig. 12. Band alignment of the AlInN/AlN heterointerface with a 76%/24% setup.

absorption will be strongly modified by these electrons being accelerated with high electric fields. In polar materials, rates for optical phonon generation dominate and they remain localized in the regions where electrons flow [187]. These optical phonons generally decay into acoustic phonons that carry heat through a variety of decay channels [188]–[190]. As hot electrons produce more phonons, AlInN/AlN exhibits self-heating due to the strong 2DEG localization as more electrons occupy the ground state [191].

Due to their extremely high growth temperatures, AlInN ternary alloys are considered one of the most complicated III-nitrides [192]. Since AlInN layers with indium content smaller than 30% is lattice matched to AlN, it allows the fabrication of strain-free AlInN/AlN heterostructures [193], [194]. In order to exploit the full potential of the device, proper modeling of the materials is required. The AlInN/AlN HEMT structure can be demonstrated with up to 20 period of superlattice, by using the optimum AlInN thickness that achieves the best heat-spreading results. With the application of a metal that has higher work function than the structure to create an ohmic contact. The gate voltage V_g required to create the hot spot can be evaluated using the force and electric field equations.

During the ON-state, the current flows between source and drain through the 2DEG and through different leakage paths in the GaN-based bulk [195]. In the usual HEMT design, the potential trapping region at

the heterointerface results in charge transport between the source and drain, i.e., a conductive channel. Then electrons will move going from source to drain when a positive bias V_D is applied. This flow can be modified by changing the gate voltage. Hot spots of elevated temperature are generally produced near the two-dimensional electron gas (2DEG) below a portion of the gate and it expands into the region below the 2DEG in which almost all of the voltage drop in the longitudinal direction occurs [191]. As illustrated in Fig. 11, the placement of a heat spreading heterostructure in the hot spot region – denoted by "$Al_xIn_{1-x}N$" (Structure for IF phonon gen.)" – can be used to generate interface optical phonons which propagate at high relative speeds before they decay into heat-generating phonons.

To reduce the hot spot temperature, a thin layer of the order on nanometers thick or layered structure such as AlN/AlInN/AlN is grown epitaxially in the region where the hot spot is predicted to occur. Fig. 12. presents a schematic for the case of a simplified layered structure composed of AlN/AlInN/AlN alignment, which retains the essential feature of a discontinuous dielectric constant at the interfaces which is important for interface (IF) and confined phonon generation. Hot electrons incident on the interfaces in Fig. 12 will produce interface phonons and confined phonons near the hot spot region which decay on the picosecond time scale to acoustic phonons which carry heat and enhance electronic transport.

The polarization properties of wurtzite III–V nitrides are calculated from first principles [196]. For $Al_xIn_{1-x}N$, low- and high-mode phonon frequencies are interpolated using Vegard's law [197]. Other physical properties such as, dielectric constant, bandgap and band offset can be estimated using the approximated linear interpolation as in Eqs. 3.12–3.14, respectively [196]. The material properties for AlN are provided in Table 2, while the calculated properties for AlInN are provided in Table 3.

$$\varepsilon_{AlInN} = -4.3x + 14.61 \tag{3.12}$$

$$E^{g}_{AlInN}(x) = \left[xE^{g}_{AlN} + (1-x)E^{g}_{InN} - bx(1-x)\right] \tag{3.13}$$

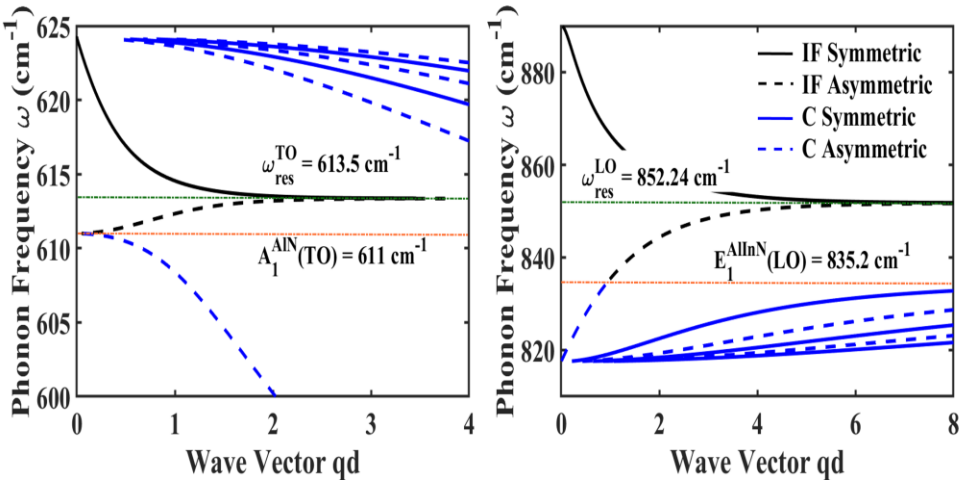

Fig. 13. Dispersion relation for AlInN quantum well surrounded by two AlN structures. The straight curves denote the symmetric modes whereas the dashed curves denote the asymmetric modes. The IF phonons are plotted in black and the confined phonons are plotted in blue.

$$\Delta E^{C}_{AlInN}(x) = 0.63\left(E^{g}_{AlInN}(x) - E^{g}_{AlInN}(0)\right) \qquad 3.14$$

where b is the bandgap bowing parameter (in eV).

where $A_1(LO)$, $A_1(TO)$, $E_1(LO)$ and $E_1(TO)$ are the characteristic frequencies of the system. AlInN frequency values were calculated using linear interpolation and AlN values were taken from Ref. [105].

Corresponding to a 76%/24% conduction band/valence band offsets, a widely accepted band gap bowing factor of 5.4 eV is assumed for AlInN [196], [198], [199]. The AlInN/AlN heterointerface is assumed to be abrupt. This yields a band gap of 4.14 eV for $Al_{0.76}In_{0.24}N$ at 300 K. The values for the band offsets are ΔE^{C}_{AlInN} = 1.37 eV and ΔE^{V}_{AlInN} = 0.62 eV. The calculated dielectric permittivity of AlInN is ε_{AlInN} = 11.34, which is in a good agreement with the value listed in Ref. [200].

Similar to the calculations for GaN/AlN and InGaN QWs and based on Eqs. 3.9–3.11, the dispersion curves for IF and confined phonon modes in AlInN/AlN QW are illustrated in Fig. 13.

Table 3. Calculated properties of selected ternary alloys with different compositions compared to GaN, AlN and InN compounds. Frequencies are in cm^{-1} and energies are in eV.

Material	$A_1(LO)$	$A_1(TO)$	$E_1(LO)$	$E_1(TO)$	ϵ^0	ϵ^∞	E^g	E^C
GaN	734	531	741	559	9.7	5.35	3.42	–
AlN	890	611	912	671	9.14	4.77	6.13	–
InN	588	451	592	476	15.3	8.40	1.95	–
$Al_{0.76}In_{0.24}N$	818	573	835	624	11.34	5.56	4.14	1.370
$Al_{0.88}In_{0.12}N$	854	592	874	648	10.83	5.20	5.06	1.958
$In_{0.15}Ga_{0.85}N$	712	519	718	547	10.93	5.80	2.88	0.586
$In_{0.10}Ga_{0.90}N$	719	523	726	551	10.71	5.66	3.05	0.693
$In_{0.05}Ga_{0.95}N$	727	527	734	555	10.49	5.52	3.23	0.806
$Al_{0.10}Ga_{0.90}N$	750	539	758	570	10.28	5.32	3.60	0.113

3.3.4 Estimation of physical properties for III-nitride ternary alloys

It is suitable to investigate additional nitride-based structures due to their unique properties such as good thermal, mechanical and chemical stability. Many challenges in the growth of these materials are yet to be overcome. For example, in epitaxially-grown materials, the positions of atoms or molecules are repeating with fixed distances determined by the unit cell parameters. In some instances, nonetheless, the arrangement of atoms or molecules in crystalline materials may not be aligned perfectly. In general, experimental studies on these materials is clearly on its infancy. We provide below a calculation of the electronic properties of a selection of quantum wells based on the work reported by Ambacher et al. (2002) [196] including: 1) AlN/$Al_{0.88}In_{0.12}N$/AlN, 2) GaN/$In_{0.1}Ga_{0.9}N$/GaN, 3) GaN/$In_{0.05}Ga_{0.95}N$/GaN and 4)

GaN/$Al_{0.1}Ga_{0.9}N$/GaN. Henceforth, further research can be carried on based on these data. By rewriting Eqs. 3.12–3.14 for different materials indicated in the scripts

$$\varepsilon_{AlGaN} = 0.03x + 10.28 \quad (3.15)$$

$$\varepsilon_{InGaN} = 4.33x + 10.28 \quad (3.16)$$

$$\varepsilon_{AlInN} = -4.3x + 14.61 \quad (3.17)$$

$$E^{g}_{AlGaN}(x) = [6.13x + 3.42(1-x) - 1.0x(1-x)] \quad (3.18)$$

$$E^{g}_{InGaN}(x) = [1.95x + 3.42(1-x) - 2.5x(1-x)] \quad (3.19)$$

$$E^{g}_{AlInN}(x) = [6.13x + 1.95(1-x) - 5.4x(1-x)] \quad (3.20)$$

$$\Delta E^{C}_{AlGaN}(x) = 0.63\left(E^{g}_{AlGaN}(x) - E^{g}_{AlGaN}(0)\right) \quad (3.21)$$

$$\Delta E^{C}_{InGaN}(x) = 0.63\left(E^{g}_{InGaN}(x) - E^{g}_{InGaN}(0)\right) \quad (3.22)$$

$$\Delta E^{C}_{AlInN}(x) = 0.63\left(E^{g}_{AlInN}(x) - E^{g}_{AlInN}(0)\right) \quad (3.23)$$

In Table 3, the calculations of the high-frequency dielectric constants were obtained with the help of the famous generalized Lyddane-Sachs-Teller relation [201], which indicates that the dielectric constants at visible ranges (ϵ^{∞}) can be obtained by $\epsilon^{\infty} = \epsilon^{0}\frac{\omega_{LO}^{2}}{\omega_{TO}^{2}}$, where ϵ^{0} is the static, or zero-frequency, dielectric constant. Looking at Eqs. 3.15–3.23, it becomes clear that the bandgaps, dielectric constants and band offsets depend linearly on the nitride composition; for example, the case for AlInN has been verified by Schulz et al. (2013) [202]; Ponce et al. (2013) observed different emission energies with different nitride compositions for InGaN layers [203]. Therefore, it is worth commenting on this segment that alloy compositions have a profound effect on its thermal properties, which determine the temperature field, its mechanical properties, which influence the response of the material to the strains caused by the thermal field, and its thermal conductivity.

3.4 Hot electron relaxation rates

This section details a study of the uniaxial dielectric continuum model to investigate the electron-phonon interaction mechanism in GaN- and AlN-based QWs. A formalism for the calculation of the scattering rate in wurtzite-type (QWs) is developed taking into account features of the optical phonon spectra in an optically anisotropic medium. In Section 3 of this chapter, we have introduced the dispersion relation through phonon engineering via dimensional confinement effects and the resonant frequencies of the system for both high and low intervals and the link between them and the energies required to emit longitudinal optical (LO) and transverse optical (TO) modes.

The phonon potentials inside and outside the QWs for confined modes are given by [80]

$$\Phi_1(z) = \Phi_0 \cos\left(2\alpha q \frac{z}{d}\right) \tag{3.24}$$

$$\Phi_2(z) = A\cos(\alpha q)\, e^{\beta q\left(1-2\frac{z}{d}\right)} \tag{3.25}$$

and for interface modes

$$\Phi_1(z) = A\cosh(2\alpha q z) \tag{3.26}$$

$$\Phi_2(z) = A\cosh(\alpha q d)\, e^{\beta q d\left(1-2\frac{z}{d}\right)} \tag{3.27}$$

where $\alpha = \frac{1}{2}\sqrt{|\epsilon_{1t}/\epsilon_{1z}|}$, $\beta = \frac{1}{2}\sqrt{|\epsilon_{2t}/\epsilon_{2z}|}$, q is the phonon wave vector, z is defined within $-d/2 \leq z \leq d/2$ and Φ_0 and A are the normalization conditions determined from the continuity of the heterointerfaces.

From Eqs. 3.24–3.27 and satisfying the boundary conditions at the interfaces [168]

$$\Phi_1(z) = \Phi_2(z) \tag{3.28}$$

$$\frac{\partial \Phi_1(z)}{\partial x} = \frac{\partial \Phi_2(z)}{\partial x}$$

For further simplifications, we define the following relations

$$\cos^2(\alpha q) = \frac{1}{1 + \left(\frac{\xi_2}{\xi_1}\right)^2} \tag{3.29}$$

$$\cos(\alpha q)\sin(\alpha q) = \frac{\mu\frac{\xi_2}{\xi_1}}{1 + \left(\frac{\xi_2}{\xi_1}\right)^2} \tag{3.30}$$

$$\alpha q d = n\pi + arctan\left(\mu\frac{\xi_2}{\xi_1}\right) \tag{3.31}$$

with $\xi_1 = \sqrt{|\epsilon_{1t}\epsilon_{1z}|}$, $\xi_2 = \sqrt{|\epsilon_{2t}\epsilon_{2z}|}$

Within the context of the dielectric continuum approximation and Loudon's models for uniaxial crystals, the scattering rate by emission and absorption is calculated with the perturbation theory of Fermi's golden rule. The equation is defined as [151]

$$\frac{1}{\tau} = 2e^2\int_0^{\pi} d\theta \times \int \left(N_q + 0.5 \mp 0.5\right) D(q,\omega)\delta\left(E_{k+q} - E_k \mp \hbar\omega\right) dq \tag{3.32}$$

where $E_{k+q} - E_k \mp \hbar\omega$ represents the delta function (Γ). The upper sign is defined for absorption and the lower sign is for emission. The phonon potentials were used to obtain $D(q,\omega)$ which was derived for interface and confined modes using the form factor $({}^{f^2}/_{F})$. f and F were defined for wurtzite materials as [156]

$$f = \frac{\Upsilon^2}{\sqrt{1 + \left(\frac{\xi_2}{\xi_1}\right)}}\left[\frac{\cos^2\left(k_1\frac{d}{2}\right)}{k_2 + \beta q} + \frac{\left(2\cos^2\left(k_1\frac{d}{2}\right)\alpha^2q^2 \mp k_1^2\right)\mu\frac{\xi_2}{\xi_1} \mp \alpha q k_1 \sin(k_1 d)}{2\alpha q(\alpha^2q^2 \mp k_1^2)}\right] \tag{3.33}$$

and

$$F = \frac{1}{1+\left(\frac{\xi_2}{\xi_1}\right)}\left[2\beta\frac{\partial\epsilon_{2z}}{\partial\omega} + \frac{1}{2\beta}\frac{\partial\epsilon_{2t}}{\partial\omega} \pm \mu\xi_2\left(\frac{1}{|\epsilon_{1t}|}\frac{\partial\epsilon_{1t}}{\partial\omega} \mp \frac{1}{|\epsilon_{1z}|}\frac{\partial\epsilon_{1z}}{\partial\omega}\right)\right. \tag{3.34}$$

$$\left. + \alpha qd\left(2\alpha\frac{\partial\epsilon_{1z}}{\partial\omega} \pm \frac{1}{2\alpha}\frac{\partial\epsilon_{1t}}{\partial\omega}\right)\right]$$

with

$$\begin{cases} \sin(\alpha qd) = \sin\left(n\pi + arctan\left(\mu\frac{\xi_2}{\xi_1}\right)\right) = \pm\frac{\mu\frac{\xi_2}{\xi_1}}{\sqrt{1+\left(\frac{\xi_2}{\xi_1}\right)^2}} \\ \cos(\alpha qd) = \pm\frac{1}{\sqrt{1+\left(\frac{\xi_2}{\xi_1}\right)^2}} \end{cases} \tag{3.35}$$

where $n = 0$ in even numbers.

Therefore,

$$D^{\binom{C}{IF}}(q,\omega) \tag{3.36}$$

$$= \frac{\left[\frac{\Upsilon^2}{(\alpha^2q^2 \mp k_1^2)}\left[\cos^2\left(k_1\frac{d}{2}\right)\left(\frac{k_1^2 \mp \alpha^2q^2}{k_2+\beta q}\xi_1 - 2\alpha q\mu\xi_2\right) \pm \frac{k_1^2\mu\xi_2}{2\alpha q} + \frac{1}{2}k_1\xi_1\sin(k_1d)\right]\right]^2}{{\xi_1}^2\xi^+(\beta) \pm \mu\xi_1\xi_2\xi^\mp(\alpha) + \alpha qd\xi^\pm(\alpha)(\xi_1^2 \pm \xi_2^2)}$$

A detailed verification of the form factor and $D^{\binom{C}{IF}}(q,\omega)$ function is given in Appendix A.

Here, the upper sign is for confined phonons and the lower sign is for IF phonons. k_1 and k_2 are the parameters characterizing the envelope of the materials. They were obtained by solving Schrodinger's wave equation for finite potential well for the ground state. The amplitude of the electron wave function

is written as $\Upsilon = \left[\frac{\cos(k_1 d)\sin(k_1 d)}{k_1} + \frac{d}{2} + \frac{\cos^2(k_1\frac{d}{2})}{k_2}\right]^{-1/2}$, $\xi^{+}(\beta) = 2\beta\frac{\partial\epsilon_{2z}}{\partial\omega} + \frac{1}{2\beta}\frac{\partial\epsilon_{2t}}{\partial\omega}$ and $\xi^{\pm}(\alpha) = 2\alpha\frac{\partial\epsilon_{1z}}{\partial\omega} \pm \frac{1}{2\alpha}\frac{\partial\epsilon_{1t}}{\partial\omega}$.

To obtain an expression for the hot electron energy relaxation rate we start by expressing dq as $\left|\frac{d\Gamma}{dq}\right|^{-1} d\Gamma$ in Eqn. 3.32

$$\frac{1}{\tau} = 2e^2 \int_0^{\pi} d\theta \times \int (N_\omega) D(q,\omega) \left|\frac{d\Gamma}{dq}\right|^{-1} \delta(\Gamma)\, d\Gamma \tag{3.37}$$

To find $\left|\frac{d\Gamma}{dq}\right|$ we differentiate the delta function (Γ) given in Eqn. 3.32

$$\left|\frac{d\Gamma}{dq}\right| = \frac{\hbar^2 q}{m} + k\cos\theta\frac{\hbar^2}{m} - \hbar\frac{d\omega}{dq} \tag{3.38}$$

which yields

$$\frac{1}{\tau} = 2e^2 \int_0^{\pi} d\theta \frac{(N_\omega) D(q,\omega)}{\frac{\hbar^2 q}{m} + k\cos\theta\frac{\hbar^2}{m} - \hbar\frac{d\omega}{dq}}$$

$$= \frac{2m}{\hbar^2} e^2 \int_0^{\pi} d\theta \frac{(N_\omega) D(q,\omega)}{q + k\cos\theta - \frac{m}{\hbar}\frac{d\omega}{dq}} \tag{3.39}$$

Let us work out the denominator in Eqn. 3.39 using the well-known relation $\cos\theta = \frac{m\omega}{kq\hbar} - \frac{q}{2k}$,

$$q + k\cos\theta - \frac{m}{\hbar}\frac{d\omega}{dq} = q + k\left(\frac{m\omega}{kq\hbar} - \frac{q}{2k}\right) - \frac{m}{\hbar}\frac{d\omega}{dq} = q + \frac{m\omega}{q\hbar} - \frac{q}{2} - \frac{m}{\hbar}\frac{d\omega}{dq} = \frac{q}{2} + \frac{m}{\hbar}\left(\frac{\omega}{q} - \frac{d\omega}{dq}\right)$$

Then Eqn. 3.39 becomes

$$\frac{1}{\tau} = \frac{2m}{\hbar^2} e^2 \int_0^{\pi} \frac{(N_\omega) D(q,\omega)}{\frac{q}{2} + \frac{m}{\hbar}\left(\frac{\omega}{q} - \frac{d\omega}{dq}\right)} d\theta \tag{3.40}$$

Now we express $d\theta$ as $\frac{d\theta}{d\omega}d\omega$ and take the derivative of $\cos\theta = \frac{m\omega}{kq\hbar} - \frac{q}{2k}$

$$-\sin\theta\, d\theta = \frac{m}{k\hbar}\left[d\left(\frac{\omega}{q}\right) - \frac{\hbar q}{2m}\right]d\omega \qquad 3.41$$

where $\frac{d\left(\frac{\omega}{q}\right)}{d\omega} = \frac{q\frac{d\omega}{d\omega} - \omega\frac{dq}{d\omega}}{q^2} = \frac{q - \omega\frac{dq}{d\omega}}{q^2}$

$$-\sin\theta\, d\theta = \frac{m}{k\hbar}\left[\frac{q - \omega\dfrac{dq}{d\omega}}{q^2} - \frac{\hbar\dfrac{dq}{d\omega}}{2m}\right]d\omega = \frac{m}{k\hbar q^2}\left[q - \omega\frac{dq}{d\omega} - \frac{\hbar q^2\dfrac{dq}{d\omega}}{2m}\right]d\omega$$

Therefore, 3.42

$$\sin\theta = \sqrt{1 - \cos^2\theta} = \sqrt{1 - \left[\frac{m\omega}{kq\hbar} - \frac{q}{2k}\right]^2}$$

Rearranging Eqn. 3.41 and substituting for $\sin\theta$ from Eqn. 3.42 yields

$$\frac{d\theta}{d\omega} = -\frac{\left[mq - m\omega\dfrac{dq}{d\omega} - \dfrac{\hbar q^2\dfrac{dq}{d\omega}}{2}\right]}{k\hbar q^2\sqrt{1 - \left[\dfrac{m\omega}{kq\hbar} - \dfrac{q}{2k}\right]^2}} = -\frac{\left[mq - \dfrac{dq}{d\omega}\left(m\omega + \dfrac{\hbar q^2}{2}\right)\right]}{k\hbar q^2\sqrt{1 - \left[\dfrac{m\omega}{kq\hbar} - \dfrac{q}{2k}\right]^2}}$$

$$= \frac{\left[\dfrac{dq}{d\omega}\left(\omega + \dfrac{\hbar q^2}{2m}\right) - q\right]}{q^2\dfrac{\hbar k}{m}\sqrt{1 - \left[\dfrac{m\omega}{kq\hbar} - \dfrac{q}{2k}\right]^2}} \qquad 3.43$$

The denominator in Eqn. 3.43 can be worked out as follows

$$q^2\frac{\hbar k}{m}\sqrt{1-\left[\frac{m\omega}{kq\hbar}-\frac{q}{2k}\right]^2}=q^2\sqrt{\frac{\hbar^2k^2}{m^2}-\frac{\hbar^2k^2}{m^2}\left[\frac{m\omega}{kq\hbar}-\frac{q}{2k}\right]^2}$$

$$=q^2\sqrt{\frac{1}{m}\left(\frac{\hbar^2k^2}{m}-\frac{\hbar^2k^2}{m}\left[\frac{m^2\omega^2}{k^2q^2\hbar^2}-\frac{m\omega}{k^2q\hbar}+\frac{q^2}{4k^2}\right]\right)}$$

$$=q^2\sqrt{\frac{1}{m}\left(\frac{\hbar^2k^2}{m}\right)-\left[\frac{m\omega^2}{q^2}-\hbar\omega+\frac{\hbar^2q^2}{4m}\right]}$$

$$=q^2\sqrt{\frac{1}{m}\left(\frac{\hbar^2k^2}{m}-\frac{\hbar^2q^2}{4m}+\hbar\omega-\frac{m\omega^2}{q^2}\right)}$$

$$=q^2\sqrt{\frac{1}{m}\left(2E_k-0.5E_q+\hbar\omega-\frac{m\omega^2}{q^2}\right)}=q^2\sqrt{\frac{1}{m}\left(2E_k-0.5E_q+\hbar\omega\right)-\frac{\omega^2}{q^2}}$$

$$\frac{d\theta}{d\omega}=\frac{\left[\frac{dq}{d\omega}\left(\omega+\frac{\hbar q^2}{2m}\right)-q\right]}{q^2\sqrt{\frac{1}{m}\left(2E_k-0.5E_q+\hbar\omega\right)-\frac{\omega^2}{q^2}}}=\frac{\left[\frac{dq}{d\omega}\left(\frac{\omega}{q^2}+\frac{\hbar}{2m}\right)-\frac{1}{q}\right]}{\sqrt{\frac{1}{m}\left(2E_k-0.5E_q+\hbar\omega\right)-\frac{\omega^2}{q^2}}} \quad 3.44$$

The formalism of obtaining the electron-phonon scattering rates is based on integrating over the energy conversion delta function (Γ). For the case of emission, the scattering rate equation is finally expressed as

$$\frac{1}{\tau_e^{(a)}}=\pm\frac{2m^*}{a_B}\sum_n\int_{\omega1}^{\omega2}\frac{\left(N(\omega)+\frac{1}{2}\mp\frac{1}{2}\right)D(q,\omega)\left[\left(\frac{\omega}{q^2}\pm\frac{\hbar}{2m}\right)\frac{\partial q}{\partial\omega}-\frac{1}{q}\right]}{\left(\frac{q}{2}\pm\frac{m}{\hbar}\left[\frac{\omega}{q}-\frac{\partial\omega}{\partial q}\right]\right)\sqrt{\frac{1}{m}\left(2E_k-\frac{1}{2}E_q\pm\hbar\omega\right)-\frac{\omega^2}{q^2}}}d\omega \quad 3.45$$

where $a_B=\frac{\hbar^2}{m_0e^2}$ is defined as the Bohr radius in free space, n is an integer which represents the quantum number of phonons in the field and $N(\omega)=\frac{1}{exp\left(\frac{\hbar\omega}{kT}\right)-1}$ is the phonon occupation number with the energy of a single phonon being $\hbar\omega$. The integration variable is the electron energy of the lowest subband given

by $E_k = \frac{\hbar^2 k^2}{2m}$. The phonon's phase velocity (v_{ph}) and group velocity (v_{gr}) are expressed as $\frac{\omega}{q}$ and $\frac{\partial \omega}{\partial q}$, respectively. The group velocity is found numerically and discussed for IF and confined cases later on this thesis. Here, $E_q = \frac{\hbar^2 q^2}{2m}$ is a collection of the phonon's wave number, Planck's constant and the electron's effective mass, $m = m^* m_0$.

To further understand the electron-phonon scattering process, let us look at the matrix element for the excitation of electron from a state E_k to E_{k+q}. To describe the probability of a transition of an electron with wavevector k in the subband by a phonon of wavevector q, the matrix element can be defined as

$$\left|M^{\binom{C}{IF}}(q,\omega)\right|^2 = \frac{C\left(N(\omega)+\frac{1}{2}\mp\frac{1}{2}\right)D(q,\omega)\left[\left(\frac{\omega}{q^2}\pm\frac{\hbar}{2m}\right)\frac{\partial q}{\partial \omega}-\frac{1}{q}\right]}{q\left(\frac{q}{2}\pm\frac{m}{\hbar}\left[\frac{\omega}{q}-\frac{\partial \omega}{\partial q}\right]\right)\sqrt{\frac{1}{m}\left(2E_k-\frac{1}{2}E_q\pm\hbar\omega\right)-\frac{\omega^2}{q^2}}} \quad 3.46$$

where C is a constant expressed in Kilogram.Ampere. The largest scattering probability for small q can be justified by the $1/q$ dependence in Eqn. 3.46 which conserves both energy and momentum whereas the angle dependence was removed by expressing $d\theta$ as $\frac{d\theta}{d\omega}d\omega$ when employing $cos\,\theta = \frac{m^* m_0 \omega}{kq\hbar} - \frac{q}{2k}$.

In Eqn. 3.35, the summation over the quantum number n, identical to the ones in Eqs. 3.9–3.11 is included to consider scattering with all possible symmetric and asymmetric confined mode phonons. For each n, the proper dispersion relation between q and ω should be imposed through Eqs. 3.9–3.11. In our numerical calculation of the scattering rates, we find that a practical number for the upper limit is $n = 5$; contributions to the electron–phonon scattering rate from confined modes with n larger than 5 are negligible. Also, the symmetric and asymmetric confined modes must be considered separately as the dispersion relations are different from each other. For the case of interface modes, the summation is omitted because only one interface mode exists in a given range of phonon frequency $[\omega_1, \omega_2]$. In the

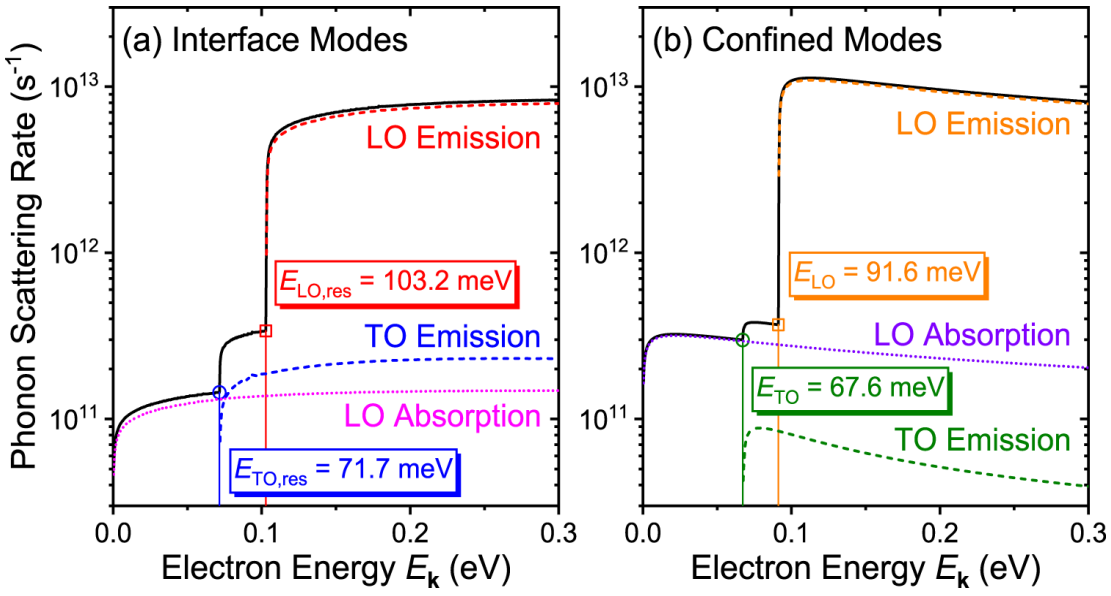

Fig. 14. (a) Interface and (b) confined mode phonon scattering rates are calculated and plotted as a function of electron energy. For both modes, the total interface phonon scattering rate combining all phonon modes (including the TO absorption scattering rate) is shown as the black solid line. The droplines with symbols are shown to indicate the threshold energies of TO emission and LO emission scattering. For interface mode scattering, these energies correspond to the TO and LO interface phonon resonant frequency energies $\hbar_{res}^{TO} = 71.7$ meV and $\hbar_{res}^{LO} = 103.2$ meV, respectively. For confined mode scattering, the threshold energies are at the vicinity of the TO and LO phonon energies of GaN.

---

original formula [156], where the integral is assessed over the angle θ between the phonon wave vector and the optical axis c, the lower and upper limits of the integral are set to $\theta = 0$ and 2π. In order to separately calculate the matrix elements of the Fermi golden rule for each phonon mode of uniaxial wurtzite crystals, the formula with the integral over θ is transformed into Eqn. 3.45 as provided in this segment where the integral is over ω. Considering the energy and momentum conservation of the electron–phonon scattering process, the limits of the integral over ω may also be transformed according

to the relations $cos\,\theta = \pm\left(\frac{m^* m_0 \omega}{kq\hbar} - \frac{q}{2k}\right)$ where the $+$ sign represents the case for absorption and the $-$ sign represents the case for emission. Eqn. 3.35 defines the case for both confined and interface phonon scattering rates, with the summation over n in the IF case is omitted [156]. The integral in Eqn. 3.35 is an integration over the range of allowed phonon frequencies $[\omega_{1z}, \omega_{2z}]$, indicated by ω_1 and ω_2 and determined from the relation $cos\,\theta = \pm\left(\frac{m^* m_0 \omega}{kq\hbar} - \frac{q}{2k}\right)$, however, the practical limits of the numerical integration are the allowed range of frequency for the phonon mode in question.

Figs. 14–16 show the interface and confined mode phonon emission scattering rates for a double heterostructure system. We consider an initial design of a 5 nm QW of a hexagonally ordered wurtzite material sandwiched between two other hexagon planes of a dissimilar wurtzite material. We then adjust the thickness of the well layer. Compared to the d = 5 nm case, indeed, the interface mode scattering rate for electron energy larger than the threshold energies becomes approximately 8 times larger than the confined mode [140] in GaN/AlN QW with d = 1 nm, at least 6 times larger in InGaN/GaN QW with d = 2 nm [186] and ~ 5 times larger in AlInN/AlN QW with d = 1 nm [204]. Also notice that the interface mode scattering curve shows more than two of the step-like features. This is due to the emission threshold energy split between the symmetric and asymmetric interface modes. With d = 5, the wave vector q is only large enough to satisfy the emission condition at phonon frequencies of $\omega = \omega_{TO(LO),res}$. However, with smaller d, this is no longer the case and the condition is satisfied with phonon frequencies slightly away from the resonant frequencies. As the symmetric and asymmetric interface modes are defined in separate phonon frequencies, except at the limit of $\omega \to \omega = \omega_{TO(LO),res}$ the threshold energies are split and causes the scattering rate curve to show more step-like increases. For all cases, the scattering rates decrease according to the perturbation theory [156].

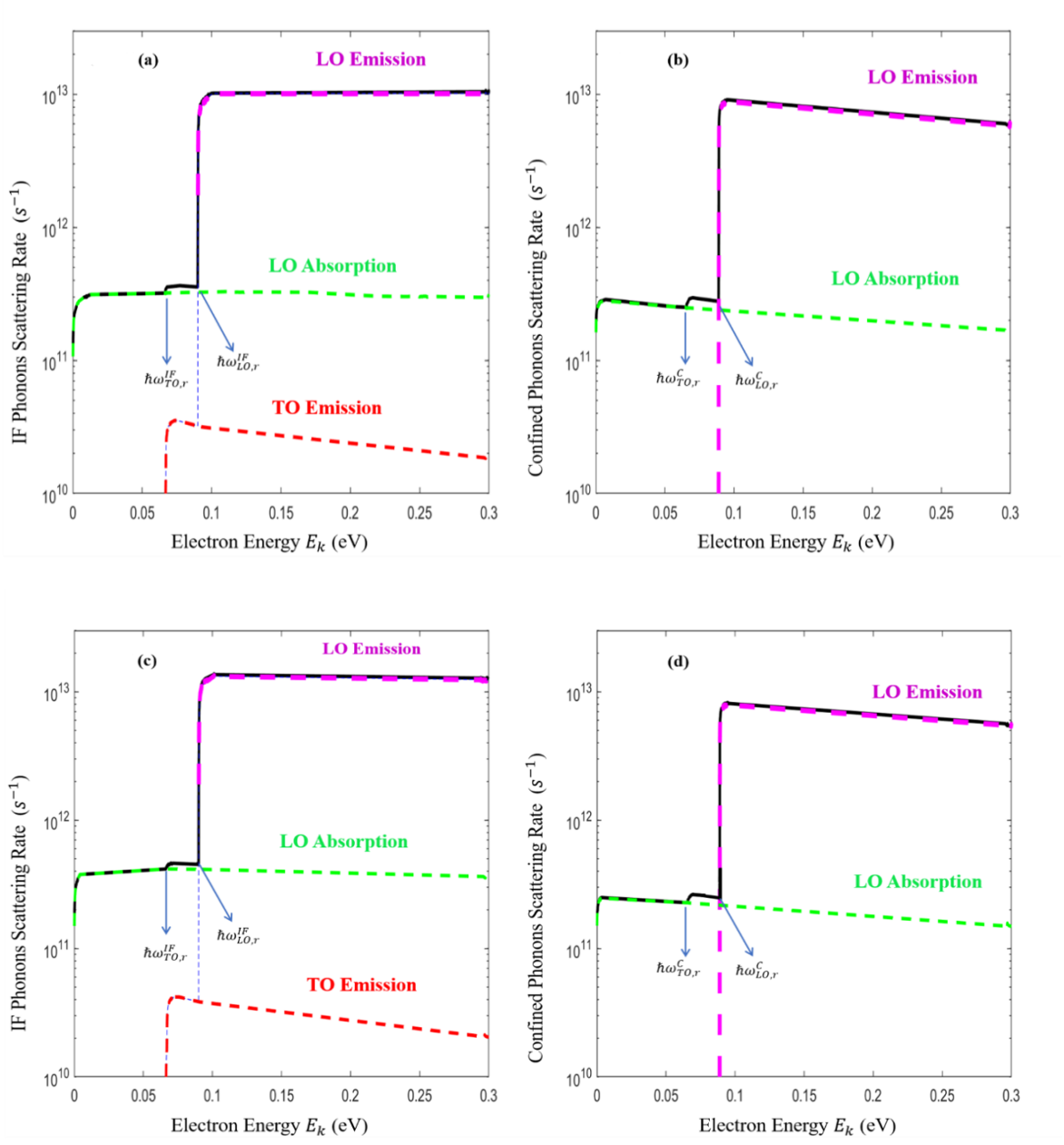
(a)
LO Emission
LO Absorption
TO Emission
IF Phonons Scattering Rate (s^{-1})
Electron Energy E_k (eV)
(b)
LO Emission
LO Absorption
Confined Phonons Scattering Rate (s^{-1})
Electron Energy E_k (eV)
(c)
LO Emission
LO Absorption
TO Emission
IF Phonons Scattering Rate (s^{-1})
Electron Energy E_k (eV)
(d)
LO Emission
LO Absorption
Confined Phonons Scattering Rate (s^{-1})
Electron Energy E_k (eV)

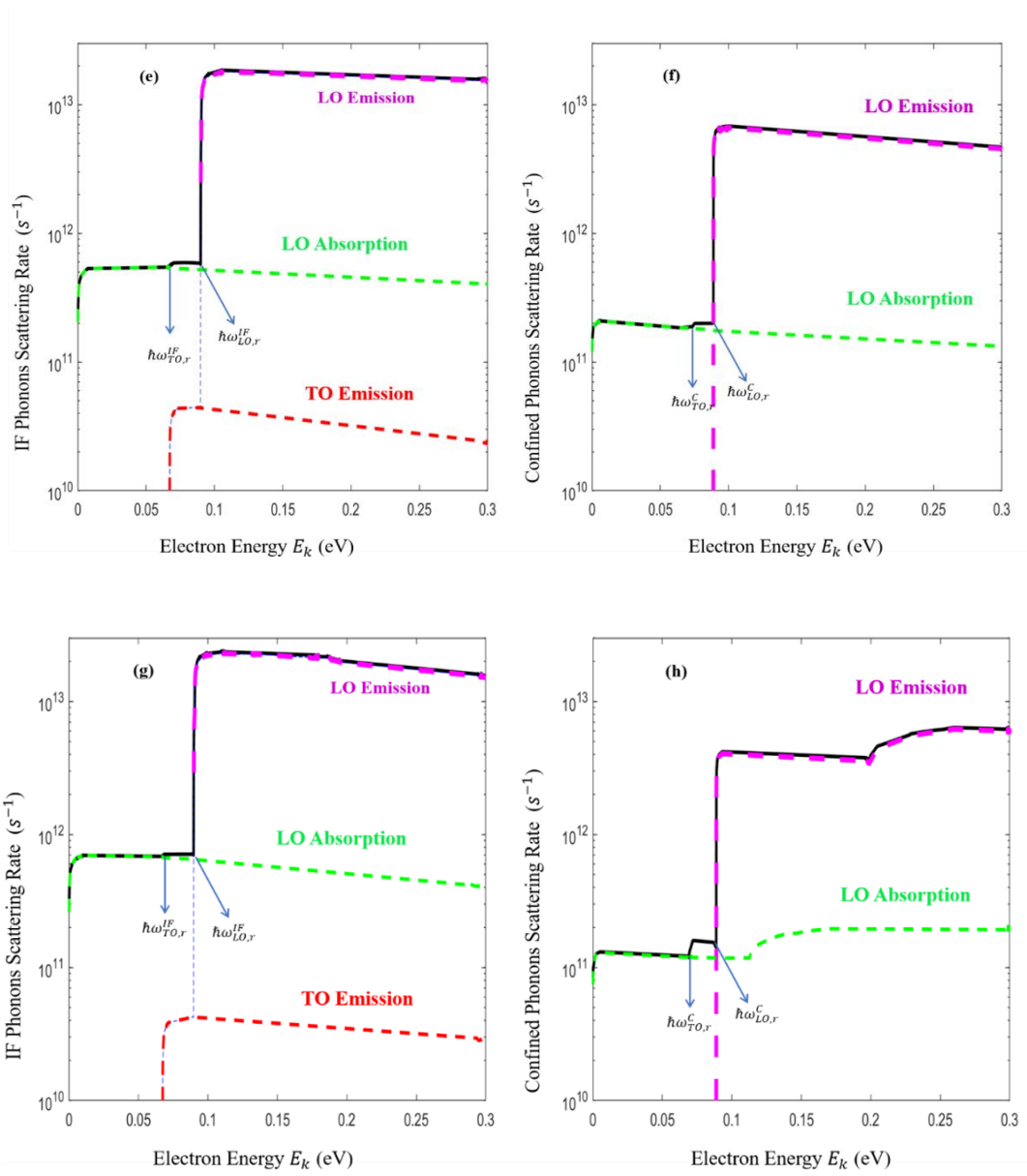

Fig. 15. Total emission electron scattering rate as a function of the electron energy in the three-layered heterostructure of wurtzite GaN/InGaN/GaN quantum wells. The case $d = 5$ nm is shown for interface in (a) and confined in (b). The thickness is set to 4nm in (c) and (d), 3 nm in (e) and (f) and 2 nm in (g) and (h). Only the phonon-assisted emission for IF (a, c, e, g) and confined modes (b, d, f, h) is considered. The black solid line corresponds to the total emission rate, which is the sum of the IF LO emission, LO

absorption and the TO emission rates. For both symmetric and asymmetric emission, the magenta line corresponds to LO emission rates, the green line corresponds to LO absorption rates, the red line corresponds to TO emission rates. The TO emission threshold energies are indicated by blue arrows and are labeled in the graphs as $\hbar\omega_{TO,r}^{C}$ for confined and $\hbar\omega_{TO,r}^{IF}$ for IF while the LO emission threshold energies are labeled as $\hbar\omega_{LO,r}^{C}$ for confined and $\hbar\omega_{LO,r}^{IF}$ for IF.

3.5 Heat transport in high-performance HEMT structures

In Eqn. 3.35, the phase ($v_p = \frac{\omega}{q}$) and group velocity ($v_g = \frac{\partial\omega}{\partial q}$) of the phonon modes (or its reciprocal) are frequently used in the equation. Given the complex form of the phonon wave vector q, instead of expressing these velocities in a closed form equation, we calculate the velocities numerically. The group velocity is not only a component of the integral but also a crucial factor that describes the behavior of the phonons, and furthermore, the thermal characteristics of the system. Fig. 17 shows the group velocity of the interface and confined phonon modes as a function of phonon frequency. As expected by the dispersion relation shown in Fig. 6, the interface mode phonons possess a considerably larger group velocity compared to the confined mode phonons. The largest confined mode group velocity is less than 7 km/s at ω ~ 552 cm^{-1} (TO mode), whereas the largest interface mode group velocity reaches up to 138 km/s (or 138 nm/ps) at $\omega = \omega_{1Lt}$ (LO mode).

It is easily deduced that if the full spectrum of interface phonon modes can be utilized; the phonons can carry a portion of the generated heat away along the heterointerface. This would be an additional heat transport mechanism, on top of the always existing acoustic phonon heat transport, that can help the system dissipate heat more efficiently. To better understand the electron interaction with these interface and confined mode phonons, we evaluate Eqn. 3.35 and calculate the scattering rates between the electrons and optical phonons. Fig. 14 shows the (a) interface and (b) confined mode phonon scattering rates as a

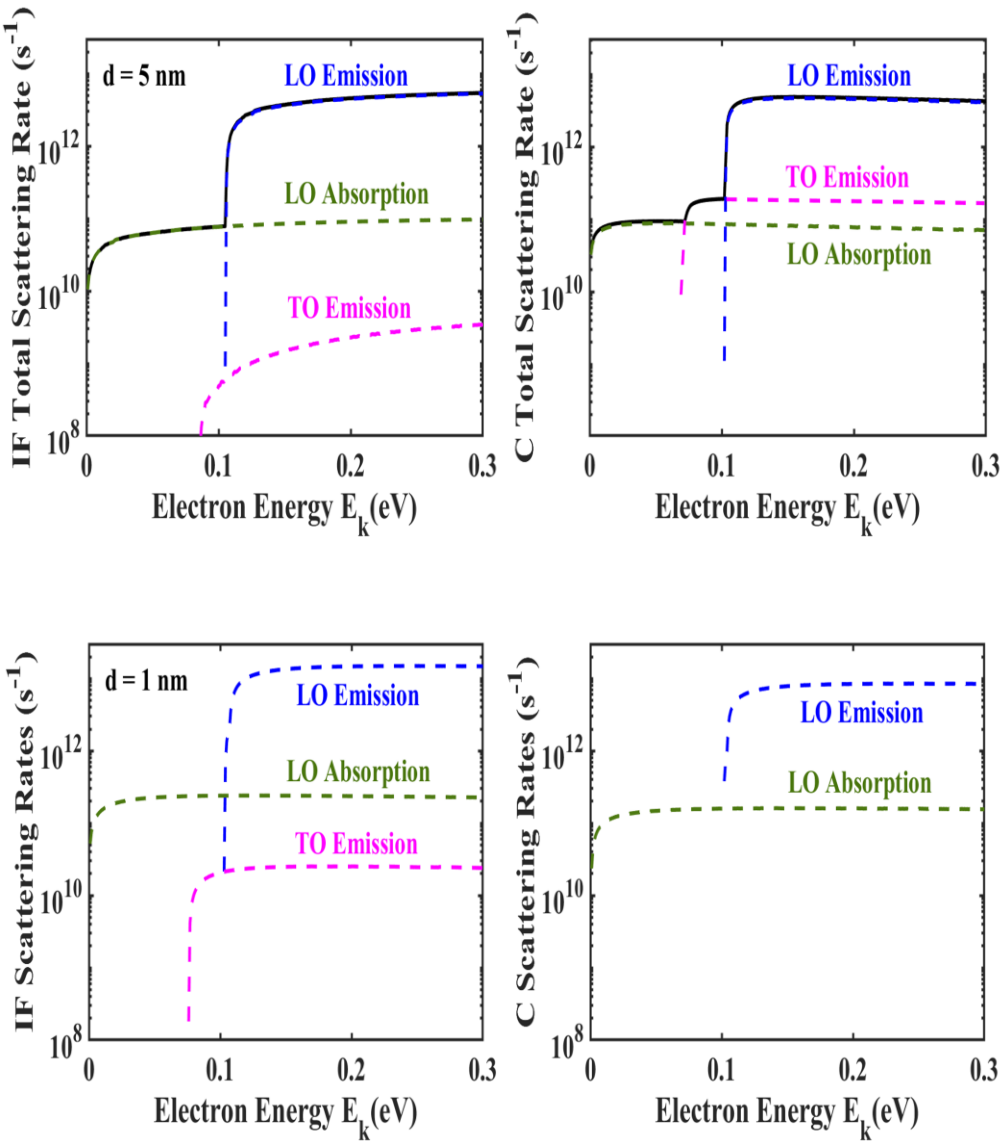

Fig. 16. (a) Total phonon relaxation rates as a function of the electron energy for AlInN quantum well thickness (d) of 5 nm. (b) Emission and absorption rates for AlInN/AlN QW with d = 1 nm.

---

function of electron energy E_k for GaN/AlN QW. For both (a) interface and (b) confined modes, the black solid line shows the total scattering rate which combines all contributions from each process indicated as dashed and dotted color lines. The general behavior of the scattering rate curves for both modes are similar. The LO emission scattering rates [(a) red and (b) orange dashed lines] start to dominate once the electron

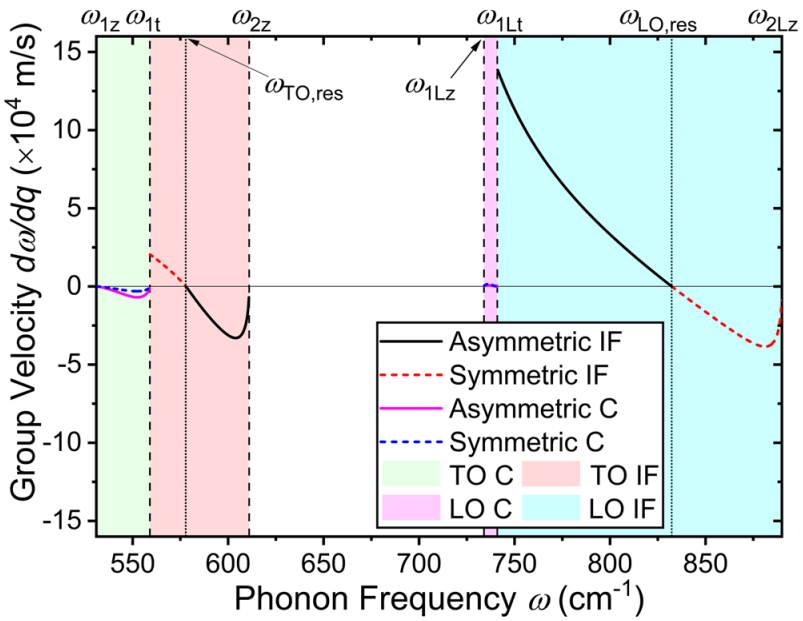

Fig. 17. The numerically calculated group velocities of interface and confined mode phonons are shown as a function of phonon frequency. For both interface and confined modes, the solid and dashed lines indicate the asymmetric and symmetric phonon modes, respectively. The group velocity of interface phonons go to zero close to the TO and LO resonant frequency shown in vertical dotted lines. Maximum group velocity of 138 km/s occurs at $\omega = \omega_{1Lt}$ for the interface mode phonons. This value is almost 20 times larger than the maximum group velocity of the confined mode phonons.

---

energy exceeds the threshold energy. The TO absorption processes are negligible compared to the others (not plotted in the figures). Due to mode mixing in wurtzites, the TO emission scattering rate is comparable to the LO absorption scattering rate. This causes the total scattering rate to show a two-step-like shape. The total scattering rate of both modes show roughly similar values that converge to ~ 10^{13} s^{-1} with E_k = 0.3 eV in the current system where the GaN thickness is set to $d = 5$ nm. As shown in Fig. 17, since we know that the interface mode phonons typically show larger group velocity, a comparable scattering rate

between the interface and confined mode phonons indicates that the average phonon velocity of the phonons emitted due to these processes may be large enough to help dissipate the heat.

Focusing on the interface mode LO emission scattering rate in red dashed curve in (a), we observe that the emission threshold energy is 103.2 meV. This energy corresponds to the energy of the LO resonant phonon frequency of 832.3 cm^{-1}. The LO phonon emission process through electron–phonon scattering can only occur when the electron possess more energy than the phonon to be emitted. The emission threshold energy of 103.2 meV indicates that phonons with at least this amount of energy are most likely to be emitted. From Fig. 17, we see that the group velocity of phonons with the resonant frequencies $\omega_{LO,res}$ and $\omega_{TO,res}$ are zero. The TO emission threshold energy (71.7 meV) also corresponds to the energy of TO resonant phonon frequency of 577.8 cm^{-1}. These observations of Fig. 14 suggest that, however large the group velocity of interface phonons could be, simply increasing the interface phonon mode scattering rate with respect to the confined phonon mode scattering rate may not improve the heat dissipation efficiency of the system.

Let us now consider GaN/InGaN QWs. Numerous studies have discussed the growth and the detection of lattice matched GaN/InGaN QWs with well thicknesses as low as 1 nm [205], [206]. In this segment, it is shown that inserting a GaN/$In_{0.15}Ga_{0.85}N$/GaN quantum well in the hot spot region of a GaN HEMT, results in the emission of confined and interface phonons instead of bulk phonons as a result of emission from hot electrons, moreover, the phonons can be engineered to enhance the production of fast-moving interface phonons. Indeed, the IF and confined modes emission rates of GaN/$In_{0.15}Ga_{0.85}N$/GaN heterostructure with $In_{0.15}Ga_{0.85}N$ thickness of d = 5, 4, 3, and 2 nm are numerically calculated and plotted in Fig. 15. The thicknesses included in this paper allow us to grow GaN/InGaN QWs without misfit dislocations since they are below the critical thickness values [207]. In Fig. 15, the left curves denote the IF scattering rates and the right curves denote the confined scattering rates. The total emission rate is

presented in black which encompasses the LO emission in magenta, the LO absorption in green and the TO emission in red whereas the TO absorption is disregarded since it has a value well below 10^{10} s^{-1}. These rates include both symmetric and asymmetric phonon process. The emission of TO-like and LO-like modes causes the first and the second step-like features in the black curves, respectively. In the d = 5 nm case, hot electrons produce less confined phonons in GaN/InGaN QWs compared to GaN/AlN, this is referred to the weak confinement of phonons due to the lower potential barrier of the former QW.

In the hexagonal structure of GaN/InGaN, the medium anisotropy causes the splitting of LO and TO modes. Compared to the emission of LO phonons which has the highest scattering rates in the order of 10^{13} s^{-1}, the emission of the TO phonons is much lower and in the order of 10^{10} to 10^{11} s^{-1} due to their weak coupling to electrons, thus the contribution from the TO modes is normally neglected. As can be seen from the graphs, the emission of LO (TO) phonons starts when the energy of the electron reaches a value right before $\hbar\omega_{LO}$ ($\hbar\omega_{TO}$). From the analysis of the IF (confined) resonance frequencies, we should predict LO phonons to be emitted at 90.16 meV (89.25 meV) and TO phonons to be emitted at 66.89 meV (65.1 meV). The values of E_k required to emit LO and TO phonons are illustrated on Fig. 15 by $\hbar\omega_{LO,r}^{IF} = 0.092$ eV, $\hbar\omega_{TO,r}^{IF} = 0.066$ eV for IF modes and $\hbar\omega_{LO,r}^{C} = 0.089$ eV, $\hbar\omega_{TO,r}^{C} = 0.065$ eV for confined modes. We find that the values portrayed in Fig. 15 are in close proximity to the resonant values.

When the InGaN thickness is set to 5 nm, IF (confined) emission rate reaches $1.13 \times 10^{13}\ s^{-1}$ ($9.75 \times 10^{12}\ s^{-1}$) which means that approximately 53% of the hot electron energy is emitted as IF phonons. A modest increase (decrease) occurs with a QW thickness of 4nm to a maximum value of $1.45 \times 10^{13}\ s^{-1}$ ($8.345 \times 10^{12}\ s^{-1}$), i.e., an increase in the probability of emitting IF phonons relative to confined phonons to about 63%. Following the analysis as mentioned, we find emission rates for IF (confined) approaching values of $1.89 \times 10^{13}\ s^{-1}$ ($6.83 \times 10^{12}\ s^{-1}$) and $2.4 \times 10^{13}\ s^{-1}$ ($4.35 \times$

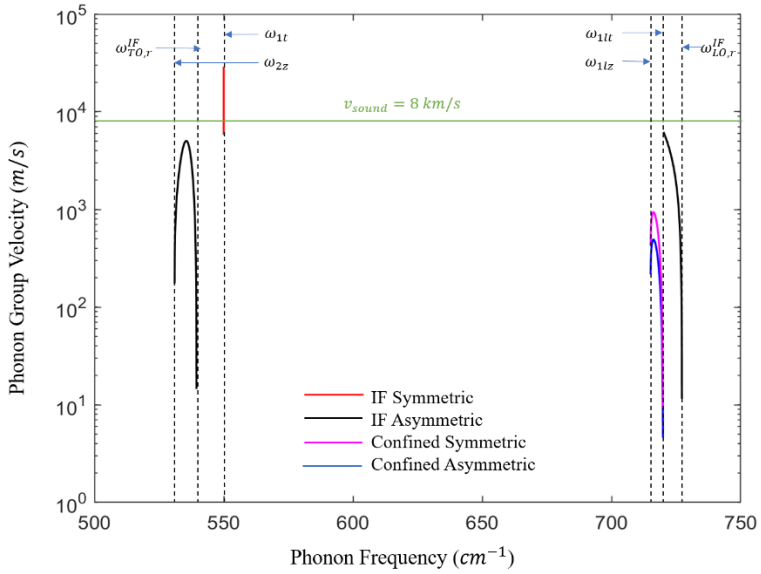

Fig. 18. The group velocities of the IF and confined phonons against the phonon frequencies for the case of InGaN well of d = 5 nm. Only the modes in the intervals $[\omega_{2z}, \omega_{1t}]$ and $[\omega_{1lz}, \omega_{LO,r}^{IF}]$ which show significant group velocities are plotted. The symmetric IF (confined) phonons are plotted in red (magenta) and the asymmetric IF (confined) phonons are plotted in black (blue). For both modes, the group velocity is referenced to the acoustic sound velocity highlighted in green. Only the first confined mode is considered in the LO region for each symmetric and asymmetric mode. The resonance frequencies along with the system's characteristic frequencies are shown by the horizontal blue arrows.

$10^{12}\ s^{-1}$) for 3 and 2 nm thicknesses, respectively. From the trends of $\frac{1}{\tau}$ in Fig. 5, the highest emission rates for confined phonons are located around their resonant frequencies but are becoming more difficult to produce in smaller QW thicknesses; hence one expects that these rates should be positioned at the onset of LO emission around $E_k = 89.25$ meV. Similarly, IF phonons are generated in greater numbers within

the available frequency ranges. Therefore, presumably, the IF phonons that help dissipate heat more efficiently have energies above the emission threshold at $E_k = 90.16$ meV.

Normally, optical phonons are not considered as heat carriers as they have smaller group velocities compared to the acoustic phonons. As can be found in Fig. 18, the group velocities of the optical modes in the interval $[\omega_{2z}, \omega_{1t}]$ with d = 5 nm are noticeable and surprisingly the group velocity of the low-order optical branches approaches that of the acoustic branches ($v_{sound} = 8\ km/s$). We note that even the highest frequency optical phonons are significantly dispersive. The group velocity v_{gr} of the highest confined mode is 0.936 km/s as it is clear from Fig. 18. This mode oscillates at 716.5 cm^{-1} and reduce to a minimum value near its resonance frequency of 719.9 cm^{-1}. On the other hand, IF asymmetric-type phonons (denoted by black lines) propagate at $[\omega_{2z}, \omega_{TO,r}^{IF}]$ and $[\omega_{1lt}, \omega_{LO,r}^{IF}]$. A sharp increase occurs in their group velocities where they move with speeds near the sound velocity and reduce to minimum values at the resonance frequencies. The highest IF symmetric-type phonon (denoted by red line) approaches a velocity of 29 km/s at 550 cm^{-1}. Going back to Fig. 15 (a), the added layer of InGaN produces IF phonons with rates that are ~ 2.5 times larger than the confined phonons rates. We observe at smaller widths that the emission of IF modes dominates over confined modes. Of course, there is a tradeoff between increasing $\frac{1}{\tau}$ with decreasing d as v_{gr} drops accordingly. Moving from $d = 5\ nm$ to $d = 2\ nm$, the probability of emitting IF phonons increases by ~ 31% to almost 84%, while v_{gr} drops by a factor of ~ 2.5 for each mode plotted in Fig. 6. Engineering IF with high group velocity becomes most useful when we have comparable IF and confined emission rates such as the case in AlN/GaN/AlN QW. Compared to the increasing IF emission rates in GaN/InGaN/GaN, the average probability of IF emission in AlN/GaN/AlN with GaN thickness of 5, 4 and 3 nm was found to be between 50 and 55%. Therefore, we must prioritize the consideration of engineering v_{gr} to become as high as possible in order for IF optical phonons to reduce

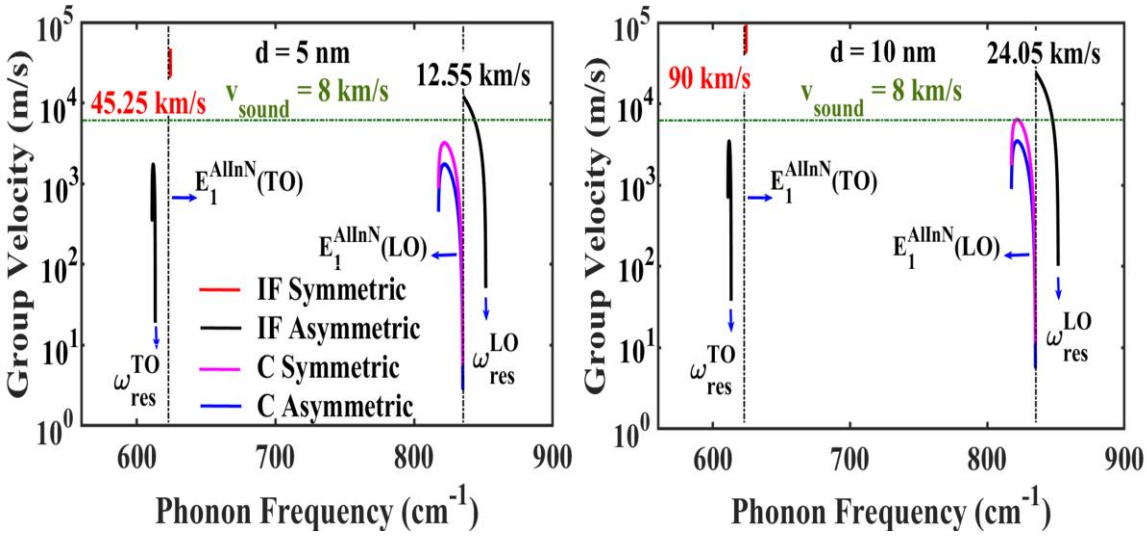

Fig. 19. Comparison of the group velocities of different phonon modes for AlInN QW of 5 and 10 nm thicknesses.

---

the junction temperature, consequently they can propagate at high relative speeds away from the hot spot before they decay in picoseconds into heat-carrying phonons.

Thus far, we have considered the energy loss rates by phonon emission. Optical phonon confinement has an effect on the phonon linewidth, the frequency shift observed through Raman scattering and the phonon lifetimes, but the confinement-related change in lifetime is generally no more than about a factor of 2 [98]. Evidently, the IF phonon lifetime is important to determine their contribution to heat generation in the semiconductor channel. For GaN, it was reported that A_1(LO) mode decays into a lower energy optical mode and an acoustic mode via the Ridley channel after some time 0.1 ps. Since the E_1(LO) mode is polarized along the quantum well interfaces – as opposed to normal to the quantum well interfaces as for the A_1(LO) mode – the production of E_1(LO) modes is more likely for our case; it is known that the E_1(LO) has a lifetime of 3.34 ps [207]. From the calculations obtained for the group velocities in Fig. 6, we observe that different modes contribute to the size of the hot spot. For the E_1(LO) mode, the asymmetric mode,

labeled in black color in Fig. 18, propagates with group velocity $v_{gr} = 5 \times 10^3\ m/s$, this results in a spreading of the hot spot to approximately 17 nm. Similarly, the asymmetric mode in the high energy interval with $v_{gr} = 6.2 \times 10^3\ m/s$ extends the hot spot by about 21 nm. The highest velocity symmetric mode labeled in red in Fig. 18 extends the hot spot by the largest amount of ~ 97 nm. These distances are very large compared to the hot spot sizes of a few nm observed in bulk GaN HEMTs [208].

Finally, for AlInN/AlN QW, Fig. 16 (left) depicts the total scattering rates in the black sold line which combines the contributions of all modes including LO emission scattering in blue dashed lines, LO absorption scattering in green dashed lines and TO emission in purple dashed lines. TO absorption scattering is negligible with rates below 10^8 s^{-1} and therefore not plotted here. The dominant mechanism underlying our theory is the LO emission upon exceeding the threshold energy. The LO emission scattering rate for both interface and confined modes when AlInN well thickness is set to 5 nm converge roughly at around 5×10^{12} s^{-1}. Since interface phonons are projected to have higher group velocity, we use the thickness optimization method such that the system has enough interface phonons emitted comparable to or higher than the confined modes in order to optimize the production of interface modes which propagate rapidly (> 3×10^3 m/s as shown in Fig. 19) and delocalize the energy before they decay into heat carrying acoustic phonons; this is in contrast to the bulk phonons which have near-zero velocities and play no role in delocalizing the heat. As shown in Fig. 16 (right), when the AlInN thickness is set to 1 nm, the interface phonons scattering rates show a significant jump to close to 10^{13} s^{-1}. Hence, by changing the width of the heterostructure, the production of interface modes can be enhanced with the result that heat is spread more efficiently.

Fig. 19 shows the calculated group velocities of the 2DEG in the AlInN, 5 nm, channel HEMTs. Parallel to the heterointerface, the production of E_1(LO) modes dominate [188], [209]. During scattering between electrons and phonon, both momentum (wavevector) and energy conservation are invoked when applying

the Fermi Golden Rule to calculate scattering rates. For emission, $E_k \geq \hbar\omega$, which translates to an emission threshold in energy of 0.105 eV for an AlInN thickness of 5 nm, a value close to the resonant frequency. The electron scatters with optical phonons beyond that point with group velocities comparable to the acoustic sound velocity as described in Fig. 19. Averaging the different modes presented in Fig. 19, we report a 95% increase in the group velocities going from d = 5 to 10 nm, i.e., close to an AlInN bulk value.

The phonon lifetimes are determined by the anharmonic term in the phonon potential. In order to make a straightforward estimate of the approximate reduction in the hot spot temperature in the AlInN QW, we have used known values of the anharmonic LO-phonon decay times for selected x-values for Al(x)In(1-x)N; namely, using the known values of 0.9 and 1.5 ps for the E_1(LO) phonons in AlN and InN, respectively [132], [210], we find that the hot spot is elongated by $0.9\ \text{ps} \times \text{velocity}\ (12.55\ \text{km/s}) = 11.30\ nm$, and $1.5\ \text{ps} \times \text{velocity}\ (12.55\ \text{km/s}) = 18.83\ nm$. For a 5-nm diameter hot spot [211], since heat-carrying acoustic phonons are produced when these LO phonons decay, this results in an elongation of $[(11.30-5)/5] = 126\%$ to $[(18.83-5)/5] = 276.6\%$. Assuming IF and confined phonons are emitted with the same rates, i.e. 50% of the hot electron energy is radiated as interface phonons, these results portend a corresponding decrease in the hot spot temperature of $[50\% \times (11.30-5)/11.3] = 27.9\%$ to $50\% \times [(18.83-5)/18.83] = 36.7\%$ which implies that the phonon engineering techniques in this chapter may be usefully employed to reduce hot spot temperatures.

3.6 Remote interface polar phonons in wurtzite-based structures

Charge carriers in 2D materials, diamond, graphene and carbon nanotubes can remotely couple to surface polar phonons (SPP) when brought in close proximity to a polar substrate via a mechanism usually known as remote interface phonon (RIP) scattering [212], [213]. In this phenomenon, the remote coupling

between charge carriers and surface polar phonons in the underlying polar substrates is facilitated by oscillating electric fields created by SPPs and accompanied by energy exchange and momentum. Because of the inelastic nature of SPPs, they also provide a pathway to saturation of current in conjunction with intrinsic optical phonons [214]. Indeed, remote interface phonons, such as Rayleigh waves, can penetrate, with an exponential fall-off, up to 10s of nanometers and thus plays a critical role on scales of 10 nm or even less. In this segment, we will provide an investigation of the role of remote interface polar phonon modes on the electronic transport properties of dimensionally confined diamond structures. We employ a dielectric continuum mode to calculate the scattering rates, hole mobility and relaxation times in mesoscopic diamond-based devices. Hereafter, we analyze the performance of the device by inserting polar over layers on diamond with wide bandgap materials such as AlN or *w*–BN. Hopefully, the present research will provide a milestone for understanding interface phonons that penetrate to the two-dimensional hole gas (2DHG) in confined diamond structures as compared to their bulk counterparts and can also be applied to other polar materials used for doping.

3.6.1 Application of AlN overlayer

AlN interlayer can be grown diamond which provides GaN-on-diamond structures with improved thermal mismatch. AlN could also be incorporated into a GaN buffer stack and/or grown onto a Si substrate [16]. AlN-on-diamond structures were also shown to offer a rectifying I-V behavior [215]. These interface phonons in diamond devices penetrate to the two-dimensional hole gas (2DHG) which is located only a few nanometers from the diamond surface exhibiting p-type conductivity. Researchers have provided a solid foundation in the understanding of the mechanisms leading to the formation of a high mobility 2DHG under the surface of H-terminated diamond [216]. Here, we have taken into account the insertion of AlN polar material on top of the diamond substrate, which is often neglected during the study of the mobility in diamond-based devices in order to understand its effectiveness and importance in depth.

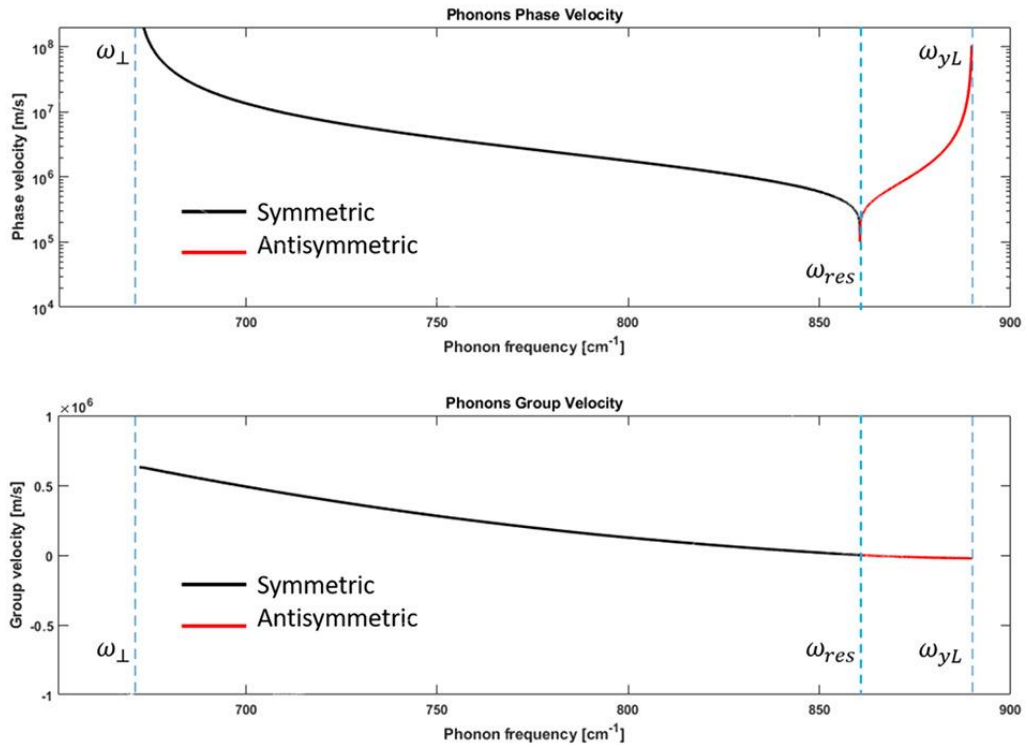

Fig. 20. Phase (top) and Group (bottom) velocity for the IF polar phonons in AlN layer.

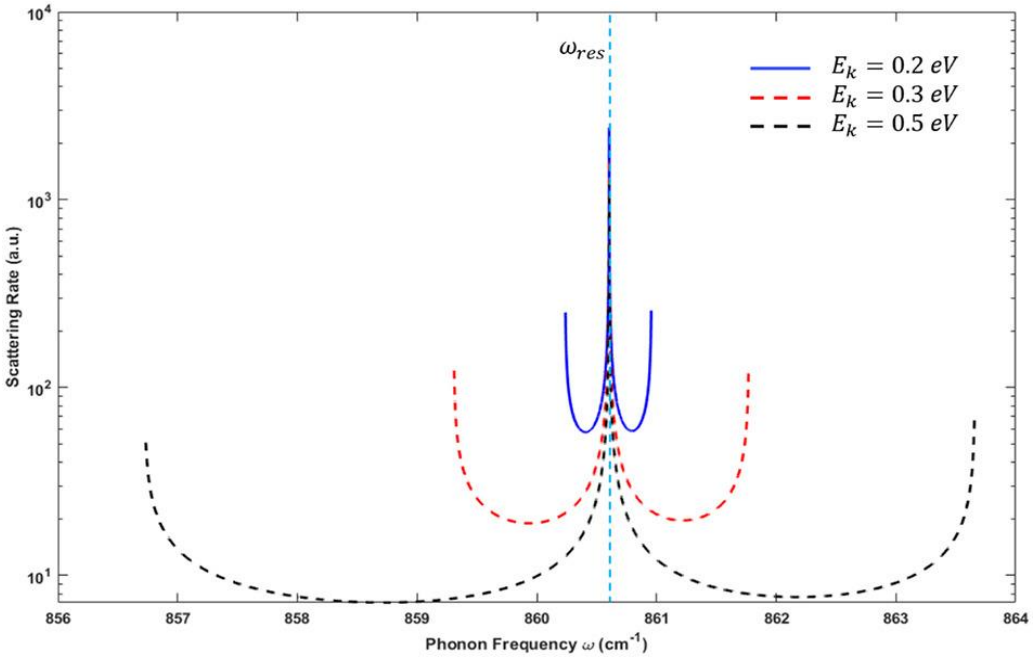

Fig. 21. Frequency distribution of the phonon emission for the case of AlN layer for different hole energies E_k.

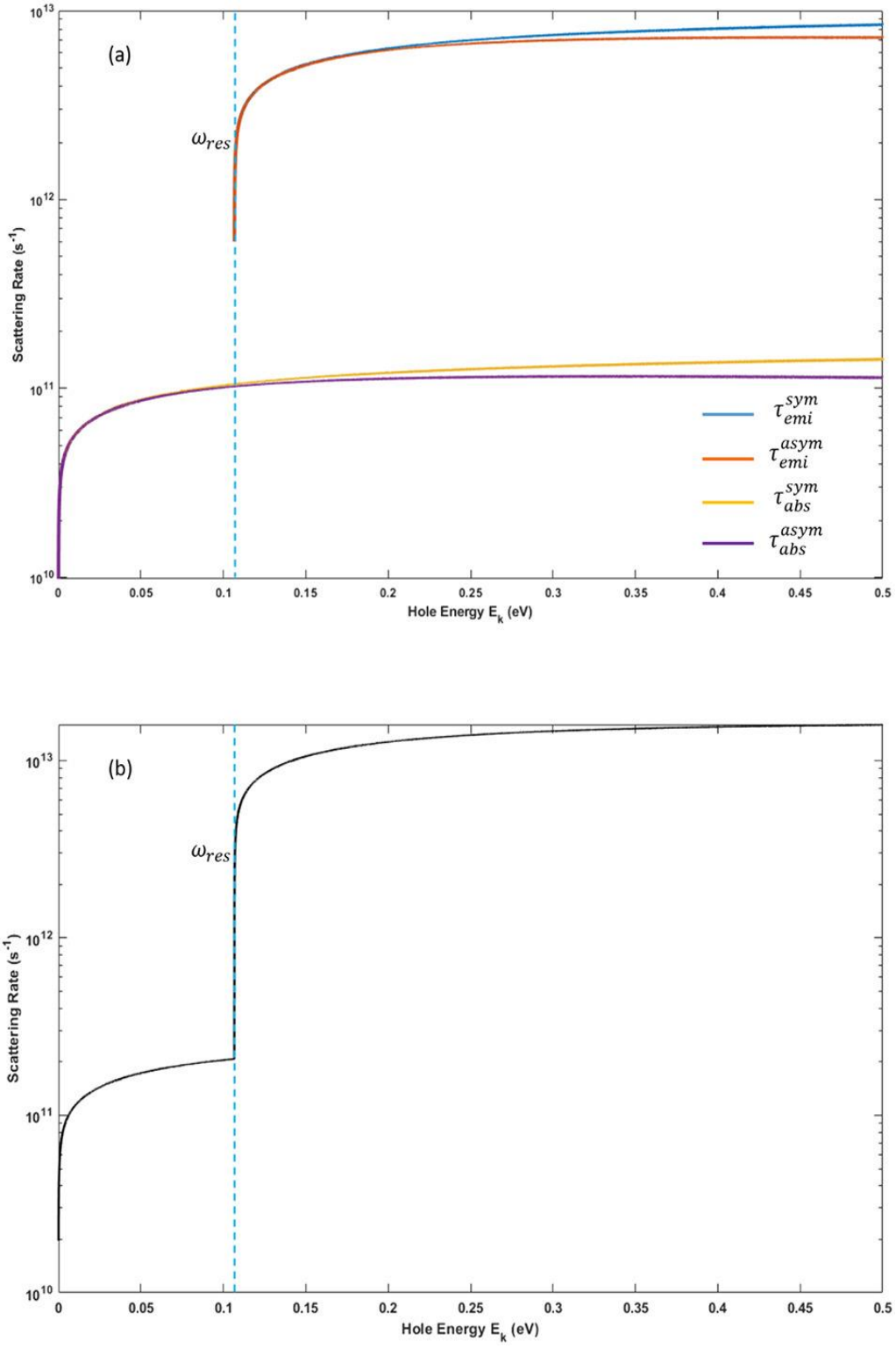

Fig. 22. Scattering rate for symmetric and antisymmetric absorption and emission (a) and their summation (b) for the AlN case.

A MATLAB code employing the dielectric continuum mode for interface phonons (described extensively in this chapter) is provided in Appendix B and the results are provided herein. The phonon's phase and group velocities for the optical phonons are plotted as in Fig. 20. Evidently, the lowest velocities is located in the surroundings of the resonant frequency of symmetric and antisymmetric modes. According to the relation in Eqn. 3.35, which satisfies the momentum and energy conservation conditions, the results portend a higher emission associated to the resonant frequency. This behavior is depicted in Fig. 21, in which the number of phonons emitted with respect to the frequency is represented for three different values of hole energies E_k. The localization of the emission of phonons in a narrow range of values close to the resonant frequency is also related to the relatively high effective mass of diamond. The scattering rates obtained via the numerical integration are depicted in Fig. 22. As predicted, the emission contributions appear for a value of hole energy equivalent to the resonant frequency of the IF modes.

3.6.2 Application of *w*-BN overlayer

It is worth noticing that, when drawing the dispersion relations, in comparison to the curves obtained for the case of AlN layer, the resonant frequency for the *w*–BN layer happens for a higher value of phonon frequency as evident by the frequency values reported in Table 2. Based on the dispersion curve estimations, the phase and group velocities for the IF optical phonons are obtained as in Fig. 23. Also, in this case, the lowest velocities is located in the region surrounding the resonant frequency of symmetric and antisymmetric modes, which yields higher emission associated to the resonant frequency, as depicted in Fig. 24. In comparison to the AlN case, the emission of phonons is localized in a narrow range of values close to the resonant frequency. This could be explained with the higher phonons' phase velocity in the case of *w*–BN. The scattering rates obtained via the numerical integration are plotted as in Fig. 25. The emission contribution appears for hole energies equivalent to the resonant frequency of the IF modes, which leads to a spike in the scattering rate localized at higher energies in respect to the AlN case.

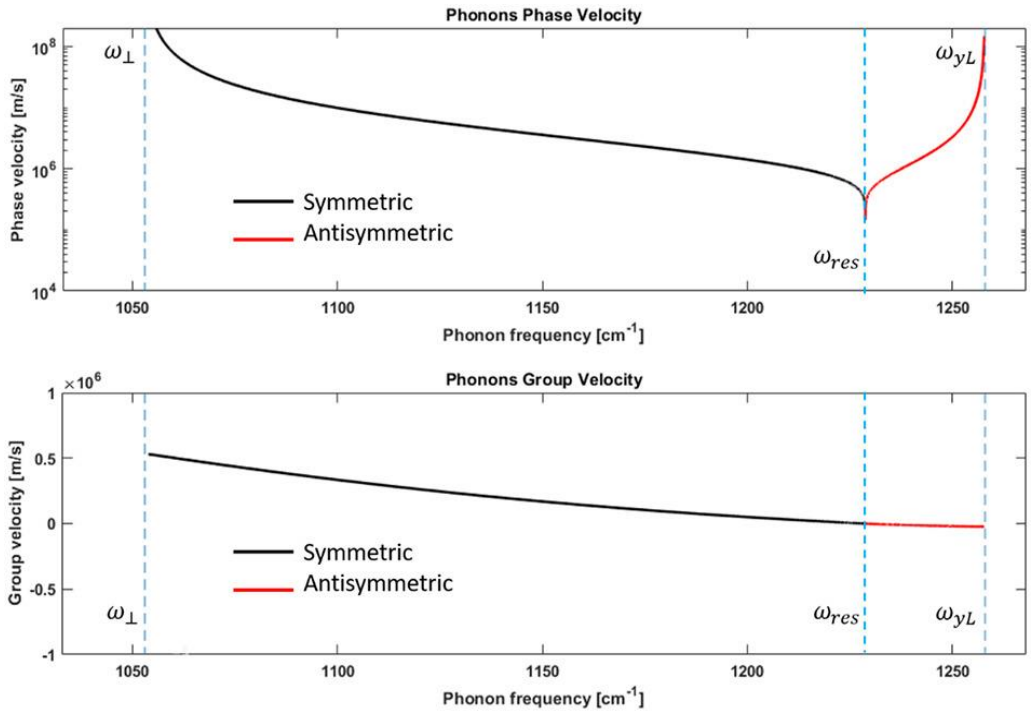

Fig. 23. Phase (top) and Group (bottom) velocity for the IF polar-phonons in *w*-BN layer.

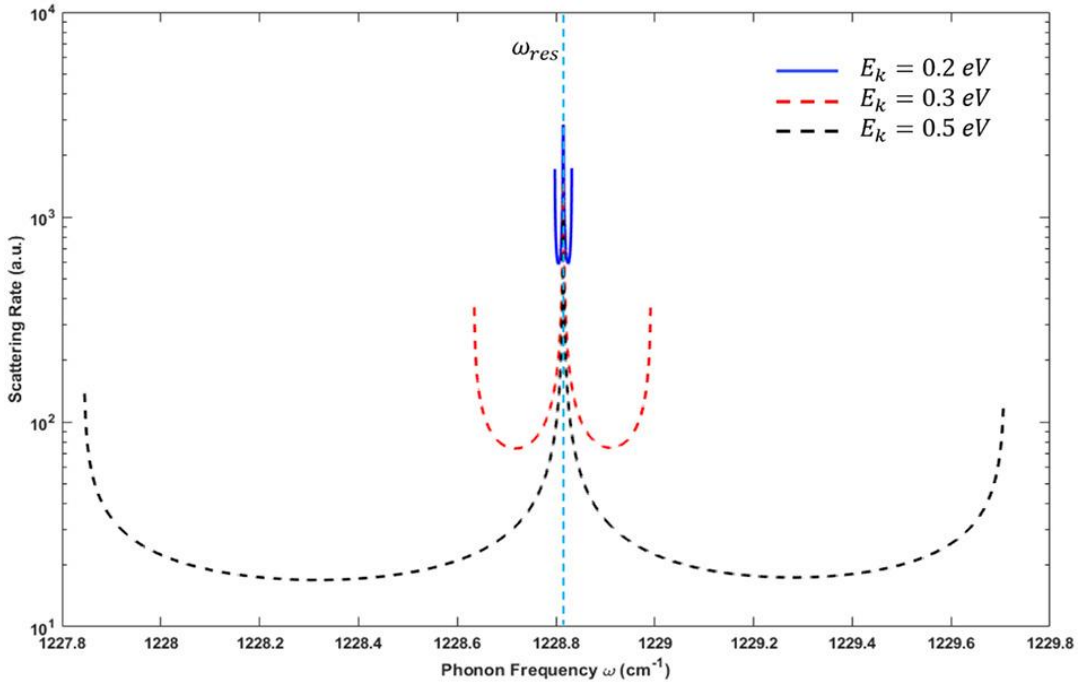

Fig. 24. Frequency distribution of the phonon emission for the case of a *w*-BN layer for different hole energies E_k.

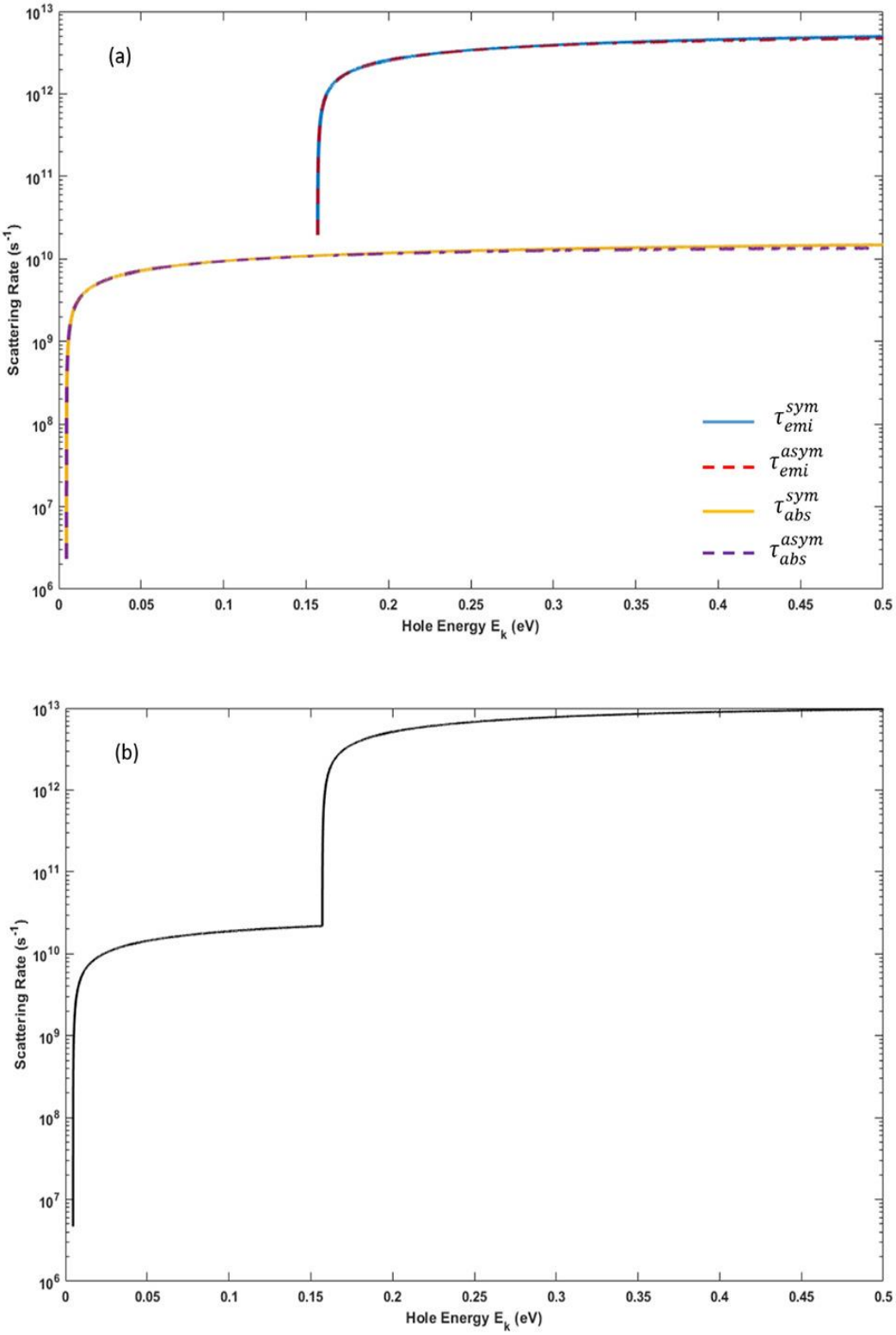

Fig. 25. Scattering rate for symmetric and antisymmetric absorption and emission (a) and their summation (b) for the *w*-BN case.

3.7. Summary

In conclusion, we have theoretically studied the interface and confined mode optical phonons of multiple wurtzite double heterostructure quantum wells and their interaction with electrons based on the uniaxial dielectric continuum model. The phonon dispersion relation of these phonon modes and the electron–phonon scattering rates were calculated numerically to derive the average group velocity of the emitted optical phonons to explore the possibility of exploiting the interface mode phonons as an additional heat dissipation channel. Our estimations show that the average group velocity of phonons that are emitted through electron–phonon scattering processes with electron energy slightly larger than the threshold energy is very small (for the d = 5 nm case, 0.9 nm/ps) compared to the LA phonon propagation velocity of bulk GaN (v_{sound} = 8 nm/ps). This is due to the dispersion relation of interface mode phonons which shows curves that converge to the resonant phonon frequency at large phonon wave vector q. upon increasing electron energies, the average optical group velocity can exceed the acoustic phonon velocity. Given the energy distribution of electrons, we report that the quantum well thickness can be engineered to exploit the interface mode phonons, which can propagate a distance of few tens of nanometers before decaying into heat-carrying acoustic phonons.

The scattering rates of holes by remote interface polar phonons in the diamond structure was also discussed in this chapter. The results indicate clearly that the hole scattering from remote polar phonons can be comparable to, or dominate over, other hole-phonon scattering mechanisms representing a fundamental contribution in the determination of the hole mobility. While the application of polar overlayers may contribute to achieving the desired doping effects, there is a substantial penalty associated with hole remote-polar-phonon scattering [217]. The model adopted in the case of remote IF polar phonons is suitable to describe several other promising polar materials currently adopted for the realization of diamond based MISFETs and HFET due to their wide bandgaps. The obtained formulations facilitate

taking into account the scattering mechanisms in the calculation of hole mobilities in diamond, affording a more complete picture of the involved contributions.

[3]Chapter 4

Nanomechanical systems with normalized and coupled acoustic and electromagnetic modes in piezoelectric structures

4.1 Introduction

This chapter deals with the quantization of the acoustic modes in nanomechanical systems with coupled acoustic and electromagnetic modes in piezoelectric structures. Specifically, the well-known Bleustein-Gulyaev (BG) modes in the theory of surface acoustic wave devices, are second quantized so that the relationship between the acoustic modes and the electromagnetic modes can be examined in the limit where the acoustic mode is a single acoustic phonon. By considering a theory where the quantized acoustic phonons are explicitly related to the electromagnetic modes, this treatment allows a description of nanomechanical systems where acoustic and electromagnetic modes can be described in the nanoscale limit. This effort will examine quantitatively the electromagnetic-acoustic interaction caused by the piezoelectricity in the limit where the classical acoustic waves must be described in terms of phonons.

As is well-known, the Bleustein-Guylaev modes are a cornerstone of modern electro-acoustic technology. These modes are shear-horizontal (SH) electro-acoustic surface modes that exist in the class of transversely isotropic piezoelectric media – notably 6mm media such as GaN – where electromagnetic modes in the isotropic planes couple to surface acoustic modes polarized in the direction normal to the plane of the transverse electromagnetic modes [218]. In this chapter, appropriate to the nanoscale, the classical Bleustein-Guylaev modes are second-quantized in order to describe the interactions between

[3] This chapter is partially published in *Solid State Communications*, [249].

acoustic modes, electromagnetic modes, and charge carriers in terms of phonons instead of classical acoustic waves. Knowing the quantized phonon modes, facilitates phonon engineering and the modification of device characteristics as discussed in Refs. [80], [219]–[223].

4.2 Acoustic and electromagnetic waves in piezoelectric solids

Sound waves are longitudinal and need a material to move in, electromagnetic waves are transverse and do not need a material to move through. Sound waves are compression waves in air. They are waves of successive compressions and rarefactions. Electromagnetic waves are transverse and are comprised of electric and magnetic fields. Both waves carry energy from one place to another and are characterized by their frequency, wavelength and velocity. The velocity of sound waves is much slower than that of electromagnetic waves.

Since the effects of piezoelectricity are widely known [224], the propagation of plane waves in a piezoelectric material has been deduced with varying symmetries [225]. A simultaneous solution of Maxwell's field equations and Newton's law of force gives the necessary conditions for wave propagation in the infinite medium. In the presence of piezoelectric coupling, every electromagnetic wave has a corresponding elastic wave. In piezoelectric media, the electromagnetic and elastic modes are coupled, therefore giving five phase velocities for both the electromagnetic and acoustic waves. The elastic waves are associated with the slower electromagnetic waves, while the electromagnetic waves are associated with fast elastic waves.

Now, surface acoustic waves (SAW) and bulk acoustic waves (BAW) are two types of acoustic wave that dominate the latest research in group-III nitride devices. Solid substrates and micromachined suspended beam structures have been both used to study these devices [226]–[228]. In SAW devices, atoms are displaced about their equilibrium positions along the interface of piezoelectric film and solid substrate

when an elastic wave travels on the surface of a piezoelectric medium. SAW devices utilize the piezoelectric effect exhibited by certain materials, since applying an electric field to a piezoelectric material introduces a mechanical strain. The relationship between electric field and strain is described by the piezoelectric coupling coefficient (β), which is also a function of the frequency of the material. The utility of BG waves in surface acoustic wave systems has been demonstrated for a variety of materials including liquid-loaded 6 mm materials [229]–[232]. The case considered here is the quantization of the classical BG modes of Ref. [218] for a grounded thin conducting film on a piezoelectric half-space.

4.3 Quantization of Bleustein-Guylaev modes

Herein, emphasis is given to formulating a quantized treatment of BG modes that is amenable to the study of phonon engineering of the BG modes on the nanoscale. In particular, the elastic continuum model, discussed at length in Ref. [80], will be used to quantize the phonon amplitude analytically based on the analytical solutions for the BG modes given by Li (1996) [218]. The analytical solutions of Ref. [80] provide a convenient starting point for the second quantization of the acoustic modes which are required to model phonon effects properly in broad classes of nanostructures. Indeed, Stroscio and Dutta (2001) discuss the validity of the elastic continuum and dielectric continuum models in the nanoscale regime; in particular, these models give an accurate representation of the normalized mode envelopes for structures even down to the scale on a couple of monolayers and for ensembles of as few as 60 atoms [152], [173], [174], [221], [233]–[240].

In these quantized continuum models the phonon mode amplitude is normalized so that the energy in each mode is $\hbar\omega$ where ω is the frequency of the acoustic or optical phonon mode. In addition, these normalized continuum modes may be used to formulate piezoelectric, deformation potential and Frohlich interactions in nanoscale devices as discussed at length in Ref. [80]. Of particular interest in the present study is the

piezoelectric interaction in 6mm hexagonal structures such as GaN, AlN, and $Ga_{(x)}Al_{(1-x)}N$. As discussed previously, the mode normalization required to formulate the second-quantized BG modes will be investigated for the case of high interest in nanodevices surface wave applications where a grounded thin conducting film bounds a piezoelectric half space.

Our quantization procedure will be used to quantize the classical BG modes of Ref. [218] which are in turn based on the analysis of Ref. [241]. To find the classical (unquantized) acoustic modes, the underlying equations are formulated as follows [218], [241]:

Maxwell's electromagnetic equations for a lossless medium with no sources are given by Eqs. 4.1 and 4.2

$$-\nabla \times E = \frac{\partial B}{\partial t} \tag{4.1}$$

$$\nabla \times H = \frac{\partial D}{\partial t} \tag{4.2}$$

where, $E =$ electric field, $B =$ magnetic field, $H =$ magnetic field strength and $D =$ electric displacement field.

Equation of motion describing the acoustic fields is given by

$$\nabla .\ T = \frac{\partial P}{\partial t} - F \tag{4.3}$$

where T, is the stress tensor field, P is the particle momentum field, $\rho = \partial u/\partial$t, and F is the body force distribution.

Constitutive equations for an anisotropic hexagonal piezoelectric crystal [242] (class 6mm):

$$B = \mu_0 H \tag{4.4}$$

$$D = \epsilon_{xx}^{s} \cdot E + e_{x5} : S \tag{4.5}$$

$$T = -e_{x5} \cdot E + c_{44}^{E} : S \tag{4.6}$$

where μ_0 is the vacuum magnetic permeability constant, $S = \nabla_s u$ is the strain tensor, ϵ_{xx}^{S}, e_{x5} and c_{44}^{E} are the dielectric strain constant, piezoelectric stress constant and elastic stiffness constant under constant electric intensity, respectively. For a piezoelectric medium with no body force sources ($F = 0$), the Christoffel equations may be derived by manipulating the governing equations

$$\nabla \cdot c_{44}^{E} : \nabla_s u = \rho \frac{\partial^2 u}{\partial t^2} + \nabla \cdot e_{x5} \cdot E \tag{4.7}$$

$$-\nabla \times \nabla \times E = \mu_0 \epsilon_{xx}^{s} \left(\frac{\partial^2 E}{\partial t^2} \right) + \mu_0 e_{x5} : \nabla_s \cdot \frac{\partial^2 u}{\partial t^2} \tag{4.8}$$

As is well-known, the elastic stiffness increases from c_{44}^{E} to $\overline{c_{44}} = c_{44}^{E} + \frac{e_{15}^2}{\epsilon_{11}^{s}}$, due to the piezoelectric stiffness phenomenon [241], [242].

Based on these equations, Ref. [218] has considered the BG mode coupling between the anti-plane acoustic mode and the in-plane electromagnetic mode

$$u = [0, 0, \omega(x_1, x_2, t)] \tag{4.9}$$

$$E = [E_1(x_1, x_2, t), E_2(x_1, x_2, \mathrm{t}), 0] \tag{4.10}$$

where x_1 and x_2 are in the hexagonal plane of the 6mm materials and x_3 is in the direction of the c-axis; the surface of the surface wave device is in the $x_1 - x_3$ plane.

As in Ref. [218], the wave forms are taken to be

$$\omega(x_1, x_2, \mathrm{t}) = \omega_o exp[-ik_1 x_2] \exp[i(\omega t - k x_1)] \tag{4.11}$$

$$\psi(x_1, x_2, \mathrm{t}) = \psi_o exp[-ik_2 x_2] \exp[i(\omega t - k x_1)] \tag{4.12}$$

$$A_{1,2}(x_1, x_2, \mathrm{t}) = A_{1,20} \exp[-ik_2 x_2] \exp[i(\omega t - k x_1)] \tag{4.13}$$

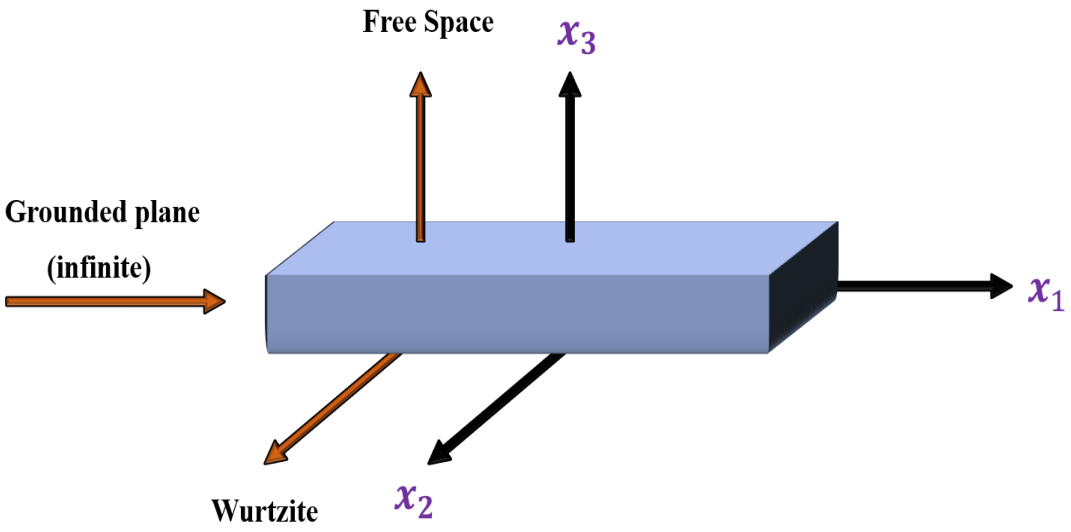

Fig. 26. Schematic of a piezoelectric half space bounded with a grounded perfectly conducting thin film.

---

where $k^2 - {k_1}^2 = (\omega/c_a)^2$; $k^2 - k_2^2 = (\omega/c_l)^2$; $c_a = (\overline{c_{44}}/\rho)^{1/2}$; $c_l = (\mu_o \epsilon_{11}^s)^{-1/2}$ and $A_{1,2}$ are coefficients in the vector potential, A, related to E.

Ψ and f are defined by Eqs. 4.14 and 4.15, respectively

$$\Psi \coloneqq \phi - \frac{e_{15}}{\epsilon_{11}^s} f\omega \tag{4.14}$$

$$f \coloneqq \frac{c_l^2}{c_l^2 - c_a^2} \tag{4.15}$$

Moreover, ω and Ψ satisfy Helmholtz-like equations

$$\begin{cases} \nabla^2\omega - \dfrac{1}{c_a^2}\dfrac{\partial^2\omega}{\partial t^2} = 0 \\ \nabla^2\Psi - \dfrac{1}{c_l^2}\dfrac{\partial^2\Psi}{\partial t^2} = 0 \end{cases} \tag{4.16}$$

Finally, the coefficients ω_0 and $A_{1,20}$ satisfy

$$A_{10} = -\frac{\mu_0 e_{15}\, c_l \omega\, k}{(k_1^2 - k^2) + \omega^2 \,/\, C_l^2}\,\omega_0 \tag{4.17}$$

$$A_{20} = i\,\frac{\mu_0 e_{15}\, c_l \omega\, k_1}{(k_1^2 - k^2) + \omega^2 \,/\, C_l^2}\,\omega_0 \tag{4.18}$$

4.4 Piezoelectric half-space boundary conditions

For the case depicted in Fig. 26 where a 6 mm piezoelectric half-space, $(x_2 < 0)$, bounded at $x_2 = 0$ with a perfectly conducting thin film in the $x_1 - x_3$ plane, the boundary conditions are $T_{23} = 0$ and $\varphi = 0$; applying these boundary conditions, as in Ref. [218] yields, the conditions

$$k_1 = \frac{e_{15}^2}{\overline{c_{44}}\epsilon_{11}^s} f k_2 \tag{4.19}$$

and taking $\beta'^2 = \frac{e_{15}^2}{\overline{c_{44}}\epsilon_{11}^s} f = \beta^2 f$, and $f' = \frac{c_l^2}{c_l^2 - \beta'^4 c_a^2}$, where β is the piezoelectric coupling coefficient in the quasi-static approximation; accordingly, the velocity equation for the electromagnetic-acoustic surface wave is

$$v_e = c_a[f'(1 - \beta'^4)]^{1/2} \tag{4.20}$$

where, in the limit, $c_a / c_l \to 0$, $f \to 1$, $\beta'^2 \to \beta^2$, $f' \to 1$, so that $v_e = c_a(1 - \beta^4)^{1/2}$ which is the standard Bleustein-Gulyaev solution.

The equations relating the coefficients ω_0 and $A_{1,20}$ are significant because they relate the coefficients of the acoustic mode, ω_0, and those of the vector potential, $A_{1,20}$. On the nanoscale, it is necessary to quantize the amplitude of the acoustic field, ω_0, so that acoustic wave may be treated in term of phonons. The first task in this research will be to quantize ω_0. In particular, ω_0 will be quantized for the case described above of grounded thin conducting film on a piezoelectric half space. Having these quantized fields for the acoustic modes, equations relating the coefficients ω_0 and $A_{1,20}$ will be used to obtain the corresponding

fields for the vector potential. Together this will facilitate the description of the BG modes in nanoscale SAW devices in terms of phonons instead of classical acoustic waves.

Acoustic wave devices, including those based on Bleustein-Gulyeav waves, should manifest a high-quality factor for being used in high performance applications. The Q value may be used as a measure of the utility of devices over a range of frequencies. As is well known, phonon-phonon interactions define a time scale intrinsic energy dissipation mechanism and simple scaling equations are available for estimating the Q value associated with phonon-phonon interactions [243], [244]. As an estimate of the loss associated with phonon-phonon interactions, the $Q \cdot f$ products of GaN and AlN are calculated based on anharmonic phonon scattering. To make such estimates, the thermal phonon relaxation time (τ_{TH}) must be obtained; a convenient form for this relaxation time is

$$\frac{1}{\tau_{TH}} \approx \frac{C_v V_D^2}{3n\kappa} \tag{4.21}$$

where C_v is the volumetric heat capacity, n is the correction factor (in shear waves n ≅ 1), κ is the thermal conductivity, and V_D is the mean Debye velocity, which can be calculated as

$$\frac{3}{V_D^3} = \frac{1}{V_l^3} + \frac{2}{V_t^3} \tag{4.22}$$

where V_t and V_l are the transverse and longitudinal velocities, respectively.

In the so-called Akhiezer regime where $\omega\tau < 1$, the value of $Q \cdot f$ due to phonon-phonon interactions, is given by [243]–[246]

$$Q \cdot f = \frac{\rho v^2 (1 + (\omega.\tau)^2)}{2\pi\gamma^2 C_v T \tau_{TH}} \tag{4.23}$$

where, γ is Grüneisen parameter, ρ is the density of the material, v is acoustic velocity, and T is the absolute temperature.

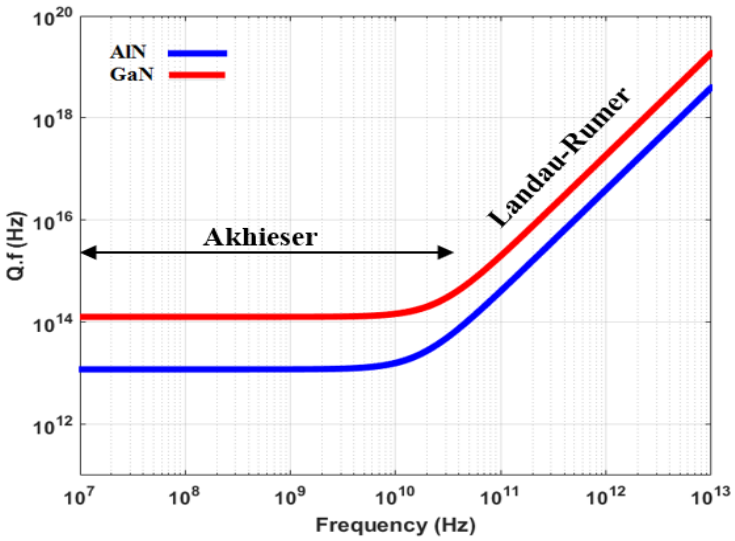

Fig. 27. $Q \cdot f$ products for AlN and GaN in the Akhiezer and Landau-Rumer regimes; in the region from approximately 10^{10} to 10^{11} Hz these curves are extrapolated between the Akhieser and Landau-Rumer regimes.

In the so-called Landau-Rumer regime where $\omega\tau > 1$, the value of $Q \cdot f$ due to phonon-phonon interactions, is given by [247]

$$f \cdot Q_{\mathrm{ph-ph}} = \frac{15\rho v^5 \mathrm{h}^3}{\pi^5 \gamma^2 \mathrm{K}^4 T^4}\omega \qquad 4.24$$

The material properties summarized in Ref. [248] are used to evaluate these expressions. Fig. 27 summarizes the $Q \cdot f$ products over a range of frequencies for AlN and GaN; the region from approximately 10^{10} to 10^{11} Hz these curves are extrapolated between the Akhieser and Landau-Rumer regimes. As can be seen from Fig. 27, Q values are of at least 10^5 up to 10^{12} Hz frequency range.

4.5 Quantization of phonon amplitudes in BG waves

Past studies [80] indicate that displacement amplitudes must be modified when the phonon occupation numbers become small; indeed, the mode amplitudes must be quantized. Thus, phonon mode quantization

is essential for phonon occupation numbers close to unity. As is well-known [80], the elastic continuum model may be used for phonon mode quantization by requiring that the mode normalization be such that the energy in the mode is $\hbar\omega_n$.

Indeed, such phonon amplitude quantization is essential when the phonon occupation approaches unity. The thermal equilibrium phonon occupation number (n_k) for each phonon mode is given by the Bose-Einstein distribution. The phonon occupation numbers for seven different phonon frequencies and at five different environment temperatures are calculated and listed in Table 4.

The quantization of the phonon amplitude is critical when the phonon occupation number approaches unity (very roughly 10 or less). In this work, by considering seven different oscillation frequencies at five different temperatures between $0.1\ K$ to $300\ K$, the phonon occupation is calculated as a guide to where quantization is necessary; these results are shown in Table 4.

Table 4. Phonon occupation number for a variety of temperatures and frequencies.

Angular frequency (ω_k) ($\times 10^{11}$rad/s)	**Temperature (T) (K)**	**n_k**
10	300	246.406
	50	40.653
	20	15.965
	1	0.422
	0.1	5.286E-6
	300	820.798

3	50	136.384
	20	54.255
	1	2.268
	0.1	0.0266
1	300	2466.23
	50	410.622
	20	163.949
	1	7.733
	0.1	0.421
0.3	300	8229.7
	50	1371.2
	20	548.18
	1	26.937
	0.1	2.2737
0.1	300	24690.101
	50	4114.6
	20	1645.54

	1	81.8030
	0.1	7.7403
0.03	300	82301.502
	50	13716.5
	20	5486.3
	1	273.84
	0.1	26.937
0.01	300	246905.506
	50	41150.501
	20	16459.9
	1	822.52
	0.1	81.803

It is evident from these calculated results that average phonon occupation numbers near or less than unity are obtainable for higher frequencies and at lower temperatures.

The normalization constant of the shear acoustic phonon modes propagating in the structure shown in Fig. 27, can be obtained by following the quantization theory procedure [219], to ensuring that the displacement is such that the energy in each phonon mode is $\hbar\omega_k$.

As discussed by Stroscio and Dutta (2001), acoustic (and optical) phonon mode quantization is accomplished using the techniques of quantizing acoustic phonons using the elastic continuum model (as in this chapter) and on quantizing optical phonons using the dielectric continuum model. Stroscio and Dutta (2001) give numerous examples demonstrating that quantizing phonon modes for the continuum models provides an accurate description of the quantized phonons modes. Specifically, the models provide dispersion relations and mode envelopes that apply for scales from a few monolayers to the microscale and beyond. As indicated previously, the mode envelopes are given by the continuum models, the amplitudes of the modes must be determined such that the energy in a mode of frequency ω_k is $\hbar\omega_k$. Or three-dimensional second-quantization the following condition ensures that the energy in the phonon mode is $\hbar\omega_k$ for a structure with the width of a, height of b and the length of c, is given by

$$\frac{1}{abc}\int_{-\frac{a}{2}}^{\frac{a}{2}} dx \int_{-\frac{b}{2}}^{\frac{b}{2}} dy \int_{-\frac{c}{2}}^{\frac{c}{2}} dz\, u(k,x,y,z)\cdot u^*(k,x,y,z) = \frac{\hbar}{2m\omega_k} \tag{4.25}$$

where k is the phonon wave vector, ω_k is the phonon mode angular frequency, x, y, and z denote the usual Cartesian coordinates, with the relationship between u, a_k and $a_k^\dagger$ given by Eqs. 4.26–4.28

$$u(r) = \frac{1}{\sqrt{N}}\sum_k [u(k,r)a_k + c.c.] \tag{4.26}$$

$$u_k = \sqrt{\frac{\hbar}{2m\omega_k}}\,(a_k + a_k^\dagger) \tag{4.27}$$

$$u(r) = \frac{1}{\sqrt{N}}\sum_k \sum_{j=1,2,3} \sqrt{\frac{\hbar}{2m\omega_k}}\left(a_k e^{ikr}\hat{e}_{k,j} + a_k^\dagger e^{-ikr}\hat{e}_{k,j}^*\right)$$

$$= \frac{1}{\sqrt{N}}\sum_k \sum_{j=1,2,3} \sqrt{\frac{\hbar}{2m\omega_k}}\,\hat{e}_{k,j}\left(a_k + a_{-k}^\dagger\right)e^{ikr} \tag{4.28}$$

$$= \sum_{k} u_k e^{ikr}$$

wherein N is the number of the unit cells in the volume, V, r is the position vector, $c.c.$ stands for the complex conjugate of the first argument in the summation, u_k is the amplitude associated with the annihilation (a_k) or creation ($a_k^\dagger$) of one phonon. According to Stroscio and Dutta (2001),

$$a_k^\dagger |N_k\rangle = \sqrt{n_k + 1}|N_k + 1\rangle \quad 4.29$$

$$a_k|N_k\rangle = \sqrt{n_k}|N_k - 1\rangle \quad 4.30$$

where n_k is the number of phonons having wave vector k.

The eigenstate $|N_k\rangle$ satisfies the eigenvalue equation

$$N_k|N_k\rangle = n_k|N_k\rangle \quad 4.31$$

where $N_k = a_k^\dagger a_k$, and as a result of orthogonality, it follows that

$$\langle N_k'||N_k\rangle \equiv \langle N_k'|N_k\rangle = \delta_{N_k', N_k} \quad 4.32$$

wherein δ_{N_k', N_k} is the Kronecker-delta function.

Based on these classical BG and the normalization procedure, the analytical second-quantized solution is obtained based on the general quantization procedure derived and discussed by Stroscio and Dutta (2001)

$$\frac{1}{L}\int_0^\infty \omega_o^2 \exp(-2k_1 x_2)\, dx_2 = \frac{\hbar}{2m\omega_n} \quad 4.33$$

which yields

$$\omega_0 = \sqrt{2k_1}\left(\frac{\hbar}{2A\rho\omega}\right)^{\frac{1}{2}} \quad 4.34$$

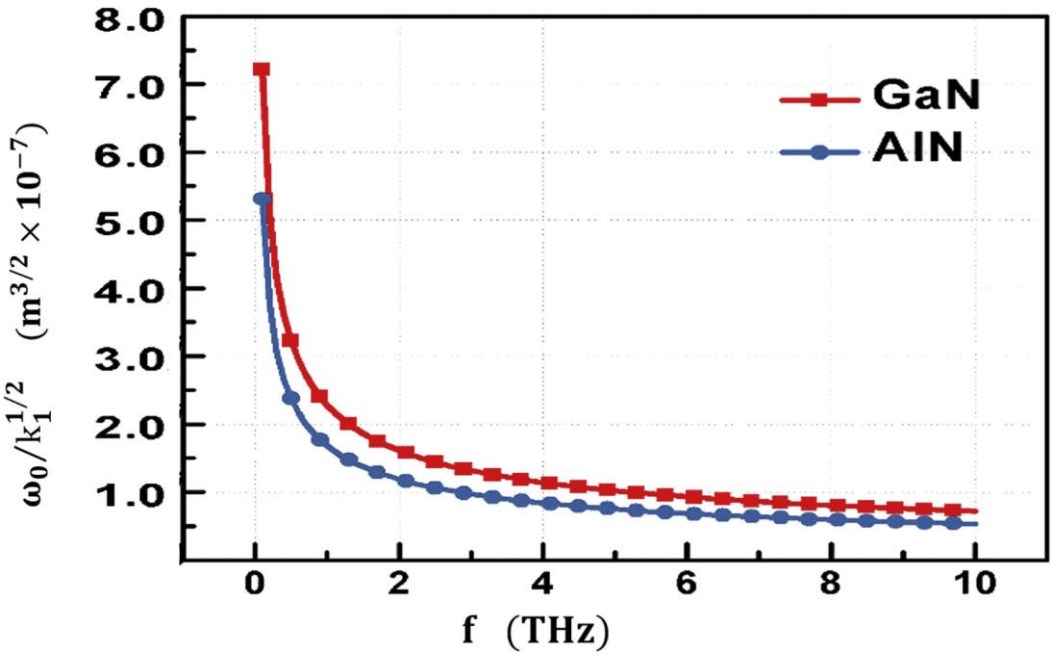

Fig. 28. This figure plots the values of $\omega_0/\sqrt{k_1}$ with respect to frequency (f) in the THz range for both GaN and AlN.

Here, m is the mass of a unit cell, and ω is the angular frequency of the wave. This last result ensures that the total energy in a vibrational mode, having a frequency of ω_n, is $\hbar\omega_n$.

Using the results in Ref. [80], Eqs. 4.17 and 4.18 can be derived using the amplitude coefficients and normalization factor listed below.

Using the amplitude coefficients A_{10} and A_{20}

$$A_{10} = -\frac{\mu_0 e_{15}\, c_l \omega\, k}{(k_1^2 - k^2) + \omega^2 / C_l^2}\,\omega_0 \qquad 4.35$$

$$A_{20} = i\frac{\mu_0 e_{15}\, c_l \omega\, k_1}{(k_1^2 - k^2) + \omega^2 / C_l^2}\,\omega_0 \qquad 4.36$$

Given that

$\omega_0 = \sqrt{2k_1}(\frac{\hbar}{2A\rho\omega})^{\frac{1}{2}}$ and $k^2 - {k_1}^2 = (\omega/c_a)^2$

In Fig. 28, the values of $\omega_0/\sqrt{k_1}$ has been plotted against the frequency (f). Values of f are in the THz range and A has been considered to be 10^{-12} m^2. For GaN, $\rho = 6.1 \times 10^3\ kg/m^3$ while for AlN, $\rho = 3.25 \times 10^3\ kg/m^3$.

We can then rewrite A_{10} and A_{20} substituting this for ω_0

$$A_{10} = -\frac{\mu_0 e_{15}\, c_l \omega\, k}{(k_1^2 - k^2) + \omega^2 / C_l^2}\omega_0 = -\frac{\mu_0 e_{15}\, c_l \omega\, k}{(k_1^2 - k^2) + \omega^2 / C_l^2}\sqrt{2k_1}(\frac{\hbar}{2A\rho\omega})^{\frac{1}{2}} \quad 4.37$$

$$A_{20} = i\frac{\mu_0 e_{15}\, c_l \omega\, k_1}{(k_1^2 - k^2) + \omega^2 / C_l^2}\omega_0 = i\frac{\mu_0 e_{15}\, c_l \omega\, k_1}{(k_1^2 - k^2) + \omega^2 / C_l^2}\sqrt{2k_1}(\frac{\hbar}{2A\rho\omega})^{\frac{1}{2}} \quad 4.38$$

and further rearranging this work, we can write the two terms A_{10} and A_{20} using the relation

$$k^2 - {k_1}^2 = (\omega/c_a)^2$$

Therefore, we obtain equations Eqs. 4.39 and 4.40 as

$$A_{10} = -\frac{\mu_0 e_{15}\, c_l \omega \sqrt{{k_1}^2 + \frac{\omega^2}{{c_a}^2}}}{\omega^2/C_l^2 - \omega^2 / C_a^2}\sqrt{2k_1}(\frac{\hbar}{2A\rho\omega})^{\frac{1}{2}} \quad 4.39$$

$$A_{20} = i\frac{\mu_0 e_{15}\, c_l \omega\, k_1}{\omega^2 / C_l^2 - \omega^2 / C_a^2}\sqrt{2k_1}(\frac{\hbar}{2A\rho\omega})^{\frac{1}{2}} \quad 4.40$$

Assuming the wave form

$$A_{1,2}(x_1, x_2, t) = A_{10,20} exp[-k_1 x_2] exp[i(\omega t - k x_1)] \quad 4.41$$

And using the Lorentz gauge constraint

$$\nabla \cdot A + \frac{1}{c_l}\frac{\partial \Phi}{\partial t} = 0 \quad 4.42$$

$$\nabla \cdot A = \frac{\partial A_1}{\partial x_1} + \frac{\partial A_2}{\partial x_2} \tag{4.43}$$

$$\frac{\partial A_1}{\partial x_1} = -kA_{10}\exp\left[-k_1 x_2\right]\exp[\mathrm{i}(\omega \mathrm{t} - \mathrm{k}x_1)] \tag{4.44}$$

$$\frac{\partial A_2}{\partial x_2} = -k_1 A_{20}\exp\left[-k_1 x_2\right]\exp[\mathrm{i}(\omega \mathrm{t} - \mathrm{k}x_1)] \tag{4.45}$$

So, $$\nabla \cdot A = -\exp\left[-k_1 x_2\right]\exp[\mathrm{i}(\omega \mathrm{t} - \mathrm{k}x_1)](kA_{10} + k_1 A_{20}) \tag{4.46}$$

From the constraint, we get

$$\frac{\partial \Phi}{\partial t} = c_l(\exp\left[-k_1 x_2\right]\exp[\mathrm{i}(\omega \mathrm{t} - \mathrm{k}x_1)])(kA_{10} + k_1 A_{20}) \tag{4.47}$$

In solving for ϕ, we get

$$\Phi = \frac{c_l}{i\omega}(\exp\left[-k_1 x_2\right]\exp[\mathrm{i}(\omega \mathrm{t} - \mathrm{k}x_1)])(kA_{10} + k_1 A_{20}) + c_1 \tag{4.48}$$

where c_l is the integration constant.

This will lead to solving for Ψ using the relation from Ref. [218]

$$\Psi \coloneqq \phi - \frac{e_{15}}{\epsilon_{11}^s} f\omega \tag{4.49}$$

which gives the following representation for Ψ

$$\Psi \coloneqq \frac{c_l}{i\omega}(\exp\left[-k_1 x_2\right]\exp[\mathrm{i}(\omega \mathrm{t} - \mathrm{k}x_1)])(kA_{10} + k_1 A_{20}) - \frac{e_{15}}{\epsilon_{11}^s} f\omega + c_1 \tag{4.50}$$

Substituting for A_{10} and A_{20} and writing this in terms of k_1 alone, we get

$$\Psi \coloneqq \frac{c_l}{i\omega}\left(\exp\left[-k_1 x_2\right]\exp\left[\mathrm{i}\left(\left(\omega \mathrm{t} - \sqrt{{k_1}^2 + \frac{\omega^2}{{c_a}^2}}\right) * x_1\right)\right]\right)\left(-\sqrt{{k_1}^2 + \frac{\omega^2}{{c_a}^2}}\frac{\mu_0 e_{15}\, c_l \omega \sqrt{{k_1}^2 + \frac{\omega^2}{{c_a}^2}}}{\omega^2 / C_l^2 - \omega^2 / C_a^2}\sqrt{2k_1}\left(\frac{\hbar}{2A\rho\omega}\right)^{\frac{1}{2}} + k_1 i \frac{\mu_0 e_{15}\, c_l \omega\, k_1}{\omega^2 / C_l^2 - \omega^2 / C_a^2}\sqrt{2k_1}\left(\frac{\hbar}{2A\rho\omega}\right)^{\frac{1}{2}}\right) - \frac{e_{15}}{\epsilon_{11}^s} f\omega + c_1 \qquad 4.51$$

Based on these classical BG results, the analytical second-quantized solution is obtained based on the general quantization procedure shown in Eqn. 4.33 derived and discussed by Stroscio and Dutta (2001)

$$\frac{1}{L}\int_0^\infty \omega_o^2 \exp(-2k_1 x_2)\, dx_2 = \frac{\hbar}{2m\omega_n}$$

which yields

$\omega_0 = \sqrt{2k_1}\left(\frac{\hbar}{2A\rho\omega}\right)^{\frac{1}{2}}$ where, as discussed previously, $k^2 - {k_1}^2 = (\omega/c_a)^2$

where m is the mass of a unit cell, and ω is the angular frequency of the wave. This last result ensures that the total energy in a vibrational mode, having a frequency of ω_n, is indeed $\hbar\omega_n$.

4.6 Summary

In this work we have quantized the classical acousto-electromagnetic BG surface acoustic waves for the case of a grounded thin conducting film on a 6mm piezoelectric half space. This method facilitates the description of the BG modes in nanoscale surface acoustic wave devices in terms of phonons instead of

classical acoustic waves and it describes the coupling between the acoustic waves (phonons) and the quanta of the electromagnetic field.

[4]Chapter 5

Acoustic phonons in anisotropic and quasi-isotropic nitride-based structures

5.1 Introduction

Due to their large group velocities, longitudinal acoustic waves in AlN layers are of great interest in high-power, high-frequency applications. We extend recent advances in phonon engineering through a description of the piezoelectric structures in the nanoscale regime [80], [249]. The improved understanding of phonons and the advent of new studies have expanded the possibilities of investigating the effects of electron-phonon interactions at room temperature and of elucidating its role in various physical phenomena including the possibility of heat removal [140], [186], [204], [249]. In contrast, and even though acoustic phonons are the major heat carriers in semiconductors, their effect on heat transfer through the deformation potential has been considered to be insignificant, due to their weak coupling to electrons. Here, we demonstrate, by theoretical means, that significant energy transition and heat flux via longitudinal acoustic (LA) modes are possible if the acoustic phonons can induce an electric field, which then can leak into the heterointerface. The seminal findings by Balandin, Pokatilov and Nika (2007) [161] have enabled more research on bandgap engineering, piezoelectric scattering and deformation scattering. These results joined with the recent advances in growth technologies [250] have opened further venues to tackle the reliability issue of GaN- and AlN-based devices. In an earlier study, by Nougaoui and Rouhani (1987), which provides an important foundation for this work, it is shown that the GaN/AlN superlattice

[4] This chapter is partially published in IEEE Electron Device Letters, [264] and IOP Journal of Physics: Condensed Matter, [295].

behaves like an effective medium with acoustic phonon velocities intermediate between those of GaN and AlN [251].

As acoustic phonons must decay, based on the perturbation theory, anharmonic three-phonon coupling encompasses a great variety of decay processes. Considering that only transverse phonons are degenerate, either one single phonon decays into two phonons, or two phonons combine to form a new phonon via an up-conversion process [102, 103], [123]. More particles can partake in the decay process such as the decay of LA phonons into three TA phonons [252]. The decay mechanism of a phonon can be obtained from the temperature-dependent frequencies and linewidths of phonon modes [125].

This chapter presents the possibility of using the effective medium model coupled with the piezoelectric stiffening to quantitatively explain and engineer acoustic phonons as a heat dissipation channel in GaN-based devices. These effects will be described for a GaN/AlN superlattice that exhibits enhanced acoustic phonon velocities as compared with bulk GaN. We numerically calculate the stiffened elastic constant values and apply them within the effective medium model for elastic constants. With the recent advances in epitaxial GaN growth technology, it may be possible to consider this phonon engineering option to investigate the effect on the longitudinal sound velocity to increase the rate of heat transport in GaN/AlN superlattice.

This chapter also reports for the first time an estimation of the spontaneous decay rates at room temperature in a selection of nitride-based nanostructures that are quasi-isotropic. We numerically calculate the phonon distribution functions and the decay rates and find that the decay channel LA $\rightarrow$ TA + TA dominates over the decay channel LA $\rightarrow$ LA + TA, which confirms Klemens' prediction [253] that LA phonon will primarily split into two doubly degenerate TA phonons through a greater variety of decay channels compared to the decay of LA into two modes, one belonging to the longitudinal acoustic and the other to the transverse acoustic branch.

5.2 Phonon scattering via deformation potential in hexagonal-layered materials

Acoustic waves in layered media have been studied extensively [254], as well as several efforts that have been devoted to investigating the propagation of elastic waves in superlattices developed using alternating layers of two different crystals such as GaN and AlN [255]–[257]. The folded acoustic phonons propagating perpendicular to the layers have been corroborated by Raman studies on semiconductor superlattices [258].

In the hexagonal crystal (0001), the medium can be described using five independent elastic coefficients in the form

$$\begin{pmatrix} C_{11}^E & C_{12}^E & C_{13}^E & 0 & 0 & 0 \\ C_{12}^E & C_{11}^E & C_{13}^E & 0 & 0 & 0 \\ C_{13}^E & C_{13}^E & C_{33}^E & 0 & 0 & 0 \\ 0 & 0 & 0 & C_{44}^E & 0 & 0 \\ 0 & 0 & 0 & 0 & C_{44}^E & 0 \\ 0 & 0 & 0 & 0 & 0 & (C_{11}^E - C_{12}^E)/2 \end{pmatrix} \quad 5.1$$

where $C_{11}^E = C_{22}^E$, $C_{12}^E = C_{21}^E$, $C_{13}^E = C_{23}^E$, C_{33}^E, $C_{44}^E = C_{55}^E$, $C_{66}^E = (C_{11}^E - C_{12}^E)/2$

We focus here on the propagation of waves in anisotropic medium. This propagation can be obtained by solving Christoffel equation [241] which is referenced to describe the propagation of acoustic wave in solid including general medium and piezoelectric medium. In constant electric field, the piezoelectric stress constant is given by

$$e = \begin{bmatrix} 0 & 0 & 0 & 0 & e_{x5} & 0 \\ 0 & 0 & 0 & e_{x5} & 0 & 0 \\ e_{z1} & e_{z2} & e_{z35} & 0 & 0 & 0 \end{bmatrix} \quad 5.2$$

And the clamped dielectric constant is given by

$$\varepsilon^s = \begin{bmatrix} \varepsilon_{xx}^s & 0 & 0 \\ 0 & \varepsilon_{yy}^s & 0 \\ 0 & 0 & \varepsilon_{zz}^s \end{bmatrix} \quad 5.3$$

To obtain the plane wave propagation in the crystal axis, we solve the velocity equation by substituting the projections of (0001) to get the equation

$$\begin{bmatrix} \left(\frac{k}{\omega}\right)^2 [C_{11}\iota_x^2 + C_{44}(1-\iota_x^2)] - \rho & \left(\frac{k}{\omega}\right)^2 (C_{12}+C_{44})\iota_x\iota_y & \left(\frac{k}{\omega}\right)^2 (C_{12}+C_{44})\iota_x\iota_z \\ \left(\frac{k}{\omega}\right)^2 (C_{12}+C_{44})\iota_x\iota_y & \left(\frac{k}{\omega}\right)^2 [C_{11}\iota_y^2 + C_{44}(1-\iota_y^2)] - \rho & \left(\frac{k}{\omega}\right)^2 (C_{12}+C_{44})\iota_y\iota_z \\ \left(\frac{k}{\omega}\right)^2 (C_{12}+C_{44})\iota_x\iota_z & \left(\frac{k}{\omega}\right)^2 (C_{12}+C_{44})\iota_y\iota_z & \left(\frac{k}{\omega}\right)^2 [C_{11}\iota_z^2 + C_{44}(1-\iota_z^2)] - \rho \end{bmatrix} = 0 \quad 5.4$$

That yields

$$\left[\left(\frac{k}{\omega}\right)^2 C_{11} - \rho\right]\left[\left(\frac{k}{\omega}\right)^2 C_{44} - \rho\right]\left[\left(\frac{k}{\omega}\right)^2 C_{44} - \rho\right] = 0 \quad 5.5$$

Eqn. 5.5 has three solutions, one is

$$\left(\frac{k}{\omega}\right)^2 C_{11} - \rho = 0, V_l = \sqrt{C_{11}/\rho} \quad 5.6$$

And the other two solutions are

$$\left(\frac{k}{\omega}\right)^2 C_{44} - \rho = 0, V_s = \sqrt{C_{44}/\rho} \quad 5.7$$

Eqn. 5.6 denotes the solution for the LA mode wave with a phase velocity V_l in the crystal direction. The second and third solutions in Eqn. 5.7 denote the shear mode wave with a phase velocity V_s in the crystal direction.

5.3 Effective medium model

When the acoustic phonon wavelength becomes large compared to the period of the superlattice, namely the long wavelength regime, the superlattice behaves like an effective medium whose elastic constants can be expressed as functions of its coefficients [251]. Meanwhile, Grimsditch (1985) introduced a method which enabled him to obtain the effective medium elastic constants in orthorhombically symmetric layers [259]. Nougaoui and Rouhani (1987) provided a formal generalization of this method for any layer symmetry [260]. Therefore, using the results obtained in Ref. [261], the effective medium for hexagonal layers with piezoelectric media has elastic constants given by

$$\frac{1}{C_{33}^{e}} = \frac{x}{C_{33}} + \frac{1-x}{C'_{33}} \tag{5.8}$$

$$C_{13}^{e} = C_{33}^{e}\left[x\frac{C_{13}}{C_{33}} + (1-x)\frac{C'_{13}}{C'_{33}}\right] \tag{5.9}$$

$$C_{11}^{e} = \frac{(C_{13}^{e})^2}{C_{33}^{e}} + x\left(C_{11} - \frac{(C_{13})^2}{C_{33}}\right) + (1-x)\left(C'_{11} - \frac{(C'_{13})^2}{C'_{33}}\right) \tag{5.10}$$

$$\frac{1}{C_{44}^{e}} = \frac{x}{C_{44}} + \frac{1-x}{C'_{44}} \tag{5.11}$$

$$C_{66}^{e} = xC_{66} + (1-x)C'_{66} \tag{5.12}$$

where $x = d/(d+d')$, d is the medium thickness for GaN while d' is the medium thickness for AlN, C_{ij}^{e} denotes the effective medium material elastic constant which describes the behavior of the anisotropic media when the media is not piezoelectric.

$$C_{11}^{e} = \frac{C_{33}C'_{33}}{(1-x)C_{33} + xC'_{33}}\left[x\frac{C_{13}}{C_{33}} + (1-x)\frac{C'_{13}}{C'_{33}}\right]^2 + x\left(C_{11} - \frac{{C_{13}}^2}{C_{33}}\right) + (1-x)(C'_{11} - \frac{{C'_{13}}^2}{C'_{33}}) \tag{5.13}$$

5.4 Heat transport in hexagonal-layered superlattices

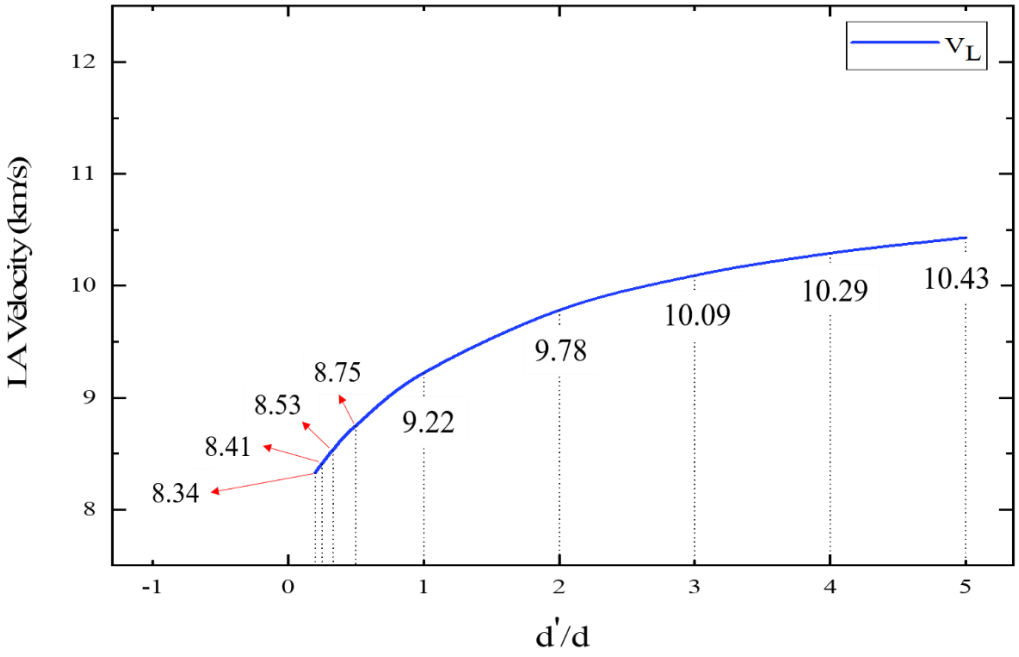

Fig. 29. Longitudinal sound velocities of acoustic phonons (LA) carrying heat in hexagonal GaN/AlN structure versus the rate of change in AlN-to-GaN thickness ratios.

In GaN transistors, energetic hot electrons launch interface and confined optical phonon modes instead of bulk modes; they remain localized in the regions where electrons emit longitudinal optical (LO) phonons as discussed in detail in Chapter 3. Since bulk LO phonons have small group velocity, they tend to accumulate and store energy, and as a consequence, heat is generated when these phonons decay anharmonically. In a related process, it has been suggested by suitably placing a superlattice in a region of heat flow, the group velocity of the launched interface and confined phonons can be engineered to smear out the hot spot. The optical phonons will move a few hundreds of nanometers and decay into acoustic phonons elongating the hot spot and decreasing the hot spot temperature. Herein, we consider using a several-period superlattice to enhance heat transport. However, it is well-known that polycrystalline materials and AlN/GaN superlattices have a thermal conductivity significantly smaller

than the bulk value [65]. Researchers have studied the development of GaN devices on very high thermal conductivity substrates. Epitaxial growth of GaN epilayers on single crystal diamond substrates has also been reported [262]. However, the use of superlattice or other multi-layered structures required to manage the stress from GaN-diamond lattice mismatch makes the growth process challenging and may create a large thermal resistance due to interfacial imperfections.

Rewriting the longitudinal sound velocity equation Eqn. 5.6 for the effective medium [241], [263]

$$V_l = \sqrt{C_{11}^e/\rho^e} \tag{5.14}$$

where ρ^e is the effective density for the elastic medium which given by the equation

$$\rho^e = x\rho + (1-x)\rho' \tag{5.15}$$

where ρ is the density of GaN and ρ' is the density of AlN.

We use Eqs. 5.14 and 5.15 to plot the acoustic phonon velocities of acoustic phonons carrying heat by phonon engineering in a superlattice versus the thickness of AlN layer (d') in each period of the superlattice divided by the thickness of the GaN layer (d) in each period of the superlattice. The results are shown in Fig. 29 [264].

5.5 Christoffel equation and piezoelectric stiffening

The elastic behavior of an anisotropic piezoelectric media at zero electric displacement is characterized by the material elastic constants using Christoffel equation [241]

$$C_{ij} = C_{KL} + \frac{[e_{kj}l_j][l_i e_{il}]}{l_i \epsilon_{ij}^s l_j} \tag{5.16}$$

Here, e_{kj} is the piezoelectric polarization tensor (in C/m^2), e_{il} is the piezoelectric acoustic tensor (in C/m^2), l_i and l_j characterize the directions of the wave vector and ϵ_{ij}^s is the static permittivity.

Table 5. The values of the medium densities, the stiffened elastic constants and the piezoelectric moduli used in the effective medium model calculations.

Material	**AlN**	**GaN**
$\rho\ (\mathrm{g}\cdot cm^{-3})$	3.255 [265]	6.15 [265]
$C_{11}^{*}(GPa)$	332.80 [266]	397.80 [267]
$C_{13}^{*}(GPa)$	101.97 [266]	107.06 [267]
$C_{33}^{*}(GPa)$	392.89 [266]	399.59 [267]
$e_{31}(\mathrm{C}/m^2)$	−0.58 [268]	−0.33 [268]
$e_{33}(\mathrm{C}/m^2)$	1.55 [268]	0.65 [268]

With the electromechanical coupling constant given by

$$[K_{kl}(i)]^2 = \frac{[e_{kj}I_j][I_i e_{il}]}{l_i \epsilon_{ij}^{s} I_i C_{KL}} \tag{5.17}$$

therefore,

$$C_{ij}^{e} = C_{KL}(1 + [K_{kl}(i)]^2) \tag{5.18}$$

Expanding Eqn. 5.17, the electromechanical coupling constants have the following relation with the matrix of piezoelectric moduli e_{ij}

$$[K_{kl}(i)]^2 = \frac{1}{l_i \epsilon_{ij}^{s} l_j C_{KL}} \begin{pmatrix} e_{33}^2 & e_{31}e_{33} & e_{31}e_{33} & 0 & 0 & 0 \\ e_{31}e_{33} & e_{31}^2 & e_{31}^2 & 0 & 0 & 0 \\ e_{31}e_{33} & e_{31}^2 & e_{31}^2 & 0 & 0 & 0 \\ 0 & 0 & 0 & 0 & 0 & 0 \\ 0 & 0 & 0 & 0 & 0 & 0 \\ 0 & 0 & 0 & 0 & 0 & 0 \end{pmatrix} \tag{5.19}$$

Based on the results of Ref. [269], the electromechanical coupling constant values for GaN and AlN are given as

$$[K_{kl}(i)]^2 = \begin{pmatrix} 0.02 & -0.02 & -0.02 & 0 & 0 & 0 \\ -0.02 & 0.004 & 0.01 & 0 & 0 & 0 \\ -0.02 & 0.01 & 0.004 & 0 & 0 & 0 \\ 0 & 0 & 0 & 0 & 0 & 0 \\ 0 & 0 & 0 & 0 & 0 & 0 \\ 0 & 0 & 0 & 0 & 0 & 0 \end{pmatrix} \tag{5.20}$$

and

$$[K_{kl}(i)]^2 = \begin{pmatrix} 0.08 & -0.12 & -0.12 & 0 & 0 & 0 \\ -0.12 & 0.01 & 0.03 & 0 & 0 & 0 \\ -0.12 & 0.03 & 0.01 & 0 & 0 & 0 \\ 0 & 0 & 0 & 0 & 0 & 0 \\ 0 & 0 & 0 & 0 & 0 & 0 \\ 0 & 0 & 0 & 0 & 0 & 0 \end{pmatrix}, \tag{5.21}$$

respectively.

The modified expression for the effective medium elastic constant considering piezoelectric stiffening effect is given by

$$C_{11}^{e,*} = \frac{C_{33}^* C_{33}^{\prime,*}}{(1-x)C_{33}^* + xC_{33}^{\prime,*}} \left[x\frac{C_{13}^*}{C_{33}^*} + (1-x)\frac{C_{13}^{\prime,*}}{C_{33}^{\prime,*}} \right]^2 + x\left(C_{11}^* - \frac{{C_{13}^*}^2}{C_{33}^*} \right) + (1-x)(C_{11}^{\prime,*} - \frac{{C_{13}^{\prime,*}}^2}{C_{33}^{\prime,*}}) \tag{5.22}$$

$C_{ij}^{e,*}$ denotes the effective medium of the elastic coefficients with piezoelectric stiffening when the media is piezoelectric.

The stiffened elastic constants relevant to our work are calculated using Christoffel equation and presented as shown in Table 5.

Table 6. Comparison of acoustic phonon velocities versus rates of thickness optimization of GaN/AlN hexagonal-layered superlattice considering a piezoelectric-stiffened medium.

d'/d	$V_l\ (km/s)$	$V_l^*\ (km/s)$
0.2	8.34	8.46
0.25	8.41	8.54
0.33	8.53	8.68
0.5	8.75	8.92
1.00	9.22	9.45
2.00	9.78	10.07
3.00	10.09	10.41
4.00	10.29	10.64
5.00	10.43	10.79

The longitudinal sound velocity for the effective medium with the piezoelectric stiffening phenomena can be expressed as [241], [263]

$$V_l^* = \sqrt{C_{11}^{e,*}/\rho^e} \tag{5.23}$$

Utilizing Eqs. 5.15 and 5.23, the longitudinal sound velocity is once again numerically calculated for different ratios of GaN/AlN superlattice using the effective medium model with piezoelectric stiffening taken into account. The results are summarized in Table 6. Simply by modifying the period of the superlattice, we report ~ 25% increase in the rate of LA modes and an extra 3% with the application of the piezoelectric stiffening.

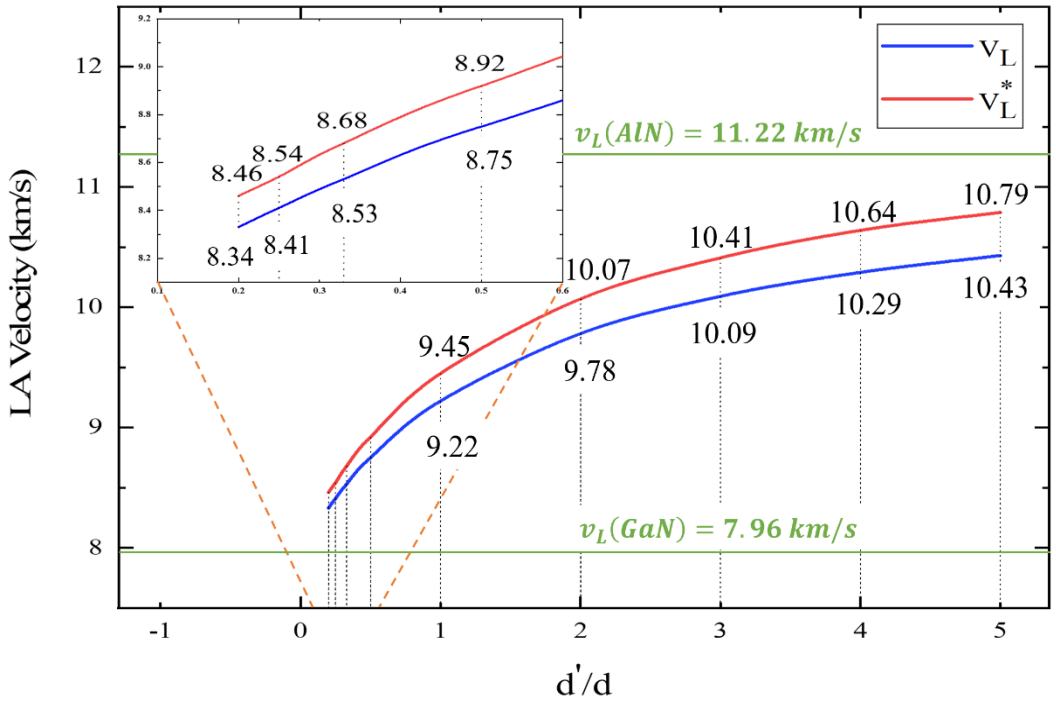

Fig. 30. The LA sound velocities for the effective medium superlattice with and without piezoelectric stiffening effect versus the thickness ratio of AlN-to-GaN referenced against the velocities of pure GaN and AlN wurtzite materials.

5.6 Anharmonic decay of high-frequency LA modes in quasi-isotropic III-nitrides

In polar materials, hot electron energy is dissipated predominantly through Fröhlich electron-phonon scattering. This interaction is generally dominant when an applied electric field accelerates electrons so that $E_K > \hbar\omega$ to emit optical phonons. This form of the Fröhlich interaction produces primarily zone-center longitudinal optical (LO) phonons [80]. Due to anharmonic interactions, the LO phonons decay into traveling acoustic waves. The decay of strongly-interacting optical phonons into acoustic phonons is a phenomenon that is essential to the understanding of the electron transport properties in heterostructures.

Such applications include the influence on electron mobility [104], the thermodynamic properties of the lattice and the interaction with hot electrons in high-electric field FETs, in which, the decay of LO phonons delocalizes energy from the self-heating region in the transistors [270, 271], [204] and, consequently, controlling the lifetimes of the hot phonons generated during this energy relaxation process. Therefore, it is of importance to investigate the intrinsic phonon decay properties and the decay channels of high-quality materials as their understanding is critical to self-heating and future phonon engineering efforts to improve the device performance.

Acoustic phonons are associated with all thermal properties of a solid, such as its heat content and transport. The Phonon deformation potentials help explain the stress-induced energy shifts which, in turn, is modified primarily by the uniaxial stress. The elastic moduli vary with both temperature and pressure as has been reported by Nichols et al. (1980) [272]. The anharmonic part of lattice oscillations causes the decay of LA phonons into lower-order modes. TA phonons, however, require the presence of excited phonons with energies ~ $\hbar\omega$ which results in a long lifetime of the TA phonons [139].

It has been demonstrated that the lifetime of acoustic phonons is in the timescale of hundreds of nano to microseconds [273]. It is possible to conclude from the available research that the depopulation of hot phonons into heat carrying acoustic phonons takes place on a timescale on the order of nano to picoseconds; such efforts include the calculations of decay times in the range of 150 – 740 ps which was obtained through time-resolved photoluminescence for GaN doped with Si by Kwon et al. (2000) [274]. Similar ranges were obtained by Chichibu et al. (1999) and Izumi et al. (2000) for bulk GaN [275], [276].

To the best of our knowledge, there have not been accurate estimations, or any measurements for that matter, of the decay times of acoustic phonons in nitride-based structures at 300 K. To cite a few studies relative to the anharmonic decay of acoustic phonons, Slonimskii (1937) suggested for the first time that LA phonons can decay into two lower-frequency modes that have a lifetime increasing as ω^5 [277].

Baumgartner et al. (1981) provided the first experimental verification of frequency-dependent anharmonic lifetimes of high-frequency acoustic phonons at low crystal temperature for CaF_2 [278]. Tamura (1985) calculated the decay times of LA phonons for a selection of quasi-isotropic crystals by accounting for the anharmonicity on the basis of the continuum elasticity theory [136]. Tamura was able to provide diverse estimates of the decay times of both down-conversion processes along with their branching ratios for crystals including Si, Ge and GaAs. In this paper, we extend these results to quasi-isotropic III-nitrides. Tamura's results challenged both the work by Orbach and Vredevoe (1964) [139], who found that the dominant decay channel is LA → LA + TA, as well as the branching ratios of the two processes obtained by Guseinov and Levinson (1983) [279], Lax et al. (1984) [280], Markiewicz (1980) [281] and Bron (1980) [282].

5.6.1 Issue of anharmonicity and anisotropy of the III-nitride crystals

Owing to their important role in solid-state physics, knowledge of higher-order elastic constants including second- and third-order elastic constants is essential for the study of the anharmonic properties of solids. The hexagonal crystals have six second-order elastic constants and ten third-order elastic constants. Elastic constants also provide insight into the nature of the anharmonicity of the material which, in turn, is helpful in the discussions of the deformation potential and the elastic properties [283]. In the THz frequency regime, the decay processes can be assessed quantitatively as the anharmonic coupling coefficients are determined by the second- and third-order elastic moduli as confirmed by Tamura [136]. Similarly, the elastic constants and the phonon density of states, depicted through the phonon dispersion, are sensitively related to each other. The phonon density of states is, in turn, important in the discussion of the dominant decay channel at the THz frequencies in III-nitrides. Data of applied stress on elastic constants facilitate the determination of the third-order elastic stiffness constants. For the hexagonal point groups, the ten

a- GaN

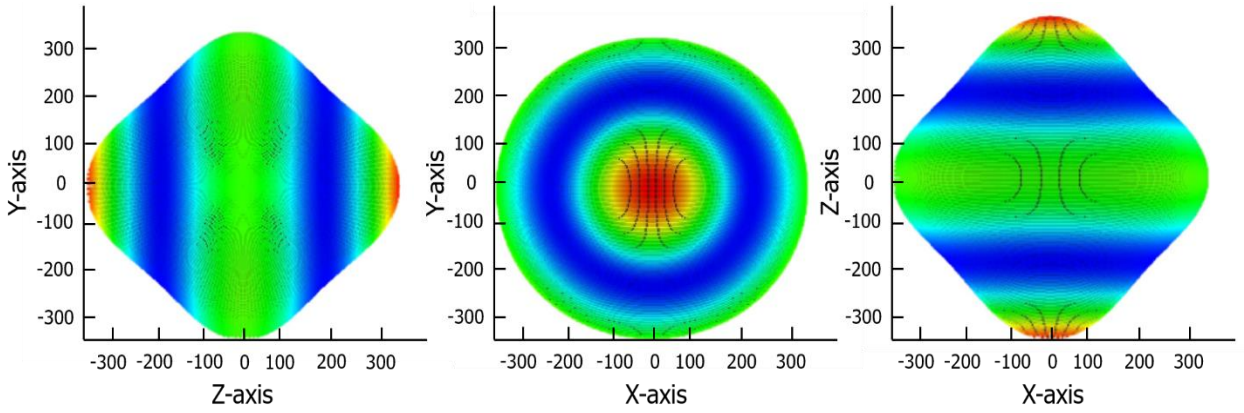

b- AlN

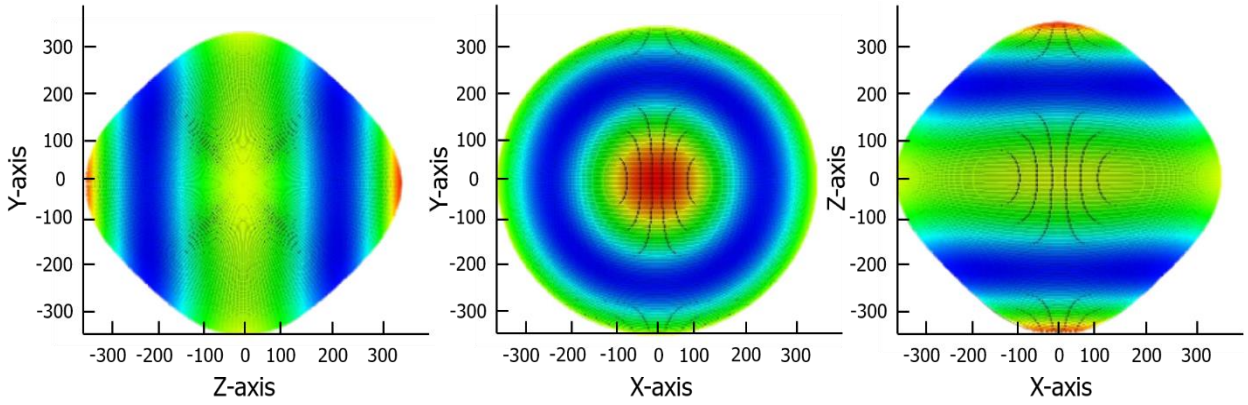

c- InN

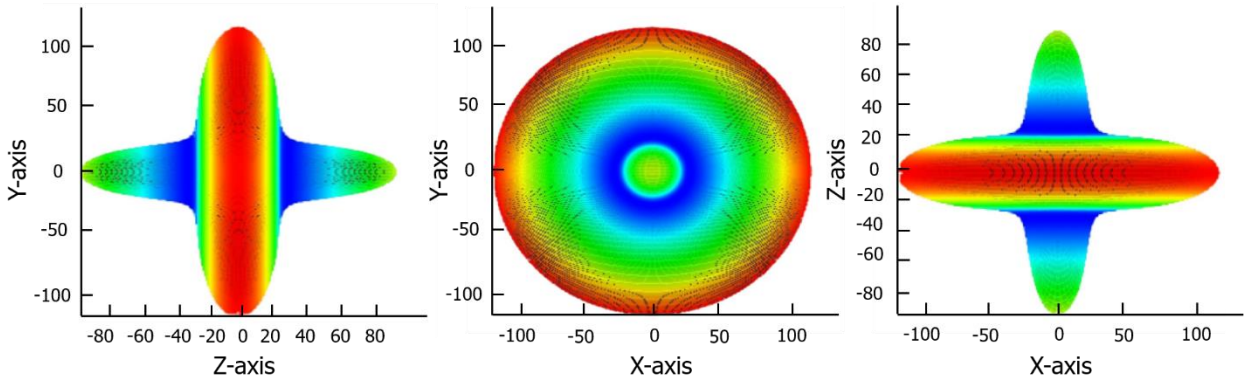

d- *w*–BN

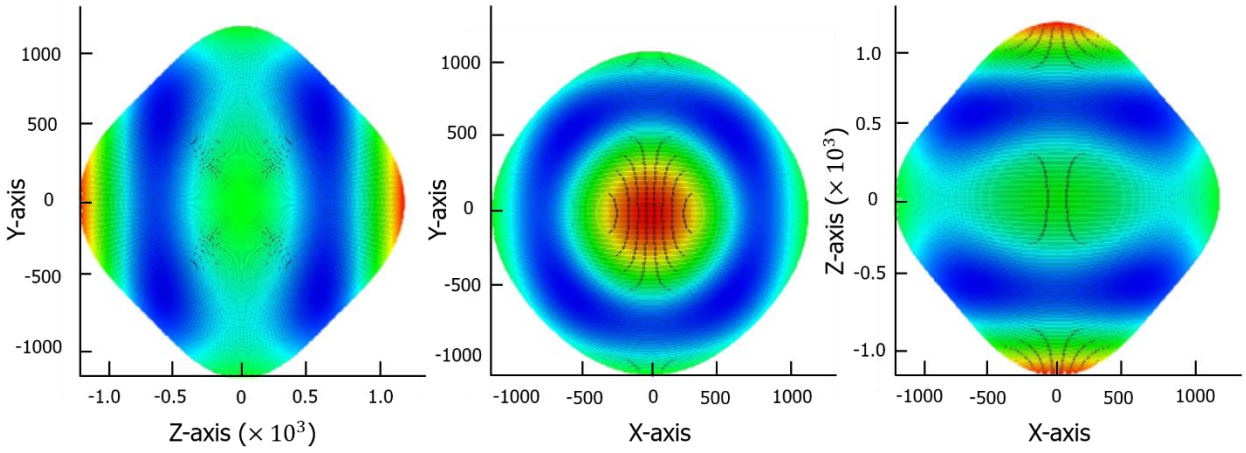

Fig. 31. Young's modulus of wurtzite III-nitride compounds with directional dependence represented in GPa.

---

independent components of the third-order elastic tensor can be written as C_{111}, C_{112}, C_{113}, C_{123}, C_{133}, C_{144}, C_{155}, C_{222}, C_{333} and C_{344} [284].

We should note that it is difficult to model obviously anisotropic crystals due to the great number of elastic constants. Fortunately, many solids that are relatively isotropic still have certain material symmetries in accord to their propagation direction, which could simplify the process [285]. We, however, take account of the anisotropy and of the anharmonicity by using experimentally known elastic constant values of second- and third-order. The elastic constant values at 300 K are listed in Tables 2 and 3.

In Table 3, C_{122}, C_{166} and C_{456} are calculated for III-nitrides using the relations [289]

$C_{122} = C_{111} + C_{112} - C_{222}$, $C_{166} = 1/4(3C_{222} - 2C_{111} - C_{112})$ and $C_{456} = 1/2(C_{155} - C_{144})$

Before proceeding with the calculation, it is important to discuss the degree of the anisotropy of the crystals under investigation. To that end, we calculate the Young's modulus of a selection of III-nitride

Table 7. Second-order elastic constants and the calculated sound velocities of III-nitrides.

	C_{11}	C_{33}	C_{66}	C_{44}	C_{12}	$v_{\perp}^{l}$	v_{z}^{l}	$v_{\perp}^{S}$	v_{z}^{S}
GaN[a]	382	384.4	144	97	93.8	7.87	7.899	4.837	3.97
AlN[a]	408	384.3	154	101	100.18	11.9	10.86	6.878	5.57
InN[a]	228.3	221	86.13	57	112	5.79	5.69	3.55	2.893
***h*-BN**[b]	750	32	300	3	150	18.55	3.83	11.73	1.173
***w*-BN**[c]	982	1077	424	388	134	16.78	17.57	11.03	10.55

[a]Pandey et al., 2007, Ref. 286.

[b]Green et al., 1976, Ref. 287.

[c]Shimada et al., 1998, Ref. 288.

Table 8. Third-order elastic constants of III-nitrides.

	C_{111}	C_{112}	C_{222}	C_{122}	C_{123}	C_{144}	C_{155}	C_{166}	C_{456}
GaN[a]	−287.6	−48.1	−225.6	−110.1	−15	−14.5	−9.7	−13.375	2.4
AlN[a]	−307.2	−51.4	−241.3	−117.3	−15.5	−15	−10.0	−14.525	2.5
InN[a]	−171.9	−28.8	−138.8	−61.9	−8.8	−8.5	−5.7	−10.95	1.4
***h*-BN**[b]	−687.2	−107.5	−544.7	−249.8	−28.3	−34.8	−23.2	−38.05	5.8

[a]Pandey et al., 2007, Ref. 286.

[b]Mathew et al., 2002, Ref. 290.

crystals and confirm the results by calculating the elastic anisotropy factor (F). The anisotropy is modelled by means of the compliance tensor matrices (S_{ij}), which are calculated for GaN, AlN, InN and wurtzite BN, and given in matrix forms. The visualized results are finally presented in Fig. 1. As has been

established, relatively isotropic crystals show an anisotropy factor that is close to unity. The results show that, in wurtzite GaN, AlN and BN, F of planes propagating along the [100] axis is 0.729, 0.833 and 0.814, respectively, while in wurtzite InN, F is much smaller than 1, indicating wurtzite lnN displays obvious anisotropic characteristics in this plane. Similarly, *h*-BN is a highly anisotropic layered material. As shown in Table 2, *h*-BN has very large acoustic velocities, which could be attributed to the strong in-plane covalent bonding of B and N atoms. The anisotropy simulation results suggest that *w*-BN should be an interesting candidate for our study; unfortunately, the third-order elastic constants for the wurtzite crystal at room temperature are not available. In his 1985 paper, Tamura analyzed the decay rate of acoustic phonons from variations of the mass density by obtaining an isotropic approximation, hence, using his results to model obviously anisotropic crystals may not be valid with a certain degree of certainty.

$$S_{ij}^{GaN} = \begin{bmatrix} 0.0031 & -0.0010 & -0.0006 & 0 & 0 & 0 \\ -0.0010 & 0.0031 & -0.0006 & 0 & 0 & 0 \\ -0.0006 & -0.0006 & 0.0028 & 0 & 0 & 0 \\ 0 & 0 & 0 & 0.0095 & 0 & 0 \\ 0 & 0 & 0 & 0 & 0.0095 & 0 \\ 0 & 0 & 0 & 0 & 0 & 0.0081 \end{bmatrix},$$

$$S_{ij}^{AlN} = \begin{bmatrix} 0.0029 & -0.0009 & -0.0005 & 0 & 0 & 0 \\ -0.0009 & 0.0029 & -0.0005 & 0 & 0 & 0 \\ -0.0005 & -0.0005 & 0.0028 & 0 & 0 & 0 \\ 0 & 0 & 0 & 0.0080 & 0 & 0 \\ 0 & 0 & 0 & 0 & 0.0080 & 0 \\ 0 & 0 & 0 & 0 & 0 & 0.0077 \end{bmatrix},$$

$$S_{ij}^{InN} = \begin{bmatrix} 0.0096 & -0.0021 & -0.0050 & 0 & 0 & 0 \\ -0.0021 & 0.0096 & -0.0050 & 0 & 0 & 0 \\ -0.0050 & -0.0050 & 0.0121 & 0 & 0 & 0 \\ 0 & 0 & 0 & 0.1000 & 0 & 0 \\ 0 & 0 & 0 & 0 & 0.1000 & 0 \\ 0 & 0 & 0 & 0 & 0 & 0.0233 \end{bmatrix},$$

$$S_{ij}^{h-BN} = \begin{bmatrix} 0.001 & -0.0003 & -0.000035 & 0 & 0 & 0 \\ -0.0003 & 0.001 & -0.000035 & 0 & 0 & 0 \\ -0.000035 & -0.000035 & 0.0313 & 0 & 0 & 0 \\ 0 & 0 & 0 & 0.333 & 0 & 0 \\ 0 & 0 & 0 & 0 & 0.333 & 0 \\ 0 & 0 & 0 & 0 & 0 & 0.00333 \end{bmatrix},$$

$$S_{ij}^{w-BN} = \begin{bmatrix} 0.001 & -0.0001 & -0.00006 & 0 & 0 & 0 \\ -0.0001 & 0.001 & -0.00006 & 0 & 0 & 0 \\ -0.00006 & -0.00006 & 0.0009 & 0 & 0 & 0 \\ 0 & 0 & 0 & 0.0026 & 0 & 0 \\ 0 & 0 & 0 & 0 & 0.0026 & 0 \\ 0 & 0 & 0 & 0 & 0 & 0.0024 \end{bmatrix}$$

5.6.2 Modeling of the population densities and the decay rates of LA phonons

We assume a high-purity sample and consider the acoustic phonon scattering independent of temperature. The total decay rate along with the property of the materials are initially taken in the [100] propagation direction and finally compared with the [001] direction. The decay rate depends on the dot-product of the polarization vectors of the initial and the final phonons. We assume that the spontaneous splitting of the longitudinal phonon into two lower-energy phonons, which is the dominant anharmonic interaction, can occur through two processes only: (1) LA → LA + TA that shall be named as process 1 and (2) LA → TA + TA that shall be named as process 2 through the remainder of this paper. We plot a Herring-like vector diagram in Fig. 2 to specify which wave vectors and branch combinations will simultaneously fulfill the energy and momentum conservation conditions. Here, q is the incoming LA phonon wave vector, q' is the final LA phonon wave vector and q'' is the final TA phonon wave vector for process 1, both q' and q'' represent the final TA phonon wave vectors for process 2, θ is the angle between q and q' and t is the angle between q and q''. We define the following relations from Fig. 2:

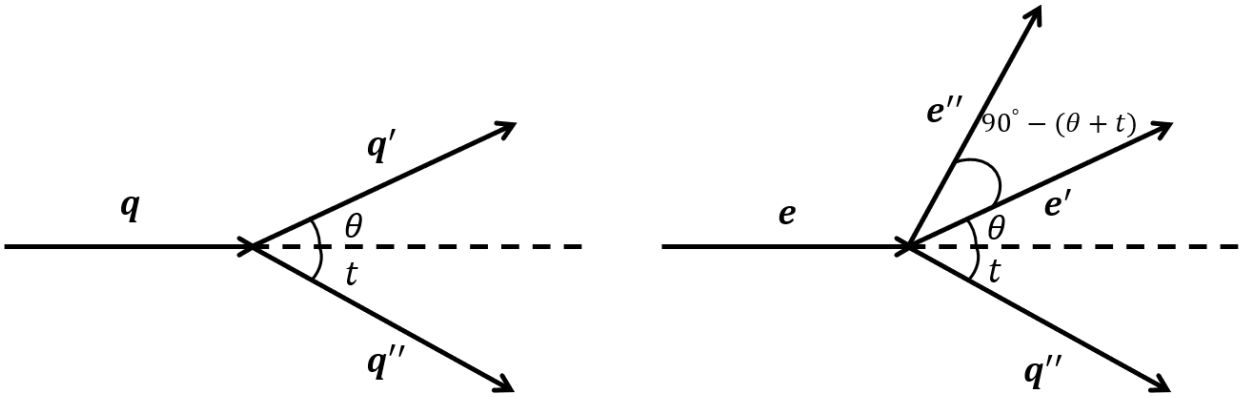

Fig. 32. Vector diagrams for normal three-phonon process which conserves both energy and momentum. The phonon wave vector propagation is shown on the left whereas the polarization vectors propagation is shown on the right.

$q' \cdot q'' = cos(\theta + t)$; $q'' \cdot q = cos(t)$; $q' \cdot q = cos(\theta)$; $e'' \cdot e = sin(t)$; $e' \cdot e = cos(\theta)$; $e' \cdot e'' = sin(\theta + t)$ where $q'' \cdot e'' = 0$, $q' \cdot e' = q'$, $q \cdot e = q$. Therefore, $q' sin(\theta) = q'' sin(t)$ and $q' cos(\theta) + q'' \cos(t) = q$. From the vector diagram, we can obtain the energy and momentum conservation conditions as

$$vq = v'q' + v''q'' \tag{5.24}$$

$$q^2 = (q'')^2 - (q')^2 + 2qq' cos\theta \tag{5.25}$$

To obtain an expression of the spontaneous decay rate (Γ) of LA phonons, we adopt the notations in Tamura's paper (1985) and start from the nonlinear elasticity theory which describes the acoustic wave propagation in the elastic medium by the displacement vector

$$u(r) = \frac{1}{(V\rho)^{1/2}} \sum_{qj} exp(iq \cdot r) \hat{e}(\hat{q}j) Q(qj) \tag{5.26}$$

Since the rates depend on the polarization vectors, the deformation parameter is obtained by

$$\xi_{ij} = \frac{\partial_j u_i}{\partial r} = \frac{1}{(V\rho)^{1/2}} \sum_{qj} exp(iq \cdot r)\hat{e}(\hat{q}j)Q(qj) \quad 5.27$$

The potential energy function is written as [291]

$$W = \frac{1}{8}(C_{11} - C_{12})(\xi_{ik} + \xi_{ki})^2 + \frac{1}{2}C_{12}\xi_{ii}\xi_{jj} + (\frac{1}{2}C_{12} + 3C_{155} - 6C_{456})\xi_{ii}\xi_{jk}^2 + (\frac{1}{2}C_{11} - \frac{1}{2}C_{12} + 6C_{456})\xi_{ij}\xi_{ki}\xi_{kj} + (3C_{155} - 6C_{456})\xi_{ii}\xi_{jk}\xi_{kj} + (C_{111} - 6C_{155} + 4C_{456})\xi_{ii}\xi_{jj}\xi_{kk} + 2C_{456}\xi_{ij}\xi_{jk}\xi_{ki} \quad 5.28$$

Now, the particle displacement can be quantized as

$$u(r) = i \sum_{qj} (\hbar/2V\rho\omega(q))^{1/2} exp(iq \cdot r)[a(q) - a^*(-q)] \quad 5.29$$

And the spontaneous decay rate expression is provided by

$$\Gamma = \frac{\pi\hbar}{8\rho^3 V\omega} \iint \left[\frac{M^2}{\omega'\omega''}\right] \tau(\omega - \omega' - \omega'') \quad 5.30$$

By using the vector diagram equations, we eliminate the trigonometric functions of the angle t and substitute for the dot-products in Eqn. 5.28 which gives the matrix element expression

$$M = (\beta + \lambda)\left\{\frac{qq'}{q''}(q^2 - (q')^2)cos\theta sin\theta\right\} + \gamma\left\{\frac{qq'}{q''}(q^2 - (q')^2)cos\theta sin\theta\right\} + (\gamma + \lambda)\left\{\frac{3qq'}{q''}(q^2 - (q')^2)cos\theta sin\theta\right\} + \alpha\{0\} + \beta\left\{\frac{qq'}{q''}(q^2 - (q')^2)cos\theta sin\theta\right\} \quad 5.31$$

Eqn. 5.31 finally reduces to the matrix element expression given by Tamura (1985).

a. Decay of process 1

We express q'' from the energy conservation of Eqn. 5.24 as

$$q'' = (q - q')\frac{v_l}{v_t} \tag{5.32}$$

We use Eqn. 5.32 to eliminate q'' from Eqs. 5.24 and 5.25 to get

$$(q - q')^2 \frac{v_l^2}{v_t^2} = q^2 + (q')^2 - 2qq'cos(\theta) \tag{5.33}$$

which gives the expression

$$cos\theta = \frac{v_l^2}{v_t^2} - \left(\frac{q + q'}{2qq'}\right)\left(\frac{v_l^2}{v_t^2} - 1\right) \tag{5.34}$$

We set $x = \frac{q'}{q}$ and $\delta^2 = \frac{v_l^2}{v_t^2}$, so that Eqn. 5.34 can be written as

$$cos\theta = \delta^2 - \frac{1}{2}\left(x + \frac{1}{x}\right)(\delta^2 - 1) \tag{5.35}$$

We enforce the condition $-1 \leq cos\theta \leq 1$ on Eqn. 5.35

$$-1 \leq \delta^2 - \frac{1}{2}\left(x + \frac{1}{x}\right)(\delta^2 - 1) \leq 1$$

$$\rightarrow 2 \leq \left(x + \frac{1}{x}\right) \leq \frac{2(\delta^2 + 1)}{(\delta^2 - 1)} \tag{5.36}$$

By solving the inequality on the LHS and the RHS in Eqn. 5.36, we get the integration limits x_0 and 1 as

$$\frac{2(\delta^2 + 1)}{(\delta^2 - 1)} - \sqrt{\frac{\left[\frac{2(\delta^2 + 1)}{(\delta^2 - 1)}\right]^2}{4} - 1} \leq x \leq \frac{\left[\frac{2(\delta^2 + 1)}{(\delta^2 - 1)}\right]^2}{2} + \sqrt{\frac{\left[\frac{2(\delta^2 + 1)}{(\delta^2 - 1)}\right]^2}{4} - 1}$$

which reduces to

$$\frac{(\delta-1)}{(\delta+1)} \leq x \leq \frac{(\delta+1)}{(\delta-1)}$$

Here, $\delta = \frac{v_l}{v_t} > 1$, but the upper limit $\frac{(\delta+1)}{(\delta-1)} > 1$. And since that regardless of the crystal anharmonicity, anisotropy and symmetry, the incoming phonon of a given wave vector cannot decay into phonons of larger wave vector; therefore x is always ≤ 1. While $x > 0$, this constraint holds true for the lower limit $\frac{(\delta-1)}{(\delta+1)}$ of x which is denoted as x_0 by Tamura.

We adapt the expression provided by Tucker and Rampton (1973) to model process 1:

$$\Gamma_1 = \frac{\hbar q^9}{32\pi\rho^3\omega}(2\beta + 4\gamma + \lambda + 3\mu)^2 \int_{x_0}^{1}\int_{-1}^{1} dx \frac{x^4(1-x^2)^2}{\omega'\,\omega''(1+x^2-2x\,cos\theta)} sin^2\theta cos^2\theta\tau(\omega - \omega' - \omega'')d(cos\theta)$$

$$= \frac{\hbar q^6}{32\pi\rho^3 {v_l}^2 v_t}(2\beta + 4\gamma + \lambda + 3\mu)^2 \int_{x_0}^{1}\int_{-1}^{1} dx \frac{x^3(1-x^2)^2}{q''(1+x^2-2x\,cos\,\theta)} sin^2\theta cos^2\theta\tau(qv_l - q'v_l - q''v_t)\, d(cos\theta) \quad 5.37$$

The argument of the Dirac-delta function is evaluated as follows

$$\tau(qv_l - q'v_l - q''v_t) = \tau\big(q''v_t - (qv_l - q'v_l)\big) = \frac{1}{qv_t}\tau\left(\frac{q''}{q} - \frac{v_l}{v_t}\left(1 - \frac{q'}{q}\right)\right)$$

$$= \frac{1}{qv_t}\tau\left(\sqrt{(1+x^2) - 2x\,cos\,\theta} - \delta(1-x)\right) \quad 5.38$$

The argument of the Dirac-delta function goes to zero when

$$cos\theta = \frac{1 + x^2 - \delta^2(1-x)^2}{2x} \quad 5.39$$

Eqn. 5.39 provides the expression of the angular displacement given by Leman (2012) [292].

By making the necessary substitutions in Eqn. 5.37, the decay rate of process 1 can thus be expressed as

$$\Gamma_1 = \frac{\hbar\omega^5(2\beta + 4\gamma + \lambda + 3\mu)^2}{32\pi\rho^3 {v_l}^7 {v_t}^2}(\delta^2$$

$$- 1)\int_{x_0}^{1} dx\ \frac{x^3(1 - x^2)^2}{(\delta^2(1-x)^2)^{3/2}}(1$$

$$- x)^2\frac{[(x+1)^2 - \delta^2(1-x)^2][(1+x^2) - \delta^2(1-x)^2]^2}{4x^2}$$

Finally,

$$\Gamma_1 = \frac{\hbar\omega^5}{256\pi\rho^3}\frac{(\delta^2 - 1)}{{v_l}^9}(2\beta + 4\gamma + \lambda + 3\mu)^2\int_{x_0}^{1}\frac{dx(1-x^2)^2}{2\delta x(1-x)}[(x+1)^2$$

$$- \delta^2(1-x)^2][1 + x^2 - \delta^2(1-x)^2]^2 \quad 5.40$$

where ρ is the mass density, $x_0 = \frac{\delta-1}{\delta+1}$, $\delta^2 = (v_l/v_t)^2$, λ and μ are the second-order Lame's constants and β and γ are the third-order Lame's constants which were provided in Ref. 136 as

$$\lambda = 1/5(C_{11} + 4C_{12} - 2C_{44})$$

$$\mu = 1/5(C_{11} - C_{12} + 3C_{44})$$

$$\beta = 1/35(C_{111} + 4C_{112} - 5C_{123} + 19C_{144} + 2C_{166} - 12C_{456})$$

$$\gamma = 1/35(C_{111} - 3C_{112} + 2C_{123} - 9C_{144} + 9C_{166} + 9C_{456}) \quad 5.41$$

The integrand in Eqn. 5.40 represents the probability density function for phonon distribution and depends strongly on the sound velocity of the incoming phonon mode and on the ratios of the initial and the final phonon wave vectors.

b. Decay of process 2

Here, $\omega = qv_l$, $\omega' = q'v_t$ and $\omega'' = q''v_t$. q'' is therefore expressed from Eqn. 5.24 as

$$q'' = \left(q\frac{v_l}{v_t} - q'\right) \quad 5.42$$

Now, we let $x = \frac{q'}{q}$ and $\delta = \frac{v_l}{v_t}$ and substitute for q'' from Eqs. 5.24 and 5.42, we get

$$(\delta - x)^2 = 1 + x^2 - 2x\,cos\theta \quad 5.43$$

Enforcing the conditions of $cos\theta$ and rearranging the above equation leads to the inequalities

$$-1 \leq \frac{(1 + x^2 - (\delta - x)^2)}{2x} \leq 1$$

By solving the inequality on the LHS and the RHS we get the integration limits x_1 and x_2 as

$$\frac{\delta - 1}{2} \leq x \leq \frac{\delta + 1}{2}$$

For process 2, the daughter TA phonons can have two types of polarizations: (a) simultaneous polarization within the plane spanned by q and q', (b) perpendicular to the plane spanned by q and q'. Consequently, the two matrix elements in Eqn. 5.30 can be rewritten as M_a and M_b, respectively.

The argument of the delta functions for process 2 is evaluated as follows

$$\tau(qv_l - q'v_l - q''v_t) = \tau\big(q''v_t - (qv_l - q'v_t)\big) = \frac{1}{qv_t}\tau\left(\frac{q''}{q} - \left(\frac{v_l}{v_t} - \frac{q'}{q}\right)\right)$$

$$= \frac{1}{qv_t}\tau\left(\sqrt{(1+x^2) - 2x\,cos\,\theta} - (\delta - x)\right) \qquad 5.44$$

In this scenario, the argument of Dirac-delta function goes to zero when

$$cos\theta = \frac{2x\delta + (\delta^2 - 1)}{2x} \qquad 5.45$$

The decay rate as a result of the simultaneous polarization can be written as

$$\Gamma_2^a = \frac{\hbar\omega^5}{32\pi\rho^3(v_l^2 v_t)^3}\int_{x_1}^{x_2}\int_{-1}^{1} dx\,\frac{x([\beta + \lambda + 2(\gamma + \mu)](x - cos\theta)^2 - (\beta + 2\gamma + \mu)sin^2\theta)^2}{(1 + x^2 - 2x\,cos\theta)^{3/2}}$$

$$\times\,\tau\left(\sqrt{(1+x^2) - 2x\,cos\theta} - (\delta - x)\right)d(cos\theta)$$

Therefore,

$$\Gamma_2^a = \frac{\hbar\omega^5}{32\pi\rho^3(v_l^2 v_t)^3}\int_{x_1}^{x_2} dx\left\{[\beta + \lambda + 2(\gamma + \mu)]\left[\frac{2x^2 - 2x\delta + (\delta^2 - 1)}{2x(\delta - x)^3}\right]\right.$$

$$\left. + (\beta + 2\gamma + \mu)(\delta^2 - 1)\left[\frac{4x\delta - 4x^2 - (\delta^2 - 1)}{4x^2(\delta - x)^3}\right]\right\} \qquad 5.46$$

Similarly, the decay rate as a result of the perpendicular polarization can be written as

$$\Gamma_2^b = \frac{\hbar\omega^5}{32\pi\rho^3(v_l^2 v_t)^3}\int_{x_1}^{x_2}\int_{-1}^{1} dx\,\frac{x[(\beta+\lambda)(cos\theta - x) + 2(\gamma+\mu)(1-xcos\theta)cos\theta]^2}{(1+x^2-2x\,cos\theta)^{1/2}}$$

$$\times\,\tau\left(\sqrt{(1+x^2)-2x\,cos\theta} - (\delta - x)\right) d(cos\theta)$$

Therefore,

$$\Gamma_2^b = \frac{\hbar\omega^5}{32\pi\rho^3(v_l^2 v_t)^3}\int_{x_1}^{x_2}\frac{dx}{4x(\delta-x)}\Bigg\{(\beta+\lambda)(2x\delta - (\delta^2-1) - 2x^2)$$

$$+ 2(\gamma+\mu)\left(\frac{2-2x\delta+(\delta^2-1)}{2}\right)\left(2x\delta - (\delta^2-1)\right)\Bigg\}^2 \qquad 5.47$$

Finally, $\Gamma_2 = \Gamma_2^a + \Gamma_2^b$

5.6.3 Discussion

Measurements on the decay times could be very instructive in gaining an insight of the phonon coupling mechanisms with direct implications to studying the anharmonicity, the elastic moduli and the decay rates depending on temperature. In our calculations, we assume that the dephasing of phonons happens only through a three-phonon process. While we restrict our attention to the quasi-isotropic wurtzite nitride solids, in Table 9, we provide the constants used in our numerical calculations for all the materials considered here anyway.

In our numerical presentation, we calculate the phonon density function at 8 THz which are described as a characteristic function for the anisotropic medium for III-nitrides as shown in Fig. 33. The area under the characteristic function for each decay branch represents the relative probability for this type of decay process to occur. The decay rates as a function of the phonon frequencies are then numerically calculated and plotted in Fig. 34. It is clear from Figs. 33 and 34 that the decay of process 2 dominates the full

Table 9. Constants used in the present decay rates calculations.

	GaN	**AlN**	**InN**	***h*-BN**	***w*-BN**
$\boldsymbol{f}$	0.729	0.833	0.308	$\ll 0.1$	0.814
$\boldsymbol{\lambda}\ (\boldsymbol{N/m^2})$	1.128	1.213	1.125	2.663	1.484
$\boldsymbol{\mu}\ (\boldsymbol{N/m^2})$	1.158	1.222	0.575	1.088	4.024
$\boldsymbol{\beta}\ (\boldsymbol{N/m^2})$	-2.103	-4.283	-1.266	-0.509	-
$\boldsymbol{\gamma}\ (\boldsymbol{N/m^2})$	-0.4045	-0.4492	-0.3216	-0.1138	-
$\boldsymbol{v_l}\ (\boldsymbol{km/s})$	7.87	11.9	5.79	18.55	16.78
$\boldsymbol{v_t}\ (\boldsymbol{km/s})$	3.97	5.57	2.893	1.173	10.55
$\boldsymbol{\delta}$	1.982	2.136	2.001	15.814	1.591
$\boldsymbol{\rho}\ (\boldsymbol{10^3 kg/m^3})$	6.154	3.255	6.81	2.18	3.487

spectrum. To evaluate a sample of the branching ratios of each process, we tabulate the calculations undertaken at 8 THz where the acoustic phonons in the nitride structures have a high density of states in the dispersion relation as shown in the bottom diagram in Fig. 34.

The decay rate depicted in Fig. 34 is governed by the existence of the density of the initial mode and the population of the final modes but, unlike in the determination of specific heat, the decay rates depend on the frequency – and not on the population of the phonons at any given frequency region. To illustrate, if we consider the frequency range of 5 – 6 THz (7 – 8 THz), we find that AlN has smaller (larger) DOS

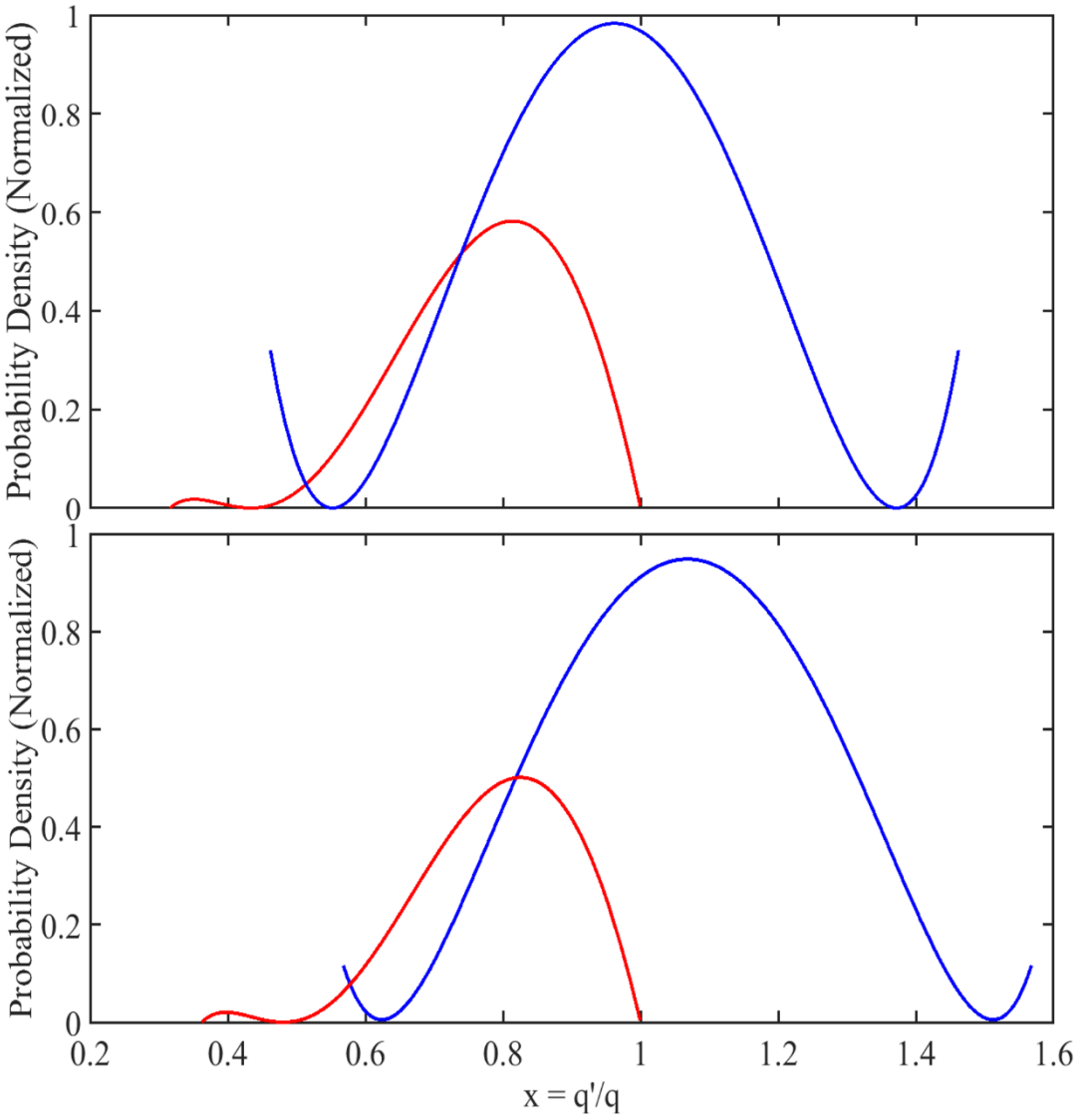

Fig. 33. Probability density function at 8 THZ for phonon distribution in GaN (top) and AlN (bottom). The red curves depict the characteristic functions for process 1 and the blue curves depict the characteristic functions for process 2.

---

than GaN and yet, in both cases, the decay rates follow the same pattern. Fig. 34 shows that the decay rate in AlN is about 5.7 times higher than the rate in GaN of process 1 and 1.6 times higher than the rate in GaN of process 2. The rates show that the new generation of acoustic phonons in GaN and AlN have

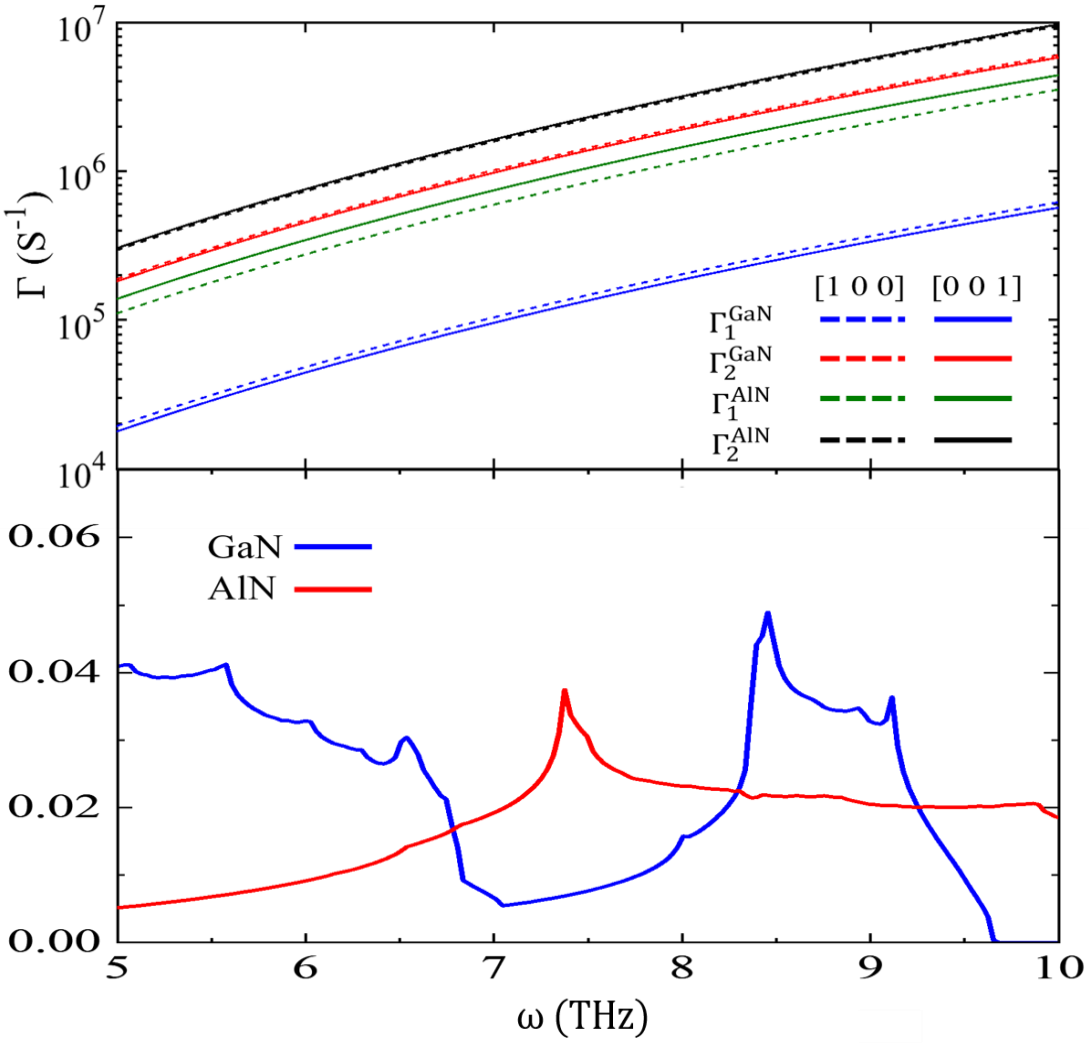

Fig. 34. The top figure represents the decay rate of LA phonons as a function of the phonon frequency for GaN and AlN calculated for the directions [100] and [001]. The bottom figure represents the phonon density of states for LA phonons calculated at the range of 5 – 10 THz.

longer lifetimes than optical phonons, which are known to have lifetimes in the order of picoseconds (table 10).

We should note that these results are a modified form of those given by Tamura in 1985 in which, for process 1, the x^2 term in the denominator is replaced by $2\delta x(1-x)$ in our calculations, and for process

Table 10. Calculated decay rates at 8 THz.

	$\Gamma_1(\%)$	$\Gamma_2(\%)$	$\Gamma_T\ (s^{-1})$	**Decay time (μs)**
GaN	9.32	90.68	2.21×10^6	0.45
AlN	27.33	72.67	4.32×10^6	0.23

2, instead of one equation, we provide two formulas to explicitly describe the two polarization conditions for the outgoing TA phonons; the numerical integration shows that the two formulations yield decay rates within a factor of 2 or less of each other. Our results verify the ω^5 dependence as confirmed by previous efforts including the work by Tua (1982) in which he mentions that ω^5 dependence is actually valid for anisotropic solids [293].

It is of interest to compare the spontaneous decay rates with different propagation directions to remark on the degree of anisotropy of the GaN and AlN crystals studied here. The anharmonic decay rates for the [100] and [001] directions are thus plotted in Fig. 34. We conclude that the anisotropy of both crystals has negligible effects on the acoustic phonon interaction in GaN and AlN. As opposed to the work of Tua and Mahan (1982) who have reported a greater discrepancy in the anharmonic lifetimes in CaF_2 in the directions [100] and [111] which has been attributed to the fact that CaF_2 crystal exhibits obvious anisotropic characteristics in those directions [294].

5.7 Summary

Compared to the velocity of pure GaN, the acoustic phonon velocity increases significantly upon increasing the AlN component compared to GaN in the superlattice as shown in Table 2. Importantly, the

acoustic phonon velocity is enhanced by the piezoelectric stiffening. These results indicate that phonon engineering of the superlattice phonons may be used to enhance heat transport in high quality superlattices with negligible interfacial roughness. Such engineered superlattices portend applications in reducing temperatures in critical components of electronic and optoelectronic devices through judicious placement of the superlattices.

The anharmonic term in the nonlinear elasticity theory suggests that the longitudinal acoustic phonon will dephase into two lower-energy phonons. In this thesis, we have developed computational techniques for a study of the decay channels of longitudinal acoustic phonons in quasi-isotropic III-nitrides by taking the spatial anisotropy into account [295]. We find that the nitride crystals exhibit decay rates in the range of $10^5 – 10^7$ s^{-1} and almost all of the down-conversion process is associated with the LA → TA + TA channel. Our estimates show that the anisotropy of GaN and AlN crystals have minimum effects on the decay rates which reveals a great degree of accuracy of the model presented herein when used for quasi-isotropic III-nitrides in their wurtzite phase.

Chapter 6

Modeling of ISFET for biosensing applications

6.1 Introduction

Because of their unique properties, including mechanical flexibility, single crystal nature and high-surface areas, nanowire transistors are considered as great candidates for many industrial applications. More specifically, nanowire Ion Sensitive Field Effect Transistors (IFETs) have been shown to possess very high sensitivities and limits of resolution suitable for bio-sensing applications [296]. Until now, efforts have been made to analyze the ion adsorption at the SiO_2 interface of ISFET [297], explain pH sensitivity [298] and the use of ad hoc based simulation programs to understand the effects of the physical parameters of silicon nanowire ISFETs to evaluate their performance [299]. Since successful application of ISFET in DNA sequencing [300], ISFETs have been applied for numerous biological sensing applications and have been well-integrated into the CMOS technology [301]. Thus, it has become desirable to perform precise and diverse numerical device simulations in TCAD to be able to support ISFET designing, extract its corresponding circuit parameters and perform device/IC analyses. Though commercial TCAD is not equipped with models for the complex and material dependent electrochemical processes that govern the ISFET operation, Bandiziol et al. (2015) have proposed an approach to describe, in commercial TCAD, the chemical reactions that occur at dielectric/electrolyte interface and make ISFET sensitive to pH [302]. This chapter seeks to perform TCAD simulations of Silicon nanowires based ISFET devices in biosensing scenarios. Site-binding model for biosensing together with quantum corrected model for electronic transport will be used to simulate characteristics of nanowire ISFETs to validate the actual fabricated devices.

6.2 Simulation of site-binding model in TCAD

The goal of this work is to revisit methodologies for isothermal DNA amplification and adapt them to non-buffered, or limited buffering, pH conditions. The extension of DNA operated by polymerases results in the production of H+ ions which can be harnessed to monitor and quantify DNA amplification [303]. This approach is currently exploited in many platforms for next-generation sequencing and is currently gaining momentum as an alternative to optical-based strategies [304]. This project, which took place in the Swiss Federal Institute of Technology (EPFL), Lausanne, Switzerland, involves building knowledge on isothermal methodologies for DNA amplification, establishing in vitro DNA amplifications and adjusting reactions to minimize or remove pH buffering which cancels out polymerase-derived pH changes. Pilot semiconductor devices provide a powerful tool to assessing the pH of reactions. In EPFL, ISFET devices in multi-nanowire configuration were being used for the purposes of DNA amplification detection and quantification.

Bandiziol et al. (2015) provided a strong foundation on implementing site-binding model in TCAD. Working on the TCAD structure, we have realized it is quite challenging to implement electrolyte model in commercial Sentaurus TCAD environment, due to lack of in-built models. The devices were fabricated in Laboratoire d'électronique des technologies de l'information (CEA-Leti) in Grenoble, France. Therefore, TCAD simulation of multi-wire ISFETs will complement the results that are expected from the fabricated devices. Therefore, throughout this segment, we present a method of implementing site-binding model for 3D simulations in TCAD. We employ the powerful Sentaurus TCAD environment to simulate MOSFET devices in Sentaurus structure editor (SDE) and use basic SDEVICE tool to simulate I-V characteristics of MOSFET devices. We use INSPECT tool in TCAD to efficiently view the *xy* plots and doping profiles. We also simulate the characteristics of multi-wire ISFET devices and verify the parameters of the nanowire devices in different simulation tools such as nanoHub. The ISFET is simulated

for its gate and drain characteristics which was achieved by applying a set of voltage biases and sweeping the biases from one point to another.

The TCAD script developed to simulate the FET structure is available in Appendix D. The I_D-V_g curve is shown in Fig. 34 while Fig. 35 presents the output characteristics of 150 nm FET. We have only considered p-type ISFET in this chapter with bulk doping using boron. The simulation results are in good agreement with the results presented by Chen et al. (2012) [305] and Iwai et al. (2011) [306].

6.3 Electrolyte modeling in nanoHUB

The use of field-effect transistor devices to detect changes at the interface due to adsorption of charged species has started way back in the seventieth. Due to their reliability, low-power consumption, high molecule detection range and low-frequency noise, ISFET has become more attractive recently for many applications in industry and biomedical studies [301].

Among many applications, ISFET is used for detecting ion concentrations such as H+ in solutions. The current traveling through the transistor will change in accord to the change in the ion concentration [307]. Here, the H+ solution is utilized as the gate electrode. An ion envelope causes a voltage difference between substrate and oxide surfaces. Electrons supplied by the source region and the drain region is needed to make electrons flow. This flow constitutes drain current I_D, and the gate voltage controls the number of electrons.

ISFET operates by accumulating H+ from solution gate. The positive charge of the gate is mirrored on the inner side of semiconductor where a channel of negative charge occurs, hence, making ISFET conductive. The lower the pH the more H+ accumulates and the more current flows between source and drain.

Fortunately, development of pH-sensitive FET models have been carried out [308]. Researchers applied the electrochemical stage in the electrolyte to calculate the current flow through the channel. After a bit of algebra, it has been indicated that the pH response of the surface oxide can be obtained by $C_S/(C_S + C_{dl})$, where C_S is the buffer capacitance and C_{dl} is the double layer capacitance. These calculations demonstrate a dimensionless parameter that varies between 0 and 1, therefore, suggesting a maximum pH response of 59.5 mV/pH at 300K known as the Nernst limit [309]. The condition of $C_S/(C_S + C_{dl}) = 1$ is not fulfilled by all gate oxides; for instance, SiO_2 has a small surface buffer capacitance, therefore, ISFETs with SiO_2 as gate oxide achieve typically a pH response of ~ 30mV/pH [310], whereas ISFETS employing Al_2O_3 or HfO_2 can exhibit the full Nernst pH response at 300 K [311]. Fig. 38 provides the I_{DS}/V_{GS} transfer characteristic with changing pH measured at V_{DS} = 0.5 V in our proposed ISFET. We observe that the threshold voltage of ISFET varies with different pH values. This variation in threshold voltage is nonlinear, which is an indication of varying sensitivity of the device per pH input. The threshold voltages of this device increased with the increased pH.

6.4 Summary

In this chapter, we have presented a comparative analysis of Silicon Nanowires based Ion Sensitive Field Effect Transistor (ISFET)-based pH sensors implemented with the help of TCAD simulation. Based on the results obtained from the pH response analysis we can determine whether the ISFET sensor has potential for commercialization and biosensing applications. Several diagrams were introduced to explain the electrical characteristics and pH response of the ISFET sensor. Based on pH input, the output characteristics are shown to be varying because of change in threshold voltage of ISFET. Site-binding model for biosensing together with quantum corrected model for electronic transport were used to simulate characteristics of nanowire ISFETs to validate the actual fabricated devices.

Table 7. Simulation parameters of FET.

L	W	H	T_{ox}	Radius	Channel doping	Bulk doping
150 nm	50 nm	50 nm	0.8 nm	5 nm	10^{16} cm^{-3} (Boron)	10^{15} cm^{-3} (Boron)

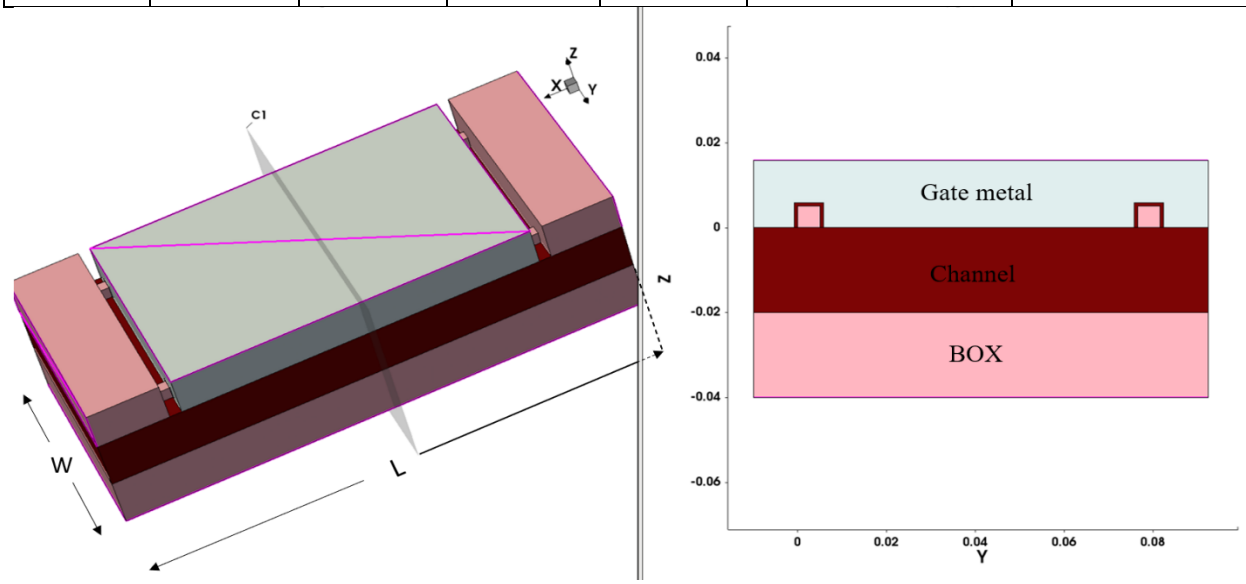

Fig. 35. TCAD structure of 150 nm NW MOSFET.

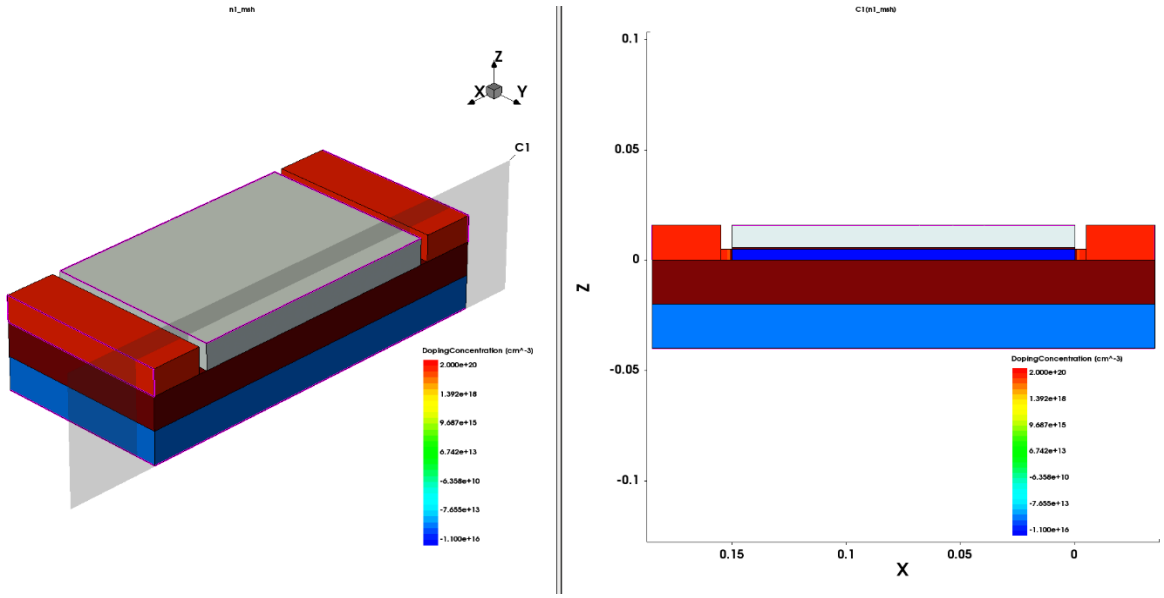

Fig. 36. Cross section of the doping profiles in 150 nm NW MOSFET structure.

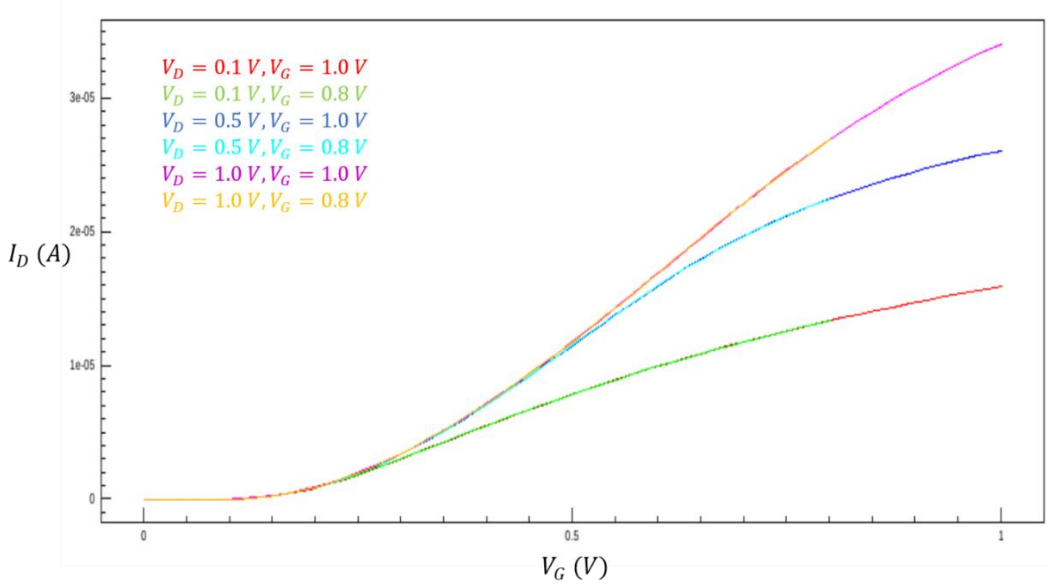

Fig. 37. Drain current versus gate voltage curve. V_G was swept up to 0.8 V (green, light blue, magenta) and up to 1 V (red, dark blue, orange) for drain voltages 0.1, 0.5 and 1V.

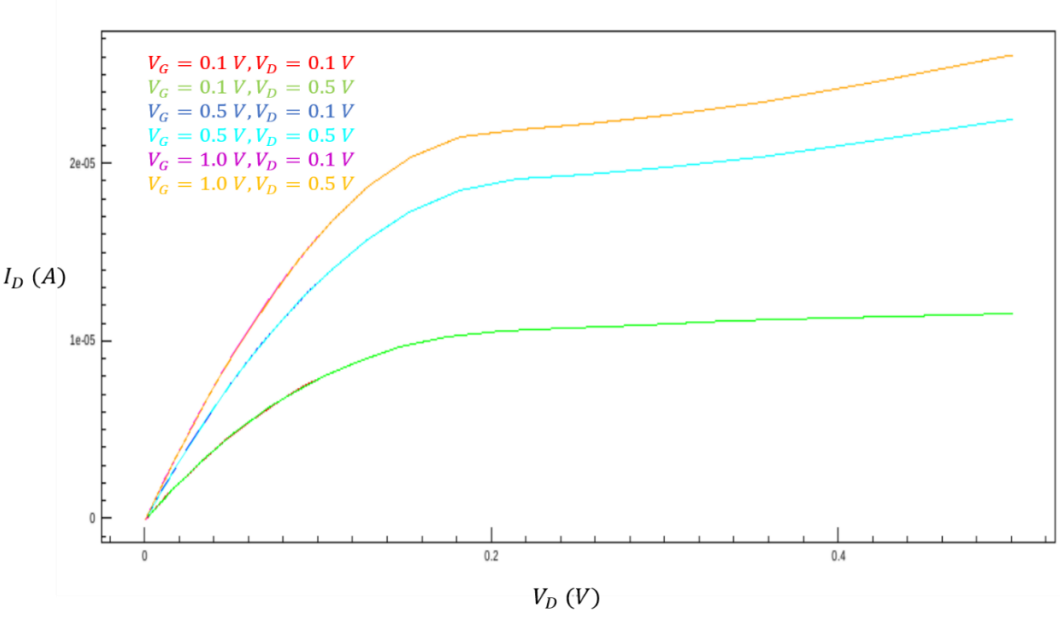

Fig. 38. Output Characteristics of ISFET drain current as a function of the drain voltage. The simulation was repeated for V_D values of 0.1 (red, dark blue, magenta) and 0.5 V (green, light blue, orange) with three V_G values of 0.1, 0.5 and 1 V.

Table 8. Geometrical parameter for electrolyte simulation.

Channel length	Film thickness	Box thickness	Insulator	Electrolyte
200 nm	20 nm	100 nm	SiO_2	NaCl

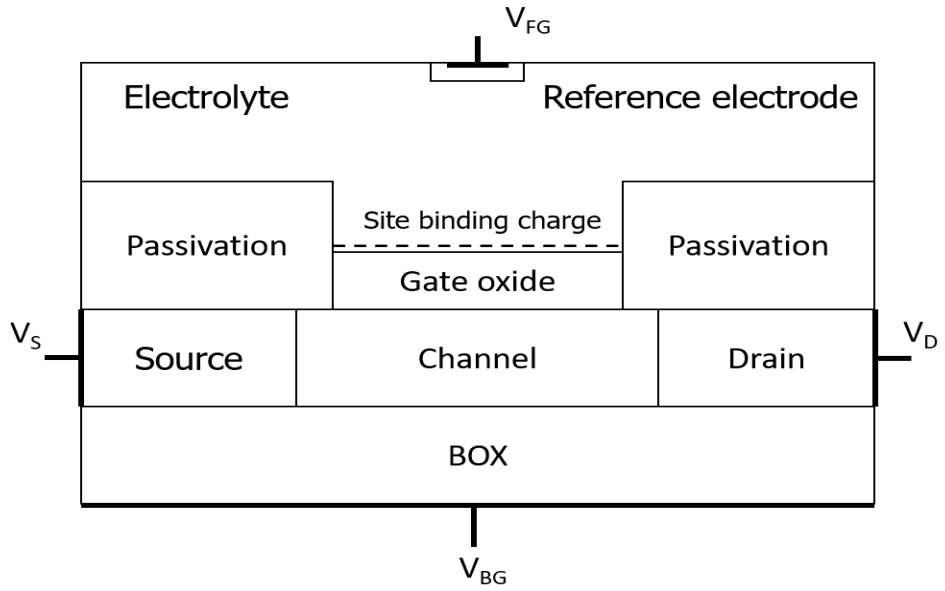

Fig. 39. Schematic diagram of ISFET sensor.

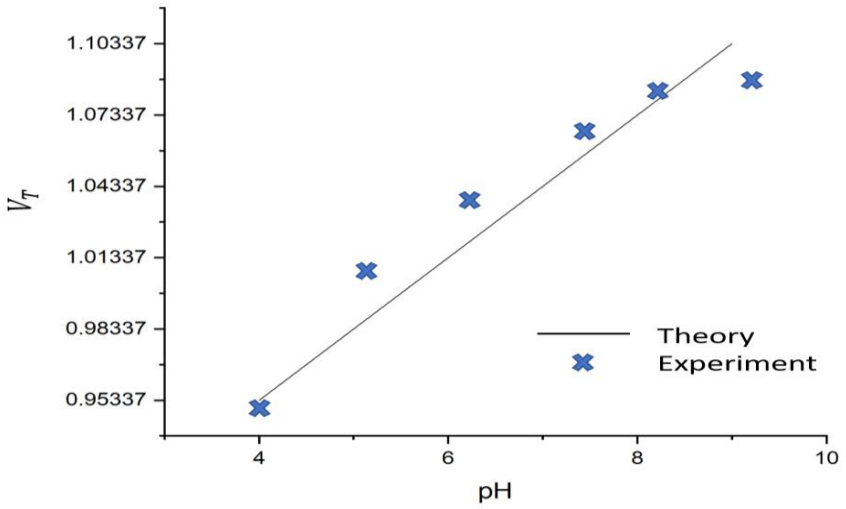

Fig. 40. ISFET sensitivity analysis curve with $I_D = 2.56027\mu A$.

[5]Chapter 7

Future work and concluding remarks

7.1 Elementary work

Throughout this thesis, we have provided a theoretical analysis of the distances of the elongated hot spots in several nitride based heterostructures using our thickness optimization method by incorporating a QW in the hot spot region to cause the production of high-velocity interface phonons that travel along the heterointerface and emit heat carrying acoustic phonons over an elongated region causing reduction in the hot spot temperature. Experimental and related diagnostics procedures require the fabrication of quantum wells in the channel of a select-group of III-V nitride transistor channels, the creation of Ohmic contacts and performing Raman measurements to detect the frequency peaks for the generated optical phonons. To generate the interface phonons useful for heat removal, the experiment needs to probe in-plane distribution of hot spot region which might involve using optothermal or electrical technique to measure in-plane phonon dynamics.

Two samples (Sample 1 and Sample 2) of GaN/AlN superlattice used for this study were epitaxially grown on sapphire substrates. First, the samples were cut with a diamond scriber, the substrate then was diced and cleaned with acetone, Isopropyl Alcohol (IPA)/deionized (DI) water. Sample 1 was unetched whereas Sample 2 was etched by applying reactive ion etching (RIE) technique. For both samples, series positive

[5] The author would like to thank Bo Hsu and Sidra Farid with the Nanoengineering Research Laboratory at the University of Illinois at Chicago for their efforts in fabricating the samples discussed in this chapter.

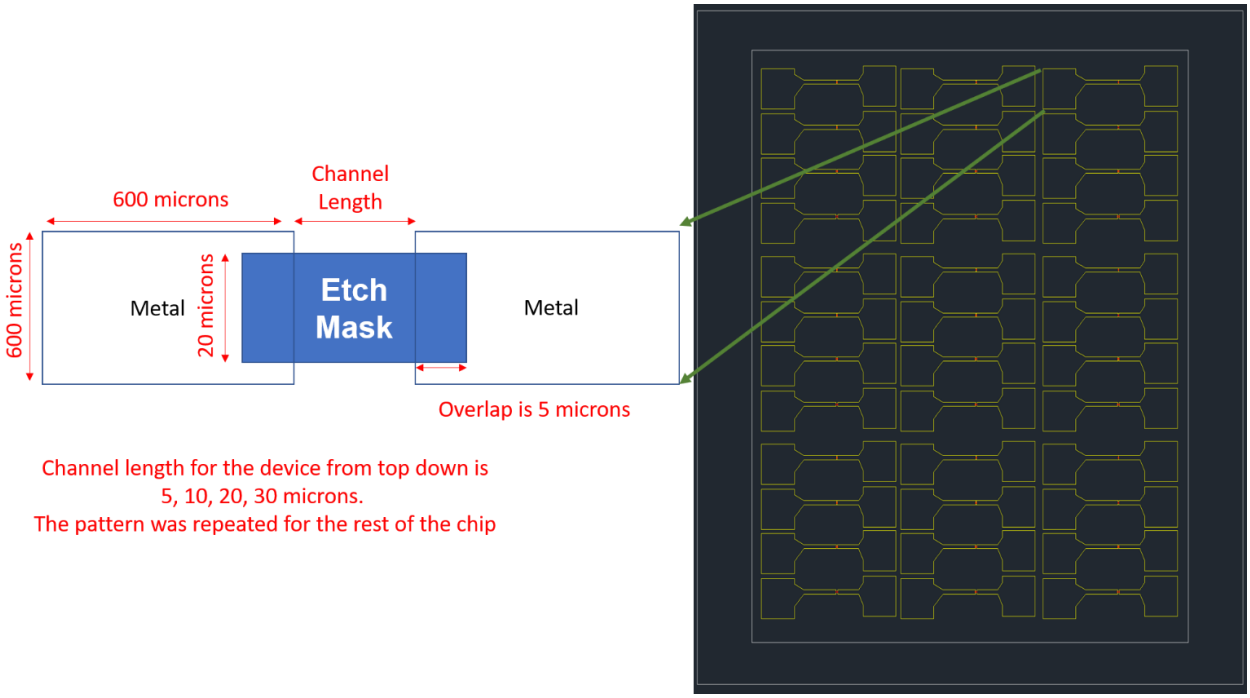

Fig. 41. Schematic of a 1 cm GaN/AlN superlattice chip. The pattern on the right is drawn using AUTOCAD.

---

photoresist (S1811) system was applied with a spin coating uniformity of 3000 rpm for 30 seconds with soft bake done at 115 ^{o}C for 60 seconds.

For Sample 2, the etchers are load lock equipped, high vacuum chambers with an etch process pressure of 240mTorr. Gas mixtures of $H_2/CH_4/Cl_2$ with a mixing ratio of 5/10/30 was developed at 100W power. It appears that the sample is difficult to etch with reactive plasma than other common materials in IC technology. While the RIE recipe with Pure Cl_2 was also tested on a different substrate, the etch rate remains low and not measurable by profilometer. If the process parameters are not proper, their etching rates might be lower than those of mask materials used for etching; therefore, the low volatility of the etchants produce low etching rates, gradual sidewall slopes of the etched samples and accumulation of residues on the etched structures [312].

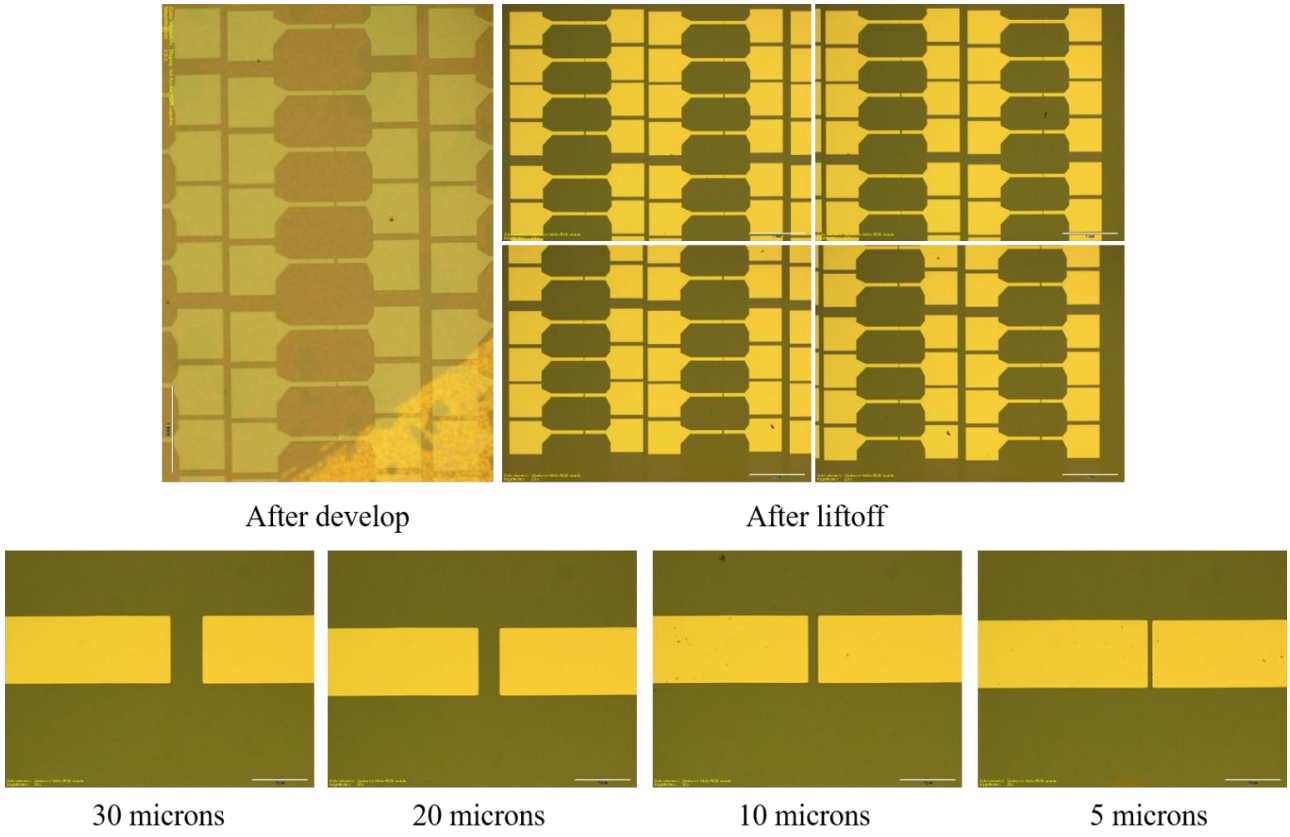

Fig. 42. Optical microscope images for Sample 2 (taken by Bo Hsu).

In the film deposition process, the solution of ZnO nanoparticles was drawn with a syringe and applied on top of the device substrate through a 0.2 μm pore size PTFE membrane syringe filter. This solution was spin-cast at 2000 rpm for 30 seconds, and the substrate was annealed on a hot plate at 825^{o}C for 30 seconds to obtain Ohmic contact.

Etch mask patterning for Sample 2 was generated using Laser writer LW405 system with lens 4 used or focusing. For beam control, we use 3% filter and beam gain of 7.8 while a proper D-step value is set to 2. The same settings were used for contact pattering samples 1 and 2. Both samples were developed using 351 developer for 30 seconds and then inspected. After development, the mask plates were rinsed in DI water to ensure that no solution is remaining.

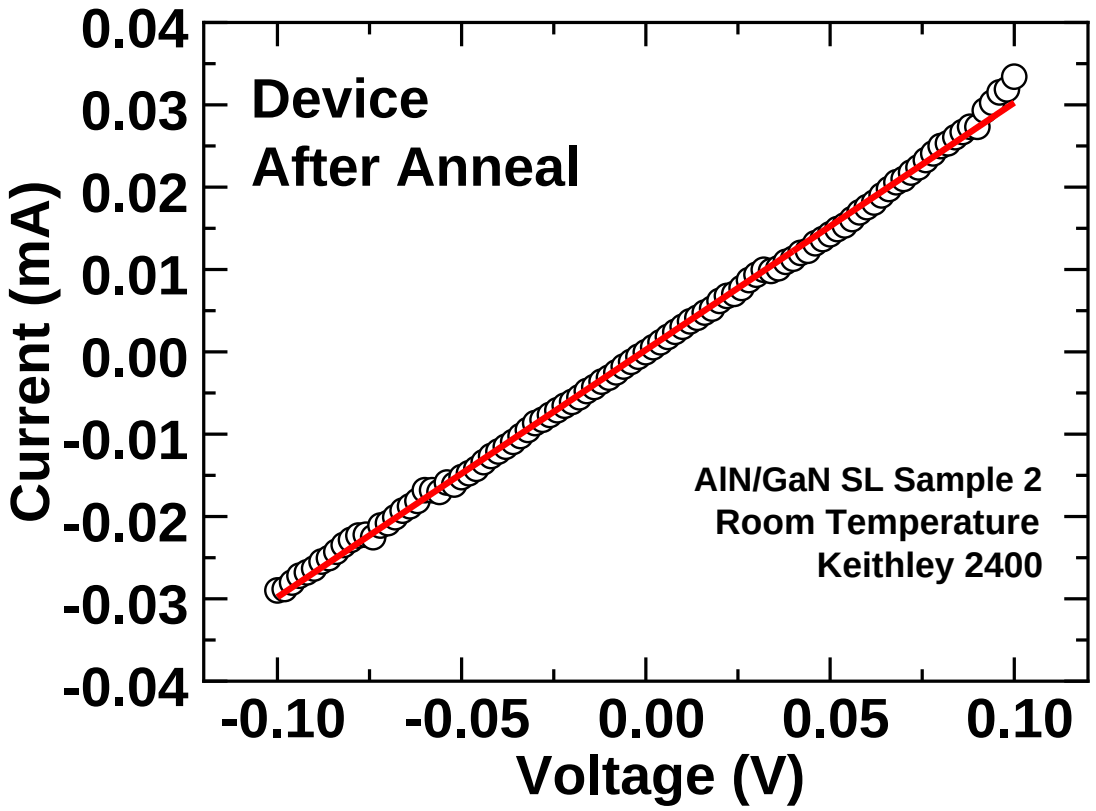

Fig. 43. I–V Characteristics of Sample 2 after thermal anneal (plotted by Bo Hsu).

Sample 2 was immersed in Nanostrip solution (H_2SO_4 + H_2O_2) for 60 seconds. The thinned PI precursor was spin-coated on top of an assembled QD-LED device at 3000 rpm for 30 seconds. Using the patterned photoresist as an etching mask, the layer was etched with plasma reactive ion etching with 100 W and process pressure of 170mTorr for 60 seconds. Samples 1 and 2 were selectively etched by reactive ion etching with Ti/Al/Au for making electrical contacts to the metal electrodes. Ti/Al/Au with a flow rate of Ti 1Å/s, Al 1.5Å/s, Au 1Å/s and RF power of 100 W for 10 min. The masking photoresist layer was subsequently removed by acetone rinsing. This metal deposition process was carried out by electron beam evaporator for both samples.

Finally, the substrate of sample 2 was annealed via rapid thermal annealing process in a vacuum oven at 200 °C for 1.5 h.

7.2 Future outlook

The theories discussed and the results obtained in this thesis require further development and experimental support. Many challenges mainly represented in realizing the proposed structures primarily in chapters 3 and 5. Herein, we discuss examples of unresolved issues and recommendations for future directions as follows:

- A promising future direction is to design and order a GaN FET-like structure and study the impact of changing the gate voltage on the device performance by fabricating samples with different gate lengths. Moreover, etching the substrate of the sample more accurately may considerably help with the Raman signals, since it has been a very likely scenario that the laser would only detect the sapphire signals and not the superlattice signals.
- The influence of an electric field on the scattering phenomena is not studied sufficiently. For further research, we need not only precise results of numerical calculations for energy dependence, but also detailed results of field dependence of the scattering rate.
- The transport of optical phonon modes and the decay channel is a particularly interesting field since the LO phonon decay mechanism is proving to be a rather complex problem. Because the Joule heat can only be removed by acoustic phonons, the acoustic phonons must be involved in the process and in the phonon decay mechanisms. Considering energy conservation alone allows the conversion of an LO phonon into four acoustic phonons, but this process is unlikely as five particles must partake in this event. Other phonon conversion schemes such as LO into TO + TA/LA do not seem to explain fully the experimentally observed dependence of the hot phonon decay/lifetime on the electron

density. Screening of the conversion potential by electrons would lead to an increase in the lifetime with increasing electron density, which disagrees with the experimental observations. Rather, the data show the hot phonon lifetime to be decreasing with electron concentration as suggested by electron-assisted decay process of LO phonons into acoustic phonons. The obvious conclusion is that more refined investigations are needed to clarify the hot phonon decay channels involved in the LO phonon decay channels.

- A potential future direction is a detailed study of the different mismatch models since the interface between dissimilar materials, densities and sound speeds result in a mismatch in the acoustic impedances. Such models include the acoustic mismatch model (AMM) and the diffuse mismatch model (DMM). As pointed out by Brendel et al. (2017) [313] and Kazan (2011) [314], these models do not work very well. In practice, people mix both models but that is subject to uncertainties about how much scattering is spectral (AMM) and how much is diffuse (DMM). If we focus on high quality interfaces like GaN-AlGaN and GaN quantum dots on AlN, that are free of misfit dislocations, the scattering of heat-carrying acoustic phonons is mostly spectral and it is easy to arrange for most of the scatter phonons to be scattered into the forward direction; that is, we have low thermal boundary resistance. However, if we have a likely rough surface like GaN-SiC, we expect diffuse scattering in many directions, which enhances the probability of backscattering that corresponds to unwanted high thermal boundary resistance.
- To the best of our knowledge, the growth of a high-quality GaN/AlN superlattice remains an outstanding question.

7.3 Concluding remarks

III-nitride semiconductors are technologically important materials and as a result of their large bandgap energies, they are suitable for the optoelectronic intersubband devices ranging from the ultraviolet to the

near infrared. Nowadays, they are widely used, for instance in lighting applications, including GaN-based white light emitting diodes or in blue-ray players, which rely on GaN-based laser diodes. They can also endure high electric power densities and high breakdown voltages, which makes them materials of interest for high-power, high-frequency electronics applications. The purpose of this research has been to exploit the potential of group-III nitrides AlN, GaN, InN and their alloys for applications in the electronic and optoelectronic device technology and characterize their structural and mechanical properties.

We started this thesis by going through the developments in theory, experiments and computations that have occurred in the past few years and summarizing the current status and the challenges of the field. We verified, throughout this thesis, that phonon interactions are tailored by the effects of dimensional quantum confinement on the phonon modes in the nanostructure. The thesis also provided a review for the mechanism of anharmonic decay of optical phonons in different systems, since phonon decay is pertinent from a thermal perspective as devices must efficiently dissipate heat to maintain operating temperatures.

We emphasized thermal transport in nanostructures, in which heat is transported by electron-phonon carrier relaxation. The innovative generation and use of propagating heat-creating interface phonons emitted by hot electrons in wurtzite nitride materials is exploited to elongate the unwanted hot spot region thereby reducing the temperature of the hot spot. Therefore, we have developed a numerical model to calculate the rates for interface optical phonon emission from hot electrons and have applied these results to model the dimensional elongation of hot spots in binary and ternary electron device structures. The results show that the use of a thin layer as a well in HEMT structures of facilitates the reduction of hot spot temperatures in different useful electronic and optoelectronic devices. To effectively dissipate this energy, optical phonon modes must decay into acoustic modes with a high group velocity at a rate appropriate with the Joule energy supplied to the structure. Lack of necessary fast phonon transformations

leads to temperature increase in the device, leading to subsequent prolonged overheating which leads to reductions in performance and reliability.

Finally, the thesis concluded by providing a detailed investigation of acoustic phonon modes in a grounded thin conducting film. Within the context of the elastic continuum model, the BG modes were analytically analyzed in nanoscale SAW devices in terms of phonons.

Bibliography

[1] H. J. Welker, "Discovery and development of III-V compounds," in *IEEE Transactions on Electron Devices*, vol. 23, no. 7, pp. 664-674, July 1976, doi: 10.1109/T-ED.1976.18471.

[2] Kasap S, Capper P, editors. Springer handbook of electronic and photonic materials. Springer; 2017 Oct 4.

[3] Tsao JY, Chowdhury S, Hollis MA, Jena D, Johnson NM, Jones KA, Kaplar RJ, Rajan S, Van de Walle CG, Bellotti E, Chua CL. Ultrawide-Bandgap Semiconductors: Research Opportunities and Challenges. Advanced Electronic Materials. 2018 Jan;4(1):1600501.

[4] Reiss P, Carriere M, Lincheneau C, Vaure L, Tamang S. Synthesis of semiconductor nanocrystals, focusing on nontoxic and earth-abundant materials. Chemical reviews. 2016 Sep 28;116(18):10731-819.

[5] Liu W, Chang AY, Schaller RD, Talapin DV. Colloidal insb nanocrystals. Journal of the American Chemical Society. 2012 Dec 19;134(50):20258-61.

[6] Shur M. Compound semiconductor electronics: the age of maturity. World Scientific; 1996.

[7] Adachi S. Physical properties of III-V semiconductor compounds. John Wiley & Sons; 1992 Nov 10.

[8] Prasad S. High-frequency compound SC devices. Materials Today. 2009 Apr 1;12(4):34-7.

[9] Hu C. Modern semiconductor devices for integrated circuits. Upper Saddle River, New Jersey: Prentice Hall; 2010.

[10] Butcher PN, Fawcett W. Calculation of the velocity-field characteristic for gallium arsenide. Physics Letters. 1966 Jun 15;21(5):489-90.

[11] Dayeh SA. Electron transport in indium arsenide nanowires. Semiconductor Science and Technology. 2010 Jan 22;25(2):024004.

[12] Neudeck PG, Okojie RS, Chen LY. High-temperature electronics-a role for wide bandgap semiconductors?. Proceedings of the IEEE. 2002 Nov 7;90(6):1065-76.

[13] Yonenaga I. Thermo-mechanical stability of wide-bandgap semiconductors: high temperature hardness of SiC, AlN, GaN, ZnO and ZnSe. Physica B: Condensed Matter. 2001 Dec 1;308:1150-2.

[14] Jackson KA. Compound semiconductor devices. Wiley-Vch; 2008.

[15] Puska MJ. Electronic structures of point defects in III-V compound semiconductors. Journal of Physics: Condensed Matter. 1989 Oct 9;1(40):7347.

[16] Li T, Mastro M, Dadgar A, editors. III–V compound semiconductors: integration with silicon-based microelectronics. CRC press; 2010 Dec 2.

[17] Abrahams MS, Ekstrom L. Dislocations and brittle fracture in elemental and compound semiconductors. Acta Metallurgica. 1960 Sep 1;8(9):654-62.

[18] Wu J, Walukiewicz W. Band gaps of InN and group III nitride alloys. Superlattices and Microstructures. 2003 Jul 1;34(1-2):63-75.

[19] Malinverni M, Lamy JM, Martin D, Lahourcade L, Feltin E, Dorsaz J, Castiglia A, Rossetti M, Duelk M, Vélez C, Grandjean N. InGaN laser diodes emitting at 500 nm with p-layers grown by molecular beam epitaxy. Applied Physics Express. 2015 Jan 26;8(2):022105.

[20] Cho HK, Lee J, Kim CS, Yang GM. Influence of strain relaxation on structural and optical characteristics of InGaN/GaN multiple quantum wells with high indium composition. Journal of applied physics. 2002 Feb 1;91(3):1166-70.

[21] Kim J, Kim H, Lee SN. Thermal degradation in InGaN quantum wells in violet and blue GaN-based laser diodes. Current Applied Physics. 2011 Jul 1;11(4):S167-70.

[22] Wen TC, Lee WI. Influence of barrier growth temperature on the properties of InGaN/GaN quantum well. Japanese Journal of Applied Physics. 2001 Sep;40(9R):5302.

[23] Kinoshita A, Hirayama H, Ainoya M, Aoyagi Y, Hirata A. Room-temperature operation at 333 nm of Al 0.03 Ga 0.97 N/Al 0.25 Ga 0.75 N quantum-well light-emitting diodes with Mg-doped superlattice layers. Applied Physics Letters. 2000 Jul 10;77(2):175-7.

[24] Nakamura S, Harada Y, Seno M. Novel metalorganic chemical vapor deposition system for GaN growth. Applied physics letters. 1991 May 6;58(18):2021-3.

[25] Semond F, Cordier Y, Grandjean N, Natali F, Damilano B, Vézian S, Massies J. Molecular Beam Epitaxy of Group-III Nitrides on Silicon Substrates: Growth, Properties and Device Applications. physica status solidi (a). 2001 Dec;188(2):501-10.

[26] Moustakas TD, Dismukes JP, Pearton SJ, editors. Proceedings of the First Symposium on III-V Nitride Materials and Processes. The Electrochemical Society.

[27] Hao Y, Zhang JF, Zhang JC. Nitride wide bandgap semiconductor material and electronic devices. CRC Press; 2016 Nov 3.

[28] Shur MS, Bykhovski AD, Gaska R. Pyroelectric and piezoelectric properties of GaN-based materials. MRS Online Proceedings Library Archive. 1998;537.

[29] Paskova T, Hanser DA, Evans KR. GaN substrates for III-nitride devices. Proceedings of the IEEE. 2009 Nov 24;98(7):1324-38.

[30] Flynn JS, Brandes GR, Vaudo RP, Keogh DM, Xu X, Landini BE, inventors; Cree Inc, assignee. III-V nitride homoepitaxial material of improved quality formed on free-standing (Al, In, Ga) N substrates. United States patent US 8,212,259. 2012 Jul 3.

[31] Zakutayev A. Design of nitride semiconductors for solar energy conversion. Journal of Materials Chemistry A. 2016;4(18):6742-54.

[32] Cardona M, Ehrenfreund E, Güntherodt G, Kash JA, von der Osten W, Page JB, Ramdas AK, Rodriguez S, Thomsen C, Tsang JC, Yacoby Y. Light scattering in solids VI: recent results, including high-Tc superconductivity. Springer Science & Business Media; 2006 Jan 21.

[33] Kim H, Thompson RM, Tilak V, Prunty TR, Shealy JR, Eastman LF. Effects of SiN passivation and high-electric field on AlGaN-GaN HFET degradation. IEEE Electron device letters. 2003 Aug 4;24(7):421-3.

[34] Chattopadhyay MK, Tokekar S. Thermal model for dc characteristics of algan/gan hemts including self-heating effect and non-linear polarization. Microelectronics Journal. 2008 Oct 1;39(10):1181-8.

[35] Wang XD, Hu WD, Chen XS, Lu W. The study of self-heating and hot-electron effects for AlGaN/GaN double-channel HEMTs. IEEE Transactions on Electron Devices. 2012 Mar 15;59(5):1393-401.

[36] Mohanty SK, Chen YY, Yeh PH, Horng RH. thermal Management of Gan-on-Si High electron Mobility transistor by copper filled Micro-trench Structure. Scientific Reports. 2019 Dec 23;9(1):1-9.

[37] Bagnall KR. *Device-level thermal analysis of GaN-based electronics* (Doctoral dissertation, Massachusetts Institute of Technology).

[38] Chung S, Lee JH, Jeong J, Kim JJ, Hong Y. Substrate thermal conductivity effect on heat dissipation and lifetime improvement of organic light-emitting diodes. Applied Physics Letters. 2009 Jun 22;94(25):168.

[39] Cho J, Li Z, Bozorg-Grayeli E, Kodama T, Francis D, Ejeckam F, Faili F, Asheghi M, Goodson KE. Improved thermal interfaces of GaN–diamond composite substrates for HEMT applications. IEEE Transactions on Components, Packaging and Manufacturing Technology. 2012 Dec 10;3(1):79-85.

[40] Sun J, Fatima H, Koudymov A, Chitnis A, Hu X, Wang HM, Zhang J, Simin G, Yang J, Khan MA. Thermal management of AlGaN-GaN HFETs on sapphire using flip-chip bonding with epoxy underfill. IEEE Electron Device Letters. 2003 Jul 22;24(6):375-7.

[41] Hiroki M, Kumakura K, Kobayashi Y, Akasaka T, Makimoto T, Yamamoto H. Suppression of self-heating effect in AlGaN/GaN high electron mobility transistors by substrate-transfer technology using h-BN. Applied Physics Letters. 2014 Nov 10;105(19):193509.

[42] Tadjer MJ, Anderson TJ, Hobart KD, Feygelson TI, Caldwell JD, Eddy CR, Kub FJ, Butler JE, Pate B, Melngailis J. Reduced self-heating in AlGaN/GaN HEMTs using nanocrystalline diamond heat-spreading films. IEEE electron device letters. 2011 Nov 16;33(1):23-5.

[43] Sadi T, Kelsall RW. Hot-phonon effect on the electrothermal behavior of submicrometer III-V HEMTs. IEEE electron device letters. 2007 Aug 27;28(9):787-9.

[44] Sadi T, Kelsall R, Pilgrim N. Simulation of electron transport in InGaAs/AlGaAs HEMTs using an electrothermal Monte Carlo method. IEEE transactions on electron devices. 2006 Jul 24;53(8):1768-74.

[45] Nuttinck S, Gebara E, Laskar J, Harris HM. Study of self-heating effects, temperature-dependent modeling, and pulsed load-pull measurements on GaN HEMTs. IEEE Transactions on Microwave Theory and Techniques. 2001 Dec;49(12):2413-20.

[46] Born M, Huang K. Dynamical theory of crystal lattices. Clarendon press; 1954.

[47] Mazumder S, Majumdar A. Monte Carlo study of phonon transport in solid thin films including dispersion and polarization. J. Heat Transfer. 2001 Aug 1;123(4):749-59.

[48] Harper PG, Hodby JW, Stradling RA. Electrons and optic phonons in solids-the effects of longitudinal optical lattice vibrations on the electronic excitations of solids. Reports on Progress in Physics. 1973 Jan;36(1):1.

[49] Heller E, Choi S, Dorsey D, Vetury R, Graham S. Electrical and structural dependence of operating temperature of AlGaN/GaN HEMTs. Microelectronics Reliability. 2013 Jun 1;53(6):872-7.

[50] Ridley BK. The LO phonon lifetime in GaN. Journal of Physics: Condensed Matter. 1996 Sep 9;8(37):L511.

[51] Shah J, Leite RC, Scott JF. Photoexcited hot LO phonons in GaAs. Solid State Communications. 1970 Jul 15;8(14):1089-93.

[52] Barman S, Srivastava GP. Long-wavelength nonequilibrium optical phonon dynamics in cubic and hexagonal semiconductors. Physical Review B. 2004 Jun 30;69(23):235208.

[53] Sikula J, Levinshtein M, editors. Advanced experimental methods for noise research in nanoscale electronic devices. Springer Science & Business Media; 2006 Feb 21.

[54] Vallabhaneni AK, Gupta MP, Kumar S. Thermal transport in high electron mobility transistors: A Boltzmann transport equation study. In2017 16th IEEE Intersociety Conference on Thermal and Thermomechanical Phenomena in Electronic Systems (ITherm) 2017 May 30 (pp. 128-134). IEEE.

[55] Hiroki M, Kumakura K, Kobayashi Y, Akasaka T, Makimoto T, Yamamoto H. Suppression of self-heating effect in AlGaN/GaN high electron mobility transistors by substrate-transfer technology using h-BN. Applied Physics Letters. 2014 Nov 10;105(19):193509.

[56] Hao Q, Zhao H, Xiao Y, Kronenfeld MB. Electrothermal studies of GaN-based high electron mobility transistors with improved thermal designs. International Journal of Heat and Mass Transfer. 2018 Jan 1;116:496-506.

[57] Matulionis A, Morkoç H. Hot phonons in InAlN/AlN/GaN heterostructure 2DEG channels. InGallium Nitride Materials and Devices IV 2009 Feb 18 (Vol. 7216, p. 721608). International Society for Optics and Photonics.

[58] Pérez JA. *Thermal Study of a GaN-based HEMT* (Doctoral dissertation, University of Notre Dame).

[59] Harris HM, Laskar J, Nuttinck S. Engineering support for high power density gallium nitride microwave transistors. GEORGIA INST OF TECH ATLANTA; 2001 Dec 31.

[60] Turin VO, Balandin AA. Electrothermal simulation of the self-heating effects in GaN-based field-effect transistors. Journal of Applied Physics. 2006 Sep 1;100(5):054501.

[61] Olsson J. Self-heating effects in SOI bipolar transistors. Microelectronic engineering. 2001 Aug 1;56(3-4):339-52.

[62] Gaska R, Osinsky A, Yang JW, Shur MS. Self-heating in high-power AlGaN-GaN HFETs. IEEE Electron Device Letters. 1998 Mar;19(3):89-91.

[63] Shi L, Li D, Yu C, Jang W, Kim D, Yao Z, Kim P, Majumdar A. Measuring thermal and thermoelectric properties of one-dimensional nanostructures using a microfabricated device. J. Heat Transfer. 2003 Oct 1;125(5):881-8.

[64] Shi L. Thermal and thermoelectric transport in nanostructures and low-dimensional systems. Nanoscale and Microscale Thermophysical Engineering. 2012 Apr 1;16(2):79-116.

[65] Koh YK, Cao Y, Cahill DG, Jena D. Heat-Transport Mechanisms in Superlattices. Advanced Functional Materials. 2009 Feb 24;19(4):610-5.

[66] Capinski WS, Maris HJ. Thermal conductivity of GaAs/AlAs superlattices. Physica B: Condensed Matter. 1996 Apr 1;219:699-701.

[67] Huxtable ST. *Heat transport in superlattices and nanowire arrays* (Doctoral dissertation, University of California, Berkeley).

[68] Eastman JA, Phillpot SR, Choi SU, Keblinski P. Thermal transport in nanofluids. Annu. Rev. Mater. Res.. 2004 Aug 4;34:219-46.

[69] Rzepka S, Banerjee K, Meusel E, Hu C. Characterization of self-heating in advanced VLSI interconnect lines based on thermal finite element simulation. IEEE Transactions on Components, Packaging, and Manufacturing Technology: Part A. 1998 Sep;21(3):406-11.

[70] Levinshtein ME, Ivanov PA, Mnatsakanov TT, Palmour JW, Das MK, Hull BA. Self-heating and destruction of high-voltage 4H-SiC rectifier diodes under a single short current surge pulse. Solid-state electronics. 2008 Nov 1;52(11):1802-5.

[71] Dowling KM, Alpert HS, Zhang P, Ramirez AN, Yalamathy AS, Köck H, Ausserlechner U, Senesky DG. The effect of bias conditions on AlGaN/GaN 2DEG Hall plates. InProc. Solid-State Sens. Actuators Microsyst. Workshop 2018 Jun (pp. 194-197).

[72] Challis L, Challis LJ, editors. Electron-Phonon Interactions in Low-Dimensional Structures. Oxford University Press on Demand; 2003.

[73] Pop E. *Self-heating and scaling of thin body transistors* (Doctoral dissertation, stanford university).

[74] Fuchs R, Kliewer KL. Optical modes of vibration in an ionic crystal slab. Physical Review. 1965 Dec 13;140(6A):A2076.

[75] Kliewer KL, Fuchs R. Optical modes of vibration in an ionic crystal slab including retardation. I. Nonradiative region. Physical Review. 1966 Apr 15;144(2):495.

[76] Kliewer KL, Fuchs R. Optical modes of vibration in an ionic crystal slab including retardation. II. Radiative region. Physical Review. 1966 Oct 14;150(2):573.

[77] Kim KW, Stroscio MA. Electron-optical-phonon interaction in binary/ternary heterostructures. Journal of applied physics. 1990 Dec 15;68(12):6289-92.

[78] Dutta M, Stroscio MA. Quantum-based electronic devices and systems. World Scientific; 1998.

[79] Dutta M, Stroscio MA. Advances in semiconductor lasers and applications to optoelectronics. World Scientific; 2000.

[80] Stroscio MA, Dutta M. Phonons in nanostructures. Cambridge University Press; 2001 Aug 23.

[81] Lee BC, Kim KW, Stroscio MA, Dutta M. Optical-phonon confinement and scattering in wurtzite heterostructures. Physical review B. 1998 Aug 15;58(8):4860.

[82] Willatzen M, Voon LC, Gandi AN, Schwingenschlögl U. 3D continuum phonon model for group-IV 2D materials. Beilstein journal of nanotechnology. 2017 Jun 30;8(1):1345-56.

[83] Shindé SL, Srivastava GP, editors. Length-scale dependent phonon interactions. NY: Springer; 2014.

[84] Plekhanov VG. Introduction to Isotopic Materials Science. Springer; 2018 Dec 5.

[85] Pawlik PS, Reisman H. Elasticity: theory and applications. Wiley; 1980.

[86] Haussühl S. MICROSCOPIC AND MACROSCOPIC PROPERTIES OF SOLIDS. In Assessment of Safety and Risk with a Microscopic Model of Detonation 2003 Jan 1 (pp. 493-554). Elsevier Science.

[87] Simon SH. The Oxford solid state basics. OUP Oxford; 2013 Jun 21.

[88] Wang S, Dou Y, Liu H, Lin Z, Zhang H. Electron Momentum and Energy Relaxation Times in Wurtzite GaN, InN and AlN: A Monte Carlo Study. Journal of Electronic Materials. 2018 Feb 1;47(2):1560-8.

[89] Böer KW, Pohl UW. Semiconductor physics. Springer; 2018.

[90] Ferry DK. High-field transport in wide-band-gap semiconductors. Physical Review B. 1975 Sep 15;12(6):2361.

[91] Bulutay C, Ridley BK, Zakhleniuk NA. Electron momentum and energy relaxation rates in GaN and AlN in the high-field transport regime. Physical Review B. 2003 Sep 26;68(11):115205.

[92] Reik HG, Risken H, Finger G. Theory of hot-electron effects in many-valley semiconductors in the region of high electric field. Physical Review Letters. 1960 Nov 1;5(9):423.

[93] Jungemann C, Emunds A, Engl WL. Simulation of linear and nonlinear electron transport in homogeneous silicon inversion layers. Solid-state electronics. 1993 Nov 1;36(11):1529-40.

[94] Wang S, Wu Z, Haifeng Z, Duan X, Han C, Wei Y, Liu H. Comparison the electron momentum and energy relaxation process in wurtzite GaN, InN and AlN by Monte Carlo method. Solid State Communications. 2019 Feb 1;288:68-73.

[95] Balkan N, Arikan MC, Gokden S, Tilak V, Schaff B, Shealy RJ. Energy and momentum relaxation of hot electrons in GaN/AlGaN. Journal of Physics: Condensed Matter. 2002 Mar 22;14(13):3457.

[96] Patane A, Balkan N, editors. Semiconductor Research: Experimental Techniques. Springer Science & Business Media; 2012 Apr 12.

[97] Chen C, Dutta M, Stroscio MA. Electron scattering via interactions with optical phonons in wurtzite crystals. Physical Review B. 2004 Aug 31;70(7):075316.

[98] Datta D, Krishnababu K, Stroscio MA, Dutta M. Effect of quantum confinement on lifetime of anharmonic decay of optical phonons in semiconductor nanostructures. Journal of Physics: Condensed Matter. 2018 Aug 7;30(35):355302.

[99] Lyon SA. Spectroscopy of hot carriers in semiconductors. Journal of luminescence. 1986 Jun 1;35(3):121-54.

[100] Shank CV, Zakharchenya BP, editors. Spectroscopy of nonequilibrium electrons and phonons. Elsevier; 2012 Dec 2.

[101] Leitenstorfer A, Laubereau A. Ultrafast electron—Phonon interactions in semiconductors: Quantum kinetic memory effects. InSemiconductors and Semimetals 2001 Jan 1 (Vol. 67, pp. 1-37). Elsevier.

[102] Dyson A, Ridley BK. Phonon-plasmon coupled-mode lifetime in semiconductors. Journal of Applied Physics. 2008 Jun 1;103(11):114507.

[103] Baroni S, De Gironcoli S, Dal Corso A, Giannozzi P. Phonons and related crystal properties from density-functional perturbation theory. Reviews of Modern Physics. 2001 Jul 6;73(2):515.

[104] Morkoç H. Handbook of nitride semiconductors and devices, Materials Properties, Physics and Growth. John Wiley & Sons; 2009 Jul 30.

[105] Davydov VY, Kitaev YE, Goncharuk IN, Smirnov AN, Graul J, Semchinova O, Uffmann D, Smirnov MB, Mirgorodsky AP, Evarestov RA. Phonon dispersion and Raman scattering in hexagonal GaN and AlN. Physical Review B. 1998 Nov 15;58(19):12899.

[106] Kaczmarczyk G, Kaschner A, Reich S, Hoffmann A, Thomsen C, As DJ, Lima AP, Schikora D, Lischka K, Averbeck R, Riechert H. Lattice dynamics of hexagonal and cubic InN: Raman-scattering experiments and calculations. Applied Physics Letters. 2000 Apr 10;76(15):2122-4.

[107] Lei X, Liang XX, Zhao GJ, Song TL. First-principle studies of the electronic band structure and the phonon dispersion properties of wurtzite BN. InJournal of Physics: Conference Series 2014 (Vol. 490, No. 1, p. 012171). IOP Publishing.

[108] Ridley BK. Electrons and phonons in semiconductor multilayers. Cambridge University Press; 2009 Apr 30.

[109] Pomeroy JW, Kuball M, Lu H, Schaff WJ, Wang X, Yoshikawa A. Phonon lifetimes and phonon decay in InN. Applied Physics Letters. 2005 May 30;86(22):223501.

[110] Bergman L, Alexson D, Murphy PL, Nemanich RJ, Dutta M, Stroscio MA, Balkas C, Shin H, Davis RF. Raman analysis of phonon lifetimes in AlN and GaN of wurtzite structure. Physical Review B. 1999 May 15;59(20):12977.

[111] Song DY, Nikishin SA, Holtz M, Soukhoveev V, Usikov A, Dmitriev V. Decay of zone-center phonons in GaN with A 1, E 1, and E 2 symmetries. Journal of Applied Physics. 2007 Mar 1;101(5):053535.

[112] Pandit P, Song DY, Holtz M. Decay of zone-center phonons in AlN with A 1, E 1, and E 2 symmetries. Journal of Applied Physics. 2007 Dec 1;102(11):113510.

[113] Cuscó R, Domènech-Amador N, Novikov S, Foxon CT, Artús L. Anharmonic phonon decay in cubic GaN. Physical Review B. 2015 Aug 21;92(7):075206.

[114] Ridley BK. Hybrid phonons in nanostructures. Oxford University Press; 2017 Mar 9.

[115] Tsen KT, Ferry DK, Botchkarev A, Sverdlov B, Salvador A, Morkoc H. Time-resolved Raman studies of the decay of the longitudinal optical phonons in wurtzite GaN. Applied physics letters. 1998 Apr 27;72(17):2132-4.

[116] Tsen KT, Kiang JG, Ferry DK, Morkoç H. Subpicosecond time-resolved Raman studies of LO phonons in GaN: Dependence on photoexcited carrier density. Applied physics letters. 2006 Sep 11;89(11):112111.

[117] Liu MS, Bursill LA, Prawer S, Nugent KW, Tong YZ, Zhang GY. Temperature dependence of Raman scattering in single crystal GaN films. Applied Physics Letters. 1999 May 24;74(21):3125-7.

[118] Kuball M, Demangeot F, Frandon J, Renucci MA, Grandjean N, Briot O. Thermal stability of GaN investigated by Raman scattering. MRS Online Proceedings Library Archive. 1998;537.

[119] Azuhata T, Sota T, Suzuki K, Nakamura S. Polarized raman spectra in GaN. Journal of Physics: Condensed Matter. 1995 Mar 6;7(10):L129.

[120] Klemens PG. Anharmonic decay of optical phonons. Physical Review. 1966 Aug 12;148(2):845.

[121] Robins LH, Horneber E, Sanford NA, Bertness KA, Brubaker MD, Schlager JB. Raman spectroscopy based measurements of carrier concentration in n-type GaN nanowires grown by plasma-assisted molecular beam epitaxy. Journal of Applied Physics. 2016 Sep 28;120(12):124313.

[122] Baroni S, Giannozzi P, Testa A. Green's-function approach to linear response in solids. Physical review letters. 1987 May 4;58(18):1861.

[123] Debernardi A, Baroni S, Molinari E. Anharmonic phonon lifetimes in semiconductors from density-functional perturbation theory. Physical review letters. 1995 Aug 28;75(9):1819.

[124] Debernardi A. Phonon linewidth in III-V semiconductors from density-functional perturbation theory. Physical Review B. 1998 May 15;57(20):12847.

[125] Lewis IR, Edwards H. Handbook of Raman spectroscopy: from the research laboratory to the process line. CRC press; 2001 Aug 8.

[126] Kuball M. Raman spectroscopy of GaN, AlGaN and AlN for process and growth monitoring/control. Surface and Interface Analysis: An International Journal devoted to the development and application of techniques for the analysis of surfaces, interfaces and thin films. 2001 Oct;31(10):987-99.

[127] Li WS, Shen ZX, Feng ZC, Chua SJ. Temperature dependence of Raman scattering in hexagonal gallium nitride films. Journal of Applied Physics. 2000 Apr 1;87(7):3332-7.

[128] Link A, Bitzer K, Limmer W, Sauer R, Kirchner C, Schwegler V, Kamp M, Ebling DG, Benz KW. Temperature dependence of the E 2 and A 1 (LO) phonons in GaN and AlN. Journal of applied physics. 1999 Dec 1;86(11):6256-60.

[129] Srivastava GP. The physics of phonons. Routledge; 2019 Jul 16.

[130] Ruf T, Serrano J, Cardona M, Pavone P, Pabst M, Krisch M, D'astuto M, Suski T, Grzegory I, Leszczynski M. Phonon dispersion curves in wurtzite-structure GaN determined by inelastic x-ray scattering. Physical review letters. 2001 Jan 29;86(5):906.

[131] Beechem T, Graham S. Temperature and doping dependence of phonon lifetimes and decay pathways in GaN. Journal of Applied Physics. 2008 May 1;103(9):093507.

[132] Kuball M, Hayes JM, Shi Y, Edgar JH. Phonon lifetimes and decay channels in single-crystalline bulk AlN. InUltrafast Phenomena in Semiconductors V 2001 Apr 23 (Vol. 4280, pp. 78-88). International Society for Optics and Photonics.

[133] Harima H. Properties of GaN and related compounds studied by means of Raman scattering. Journal of Physics: Condensed Matter. 2002 Sep 12;14(38):R967.

[134] Williamson TL, Díaz DJ, Bohn PW, Molnar RJ. Structure–property relationships in porous GaN generated by Pt-assisted electroless etching studied by Raman spectroscopy. Journal of Vacuum Science & Technology B: Microelectronics and Nanometer Structures Processing, Measurement, and Phenomena. 2004 May 26;22(3):925-31.

[135] Bovensiepen U, Petek H, Wolf M, editors. Dynamics at Solid State Surfaces and Interfaces. Wiley-VCH; 2010.

[136] Tamura SI. Spontaneous decay rates of LA phonons in quasi-isotropic solids. Physical Review B. 1985 Feb 15;31(4):2574.

[137] Herring C. Role of low-energy phonons in thermal conduction. Physical Review. 1954 Aug 15;95(4):954.

[138] Liu TM, Sun SZ, Chang CF, Pan CC, Chen GT, Chyi JI, Gusev V, Sun CK. Anharmonic decay of subterahertz coherent acoustic phonons in GaN. Applied physics letters. 2007 Jan 22;90(4):041902.

[139] Orbach R, Vredevoe LA. The Attenuation of high frequency phonons at low temperatures. Physics Physique Fizika. 1964 Sep 1;1(2):91.

[140] Park K, Mohamed A, Dutta M, Stroscio MA, Bayram C. Electron scattering via interface optical phonons with high group velocity in wurtzite GaN-based quantum well heterostructure. Scientific reports. 2018 Oct 29;8(1):1-0.

[141] Pozela J, Butkus G, Juciene V. Electron-optical phonon scattering rates in 2D structures: effects of independent electron and phonon confinement. Semiconductor science and technology. 1994 Aug;9(8):1480.

[142] Licari JJ, Evrard R. Electron-phonon interaction in a dielectric slab: Effect of the electronic polarizability. Physical Review B. 1977 Feb 15;15(4):2254.

[143] Bennett CR, Güven K, Tanatar B. Confined-phonon effects in the band-gap renormalization of semiconductor quantum wires. Physical Review B. 1998 Feb 15;57(7):3994.

[144] Yu S, Kim KW, Stroscio MA, Iafrate GJ, Ballato A. Electron–acoustic-phonon scattering rates in rectangular quantum wires. Physical Review B. 1994 Jul 15;50(3):1733.

[145] Bannov N, Aristov V, Mitin V, Stroscio MA. Electron relaxation times due to the deformation-potential interaction of electrons with confined acoustic phonons in a free-standing quantum well. Physical Review B. 1995 Apr 15;51(15):9930.

[146] Nishiguchi N. Resonant acoustic-phonon modes in a quantum wire. Physical Review B. 1995 Aug 15;52(7):5279.

[147] Svizhenko A, Balandin A, Bandyopadhyay S, Stroscio MA. Electron interaction with confined acoustic phonons in quantum wires subjected to a magnetic field. Physical Review B. 1998 Feb 15;57(8):4687.

[148] Jain JK, Sarma SD. Role of discrete slab phonons in carrier relaxation in semiconductor quantum wells. Physical review letters. 1989 May 8;62(19):2305.

[149] Ridley BK. Electron scattering by confined LO polar phonons in a quantum well. Physical Review B. 1989 Mar 15;39(8):5282.

[150] Rudin S, Reinecke TL. Electron–LO-phonon scattering rates in semiconductor quantum wells. Physical Review B. 1990 Apr 15;41(11):7713.

[151] Loudon R. The Raman effect in crystals. Advances in Physics. 1964 Oct 1;13(52):423-82.

[152] Lee BC, Kim KW, Dutta M, Stroscio MA. Electron–optical-phonon scattering in wurtzite crystals. Physical review B. 1997 Jul 15;56(3):997.

[153] Lee BC, Kim KW, Stroscio MA, Dutta M. Optical-phonon confinement and scattering in wurtzite heterostructures. Physical review B. 1998 Aug 15;58(8):4860.

[154] Komirenko SM. Phonons and phonon-related effects in prospective nanoscale semiconductor devices.

[155] Hayes W, Loudon R. Scattering of light by crystals. Courier Corporation; 2012 Dec 13.

[156] Komirenko SM, Kim KW, Stroscio MA, Dutta M. Energy-dependent electron scattering via interaction with optical phonons in wurtzite crystals and quantum wells. Physical Review B. 2000 Jan 15;61(3):2034.

[157] Schmidt MC, Kim KC, Farrell RM, Feezell DF, Cohen DA, Saito M, Fujito K, Speck JS, DenBaars SP, Nakamura S. Demonstration of nonpolar m-plane InGaN/GaN laser diodes. Japanese journal of applied physics. 2007 Feb 23;46(3L):L190.

[158] Mishra UK, Parikh P, Wu YF. AlGaN/GaN HEMTs-an overview of device operation and applications. Proceedings of the IEEE. 2002 Nov 7;90(6):1022-31.

[159] Mishra UK, Shen L, Kazior TE, Wu YF. GaN-based RF power devices and amplifiers. Proceedings of the IEEE. 2008 Jan 16;96(2):287-305.

[160] Ferry DK. Semiconductors. New York: Macmillan; 1991.

[161] Balandin AA, Pokatilov EP, Nika DL. Phonon engineering in hetero-and nanostructures. Journal of Nanoelectronics and Optoelectronics. 2007 Aug 1;2(2):140-70.

[162] Kim K, Lambrecht WR, Segall B. Elastic constants and related properties of tetrahedrally bonded BN, AlN, GaN, and InN. Physical Review B. 1996 Jun 15;53(24):16310.

[163] Gielisse PJ, Mitra SS, Plendl JN, Griffis RD, Mansur LC, Marshall R, Pascoe EA. Lattice infrared spectra of boron nitride and boron monophosphide. Physical Review. 1967 Mar 15;155(3):1039.

[164] Gadret EG, de Lima Jr MM, Madureira JR, Chiaramonte T, Cotta MA, Iikawa F, Cantarero A. Optical phonon modes of wurtzite InP. Applied Physics Letters. 2013 Mar 25;102(12):122101.

[165] Mukhopadhyay S, Stewart DA. First-principles study of the phonon dispersion and dielectric properties of wurtzite InP: Role of In 4 d electrons. Physical Review B. 2014 Feb 13;89(5):054302.

[166] Davydov VY, Emtsev VV, Goncharuk IN, Smirnov AN, Petrikov VD, Mamutin VV, Vekshin VA, Ivanov SV, Smirnov MB, Inushima T. Experimental and theoretical studies of phonons in hexagonal InN. Applied physics letters. 1999 Nov 22;75(21):3297-9.

[167] Edgar JH. Properties of group III nitrides. Institution of Electrical Engineers.

[168] Komirenko SM, Kim KW, Stroscio MA, Dutta M. Dispersion of polar optical phonons in wurtzite quantum wells. Physical Review B. 1999 Feb 15;59(7):5013.

[169] Nakamura S. Nobel Lecture: Background story of the invention of efficient blue InGaN light emitting diodes. Reviews of Modern Physics. 2015 Oct 5;87(4):1139.

[170] Nakamura S. Characteristics of InGaN multiquantum-well-structure laser diodes. MRS Online Proceedings Library Archive. 1996;449.

[171] Ridley BK. The electron-phonon interaction in quasi-two-dimensional semiconductor quantum-well structures. Journal of Physics C: Solid State Physics. 1982 Oct 10;15(28):5899.

[172] Teng HB, Sun JP, Haddad GI, Stroscio MA, Yu S, Kim KW. Phonon assisted intersubband transitions in step quantum well structures. Journal of applied physics. 1998 Aug 15;84(4):2155-64.

[173] Stroscio MA, Kim KW. Piezoelectric scattering of carriers from confined acoustic modes in cylindrical quantum wires. Physical Review B. 1993 Jul 15;48(3):1936.

[174] Stroscio MA. Interface-phonon-assisted transitions in quantum-well lasers. Journal of applied physics. 1996 Dec 15;80(12):6864-7.

[175] Moses PG, Van de Walle CG. Band bowing and band alignment in InGaN alloys. Applied Physics Letters. 2010 Jan 11;96(2):021908.

[176] Sirenko YM, Stroscio MA, Kim KW, Mitin V. Ballistic propagation of interface optical phonons. Physical Review B. 1995 Apr 15;51(15):9863.

[177] Wendler L. Electron–phonon interaction in dielectric bilayer systems. effect of the electronic polarizability. Physica status solidi (b). 1985 Jun 1;129(2):513-30.

[178] Kelekci O, Tasli P, Cetin SS, Kasap M, Ozcelik S, Ozbay E. Investigation of AlInN HEMT structures with different AlGaN buffer layers grown on sapphire substrates by MOCVD. Current Applied Physics. 2012 Nov 1;12(6):1600-5.

[179] Rahman S, Othman NA, Hatta SW, Soin N. Optimization of graded AlInN/AlN/GaN HEMT device performance based on quaternary back barrier for high power application. ECS Journal of Solid State Science and Technology. 2017 Jan 1;6(12):P805-12.

[180] Kuzmík J. Power electronics on InAlN/(In) GaN: Prospect for a record performance. IEEE Electron Device Letters. 2001 Nov;22(11):510-2.

[181] Hiroki M, Yokoyama H, Watanabe N, Kobayashi T. High-quality InAlN/GaN heterostructures grown by metal–organic vapor phase epitaxy. Superlattices and Microstructures. 2006 Oct 1;40(4-6):214-8.

[182] Park SH, Ahn D. Intraband Relaxation Time in Wurtzite GaN/InAlN Quantum-Well. Japanese journal of applied physics. 1999 Jul;38(7B):L815.

[183] Tan CK, Sun W, Borovac D, Tansu N. Large optical gain AlInN-delta-GaN quantum well for deep ultraviolet emitters. Scientific reports. 2016 Mar 10;6(1):1-7.

[184] Nicolay S, Carlin JF, Feltin E, Butté R, Mosca M, Grandjean N, Ilegems M, Tchernycheva M, Nevou L, Julien FH. Midinfrared intersubband absorption in lattice-matched Al In N⁄ Ga N multiple quantum wells. Applied Physics Letters. 2005 Sep 12;87(11):111106.

[185] Zhao S, Fathololoumi S, Bevan KH, Liu DP, Kibria MG, Li Q, Wang GT, Guo H, Mi Z. Tuning the surface charge properties of epitaxial InN nanowires. Nano letters. 2012 Jun 13;12(6):2877-82.

[186] Mohamed A, Park K, Bayram C, Dutta M, Stroscio M. Confined and interface optical phonon emission in GaN/InGaN double barrier quantum well heterostructures. PloS one. 2019;14(4).

[187] Henry AS, Chen G. Spectral phonon transport properties of silicon based on molecular dynamics simulations and lattice dynamics. Journal of Computational and Theoretical Nanoscience. 2008 Feb 1;5(2):141-52.

[188] Kuball M, Hayes JM, Shi Y, Edgar JH. Phonon lifetimes in bulk AlN and their temperature dependence. Applied Physics Letters. 2000 Sep 25;77(13):1958-60.

[189] Kazan M, Pereira S, Correia MR, Masri P. Contribution of the decay of optical phonons into acoustic phonons to the thermal conductivity of AlN. Physical Review B. 2008 May 9;77(18):180302.

[190] Tischler JG, Freitas Jr JA. Anharmonic decay of phonons in strain-free wurtzite AlN. Applied physics letters. 2004 Sep 13;85(11):1943-5.

[191] Gonschorek M, Carlin JF, Feltin E, Py MA, Grandjean N. Self heating in AlInN/AlN/GaN high power devices: Origin and impact on contact breakdown and IV characteristics. Journal of Applied Physics. 2011 Mar 15;109(6):063720.

[192] Collazo R, Dietz N. The group III-nitride material class: From preparation to perspectives in photoelectrocatalysis. RSC Publishing; 2013 Oct 2.

[193] Butté R, Carlin JF, Feltin E, Gonschorek M, Nicolay S, Christmann G, Simeonov D, Castiglia A, Dorsaz J, Buehlmann HJ, Christopoulos S. Current status of AlInN layers lattice-matched to GaN for photonics and electronics. Journal of Physics D: Applied Physics. 2007 Oct 5;40(20):6328.

[194] Minj A, Cavalcoli D, Cavallini A. Indium segregation in AlInN/AlN/GaN heterostructures. Applied Physics Letters. 2010 Sep 27;97(13):132114.

[195] Ben-Yaacov I, Seck YK, Mishra UK, DenBaars SP. AlGaN/GaN current aperture vertical electron transistors with regrown channels. Journal of applied physics. 2004 Feb 15;95(4):2073-8.

[196] Ambacher O, Majewski J, Miskys C, Link A, Hermann M, Eickhoff M, Stutzmann M, Bernardini F, Fiorentini V, Tilak V, Schaff B. Pyroelectric properties of Al (In) GaN/GaN hetero-and quantum well structures. Journal of physics: condensed matter. 2002 Mar 22;14(13):3399.

[197] Denton AR, Ashcroft NW. Vegard's law. Physical review A. 1991 Mar 1;43(6):3161.

[198] Oh TS, Kim JO, Jeong H, Lee YS, Nagarajan S, Lim KY, Hong CH, Suh EK. Growth and properties of Al-rich InxAl1− xN ternary alloy grown on GaN template by metalorganic chemical vapour deposition. Journal of Physics D: Applied Physics. 2008 Apr 3;41(9):095402.

[199] Jones RE, Broesler R, Yu KM, Ager III JW, Haller EE, Walukiewicz W, Chen X, Schaff WJ. Band gap bowing parameter of In 1− x Al x N. Journal of Applied Physics. 2008 Dec 15;104(12):123501.

[200] Gonschorek M, Carlin JF, Feltin E, Py M, Grandjean N. Exact determination of electrical properties of wurtzite Al 1− x In x N/(AlN)/GaN heterostructures (0.07≤ x≤ 0.21) by means of a detailed charge balance equation. International Journal of Microwave and Wireless Technologies. 2010 Feb;2(1):13-20.

[201] Lyddane RH, Sachs RG, Teller E. On the polar vibrations of alkali halides. Physical Review. 1941 Apr 15;59(8):673.

[202] Schulz S, Caro MA, Tan LT, Parbrook PJ, Martin RW, O'Reilly EP. Composition-dependent band gap and band-edge bowing in AlInN: a combined theoretical and experimental study. Applied Physics Express. 2013 Nov 22;6(12):121001.

[203] Ponce FA, Srinivasan S, Bell A, Geng L, Liu R, Stevens M, Cai J, Omiya H, Marui H, Tanaka S. Microstructure and electronic properties of InGaN alloys. physica status solidi (b). 2003 Nov;240(2):273-84.

[204] Mohamed A, Park K, Bayram C, Dutta M, Stroscio MA. Phonon-assisted reduction of hot spot temperature in AlInN ternaries. Journal of Physics D: Applied Physics. 2020 May 5.

[205] Nakamura S, Senoh M, Mukai T. High-power InGaN/GaN double-heterostructure violet light emitting diodes. Applied Physics Letters. 1993 May 10;62(19):2390-2.

[206] Li J, Nam KB, Kim KH, Lin JY, Jiang HX. Growth and optical properties of In x Al y Ga 1− x− y N quaternary alloys. Applied Physics Letters. 2001 Jan 1;78(1):61-3.

[207] Pristovsek M. Wavelength limits for InGaN quantum wells on GaN. Applied Physics Letters. 2013 Jun 17;102(24):242105.

[208] Kasisomayajula V, Baca AG, AHMAD I, Berg JM, Holtz M, Allerman AA, Tigges CP, Kurtz SR. Self-heating study of an AlGaN/GaN-based heterostructure field effect transistor using ultraviolet micro-Raman scattering. Sandia National Laboratories; 2005 Jan 1.

[209] Xia H, Patterson R, Feng Y, Smyth T, Liao Y, Zhang P, Dai X, Gupta N, Wen X, Chung S, Jia X. Numerical calculation of optical phonon decay rate in InN/GaN MQW. InIOP Conference Series: Materials Science and Engineering 2014 (Vol. 68, No. 1, p. 012009). IOP Publishing.

[210] Tsen KT, Kiang JG, Ferry DK, Lu H, Schaff WJ, Lin HW, Gwo S. Direct measurements of the lifetimes of longitudinal optical phonon modes and their dynamics in InN. Applied physics letters. 2007 Apr 9;90(15):152107.

[211] Nazari M, Hancock BL, Piner EL, Holtz MW. Self-heating profile in an AlGaN/GaN heterojunction field-effect transistor studied by ultraviolet and visible micro-Raman spectroscopy. IEEE Transactions on Electron Devices. 2015 Mar 31;62(5):1467-72.

[212] Perebeinos V, Rotkin SV, Petrov AG, Avouris P. The effects of substrate phonon mode scattering on transport in carbon nanotubes. Nano letters. 2009 Jan 14;9(1):312-6.

[213] Chen JH, Jang C, Xiao S, Ishigami M, Fuhrer MS. Intrinsic and extrinsic performance limits of graphene devices on SiO 2. Nature nanotechnology. 2008 Apr;3(4):206.

[214] Meric I, Han MY, Young AF, Ozyilmaz B, Kim P, Shepard KL. Current saturation in zero-bandgap, top-gated graphene field-effect transistors. Nature nanotechnology. 2008 Nov;3(11):654-9.

[215] Nair KM, Priya S, editors. Advances in electroceramic materials II. John Wiley & Sons; 2010 Dec 8.

[216] Strobel P, Riedel M, Ristein J, Ley L. Surface transfer doping of diamond. Nature. 2004 Jul;430(6998):439-41.

[217] Bonomo G, Mohamed A, Farid S, Park K, Dutta M, Stroscio MA. Contribution of remote interface polar phonons in the hole mobility of diamond. Diamond and Related Materials. 2020 Jan 1;101:107650.

[218] Li S. The electromagneto-acoustic surface wave in a piezoelectric medium: The Bleustein–Gulyaev mode. Journal of Applied Physics. 1996 Nov 1;80(9):5264-9.

[219] Raichura A, Dutta M, Stroscio MA. Elastic continuum models of phonons in carbon nanotubes. InApplied Physics of Carbon Nanotubes 2005 (pp. 89-110). Springer, Berlin, Heidelberg.

[220] Henini M, Razeghi M. Optoelectronic Devices: III Nitrides. Elsevier; 2004 Dec 17.

[221] Qian J, Allen MJ, Yang Y, Dutta M, Stroscio MA. Quantized long-wavelength optical phonon modes in graphene nanoribbon in the elastic continuum model. Superlattices and Microstructures. 2009 Dec 1;46(6):881-8.

[222] Sun K, Stroscio MA, Dutta M. Graphite C-axis thermal conductivity. Superlattices and Microstructures. 2009 Feb 1;45(2):60-4.

[223] Sun K, Stroscio MA, Dutta M. Thermal conductivity of carbon nanotubes. Journal of Applied Physics. 2009 Apr 1;105(7):074316.

[224] Gautschi G. Piezoelectric sensors. InPiezoelectric Sensorics 2002 (pp. 73-91). Springer, Berlin, Heidelberg.

[225] Vashishth AK, Gupta V. Wave propagation in transversely isotropic porous piezoelectric materials. International Journal of Solids and Structures. 2009 Oct 1;46(20):3620-32.

[226] Campbell C. Surface acoustic wave devices and their signal processing applications. Elsevier; 2012 Dec 2.

[227] Ella J, inventor; Nokia Mobile Phones Ltd, assignee. Bulk acoustic wave (BAW) filter having a top portion that includes a protective acoustic mirror. United States patent US 5,872,493. 1999 Feb 16.

[228] Xia D, Yu C, Kong L. The development of micromachined gyroscope structure and circuitry technology. Sensors. 2014 Jan;14(1):1394-473.

[229] Chu DK, Bierlein JD. Surface acoustic wave and Bleustein–Gulyaev wave generation in KTiOPO4 crystals. Applied physics letters. 1993 Oct 11;63(15):2041-3.

[230] Guo FL, Sun R. Propagation of Bleustein–Gulyaev wave in 6 mm piezoelectric materials loaded with viscous liquid. International Journal of Solids and Structures. 2008 Jun 30;45(13):3699-710.

[231] Dvoesherstov MY, Cherednick VI, Chirimanov AP, Petrov SG. Bleustein-Gulyaev wave propagation characteristics in KNbO3 and PKN crystals. In3rd International Conference on Optical Information Processing 1999 Sep 24 (Vol. 3900, pp. 290-296). International Society for Optics and Photonics.

[232] Biryukov SV, Polevoi VG, Weihnacht M. Exact expression for the impedance of a rectangular strip and second-order effects in Bleustein–Gulyaev wave scattering. Journal of applied physics. 1998 Dec 15;84(12):6698-707.

[233] Stroscio MA, Dutta M, Kahn D, Kim KW. Continuum model of optical phonons in a nanotube. Superlattices and microstructures. 2001 Jun 1;29(6):405-9.

[234] Lee BC, Yu S, Kim KW, Stroscio MA, Dutta M. Transmission of longitudinal optical phonons through a barrier in uniaxial crystals. Physical Review B. 2002 Apr 15;65(15):153315.

[235] Rufo S, Dutta M, Stroscio MA. Acoustic modes in free and embedded quantum dots. Journal of applied physics. 2003 Mar 1;93(5):2900-5.

[236] Raichura A, Dutta M, Stroscio MA. Quantized acoustic vibrations of single-wall carbon nanotube. Journal of applied physics. 2003 Sep 15;94(6):4060-5.

[237] Raichura A, Dutta M, Stroscio MA. Phonon effects in nanotubes: phase space reduction and electron conductance. InNonequilibrium Carrier Dynamics in Semiconductors 2006 (pp. 187-190). Springer, Berlin, Heidelberg.

[238] Yamanaka T, Alexson D, Stroscio MA, Dutta M, Petroff P, Brown J, Speck J. Phonon modes in self-assembled GaN quantum dots. Journal of Applied Physics. 2008 Nov 1;104(9):093512.

[239] Stroscio MA, Kisin M, Belenky G, Luryi S. Phonon enhanced inverse population in asymmetric double quantum wells. Applied physics letters. 1999 Nov 22;75(21):3258-60.

[240] Stroscio MA, Kim KW. Generalized piezoelectric scattering rate for electrons in a two-dimensional electron gas. Solid-state electronics. 1994;37(1):181-2.

[241] Auld BA. Acoustic fields and waves in solids. Рипол Классик; 1973.

[242] Bleustein JL. Some simple modes of wave propagation in an infinite piezoelectric plate. The Journal of the Acoustical Society of America. 1969 Mar;45(3):614-20.

[243] Chávez-Ángel E, Zarate RA, Gomis-Bresco J, Alzina F, Torres CS. Modification of Akhieser mechanism in Si nanomembranes and thermal conductivity dependence of the Q-factor of high frequency nanoresonators. Semiconductor Science and Technology. 2014 Nov 14;29(12):124010.

[244] Datta D, Darbandi A, Ghosh S, Stroscio MA, Dutta M. Quantization of acoustic-phonon modes in Siedel-White type waveguide nanostructures. Solid State Communications. 2017 Nov 1;267:42-7.

[245] Vallabhaneni AK, Rhoads JF, Murthy JY, Ruan X. Observation of nonclassical scaling laws in the quality factors of cantilevered carbon nanotube resonators. Journal of Applied Physics. 2011 Aug 1;110(3):034312.

[246] Braginsky VB, Mitrofanov VP, Panov VI. Systems with small dissipation. University of Chicago Press; 1985.

[247] H. E. Bömmel and K. Dransfeld, “Excitation and Attenuation of Hypersonic Waves in Quartz,” Phys. Rev., vol. 117, no. 5, pp. 1245–1252, Mar. 1960.

[248] Mazouchi M, Dutta M, Stroscio MA. Quantized acoustic-phonon shear horizontal modes in an unbounded hexagonal nitride-based piezoelectric nanostructure. Solid State Communications. 2017 May 1;258:1-6.

[249] Mohamed A, Ghosh S, Araque M, Datta D, Mazouchi M, Rane V, Dutta M, Stroscio MA. Nanomechanical systems with normalized and coupled acoustic and electromagnetic modes in piezoelectric structures. Solid State Communications. 2018 Sep 1;277:1-6.

[250] Sohi P, Martin D, Grandjean N. Critical thickness of GaN on AlN: impact of growth temperature and dislocation density. Semiconductor Science and Technology. 2017 Jun 27;32(7):075010.

[251] Nougaoui A, Rouhani BD. Elastic waves in periodically layered infinite and semi-infinite anisotropic media. Surface science. 1987 Jun 2;185(1-2):125-53.

[252] Kwok PC, Miller PB. Free energy of displacive ferroelectrics. Physical Review. 1966 Nov 11;151(2):387.

[253] Klemens PG. Decay of High-Frequency Longitudinal Phonons. Journal of Applied Physics. 1967 Nov;38(12):4573-6.

[254] Ewing MW. Elastic waves in layered media. McGraw-Hill; 1957.

[255] Nougaoui A, Ouchani N, Velasco VR, Bria D, El Boudouti EH, Ali JB. Acoustic waves in (001) InN–AlN and InN–GaN superlattices. Surface science. 2011 Jul 1;605(13-14):1324-30.

[256] Pokatilov EP, Nika DL, Balandin AA. Phonon spectrum and group velocities in AlN/GaN/AlN and related heterostructures. Superlattices and microstructures. 2003 Mar 1;33(3):155-71.

[257] Ali JB, Ouchani N, Nougaoui A, Velasco VR, Bria D, El Boudouti EH. Vibrational properties of (0 0 1) III–V nitride superlattices. Surface science. 2009 Aug 1;603(15):2318-26.

[258] Colvard C, Gant TA, Klein MV, Merlin R, Fischer R, Morkoc H, Gossard AC. Folded acoustic and quantized optic phonons in (GaAl) As superlattices. Physical Review B. 1985 Feb 15;31(4):2080.

[259] Grimsditch M. Effective elastic constants of superlattices. Physical Review B. 1985 May 15;31(10):6818.

[260] Nougaoui A, Rouhani BD. Dynamics of infinite and semi-infinite piezoelectric superlattices: shear horizontal waves and effective medium approximation. Surface science. 1987 Jun 2;185(1-2):154-74.

[261] Grimsditch M, Nizzoli F. Effective elastic constants of superlattices of any symmetry. Physical Review B. 1986 Apr 15;33(8):5891.

[262] Hageman PR, Schermer JJ, Larsen PK. GaN growth on single-crystal diamond substrates by metalorganic chemical vapour deposition and hydride vapour deposition. Thin Solid Films. 2003 Oct 22;443(1-2):9-13.

[263] Truell R, Elbaum C, Chick BB. Ultrasonic methods in solid state physics. Academic press; 2013 Oct 22.

[264] Mohamed A, Dutta M, Stroscio M. Phonon Engineering to Modify Acoustic Phonon Velocity in Hexagonal Layered Superlattices. IEEE Electron Device Letters. 2019 May 3;40(7):1175-7.

[265] Levinshtein ME, Rumyantsev SL, Shur MS, editors. Properties of Advanced Semiconductor Materials: GaN, AIN, InN, BN, SiC, SiGe. John Wiley & Sons; 2001 Feb 21.

[266] McNeil LE, Grimsditch M, French RH. Vibrational spectroscopy of aluminum nitride. Journal of the American Ceramic Society. 1993 May;76(5):1132-6.

[267] Polian A, Grimsditch M, Grzegory I. Elastic constants of gallium nitride. Journal of Applied Physics. 1996 Mar 15;79(6):3343-4.

[268] Bykhovski AD, Gelmont BL, Shur MS. Elastic strain relaxation and piezoeffect in GaN-AlN, GaN-AlGaN and GaN-InGaN superlattices. Journal of Applied Physics. 1997 May 1;81(9):6332-8.

[269] Sen B, Stroscio M, Dutta M. Piezoelectricity in wurtzite polar semiconductor nanowires: A theoretical study. Journal of applied physics. 2011 Jul 15;110(2):024506.

[270] Pop E, Sinha S, Goodson KE. Heat generation and transport in nanometer-scale transistors. Proceedings of the IEEE. 2006 Sep 25;94(8):1587-601.

[271] Ridley BK, Schaff WJ, Eastman LF. Hot-phonon-induced velocity saturation in GaN. Journal of applied physics. 2004 Aug 1;96(3):1499-502.

[272] Nichols DN, Rimai DS, Sladek RJ. Elastic anharmonicity of InP: Its relationship to the high pressure transition. Solid State Communications. 1980 Nov 1;36(8):667-9.

[273] Tsen KT, editor. Non-Equilibrium Dynamics of Semiconductors and Nanostructures. CRC Press; 2005 Nov 1.

[274] Kwon HK, Eiting CJ, Lambert DJ, Wong MM, Dupuis RD, Liliental-Weber Z, Benamara M. Observation of long photoluminescence decay times for high-quality GaN grown by metalorganic chemical vapor deposition. Applied Physics Letters. 2000 Oct 16;77(16):2503-5.

[275] Chichibu SF, Marchand H, Minsky MS, Keller S, Fini PT, Ibbetson JP, Fleischer SB, Speck JS, Bowers JE, Hu E, Mishra UK. Emission mechanisms of bulk GaN and InGaN quantum wells prepared by lateral epitaxial overgrowth. Applied physics letters. 1999 Mar 8;74(10):1460-2.

[276] Izumi T, Narukawa Y, Okamoto K, Kawakami Y, Fujita S, Nakamura S. Time-resolved photoluminescence spectroscopy in GaN-based semiconductors with micron spatial resolution. Journal of Luminescence. 2000 May 1;87:1196-8.

[277] Slonimskii GL. Concerning the attenuation of sound in solid bodies. Zh. Eksp. Theor. Fiz. 1937;7:1457-62.

[278] Baumgartner R, Engelhardt M, Renk KF. Spontaneous Decay of High-Frequency Acoustic Phonons in Ca F 2. Physical Review Letters. 1981 Nov 9;47(19):1403.

[279] Guseinov NM, Levinson YB. Diffusion of nondecaying TA-phonons. Solid State Communications. 1983 Jan 1;45(4):371-4.

[280] Lax M, Narayanamurti V, Ulbrich R, Holzwarth N. On the Propagation of Long-Lived Short Wavelength TA Phonons in GaAs. InPhonon Scattering in Condensed Matter 1984 (pp. 103-105). Springer, Berlin, Heidelberg.

[281] Markiewicz RS. Kinetics of electron-hole droplet clouds: The role of thermalization phonons. Physical Review B. 1980 May 15;21(10):4674.

[282] Bron WE. Lifetimes of high-frequency phonons. Physical Review B. 1980 Mar 15;21(6):2627.

[283] Wang WH. The elastic properties, elastic models and elastic perspectives of metallic glasses. Progress in Materials Science. 2012 Apr 1;57(3):487-656.

[284] Adachi S. Properties of Group-iv, III-v and II-VI Semiconductors. John Wiley & Sons; 2005 Jun 14.

[285] Bhushan B, editor. Nanotribology and nanomechanics: an introduction. Springer Science & Business Media; 2008 May 10.

[286] Pandey DK, Singh D, Yadav RR. Ultrasonic wave propagation in IIIrd group nitrides. Applied Acoustics. 2007 Jul 1;68(7):766-77.

[287] Green JF, Bolland TK, Bolland JW. Theoretical elastic behavior for hexagonal boron nitride. The Journal of Chemical Physics. 1976 Jan 15;64(2):656-62.

[288] Shimada K, Sota T, Suzuki K. First-principles study on electronic and elastic properties of BN, AlN, and GaN. Journal of Applied Physics. 1998 Nov 1;84(9):4951-8.

[289] Hearmon RF, Hellwege K, Hellwege A. Elastic, Piezoelectric and Related Constants of Crystals. Landolt-Börnstein Hand Book on Numerical data and Functional Relationships in Science and Technology, New Series. 1979;11:1.

[290] Mathew VM, Menon CS, Jayachandran KP. Third-order elastic constants and pressure derivatives of the second-order elastic constants of hexagonal boron nitride. Journal of materials science. 2002 Dec 1;37(24):5237-40.

[291] Tucker JW, Rampton VW. Microwave ultrasonics in solid state physics. North-Holland; 1973.

[292] Leman SW. Invited Review Article: Physics and Monte Carlo techniques as relevant to cryogenic, phonon, and ionization readout of Cryogenic Dark Matter Search radiation detectors. Review of Scientific Instruments. 2012 Sep 20;83(9):091101.

[293] Tua PF. Lifetime of High-Frequency Longitudinal Acoustic Phonons in Calcium-Fluoride at Low Temperature.

[294] Tua PF, Mahan GD. Lifetime of high-frequency longitudinal-acoustic phonons in Ca F 2 at low crystal temperatures. Physical Review B. 1982 Aug 15;26(4):2208.

[295] Mohamed A, Singh R, Dutta M, Stroscio MA. Anharmonic decay of high-frequency LA modes in quasi-isotropic III-nitrides. Journal of Physics: Condensed Matter. 2020 Nov 23;33(7):075501.

[296] Abgrall P, Nguyen NT. Nanofluidic devices and their applications. Analytical chemistry. 2008 Apr 1;80(7):2326-41.

[297] Siu WM, Cobbold RS. Basic properties of the electrolyte—SiO 2—Si system: physical and theoretical aspects. IEEE Transactions on Electron Devices. 1979 Nov;26(11):1805-15.

[298] Fung CD, Cheung PW, Ko WH. A generalized theory of an electrolyte-insulator-semiconductor field-effect transistor. IEEE Transactions on Electron Devices. 1986 Jan;33(1):8-18.

[299] Wang Y, Li G. Performance investigation for a silicon nanowire FET biosensor using numerical simulation. In2010 IEEE Nanotechnology Materials and Devices Conference 2010 Oct 12 (pp. 81-86). IEEE.

[300] Purushothaman S, Toumazou C, Georgiou J. Towards fast solid state DNA sequencing. In2002 IEEE International Symposium on Circuits and Systems. Proceedings (Cat. No. 02CH37353) 2002 May 26 (Vol. 4, pp. IV-IV). IEEE.

[301] Moser N, Lande TS, Toumazou C, Georgiou P. ISFETs in CMOS and emergent trends in instrumentation: A review. IEEE Sensors Journal. 2016 Jun 28;16(17):6496-514.

[302] Bandiziol A, Palestri P, Pittino F, Esseni D, Selmi L. A TCAD-based methodology to model the site-binding charge at ISFET/electrolyte interfaces. IEEE Transactions on Electron Devices. 2015 Aug 14;62(10):3379-86.

[303] Varadaraj K, Skinner DM. Denaturants or cosolvents improve the specificity of PCR amplification of a G+ C-rich DNA using genetically engineered DNA polymerases. Gene. 1994 Jan 1;140(1):1-5.

[304] Toumazou C, Shepherd LM, Reed SC, Chen GI, Patel A, Garner DM, Wang CJ, Ou CP, Amin-Desai K, Athanasiou P, Bai H. Simultaneous DNA amplification and detection using a pH-sensing semiconductor system. Nature methods. 2013 Jul;10(7):641.

[305] Chen MC, Chen HY, Lin CY, Chien CH, Hsieh TF, Horng JT, Qiu JT, Huang CC, Ho CH, Yang FL. A CMOS-compatible poly-Si nanowire device with hybrid sensor/memory characteristics for system-on-chip applications. Sensors. 2012 Apr;12(4):3952-63.

[306] Iwai H, Natori K, Shiraishi K, Iwata JI, Oshiyama A, Yamada K, Ohmori K, Kakushima K, Ahmet P. Si nanowire FET and its modeling. Science China information sciences. 2011 May 1;54(5):1004-11.

[307] Bergveld P. The operation of an ISFET as an electronic device. Sensors and Actuators. 1981 Jan 1;1:17-29.

[308] Lee CS, Kim SK, Kim M. Ion-sensitive field-effect transistor for biological sensing. Sensors. 2009 Sep;9(9):7111-31.

[309] Van Hal RE, Eijkel JC, Bergveld P. A novel description of ISFET sensitivity with the buffer capacity and double-layer capacitance as key parameters. Sensors and Actuators B: Chemical. 1995 Mar 1;24(1-3):201-5.

[310] Bergveld P. Development of an ion-sensitive solid-state device for neurophysiological measurements. IEEE Transactions on Biomedical Engineering. 1970 Jan(1):70-1.

[311] Bergveld P. ISFET, theory and practice. InIEEE Sensor Conference, Toronto 2003 Oct 1 (Vol. 328).

[312] Park SG, Chin-Woo K, Ho-Young S, Kim HW, Ju HM, Joo S, Park SO, Kyu-Mann L. Characteristics of Ir etching using Ar/Cl 2 inductively coupled plasmas. Journal of materials science. 2005 Sep 1;40(18):5015-6.

[313] Brendel C, Peano V, Painter O, Marquardt F. Snowflake topological insulator for sound waves. arXiv preprint arXiv:1701.06330. 2017 Jan 23.

[314] Kazan M. Interpolation between the acoustic mismatch model and the diffuse mismatch model for the interface thermal conductance: application to InN/GaN superlattice. Journal of heat transfer. 2011 Nov 1;133(11).

Appendix A

This section demonstrates the $D(q,\omega)$ for the confined and interface modes.

For the case of confined phonon modes

We have $D^{C}(q,\omega) = {f^2}/{F}$. By rearranging Eqs. 3.33 and 3.34 given in chapter 3

$$f = A^2\left[\frac{\cos^2(k_1\frac{d}{2})\cos(\alpha q d)}{k_2+\beta q} + \frac{[\sin(\alpha q d)\cos(k_1 d)+\sin(\alpha q d)]q^2\alpha^2 - \alpha q k_1\cos(\alpha q d)\sin(k_1 d) - k_1^2\sin(\alpha q d)}{2\alpha q(\alpha^2 q^2 - k_1^2)}\right]$$

$$= A^2\left[\frac{\cos^2(k_1\frac{d}{2})\cos(\alpha q d)}{k_2+\beta q} + \frac{\left[2\cos^2(k_1\frac{d}{2})\alpha^2 q^2 - k_1^2\right]\sin(\alpha q d) - \alpha q k_1\cos(\alpha q d)\sin(k_1 d)}{2\alpha q(\alpha^2 q^2 - k_1^2)}\right] \quad \text{A.1}$$

We also recall Eqn. 3.35 from chapter 3 that $\sin(\alpha q d) = \frac{-\mu^{\xi_2}/_{\xi_1}}{\sqrt{1+\left(\xi_2/\xi_1\right)^2}}$, and $\cos(\alpha q d) = \frac{-1}{\sqrt{1+\left(\xi_2/\xi_1\right)^2}}$

Substitute for f in Eq. A.1

$$f = \frac{A^2}{\sqrt{1+\left(\xi_2/\xi_1\right)^2}}\left[\frac{-\cos^2(k_1\frac{d}{2})}{k_2+\beta q}+\frac{\left[2\cos^2(k_1\frac{d}{2})\,\alpha^2q^2-k_1^2\right]\left(-\mu\,\xi_2/\xi_1\right)+\alpha q k_1\sin(k_1 d)}{2\alpha q(\alpha^2q^2-k_1^2)}\right] \quad \text{A.2}$$

with $A^2 = \frac{1}{\frac{\cos(k_1 d)\sin(k_1 d)}{k_1}+\frac{d}{2}+\frac{\cos^2(k_1\frac{d}{2})}{k_2}}$,

remember that $sin\,2(x) = 2\,sin(x)\,cos(x)$ and $sinh\,2(x) = sinh(x)\,cosh(x)$,

$$A^2 = \frac{1}{\frac{\sin(k_1 d)}{2k_1}+\frac{d}{2}+\frac{\cos^2(k_1\frac{d}{2})}{k_2}} = \Upsilon^2 \quad \text{A.3}$$

$$f^2 = \left[\frac{\Upsilon^2}{\sqrt{1+\left(\xi_2/\xi_1\right)^2}}\left[\frac{-\cos^2(k_1\frac{d}{2})}{k_2+\beta q} - \frac{2\cos^2(k_1\frac{d}{2})\,\alpha^2q^2\mu\,\xi_2/\xi_1 + k_1^2\mu\,\xi_2/\xi_1 + \alpha q k_1\sin(k_1 d)}{2\alpha q(\alpha^2q^2-k_1^2)}\right]\right]^2 \quad \text{A.4}$$

Further rearranging Eqn. A.4 gives

$$f^2 = \left[\frac{\Upsilon^2}{\sqrt{1+\left(\xi_2/\xi_1\right)^2}\,(\alpha^2q^2-k_1^2)}\left[\cos^2(k_1\frac{d}{2})\left(\frac{(-\alpha^2q^2+k_1^2)}{k_2+\beta q}-\alpha q\mu\,\xi_2/\xi_1\right)+\frac{k_1^2\mu\,\xi_2/\xi_1}{2\alpha q}+\frac{1}{2}k_1\sin(k_1d)\right]\right]^2 \quad \text{A.5}$$

Now, let us workout the denominator F:

Starting from the form factor given by Komirenko et al. (2000)

$$F = \cos^2(\alpha qd)\,\xi(\beta)^+ + \alpha qd\xi(\alpha)^+ + \sin(\alpha qd)\cos(\alpha qd)\,\xi(\alpha)^-$$

$$= \frac{1}{1+\left(\xi_2/\xi_1\right)^2}\xi(\beta)^+ + \alpha qd\xi(\alpha)^+ + \frac{\mu\,\xi_2/\xi_1}{1+\left(\xi_2/\xi_1\right)^2}\xi(\alpha)^- \quad \text{A.6}$$

We finally obtain $D^C(q,\omega) = f^2/F$ by dividing Eq. A.4 and Eq. A.6

$$D^C(q,\omega) = \frac{\left[\frac{\Upsilon^2}{\sqrt{1+\left(\xi_2/\xi_1\right)^2}\,(\alpha^2q^2-k_1^2)}\left[\cos^2(k_1\frac{d}{2})\left(\frac{(-\alpha^2q^2+k_1^2)}{k_2+\beta q}-\alpha q\mu\,\xi_2/\xi_1\right)+\frac{k_1^2\mu\,\xi_2/\xi_1}{2\alpha q}+\frac{1}{2}k_1\sin(k_1d)\right]\right]^2}{\frac{1}{1+\left(\xi_2/\xi_1\right)^2}\xi(\beta)^+ + \alpha qd\xi(\alpha)^+ + \frac{\mu\,\xi_2/\xi_1}{1+\left(\xi_2/\xi_1\right)^2}\xi(\alpha)^-}$$

$$= \frac{\left[\frac{\Upsilon^2}{(\alpha^2 q^2 - k_1^2)}\left[\cos^2(k_1\frac{d}{2})\left(\frac{(-\alpha^2 q^2 + k_1^2)}{k_2 + \beta q} - \alpha q \mu\, {\xi_2}/{\xi_1}\right) + \frac{k_1^2 \mu\, {\xi_2}/{\xi_1}}{2\alpha q} + \frac{1}{2}k_1 \sin(k_1 d)\right]\right]^2}{\xi(\beta)^+ + \alpha q d \xi(\alpha)^+ {(\xi_1^2 + \xi_2^2)}/{\xi_1^2} + \mu\, {\xi_2}/{\xi_1}\, \xi(\alpha)^-}$$

$$D^C(q,\omega)$$

$$= \frac{\left[\frac{\Upsilon^2}{(\alpha^2 q^2 - k_1^2)}\left[\cos^2(k_1\frac{d}{2})\left(\frac{(k_1^2 - \alpha^2 q^2)}{k_2 + \beta q}\xi_1 - \alpha q \mu\, {\xi_2}/{\xi_1}\right) + \frac{k_1^2 \mu \xi_2}{2\alpha q} + \frac{1}{2}\xi_1 k_1 \sin(k_1 d)\right]\right]^2}{\xi_1^2 \xi(\beta)^+ + \alpha q d \xi(\alpha)^+ (\xi_1^2 + \xi_2^2) + \mu \xi_1 \xi_2 \xi(\alpha)^-} \qquad \text{A.7}$$

Comments 1

We took n to be odd in $\sin(\alpha q d) = \sin\left(n\pi + \arctan \mu\, {\xi_2}/{\xi_1}\right)$ which gives the minus sign in Eqs. A.5 and A.6.

Starting From the values given in Chapter 3:

$$\cosh(\alpha q d) = \sqrt{\frac{\xi_1^2}{\xi_1^2 - \xi_2^2}} = \frac{\xi_1}{\sqrt{\xi_1^2 - \xi_2^2}}$$

$$\sinh(2\alpha q d) = 2\sinh(\alpha q d)\cosh(\alpha q d) \rightarrow \frac{2\xi_1 \xi_2}{\xi_1^2 - \xi_2^2} = 2\sinh(\alpha q d)\frac{\xi_1}{\sqrt{\xi_1^2 - \xi_2^2}}$$

$$\sinh(\alpha q d) = \frac{\pm \xi_2}{\sqrt{\xi_1^2 - \xi_2^2}} \qquad \text{A.8}$$

$\pm$ can be represented by the odd function μ which is a sign function, just as we did in confined phonon case.

For the case of interface phonon modes

We use the same procedure for $D^{IF}(q,\omega)$ starting from the scattering rate in wurtzite sheet, page 13:

$$f^2 = \left[\Upsilon^2 \left[\frac{\cos^2(k_1 \frac{d}{2}) \cosh(\alpha q d)}{k_2 + \beta q} + \frac{\left[2\cos^2(k_1 \frac{d}{2})\,\alpha^2 q^2 + k_1^2\right]\sinh(\alpha q d) + \alpha q k_1 \cosh(\alpha q d)\sin(k_1 d)}{2\alpha q(\alpha^2 q^2 + k_1^2)} \right] \right]^2 \quad \text{A.9}$$

And

$$F = \cosh^2(\alpha q d)\,\xi(\beta)^+ + \alpha q d \xi(\alpha)^- + \sinh(2\alpha q d)\xi(\alpha)^+ \quad \text{A.10}$$

The sign function μ appears on the final equation, however, it is missing from Eqs. A.9 and A.10. As mentioned in the comments, μ ,after being added, will switch the sign of any term that contains $\sinh(x)$ as it is an odd function while $\cosh(x)$ is an even function. Please see Comments 2 to corroborate the procedure of the addition of μ to Eqn. A.9 with the above words.

Now, we substitute for hyperbolic functions from Eqn. A.8 then divide Eqn. A.9 by Eqn. A.10

$$D^{IF}(q,\omega) = \frac{\left[\frac{\Upsilon^2}{(\alpha^2 q^2 + k_1^2)} \left[\cos^2(k_1 \frac{d}{2}) \left(\frac{\alpha^2 q^2 + k_1^2}{k_2 + \beta q} \frac{\xi_1}{\sqrt{\xi_1^2 - \xi_2^2}} - 2\alpha q \mu \frac{\xi_2}{2\sqrt{\xi_1^2 - \xi_2^2}} \right) - \frac{k_1^2 \mu}{2\alpha q} \frac{\xi_2}{\sqrt{\xi_1^2 - \xi_2^2}} + \frac{1}{2} k_1 \sin(k_1 d) \frac{\xi_1}{\sqrt{\xi_1^2 - \xi_2^2}} \right] \right]^2}{\frac{{\xi_1}^2}{\xi_1^2 - \xi_2^2}\xi(\beta)^+ + \alpha q d \xi(\alpha)^- - \frac{2\xi_1 \mu \xi_2 \xi(\alpha)^+}{\xi_1^2 - \xi_2^2}} \quad \text{A.11}$$

Multiply and divide Eqn. A.11 by $\xi_1^2 - \xi_2^2$ which becomes $\sqrt{\xi_1^2 - \xi_2^2}$ inside the square

$$D^{IF}(q,\omega) \quad \text{A.12}$$

$$= \frac{\left[\frac{\Upsilon^2}{(\alpha^2 q^2 + k_1^2)} \left[\cos^2(k_1 \frac{d}{2}) \left(\frac{\alpha^2 q^2 + k_1^2}{k_2 + \beta q} \xi_1 - 2\alpha q \mu \xi_2 \right) - \frac{k_1^2 \mu \xi_2}{2\alpha q} + \frac{1}{2} k_1 \xi_1 \sin(k_1 d) \right] \right]^2}{{\xi_1}^2 \xi(\beta)^+ + \alpha q d \xi(\alpha)^- (\xi_1^2 - \xi_2^2) - \mu \xi_1 \xi_2 \xi(\alpha)^+}$$

Comments 2

In order to find the value of $\sinh(2\alpha qd)$, we start from the expression $\sinh(2\alpha qd) = \sinh\left(n\pi + \operatorname{arctanh}\mu\,{}^{\xi_2}/_{\xi_1}\right)$, and applies the same procedure for $\sin(\alpha qd)$. Remember to take n to be odd again.

We have $arctanh(x) = \left(\frac{1}{2}\right)(ln(1+x) - ln\,(1-x))$

$$\operatorname{arctanh}(\mu\,{}^{\xi_2}/_{\xi_1}) = \frac{1}{2}\left[\ln\left(\frac{\xi_1 - \mu\xi_2}{\xi_1}\right) - \ln\left(\frac{\xi_1 + \mu\xi_2}{\xi_1}\right)\right] = \frac{1}{2}\ln\left(\frac{\xi_1 - \mu\xi_2}{\xi_1 + \mu\xi_2}\right)$$

We know that $sinh(ln(x)) = \frac{x}{2} - \frac{1}{2x}$

$$\sinh(2\alpha qd) = \sinh\left(\ln\left(\frac{\xi_1 - \mu\xi_2}{\xi_1 + \mu\xi_2}\right)\right) = \frac{1}{4}\left(\frac{\xi_1 - \mu\xi_2}{\xi_1 + \mu\xi_2} - \frac{\xi_1 + \mu\xi_2}{\xi_1 - \mu\xi_2}\right)$$

$$= \frac{1}{4}\frac{\xi_1^2 - 2\mu\xi_1\xi_2 + \xi_2^2 - (\xi_1^2 + \mu\xi_1\xi_2 + \xi_2^2)}{\xi_1^2 - \xi_2^2} = \frac{1}{4}\left(\frac{-4\mu\xi_1\xi_2}{\xi_1^2 - \xi_2^2}\right)$$

Note that in $(\xi_1 + \mu\xi_2)(\xi_1 - \mu\xi_2)$, $\mu \times \mu$ will always result in +1 (μ only takes two values -1 and 1).

$$\sinh(2\alpha qd) = \frac{-\mu\xi_1\xi_2}{\xi_1^2 - \xi_2^2}$$

We can then use this value to find $\sinh(\alpha qd) = \frac{-\mu\xi_2}{\sqrt{\xi_1^2 - \xi_2^2}}$ and $\cosh(\alpha qd) = \frac{\xi_1}{\sqrt{\xi_1^2 - \xi_2^2}}$, just as we did in the confined case, with μ included. Then, we go back to Eqs. A.9 and A.10 and substitute for the hyperbolic functions with these new values.

Appendix B

The following code is used to plot the scattering rates of phonons. Comments to explain the routes are added in the code. The script can be described as follows:

1) Two functions were defined for the dispersion relations in chapter 3 for the interface and confined phonon modes.
2) The general code that includes the scattering rate equation.
3) A script to solve the electron wave function parameters k_1 and k_2 since their values change with changing the quantum well thickness d which is defined in the full code script.

Function for interface modes

```
function [qIF,wIF,VgIF,Wk_emi,Wk_abs,dWk_emi] =
KP_IF(TOLO,w,w1,w2,eps_ 1,eps_ 2,Ek_eV,E0,k1,k2)
global hbar0 q0 kBT c0 aB m d

e1z = eps_ 1*(w.^2-w1.Lz^2)./(w.^2-w1.z^2);
e1t = eps_ 1*(w.^2-w1.Lt^2)./(w.^2-w1.t^2);
e2z = eps_ 2*(w.^2-w2.Lz^2)./(w.^2-w2.z^2);
e2t = eps_ 2*(w.^2-w2.Lt^2)./(w.^2-w2.t^2);

xi1 = sqrt(abs(e1z.*e1t));
xi2 = sqrt(abs(e2z.*e2t));

alpha = 0.5*sqrt(abs(e1t./e1z));
beta = 0.5*sqrt(abs(e2t./e2z));

if strcmp(TOLO,'TO')
    q = 0.5*log ((xi1+xi2)./(xi1-xi2))./(alpha*d);
    iq = find(imag (q)~=0,1)-1;
    q = real(q);
    q_sym = q(1:iq);
    q_asym = q(iq+1:end);
    w_sym = w(1:iq);
    w_asym = w(iq+1:end);
elseif strcmp(TOLO,'LO')
    q = 0.5*log ((xi1+xi2)./(xi1-xi2))./(alpha*d);
```

```
    iq = find(imag(q)==0,1)-1;
    q = real(q);
    q_asym = q(1:iq);
    q_sym = q(iq+1:end);
    w_asym = w(1:iq);
    w_sym = w(iq+1:end);
end

qIF = struct('Sy',q_sym,'Asy',q_asym);
wIF = struct('Sy',w_sym,'Asy',w_asym);

w_sym _cm = w_sym/100/c0;
w_asym _cm = w_asym/100/c0;

Eq = hbar0^2*q.^2/(2*m);
if strcmp(TOLO,'TO')
    Eq_sym = Eq(1:iq);
    Eq_asym = Eq(iq+1:end);
elseif strcmp(TOLO,'LO')
    Eq_asym = Eq(1:iq);
    Eq_sym = Eq(iq+1:end);
end

Nqs = length(w_sym);
Nqa = length(w_asym);

Ek = Ek_eV*q0;
[NEk,~] = size(Ek);

de1zdw = 2*eps_ 1*(w./(w.^2 - w1.z^2) - w.*(w.^2 - w1.Lz^2)./(w.^2 -
w1.z^2).^2);
de1tdw = 2*eps_ 1*(w./(w.^2 - w1.t^2) - w.*(w.^2 - w1.Lt^2)./(w.^2 -
w1.t^2).^2);
de2zdw = 2*eps_ 2*(w./(w.^2 - w2.z^2) - w.*(w.^2 - w2.Lz^2)./(w.^2 -
w2.z^2).^2);
de2tdw = 2*eps_ 2*(w./(w.^2 - w2.t^2) - w.*(w.^2 - w2.Lt^2)./(w.^2 -
w2.t^2).^2);

%-- Full D IF
zeta1p = de1tdw./(2*alpha)+2*de1zdw.*alpha;
zeta1n = de1tdw./(2*alpha)-2*de1zdw.*alpha;
zeta2p = de2tdw./(2*beta)+2*de2zdw.*beta;

ups = (sin (k1.*d)./(2*k1) + d/2 + cos (k1*d/2).^2./k2).^(-0.5);
%     FF2 = ups.^4.*((xi1./(3*beta.*q) +
xi2./(5*alpha.*q))./(1+(xi2./xi1).^2) + 2/5./(alpha.*q).*xi2 -
xi2./(5*alpha.*q)./(1+(xi2./xi1).^2)).^2;
```

```
%     f = zeta1n.*alpha.*q*d.*(xi1.^2-xi2.^2) + zeta1p.*xi1.*xi2 +
zeta2p.*xi1.^2;

FF2 = ups.^4.*(cos (k1*d/2).^2.*cosh (alpha.*q*d)./(k2+beta.*q) +
((2*cos (k1*d/2).^2.*alpha.^2.*q.^2+k1.^2).*sinh(alpha.*q*d) +
alpha.*q.*k1.*cosh
(alpha.*q*d).*sin(k1*d))./(2*alpha.*q.*(alpha.^2.*q.^2+k1.^2))).^2;
f = cosh (alpha.*q*d).^2.*zeta2p + alpha.*q*d.*zeta1n + sinh
(alpha.*q*d).*zeta1p;
DIF = FF2./f;

if strcmp(TOLO,'TO')
    DIF_sym = ones(NEk,1)*DIF(1:iq);
    DIF_asym = ones(NEk,1)*DIF(iq+1:end);
elseif strcmp(TOLO,'LO')
    DIF_asym = ones(NEk,1)*DIF(1:iq);
    DIF_sym = ones(NEk,1)*DIF(iq+1:end);
end

Vg_sym  = 2*pi*([w_sym(2:end) w_sym(end)]-[w_sym(1) w_sym(1:end-
1)])./([q_sym(2:end) q_sym(end)]-[q_sym(1) q_sym(1:end-1)]);
Vg_asym = 2*pi*([w_asym(2:end) w_asym(end)]-[w_asym(1) w_asym(1:end-
1)])./([q_asym(2:end) q_asym(end)]-[q_asym(1) q_asym(1:end-1)]);
VgIF = struct('Sy',Vg_sym,'Asy',Vg_asym);

Vp_sym = 2*pi*w_sym./q_sym;
Vp_asym = 2*pi*w_asym./q_asym;

if strcmp(TOLO,'TO')
    sigma_emi _sym = ones(NEk,Nqs);
    sigma_emi _asym = -ones(NEk,Nqa);
    sigma_abs _sym = ones(NEk,Nqs);
    sigma_abs _asym = -ones(NEk,Nqa);
elseif strcmp(TOLO,'LO')
    sigma_emi _sym = -ones(NEk,Nqs);
    sigma_emi _asym = ones(NEk,Nqa);
    sigma_abs _sym = -ones(NEk,Nqs);
    sigma_abs _asym = ones(NEk,Nqa);
end

temp1_emi _sym = ones(NEk,1)*(0.5*q_sym-(m/hbar0)*(Vp_sym-Vg_sym));
temp1_emi _asym = ones(NEk,1)*(0.5*q_asym-(m/hbar0)*(Vp_asym-
Vg_asym));
temp1_abs _sym = ones(NEk,1)*(0.5*q_sym+(m/hbar0)*(Vp_sym-Vg_sym));
temp1_abs _asym = ones(NEk,1)*(0.5*q_asym+(m/hbar0)*(Vp_asym-
Vg_asym));
```

```
%-- sqrt w/ E0
temp2_emi _sym = (sqrt(1/m*(2*Ek*ones(1,Nqs)+ones(NEk,1)*(-0.5*Eq_sym
- hbar0*2*pi*w_sym))-ones(NEk,1)*Vp_sym.^2) +
sqrt(E0/m)).^2./sqrt(1/m*(2*Ek*ones(1,Nqs)+ones(NEk,1)*(-0.5*Eq_sym -
hbar0*2*pi*w_sym))-ones(NEk,1)*Vp_sym.^2);
temp2_emi _asym = (sqrt(1/m*(2*Ek*ones(1,Nqa)+ones(NEk,1)*(-
0.5*Eq_asym - hbar0*2*pi*w_asym))-ones(NEk,1)*Vp_asym.^2) +
sqrt(E0/m)).^2./sqrt(1/m*(2*Ek*ones(1,Nqa)+ones(NEk,1)*(-0.5*Eq_asym
- hbar0*2*pi*w_asym))-ones(NEk,1)*Vp_asym.^2);
temp2_abs _sym = (sqrt(1/m*(2*Ek*ones(1,Nqs)+ones(NEk,1)*(-0.5*Eq_sym
+ hbar0*2*pi*w_sym))-ones(NEk,1)*Vp_sym.^2) +
sqrt(E0/m)).^2./sqrt(1/m*(2*Ek*ones(1,Nqs)+ones(NEk,1)*(-0.5*Eq_sym +
hbar0*2*pi*w_sym))-ones(NEk,1)*Vp_sym.^2);
temp2_abs _asym = (sqrt(1/m*(2*Ek*ones(1,Nqa)+ones(NEk,1)*(-
0.5*Eq_asym + hbar0*2*pi*w_asym))-ones(NEk,1)*Vp_asym.^2) +
sqrt(E0/m)).^2./sqrt(1/m*(2*Ek*ones(1,Nqa)+ones(NEk,1)*(-0.5*Eq_asym
+ hbar0*2*pi*w_asym))-ones(NEk,1)*Vp_asym.^2);

sigma_emi _sym(imag (temp2_emi _sym)~=0) = 0;
sigma_emi _asym(imag (temp2_emi _asym)~=0) = 0;
sigma_abs _sym(imag (temp2_abs _sym)~=0) = 0;
sigma_abs _asym(imag (temp2_abs _asym)~=0) = 0;

temp3_emi _sym = -ones(NEk,1)*((Vp_sym./q_sym - 0.5*hbar0/m)./Vg_sym-
1./q_sym);
temp3_emi _asym = -ones(NEk,1)*((Vp_asym./q_asym -
0.5*hbar0/m)./Vg_asym-1./q_asym);
temp3_abs _sym = ones(NEk,1)*((Vp_sym./q_sym + 0.5*hbar0/m)./Vg_sym-
1./q_sym);
temp3_abs _asym = ones(NEk,1)*((Vp_asym./q_asym +
0.5*hbar0/m)./Vg_asym-1./q_asym);

Nw_sym = ones(NEk,1)*(1./(exp(hbar0*2*pi*w_sym/kBT)-1));
Nw_asym = ones(NEk,1)*(1./(exp(hbar0*2*pi*w_asym/kBT)-1));

dWk_emi _sym = (2*m/aB)*sigma_emi
_sym.*(Nw_sym+1).*DIF_sym.*temp3_emi _sym./(temp1_emi _sym.*temp2_emi
_sym);
Wk_emi _sym = trapz(w_sym,dWk_emi _sym,2);
dWk_emi _asym =(2*m/aB)*sigma_emi
_asym.*(Nw_asym+1).*DIF_asym.*temp3_emi _asym./(temp1_emi
_asym.*temp2_emi _asym);
Wk_emi _asym = trapz(w_asym,dWk_emi _asym,2);
dWk_abs _sym = (2*m/aB)*sigma_abs _sym.*(Nw_sym).*DIF_sym.*temp3_abs
_sym./(temp1_abs _sym.*temp2_abs _sym);
Wk_abs _sym = trapz(w_sym,dWk_abs _sym,2);
```

```
dWk_abs _asym = (2*m/aB)*sigma_abs
_asym.*(Nw_asym).*DIF_asym.*temp3_abs _asym./(temp1_abs
_asym.*temp2_abs _asym);
Wk_abs _asym = trapz(w_asym,dWk_abs _asym,2);

M = dWk_emi _sym/q_sym;

dWk_emi = struct('Sy',dWk_emi _sym,'Asy',dWk_emi _asym);
Wk_emi = struct('Sy',Wk_emi _sym,'Asy',Wk_emi _asym);
Wk_abs = struct('Sy',Wk_abs _sym,'Asy',Wk_abs _asym);

% en = hbar0.*.2.*pi*w_asym./Nw_asym;
% figure; semilogy(q_asym*d,en,'k'); hold on; grid minor;
% hold off;

%- Figure: phonon-freq dep. scattering rate
meV120 = find(Ek_eV == 0.1);
meV300 = find(Ek_eV == 0.092);
meV500 = find(Ek_eV == 0.5);
figure;
semilogy(w_asym _cm,dWk_emi _asym(meV120,:),'b');
grid minor; hold on;
semilogy(w_asym _cm,dWk_emi _asym(meV300,:),'r');
semilogy(w_asym _cm,dWk_emi _asym(NEk,:),'k');
semilogy(w_sym _cm,dWk_emi _sym(meV120,:),'b');
semilogy(w_sym _cm,dWk_emi _sym(meV300,:),'r');

hold off;
xlabel('Phonon Frequency \omega (cm^{-1})', 'FontWeight', 'normal');
ylabel('Scattering Rate (s^{-1}/s^{-1})', 'FontWeight', 'normal');
legend('E_{k} = 0.12 eV','E_{k} = 0.3 eV','E_{k} = 0.5
eV','Location','southeast');

end
```

Function for confined modes

```
function [qc,Vg,Wk_emi,Wk_abs,dWk_emi] =
KP_CONFINED(MODE,nMODE,HILO,w,w1,w2,eps_ 1,eps_ 2,Ek_eV,E0,k1,k2)
global d hbar0 m q0 kBT aB

e1z = eps_ 1*(w.^2-w1.Lz^2)./(w.^2-w1.z^2);
e1t = eps_ 1*(w.^2-w1.Lt^2)./(w.^2-w1.t^2);
e2z = eps_ 2*(w.^2-w2.Lz^2)./(w.^2-w2.z^2);
e2t = eps_ 2*(w.^2-w2.Lt^2)./(w.^2-w2.t^2);
```

```
xi1 = sqrt(abs(e1z.*e1t));
xi2 = sqrt(abs(e2z.*e2t));

alpha = 0.5*sqrt(abs(e1t./e1z));
beta = 0.5*sqrt(abs(e2t./e2z));
mu = sign(e1z.*e2z);

qc = zeros(length(nMODE),length(w));
Nq = length(qc);

for n = nMODE
    if strcmp(MODE,'sym')
        if strcmp(HILO,'lo')
            qc(n,:) = (n*pi + mu.*atan(xi2./xi1))./(alpha*d);
        elseif strcmp(HILO,'hi')
            qc(n,:) = ((n-1)*pi + mu.*atan(xi2./xi1))./(beta*d);
        end

    elseif strcmp(MODE,'asym')
        if strcmp(HILO,'lo')
            qc(n,:) = ((n-1)*pi - mu.*atan(xi1./xi2))./(alpha*d);
        elseif strcmp(HILO,'hi')
            qc(n,:) = (n*pi - mu.*atan(xi1./xi2))./(beta*d);
        end
    end
end

Ek = Ek_eV*q0;
[NEk,~] = size(Ek);

de1zdw = 2*eps_ 1*(w./(w.^2 - w1.z^2) - w.*(w.^2 - w1.Lz^2)./(w.^2 -
w1.z^2).^2);
de1tdw = 2*eps_ 1*(w./(w.^2 - w1.t^2) - w.*(w.^2 - w1.Lt^2)./(w.^2 -
w1.t^2).^2);
de2zdw = 2*eps_ 2*(w./(w.^2 - w2.z^2) - w.*(w.^2 - w2.Lz^2)./(w.^2 -
w2.z^2).^2);
de2tdw = 2*eps_ 2*(w./(w.^2 - w2.t^2) - w.*(w.^2 - w2.Lt^2)./(w.^2 -
w2.t^2).^2);

%-- Full D C
zeta1p = de1tdw./(2*alpha)+2*de1zdw.*alpha;
zeta1n = de1tdw./(2*alpha)-2*de1zdw.*alpha;
zeta2p = de2tdw./(2*beta)+2*de2zdw.*beta;

Wk_emi = zeros(NEk,length(nMODE));
Wk_abs = zeros(NEk,length(nMODE));
```

```
Vg = zeros(length(nMODE),length(w));
Vp = zeros(length(nMODE),length(w));

for n = nMODE
    q = qc(n,:);
    Eq = hbar0^2*q.^2/(2*m);

    ups = (sin (k1.*d)./(2*k1) + d/2 + cos (k1*d/2).^2./k2).^(-0.5);
    FF2 = ups.^4.*(cos (k1*d/2).^2.*cos (alpha.*q*d)./(k2+beta.*q) +
((2*cos (k1*d/2).^2.*alpha.^2.*q.^2-k1.^2).*sin(alpha.*q*d) -
alpha.*q.*k1.*cos
(alpha.*q*d).*sin(k1*d))./(2*alpha.*q.*(alpha.^2.*q.^2-k1.^2))).^2;
    f = cos (alpha.*q*d).^2.*zeta2p + alpha.*q*d.*zeta1p + sin
(alpha.*q*d).*cos (alpha.*q*d).*zeta1n;
    DC = FF2./f;
    DC = ones(NEk,1)*DC;

    Vg(n,:) = 2*pi*([w(2:end) w(end)]-[w(1) w(1:end-1)])./([q(2:end)
q(end)]-[q(1) q(1:end-1)]);
    Vp(n,:) = 2*pi*w./q;

    sigma_emi = ones(NEk,Nq);
    sigma_abs = ones(NEk,Nq);

    temp1_emi = ones(NEk,1)*(0.5*q-(m/hbar0)*(Vp(n,:)-Vg(n,:)));
    temp1_abs = ones(NEk,1)*(0.5*q+(m/hbar0)*(Vp(n,:)-Vg(n,:)));

    temp2_emi = (sqrt(1/m*(2*Ek*ones(1,Nq)+ones(NEk,1)*(-0.5*Eq -
hbar0*2*pi*w))-ones(NEk,1)*Vp (n,:).^2) +
sqrt(E0/m)).^2./sqrt(1/m*(2*Ek*ones(1,Nq)+ones(NEk,1)*(-0.5*Eq -
hbar0*2*pi*w))-ones(NEk,1)*Vp (n,:).^2);
    temp2_abs = (sqrt(1/m*(2*Ek*ones(1,Nq)+ones(NEk,1)*(-0.5*Eq +
hbar0*2*pi*w))-ones(NEk,1)*Vp (n,:).^2) +
sqrt(E0/m)).^2./sqrt(1/m*(2*Ek*ones(1,Nq)+ones(NEk,1)*(-0.5*Eq +
hbar0*2*pi*w))-ones(NEk,1)*Vp (n,:).^2);

    sigma_emi(imag (temp2_emi)~=0) = 0;
    sigma_abs(imag (temp2_abs)~=0) = 0;

    temp3_emi = -ones(NEk,1)*((Vp (n,:)./q - 0.5*hbar0/m)./Vg(n,:) -
1./q);
    temp3_abs = ones(NEk,1)*((Vp (n,:)./q + 0.5*hbar0/m)./Vg(n,:) -
1./q);

    Nw = ones(NEk,1)*(1./(exp(hbar0*2*pi*w/kBT)-1));
```

```
    dWk_emi =
(2*m/aB)*sigma_emi.*(Nw+1).*DC.*temp3_emi./(temp1_emi.*temp2_emi);
    Wk_emi(:,n) = trapz(w,dWk_emi,2);
    dWk_abs =
(2*m/aB)*sigma_abs.*(Nw).*DC.*temp3_abs./(temp1_abs.*temp2_abs);
    Wk_abs(:,n) = trapz(w,dWk_abs,2);
end

Wk_emi = sum(Wk_emi,2);
Wk_abs = sum(Wk_abs,2);

end
```

Full code

```
global hbar0 q0 m0 kBT c0 aB hbarc m_eff m d V0
%-- Fundamental physical parameters
hbar0 = 1.05457180e-34; % [J-s]
q0 = 1.60217662e-19;    % [Coulombs]
m0 = 9.10938356e-31;    % [kg]
kB = 1.38064852e-23;    % [J/K]
T = 300;                % [K]
kBT = kB*T;             % [J]
eps0 = 8.854187817e-12; % [F/m]
c0 = 299792458;         % [m/s]
aB = hbar0^2/q0^2;      % [(J-s)^2/C^2]=[(C-V-s)^2/C^2]=[(V-s)^2]
hbarc = 2*pi*hbar0*c0;  % [J-m]: actually hc not hbarc

m_eff = 0.4;             % Change with given material
m = m_eff*m0;
d = 5.0e-9;
V0 = 1.37*q0;

[k1,k2] = SOLVE_k;

% %-- Phonon frequencies. Change with given material

%- InAlN
w_ 1z = 57260*c0;           % A1 (TO) [1/s] 0.06509 eV
w_ 1t = 62420*c0;           % E1 (TO) [1/s] 0.06819 eV
w_ 1Lz = 81752*c0;          % A1 (LO) [1/s] 0.08865 eV
w_ 1Lt = 83520*c0;          % E1 (LO) [1/s] 0.08927 eV
eps_ 1 = 11.8*eps0;         % [F/m]

%- AlN
w_ 2z = 61100*c0;           % A1 (TO) [1/s]
```

```
w_ 2t = 67100*c0;            % E1 (TO) [1/s]
w_ 2Lz = 89000*c0;           % A1 (LO) [1/s]
w_ 2Lt = 91200*c0;           % E1 (LO) [1/s]
eps_ 2 = 4.77*eps0;          % [F/m]
w1 = struct('z',w_ 1z,'t',w_ 1t,'Lz',w_ 1Lz,'Lt',w_ 1Lt);
w2 = struct('z',w_ 2z,'t',w_ 2t,'Lz',w_ 2Lz,'Lt',w_ 2Lt);

%-- Inputs
E1_TO = 5e-5*q0;       % IF cutoff energy [J]
E1_LO = 5e-5*q0;
E2_TO = 1e-5*q0;       % C cutoff energy [J]
E2_LO = 1e-5*q0;
fig_flag = 0;       % plot figures?
   Nw = 1000;          % number of omegas
NEk = 301;        % number of energies
hEk = 0.3;          % upper limit of energy
nMODE = 1:10;

Ek_eV = linspace (0,hEk,NEk)';

%-- Dielectric functions
w = linspace(30000,80000,8001)*c0;

e1z = eps_ 1*(w.^2-w1.Lz^2)./(w.^2-w1.z^2);
e1t = eps_ 1*(w.^2-w1.Lt^2)./(w.^2-w1.t^2);
e2z = eps_ 2*(w.^2-w2.Lz^2)./(w.^2-w2.z^2);
e2t = eps_ 2*(w.^2-w2.Lt^2)./(w.^2-w2.t^2);
mu = sign(e1t.*e2t);
xi1 = sqrt(abs(e1z.*e1t));
xi2 = sqrt(abs(e2z.*e2t));
alpha = 0.5*sqrt(abs(e1t./e1z));
beta = 0.5*sqrt(abs(e2t./e2z));

nw = ones(NEk,1)*(1./(exp(hbar0*2*pi*w/kBT)-1));
en = hbar0.*.2.*pi*w./(nw*q0);
figure; plot(w/c0/100,en,'k'); hold on; grid minor;
hold off;

figure; plot(w/c0/100,e1z/eps0,'k'); hold on; grid minor;
plot(w/c0/100,e1t/eps0,'r');
plot(w/c0/100,e2z/eps0,'b');
plot(w/c0/100,e2t/eps0,'m');
hold off;
plt                                                                    =
plot(w/c0/100,e1z/eps0,'k',w/c0/100,e1t/eps0,'r',w/c0/100,e2z/eps0,'b
',...
         w/c0/100,e2t/eps0,'m');
```

```
ylim([-20 30]);
xlabel('Phonon Frequency \omega (cm^{-1})', 'FontWeight', 'normal');
ylabel('Dielectric Constant Conditions', 'FontWeight', 'normal');

figure; semilogy(w/c0/100,xi1,'k');hold on; grid minor;
semilogy(w/c0/100,xi2,'r');
semilogy(w/c0/100,alpha,'b');
semilogy(w/c0/100,beta,'m');
semilogy(w/c0/100,mu,'--k');
hold off;
plt                                                                    =
semilogy(w/c0/100,xi1,'k',w/c0/100,xi2,'r',w/c0/100,alpha,'b',w/c0/10
0,beta,...
          'm',w/c0/100,mu,'--k');
xlabel('Phonon Frequency \omega (cm^{-1})', 'FontWeight', 'normal');
ylabel('Wave Parameters', 'FontWeight', 'normal');

%----- INTERFACE PHONONS -----
   wTO = linspace(w1.t/c0+10,w2.z/c0-10,Nw)*c0;
wLO = linspace(w1.Lt/c0+10,w2.Lz/c0-10,Nw)*c0;

[qIF_TO,wIF_TO,VgIF_TO,WkIF_Em   _TO,WkIF_Ab   _TO,dWkIF_Em   _TO]   =
KP_IF('TO',wTO,w1,w2,eps_ 1,eps_ 2,Ek_eV,E1_TO,k1,k2);
[qIF_LO,wIF_LO,VgIF_LO,WkIF_Em   _LO,WkIF_Ab   _LO,dWkIF_Em   _LO]   =
KP_IF('LO',wLO,w1,w2,eps_ 1,eps_ 2,Ek_eV,E1_LO,k1,k2);

wIF_SyTO _cm = wIF_TO.Sy/100/c0;
wIF_AsyTO _cm = wIF_TO.Asy/100/c0;
wIF_SyLO _cm = wIF_LO.Sy/100/c0;
wIF_AsyLO _cm = wIF_LO.Asy/100/c0;

%- IF: Average group velocity
dVgIF_SyEm _TO = dWkIF_Em _TO.Sy.*(ones(NEk,1)*abs(VgIF_TO.Sy));
dVgIF_AsyEm _TO = dWkIF_Em _TO.Asy.*(ones(NEk,1)*abs(VgIF_TO.Asy));
dVgIF_SyEm _LO = dWkIF_Em _LO.Sy.*(ones(NEk,1)*abs(VgIF_LO.Sy));
dVgIF_AsyEm _LO = dWkIF_Em _LO.Asy.*(ones(NEk,1)*abs(VgIF_LO.Asy));
VgIF_SyEm _TO = trapz(wIF_TO.Sy,dVgIF_SyEm _TO,2);
VgIF_AsyEm _TO = trapz(wIF_TO.Asy,dVgIF_AsyEm _TO,2);
VgIF_SyEm _LO = trapz(wIF_LO.Sy,dVgIF_SyEm _LO,2);
VgIF_AsyEm _LO = trapz(wIF_LO.Asy,dVgIF_AsyEm _LO,2);
VgIF_Em  =  (VgIF_SyEm  _TO+VgIF_AsyEm  _TO+VgIF_SyEm  _LO+VgIF_AsyEm
_LO)./(WkIF_Em _TO.Sy+WkIF_Em _TO.Asy+WkIF_Em _LO.Sy+WkIF_Em _LO.Asy);

%----- CONFINED PHONONS -----
   wC_TO = linspace(w1.z/c0+10,w1.t/c0-10,Nw)*c0;
wC_LO = linspace(w1.Lz/c0+10,w1.Lt/c0-10,Nw)*c0;
```

```
wC_TO _cm = wC_TO/100/c0;
wC_LO _cm = wC_LO/100/c0;

%-- Dispersion and scattering rate calculation for each branch
%- Symmetric modes
[qCSy_TO,VgCSy_TO,WkC_SyEm    _TO,WkC_SyAb    _TO,dWkC_SyEm    _TO]    =
KP_CONFINED('sym',nMODE,'lo',wC_TO,w1,w2,eps_                    1,eps_
2,Ek_eV,E2_TO,k1,k2);
[qCSy_LO,VgCSy_LO,WkC_SyEm    _LO,WkC_SyAb    _LO,dWkC_SyEm    _LO]    =
KP_CONFINED('sym',nMODE,'lo',wC_LO,w1,w2,eps_                    1,eps_
2,Ek_eV,E2_LO,k1,k2);

%- Asymmetric modes
[qCAsy_TO,VgCAsy_TO,WkC_AsyEm  _TO,WkC_AsyAb  _TO,dWkC_AsyEm  _TO]  =
KP_CONFINED('asym',nMODE,'lo',wC_TO,w1,w2,eps_                   1,eps_
2,Ek_eV,E2_TO,k1,k2);
[qCAsy_LO,VgCAsy_LO,WkC_AsyEm  _LO,WkC_AsyAb  _LO,dWkC_AsyEm  _LO]  =
KP_CONFINED('asym',nMODE,'lo',wC_LO,w1,w2,eps_                   1,eps_
2,Ek_eV,E2_LO,k1,k2);

%- Sign correction (temporary)
WkC_SyEm _TO = abs(WkC_SyEm _TO);
WkC_SyEm _LO = abs(WkC_SyEm _LO);
WkC_AsyEm _TO = abs(WkC_AsyEm _TO);
WkC_AsyEm _LO = abs(WkC_AsyEm _LO);
WkC_SyAb _TO = abs(WkC_SyAb _TO);
WkC_SyAb _LO = abs(WkC_SyAb _LO);
WkC_AsyAb _TO = abs(WkC_AsyAb _TO);
WkC_AsyAb _LO = abs(WkC_AsyAb _LO);

% %-- C: Average group velocity
% dVgC_SyEm _TO = abs (dWkC_SyEm _TO).*(ones (NEk,1).*abs(VgCSy_TO));
% dVgC_SyEm _LO = abs (dWkC_SyEm _LO).*(ones (NEk,1).*abs(VgCSy_LO));
% VgC_SyEm _TO = trapz(wC_TO,dVgC_SyEm _TO,2);
% VgC_SyEm _LO = trapz(wC_LO,dVgC_SyEm _LO,2);
%
% dVgC_AsyEm _TO = abs (dWkC_AsyEm _TO).*(ones(NEk,1)*abs(VgCAsy_TO));
%        dVgC_AsyEm        _LO       =       abs       (dWkC_AsyEm
_LO).*(ones(NEk,1)*abs(VgCAsy_LO(2,:)));
% VgC_AsyEm _TO = trapz(wC_TO,dVgC_AsyEm _TO,2);
% VgC_AsyEm _LO = trapz(wC_LO,dVgC_AsyEm _LO,2);
%  VgC_Em  =  (VgC_SyEm  _TO+VgC_AsyEm  _TO+VgC_SyEm  _LO+VgC_AsyEm
_LO)./(WkC_SyEm _TO+WkC_AsyEm _TO...
      %     +WkC_SyEm _LO+WkC_AsyEm _LO);
%
%  Vg_Em  =  (VgIF_SyEm  _TO+VgIF_AsyEm  _TO+VgIF_SyEm  _LO+VgIF_AsyEm
_LO+VgC_SyEm _TO...
```

```
       %     +VgC_AsyEm _TO+VgC_SyEm _LO+VgC_AsyEm _LO)./ ...
%            (WkIF_Em  _TO.Sy+WkIF_Em  _TO.Asy+WkIF_Em  _LO.Sy+WkIF_Em
_LO.Asy+WkC_SyEm _TO...
     %     +WkC_AsyEm _TO+WkC_SyEm _LO+WkC_AsyEm _LO);

WkC_Em _TO = WkC_SyEm _TO+WkC_AsyEm _TO;
WkC_Em _LO = WkC_SyEm _LO+WkC_AsyEm _LO;
WkC_Ab _TO = WkC_SyAb _TO + WkC_AsyAb _TO;
WkC_Ab _LO = WkC_SyAb _LO + WkC_AsyAb _LO;
WkC_Em = WkC_Em _TO + WkC_Em _LO;
WkC_Ab = WkC_Ab _TO + WkC_Ab _LO;
WkC = WkC_Em + WkC_Ab;
WkIF_TE = WkIF_Em _TO.Asy + WkIF_Em _TO.Sy;
WkIF_TA = WkIF_Ab _TO.Asy + WkIF_Ab _TO.Sy;
WkIF_LE = WkIF_Em _LO.Asy + WkIF_Em _LO.Sy;
WkIF_LA = WkIF_Ab _LO.Asy + WkIF_Ab _LO.Sy;
WkIF_Em = WkIF_TE+WkIF_LE;
WkIF_Ab = WkIF_TA+WkIF_LA;
WkIF = WkIF_Em+WkIF_Ab;
Wk = WkC + WkIF;

% %-- FIGURES
%- IF and CONFINED Dispersion
figure;
grid minor; hold on;
plot(qIF_LO.Sy*d,wIF_SyLO _cm,'k');
plot(qIF_LO.Asy*d,wIF_AsyLO _cm,'g');
plot(qCSy_LO*d,wC_LO _cm,'b');
plot(qCAsy_LO*d,wC_LO _cm,'r');
hold off;
plt    =    plot(qIF_LO.Sy*d,wIF_SyLO    _cm,'k',qIF_LO.Asy*d,wIF_AsyLO
_cm,'g',qCSy_LO*d,wC_LO _cm,'b'...
       ,qCAsy_LO*d,wC_LO _cm,'r');
xlim([0 8]);
xlabel('Wave Vector qd', 'FontWeight', 'normal');
ylabel('Phonon Frequency \omega (cm^{-1})', 'FontWeight', 'normal');
legend('Symmetric','Asymmetric','Location','southeast');
% low order modes
figure;
plot(qIF_TO.Sy*d,wIF_SyTO _cm,'b');
grid minor; hold on;
plot(qIF_TO.Asy*d,wIF_AsyTO _cm,'r');
% plot(qCSy_TO*d,wC_TO _cm,'b');
plot(qCSy_TO(2,:)*d,wC_TO _cm,'b');
plot(qCSy_TO(3,:)*d,wC_TO _cm,'b');
plot(qCSy_TO(4,:)*d,wC_TO _cm,'b');
plot(qCSy_TO(5,:)*d,wC_TO _cm,'b');
```

```
plot(qCSy_TO(6,:)*d,wC_TO _cm,'b');
plot(qCSy_TO(7,:)*d,wC_TO _cm,'b');
plot(qCSy_TO(8,:)*d,wC_TO _cm,'b');
plot(qCSy_TO(9,:)*d,wC_TO _cm,'b');

% plot(qCAsy_TO*d,wC_TO _cm,'r');
plot(qCAsy_TO(2,:)*d,wC_TO _cm,'r');
plot(qCAsy_TO(3,:)*d,wC_TO _cm,'r');
plot(qCAsy_TO(4,:)*d,wC_TO _cm,'r');
plot(qCAsy_TO(5,:)*d,wC_TO _cm,'r');
plot(qCAsy_TO(6,:)*d,wC_TO _cm,'r');
plot(qCAsy_TO(7,:)*d,wC_TO _cm,'r');
plot(qCAsy_TO(8,:)*d,wC_TO _cm,'r');
plot(qCAsy_TO(9,:)*d,wC_TO _cm,'r');
hold off;
plt    =    plot(qIF_TO.Sy*d,wIF_SyTO    _cm,'k',qIF_TO.Asy*d,wIF_AsyTO
_cm,'g',qCSy_TO(2,:)*d,wC_TO _cm...
        ,'b',qCSy_TO(3,:)*d,wC_TO         _cm,'b',qCSy_TO(4,:)*d,wC_TO
_cm,'b',qCSy_TO(5,:)*d,wC_TO _cm,'b'...
        ,qCSy_TO(6,:)*d,wC_TO             _cm,'b',qCSy_TO(7,:)*d,wC_TO
_cm,'b',qCSy_TO(8,:)*d,wC_TO _cm,'b',...
         qCSy_TO(9,:)*d,wC_TO            _cm,'b',qCAsy_TO(1,:)*d,wC_TO
_cm,'r',qCAsy_TO(3,:)*d,wC_TO            _cm,'r',qCAsy_TO(4,:)*d,wC_TO
_cm,'r',...
         qCAsy_TO(5,:)*d,wC_TO _cm...
        ,'r',qCAsy_TO(6,:)*d,wC_TO       _cm,'r',qCAsy_TO(7,:)*d,wC_TO
_cm,'r',qCAsy_TO(8,:)*d,wC_TO _cm...
        ,'r',qCAsy_TO(9,:)*d,wC_TO _cm,'r');
% ylim([560 630]);
xlim([0 8]);
xlabel('Wave Vector qd', 'FontWeight', 'normal');
ylabel('Phonon Frequency \omega (cm^{-1})', 'FontWeight', 'normal');
legend('Symmetric','Asymmetric','Location','southeast');
%
%- IF and CONFINED Group velocity
figure;
semilogy(wIF_AsyTO _cm,VgIF_TO.Asy,'k');
grid minor; hold on;
plot(wIF_SyTO _cm,VgIF_TO.Sy,'r');
plot(wIF_AsyLO _cm,VgIF_LO.Asy,'k');
plot(wIF_SyLO _cm,VgIF_LO.Sy,'r');
plot(wC_TO _cm,VgCAsy_TO(1,:),'b');
plot(wC_TO _cm,VgCSy_TO(1,:),'r');
plot(wC_LO _cm,VgCAsy_LO(2,:),'b');
plot(wC_LO _cm,VgCSy_LO(1,:),'m');
hold off;
```

```
plt        =        plot(wIF_AsyTO        _cm,VgIF_TO.Asy,'k',wIF_SyTO
_cm,VgIF_TO.Sy,'r',...
         wIF_AsyLO                        _cm,VgIF_LO.Asy,'k',wIF_SyLO
_cm,VgIF_LO.Sy,'r',wC_TO _cm,VgCSy_TO(1,:),'r'...
        ,wC_LO _cm,VgCAsy_LO(2,:),'b',wC_LO _cm,VgCSy_LO(1,:),'m');
xlabel('Phonon Frequency (cm^{-1})', 'FontWeight', 'normal');
ylabel('C Group Velocity (m/s)', 'FontWeight', 'normal');
legend('Asymmetric Modes','Symmetric Modes','Location','northeast');

%- IF and CONFINED average group velocity
figure; plot(Ek_eV,VgIF_Em,'b'); grid minor; hold on;
% plot(Ek_eV,VgC_Em,'r');
% plot(Ek_eV,Vg_Em,'k');
hold off;
xlabel('Electron Energy E_{k} (eV)', 'FontWeight', 'normal');
ylabel('Average Group Velocity v_ {g,avg}^{IF+C} (m/s)', 'FontWeight',
'normal');
legend('IF','Confined','Total','Location','southeast');

% % %- CONFINED Scattering rates all modes
% % figure; semilogy(Ek_eV,WkC_SyEm,':b'); grid minor; hold on;
% % semilogy(Ek_eV,WkC_AsyEm,'--b');
% % semilogy(Ek_eV,WkC_Em,'b');
% % semilogy(Ek_eV,WkC_SyAb,':r');
% % semilogy(Ek_eV,WkC_AsyAb,'--r');
% % semilogy(Ek_eV,WkC_Ab,'r');
% % hold off;
% % xlabel('Electron Energy E_{k}(eV)', 'FontWeight', 'normal');
% % ylabel('C Scattering Rate (s^{-1})', 'FontWeight', 'normal');
%    %    legend('Emission    S','Emission    AS','Emission','Absorption
S','Absorption AS','Absorption','Location','northeast');
%
% %- IF and CONFINED Emission scattering rate
%   figure;   semilogy(Ek_eV,WkIF_Em   _TO.Sy+WkIF_Em   _TO.Asy+WkIF_Em
_LO.Sy+WkIF_Em _LO.Asy,'b'); grid minor; hold on;
% semilogy(Ek_eV,WkC_Em,'--r');
% hold off;
% xlabel('Electron Energy E_{k} (eV)', 'FontWeight', 'normal');
% ylabel('Emission Scattering Rate (s^{-1})', 'FontWeight', 'normal');
% legend('Interface Modes','Confined Modes','Location','southeast');
%
%- CONFINED Total scattering rate
figure; semilogy(Ek_eV,WkC,'k'); grid minor; hold on;
semilogy(Ek_eV,WkC_Em,'--b');
semilogy(Ek_eV,WkC_Em _LO,'--m');
semilogy(Ek_eV,WkC_Ab _LO,'--c');
hold off;
```

```
plt   =   semilogy(Ek_eV,WkC,'k',Ek_eV,WkC_Em   _LO,'--m',Ek_eV,WkC_Ab
_LO,'--c');
ylim([1e10 3e13]);
xlabel('Electron Energy E_{k}(eV)', 'FontWeight', 'normal');
ylabel('C Total Scattering Rate (s^{-1})', 'FontWeight', 'normal');
legend('Total','Emission','Absorption','Location','southeast');
%- IF Total scattering rate
figure; semilogy(Ek_eV,WkIF,'k'); grid minor; hold on;
semilogy(Ek_eV,WkIF_Em,'--b');
semilogy(Ek_eV,WkIF_LE,'--m');
semilogy(Ek_eV,WkIF_TE,'--m');
semilogy(Ek_eV,WkIF_Ab,'--r');
hold off;
plt   =   semilogy(Ek_eV,WkIF,'k',Ek_eV,WkIF_Em,'--b',Ek_eV,WkIF_TE,'--
m',Ek_eV,WkIF_LE,'--m',Ek_eV,WkIF_Ab,'--r');
ylim([1e10 3e13]);
xlabel('Electron Energy E_{k}(eV)', 'FontWeight', 'normal');
ylabel('IF Total Scattering Rate (s^{-1})', 'FontWeight', 'normal');
legend('Total','Emission','Absorption','Location','southeast');
```

Electron wave function parameters

```
function [k1,k2] = SOLVE_k()
global hbar0 d m V0

roundd = round(d,1,'significant')*1e9;
switch roundd
    case 20
        k = 1.615130236490229e+08;
    case 10
        k = 2.9e8;
    case 5
        k = 5.659474067051942e8;
    case 4
        k = 6.901357880170896e8;
    case 3
        k = 8.838774058207904e8;
    case 2
        k = 1.227306970645387e9;
    case 1
        k = 1.987757079903387e9;
end

k1 = fzero(@(k1) k1.^2.*(1+tan (k1*d/2).^2)-2*m*V0/hbar0^2,k);
k2 = k1*tan(k1*d/2);
end
```

Appendix C

The following routes are used to obtain a description for remote interface polar phonons. The code is three-fold: dispersion relation of optical phonons, scattering rates and hole mobility.

```
get(0,'Factory');
set(0,'defaultfigurecolor',[1 1 1])

%%  Universal Constants
m0 = 9.1093837015e-31; %electron resting mass [Kg]
m = 0.908*m0; %effective mass [Kg]
hbar = 1.054571800e-34; %normalized Plank constant [J s]
e_h = 1.602176634e-19;%hole charge [C]
epsilon_0 = 8.85418781762e-12; %permittivity vacuum [F/m]
c0 = 299792458; %speed of light [m/s]
kB = 1.38064852e-23;% [J/K]
T = 300;% [K]
kBT = kB*T;% [J]
aB = hbar^2/e_h^2;% [(V s)^2]
epsilon_r = 5.7; %Diamond dieletric constant [Li et Al 2018]

syms q_sim omega_sim %symbolic variables used for dispersion and
derivative
disp('Select the material:');
disp('[1] AlN');
disp('[2] GaN');
disp('[3] c-BN');
disp('[4] w-BN');
values =input('');

if values==1 %AlN
    epsilon_bot_inf = 4.77*epsilon_0; %[F/m] values from Kihoon
    epsilon_y_inf = 4.77*epsilon_0;
    omega_y_L = 890*(c0*10^2*2*pi);
    omega_bot_L = 912*(c0*10^2*2*pi);
    omega_bot = 671*(c0*10^2*2*pi);
    omega_y = 611*(c0*10^2*2*pi);
    omega_resonance = 860.6;
    disp('-> AlN');
elseif values==2 %GaN
    epsilon_bot_inf = 5.29*epsilon_0; %[F/m] values from Komirenko
    epsilon_y_inf = 5.29*epsilon_0;
    omega_y_L = 735*(c0*10^2*2*pi);
    omega_bot_L = 743*(c0*10^2*2*pi);
```

```
    omega_bot = 561*(c0*10^2*2*pi);
    omega_y = 533*(c0*10^2*2*pi);
    disp('-> GaN');
elseif values == 3 %c-BN
    epsilon_bot_inf = 4.54*epsilon_0; %[F/m] values from Thesis
    epsilon_y_inf = 4.54*epsilon_0;
    omega_y_L = 1285*(c0*10^2*2*pi);
    omega_bot_L = 1285*(c0*10^2*2*pi);
    omega_bot = 1040*(c0*10^2*2*pi);
    omega_y = 1040*(c0*10^2*2*pi);
    disp('-> c-BN');
else %w-BN
    epsilon_bot_inf = 4.50*epsilon_0; %[F/m] values from Thesis
    epsilon_y_inf = 4.67*epsilon_0;
    omega_y_L = 1258*(c0*10^2*2*pi);
    omega_bot_L = 1281*(c0*10^2*2*pi);
    omega_bot = 1053*(c0*10^2*2*pi);
    omega_y = 1006*(c0*10^2*2*pi);
    omega_resonance = 1229;
    disp('-> w-BN');
end

d = 5e-9; %thickness of the polar layer
L = 10e-6; %thickness of the diamond substrate

num_omega = 5000; % number of omegas
epsilon_1bot         =         epsilon_bot_inf*((omega_sim.^2         -
omega_bot_L^2)./(omega_sim.^2 - omega_bot^2));
epsilon_1y          =          epsilon_y_inf*((omega_sim.^2          -
omega_y_L^2)./(omega_sim.^2 - omega_y^2));
q_limit_up = 8/d;

%% Dispersion relations for the optical phonon IF modes (Symmetric)
eq_sym                              =                              @(q_sim)
sqrt(epsilon_1bot*epsilon_1y)*tanh(sqrt(epsilon_1bot/epsilon_1y)*q_si
m*d/2) - epsilon_0;
q_sym = linspace(q_limit_up/5000,q_limit_up,num_omega);
omega_sym = zeros(1,num_omega);
for i=1:num_omega
    sol  =  vpasolve(eq_sym(q_sym(i))==0,  omega_sim,[omega_bot  +  1e6
omega_y_L - 1e6],'Random',true);
    omega_sym(i) = sol;
end
figure(1),plot(q_sym,omega_sym/(c0*10^2*2*pi),'k','Linewidth',2);
xlabel('Wave  vector  q  [1/m]','FontWeight','normal');  ylabel('Phonon
Frequency [cm^{-1}]','FontWeight','normal'); hold on
```

```
%% Dispersion relations for the optical phonon IF modes (Antisymmetric)
eq_antisym=                                                    @(q_sim)
sqrt(epsilon_1bot*epsilon_1y)*coth(sqrt(epsilon_1bot/epsilon_1y)*q_si
m*d/2) - epsilon_0;
q_antisym = linspace(q_limit_up/1000,q_limit_up,num_omega);
omega_antisym = zeros(1, num_omega);
for i=1:num_omega
    sol = vpasolve(eq_antisym(q_antisym(i))==0, omega_sim,[omega_bot +
1e6 omega_y_L - 1e6],'Random',true);
    omega_antisym(i) = sol;
end
figure(1),plot(q_antisym,omega_antisym/(c0*10^2*2*pi),'r','Linewidth'
,2); legend('Symmetric','Antisymmetric'); legend('autoupdate','off');
line([0                          q_limit_up],[omega_bot/(c0*10^2*2*pi)
omega_bot/(c0*10^2*2*pi)],'LineStyle','--');  str  =  '\omega_{\perp}';
text(q_limit_up - q_limit_up/50,omega_bot/(c0*10^2*2*pi) + 7,str);
line([0                          q_limit_up],[omega_y_L/(c0*10^2*2*pi)
omega_y_L/(c0*10^2*2*pi)],'LineStyle','--');   str   =   '\omega_{yL}';
text(q_limit_up - q_limit_up/50,omega_y_L/(c0*10^2*2*pi) - 7,str);
%line([0                               q_limit_up/2.5],[omega_resonance
omega_resonance],'LineStyle','-.');        str    =    '\omega_{res}';
text(q_limit_up/50,omega_resonance - 3,str);

q = [q_sym q_antisym];
omega= [omega_sym omega_antisym];

%% Phase and Group velocity
Vp_sym = omega_sym./q_sym;
Vp_antisym = omega_antisym./q_antisym;
figure(2),subplot(2,1,1),semilogy(omega_sym/(c0*10^2*2*pi),Vp_sym,'k'
,'Linewidth',2); hold on
semilogy(omega_antisym/(c0*10^2*2*pi),Vp_antisym,'r','Linewidth',2);
legend('Symmetric','Antisymmetric'); legend('autoupdate','off');
title('Phonons  Phase  Velocity');  xlabel('Phonon  frequency  [cm^{-
1}]','FontWeight','normal');    ylabel('Phase    velocity    [m/s]',
'FontWeight',   'normal');   axis([(omega_bot/(c0*10^2*2*pi)   -   20)
(omega_y_L/(c0*10^2*2*pi) + 10) 10^4 2*10^8]);
line([omega_bot/(c0*10^2*2*pi)         omega_bot/(c0*10^2*2*pi)],[10+3
10e+9],'LineStyle','--');        str        =        '\omega_{\perp}';
text(omega_bot/(c0*10^2*2*pi) - 5, 10^8 ,str);
line([omega_y_L/(c0*10^2*2*pi)         omega_y_L/(c0*10^2*2*pi)],[10+3
10e+9],'LineStyle','--');         str         =         '\omega_{yL}';
text(omega_y_L/(c0*10^2*2*pi) + 2, 10^8 ,str);
%line([omega_resonance  omega_resonance],[10+3  10e+9],'LineStyle','-
.'); str = '\omega_{res}'; text(omega_resonance + 2, 10^5 ,str);
```

```
Vg_sym        =    ([omega_sym(2:end)    omega_sym(end)]-[omega_sym(1)
omega_sym(1:end-1)])./([q_sym(2:end)             q_sym(end)]-[q_sym(1)
q_sym(1:end-1)]);
Vg_antisym     =      ([omega_antisym(2:end)      omega_antisym(end)]-
[omega_antisym(1)         omega_antisym(1:end-1)])./([q_antisym(2:end)
q_antisym(end)]-[q_antisym(1) q_antisym(1:end-1)]);
figure(2),subplot(2,1,2),plot(omega_sym/(c0*10^2*2*pi),Vg_sym,'k','Li
newidth',2); hold on;
plot(omega_antisym/(c0*10^2*2*pi),Vg_antisym,'r','Linewidth',2);
legend('Symmetric','Antisymmetric'); legend('autoupdate','off');
title('Phonons Group Velocity'); xlabel('Phonon frequency [cm^{-1}]',
'FontWeight', 'normal'); ylabel('Group velocity [m/s]', 'FontWeight',
'normal');         axis([(omega_bot/(c0*10^2*2*pi)         -         20)
(omega_y_L/(c0*10^2*2*pi) + 10) -10e5 10e5]);
line([omega_bot/(c0*10^2*2*pi)         omega_bot/(c0*10^2*2*pi)],[-8e+6
8e+6],'LineStyle','--');         str         =         '\omega_{\perp}';
text(omega_bot/(c0*10^2*2*pi) - 5, -9.3e5 ,str);
line([omega_y_L/(c0*10^2*2*pi)         omega_y_L/(c0*10^2*2*pi)],[-8e+6
8e+6],'LineStyle','--');          str          =          '\omega_{yL}';
text(omega_y_L/(c0*10^2*2*pi) + 2, -9.3e5 ,str);
%line([omega_resonance  omega_resonance],[-8e+6  8e+6],'LineStyle','-
.'); str = '\omega_{res}'; text(omega_resonance + 2, -9.3e5 ,str);

num_energies = 10001; % number of energies
energy_up_limit = 0.5;  % upper limit of energy [eV]
E0 =1e-4*e_h; % cutoff energy [J]
%% Phonon energy
Eq = hbar^2*q.^2./(2*m);
Eq_sym = hbar^2*q_sym.^2./(2*m);
Eq_antisym = hbar^2*q_antisym.^2./(2*m);

Ek_eV = linspace(0,energy_up_limit,num_energies)';
Ek = Ek_eV*e_h; %[J]

%% 2DEG
l = 0.0e-9; %distance 2DEG from surface
N_h= 2*10^17; %charge density [1/m^2] 2*10^13 [1/cm^2]
b       =       (33*m*e_h^2*N_h/(8*hbar^2*epsilon_0*epsilon_r))^(1/3);
%variational parameter [1/m]

%% D element
F = @(q) ((b^3)/2)*exp(b*l)*((-L^2*exp(-(b + q)*L)./(b+q)) + (l^2*exp(-
(b+q)*l)./(b+q))  +  (2./(b+q)).*[((-L*exp(-(b  +  q)*L)  +  l*exp(-(b  +
q)*l))./(b+q))  -  ((exp(-(b  +  q)*L)  -  exp(-(b  +  q)*l))./(b+q).^2)]  -
2*l*[((-L*exp(-(b + q)*L) + l*exp(-(b + q)*l))./(b + q)) - ((exp(-(b +
q)*L) - exp(-(b + q)*l))./(b + q).^2)] + l^2*[(- exp(-(b + q)*L) + exp(-
(b + q)*l))./(b+q)]);
```

```
% F obtained by integration - derivation is shown in the thesis

den_sym = diff(eq_sym,omega_sim);
den_sym = matlabFunction(den_sym);
den_sym = den_sym(omega_sym, q_sym); %derivative of the dispersion
relation (symm)
den_antisym = diff(eq_antisym,omega_sim);
den_antisym = matlabFunction(den_antisym);
den_antisym = den_antisym(omega_antisym,q_antisym); %derivative of the
dispersion relation (asymm)

C_symm = sqrt(1./abs(den_sym));
D_sym = abs(C_symm.^2.*(F(q_sym)).^2);
C_antisymm = sqrt(1./abs(den_antisym));
D_antisym = abs(C_antisymm.^2.*(F(q_antisym)).^2);

D_antisym = ones(num_energies,1)*D_antisym;
D_sym = ones(num_energies,1)*D_sym;

%% Scattering rate (Emission & Absorption)
sigma_emi_sym = -ones(num_energies,num_omega);
sigma_emi_asym = -ones(num_energies,num_omega);
sigma_abs_sym = ones(num_energies,num_omega);
sigma_abs_asym = ones(num_energies,num_omega);

temp1_emi_sym = ones(num_energies,1)*(0.5*q_sym - (m/hbar)*(Vp_sym -
Vg_sym));
temp1_emi_asym      =      ones(num_energies,1)*(0.5*q_antisym      -
(m/hbar)*(Vp_antisym - Vg_antisym));
temp1_abs_sym = ones(num_energies,1)*(0.5*q_sym +(m/hbar)*(Vp_sym -
Vg_sym));
temp1_abs_asym      =      ones(num_energies,1)*(0.5*q_antisym      +
(m/hbar)*(Vp_antisym - Vg_antisym));

temp2_emi_sym       =       (sqrt(1/m*(2*Ek*ones(1,num_omega)       +
ones(num_energies,1)*(-0.5*Eq_sym      -      hbar*omega_sym))      -
ones(num_energies,1)*Vp_sym.^2)                                     +
sqrt(E0/m)).^2./sqrt(1/m*(2*Ek*ones(1,num_omega)                    +
ones(num_energies,1)*(-0.5*Eq_sym      -      hbar*omega_sym))      -
ones(num_energies,1)*Vp_sym.^2);
temp2_emi_asym       =       (sqrt(1/m*(2*Ek*ones(1,num_omega)       +
ones(num_energies,1)*(-0.5*Eq_antisym   -   hbar*omega_antisym))    -
ones(num_energies,1)*Vp_antisym.^2)                                 +
sqrt(E0/m)).^2./sqrt(1/m*(2*Ek*ones(1,num_omega)                    +
ones(num_energies,1)*(-0.5*Eq_antisym   -   hbar*omega_antisym))    -
ones(num_energies,1)*Vp_antisym.^2);
```

```
temp2_abs_sym       =       (sqrt(1/m*(2*Ek*ones(1,num_omega)       +
ones(num_energies,1)*(-0.5*Eq_sym         +         hbar*omega_sym))-
ones(num_energies,1)*Vp_sym.^2)                                     +
sqrt(E0/m)).^2./sqrt(1/m*(2*Ek*ones(1,num_omega)                    +
ones(num_energies,1)*(-0.5*Eq_sym      +      hbar*omega_sym))      -
ones(num_energies,1)*Vp_sym.^2);
temp2_abs_asym       =       (sqrt(1/m*(2*Ek*ones(1,num_omega)      +
ones(num_energies,1)*(-0.5*Eq_antisym     +     hbar*omega_antisym))-
ones(num_energies,1)*Vp_antisym.^2)                                 +
sqrt(E0/m)).^2./sqrt(1/m*(2*Ek*ones(1,num_omega)                    +
ones(num_energies,1)*(-0.5*Eq_antisym    +    hbar*omega_antisym))    -
ones(num_energies,1)*Vp_antisym.^2);

sigma_emi_sym(imag(temp2_emi_sym)~=0) = 0;
sigma_emi_asym(imag(temp2_emi_asym)~=0) = 0;
sigma_abs_sym(imag(temp2_abs_sym)~=0) = 0;
sigma_abs_asym(imag(temp2_abs_asym)~=0) = 0;

temp3_emi_sym      =      ones(num_energies,1)*((Vp_sym./q_sym      -
0.5*hbar/m)./Vg_sym - 1./q_sym);
temp3_emi_asym   =   ones(num_energies,1)*((Vp_antisym./q_antisym   -
0.5*hbar/m)./Vg_antisym - 1./q_antisym);
temp3_abs_sym      =      ones(num_energies,1)*((Vp_sym./q_sym      +
0.5*hbar/m)./Vg_sym - 1./q_sym);
temp3_abs_asym   =   ones(num_energies,1)*((Vp_antisym./q_antisym   +
0.5*hbar/m)./Vg_antisym - 1./q_antisym);

N_omega_sym  =  ones(num_energies,1)*(1./(exp(hbar*omega_sym/kBT)-1));
%number of phonons (Bose-Einstein Distribution)
N_omega_antisym                                                     =
ones(num_energies,1)*(1./(exp(hbar*omega_antisym/kBT)-1));

TEMP_tau_inv_emi_sym                                                =
(m/aB)*(1/epsilon_r^2)*sigma_emi_sym.*(N_omega_sym                  +
1).*D_sym.*temp3_emi_sym./(temp1_emi_sym.*temp2_emi_sym);
tau_inv_emi_sym = trapz(omega_sym,TEMP_tau_inv_emi_sym,2);
TEMP_tau_inv_emi_asym
=(m/aB)*(1/epsilon_r^2)*sigma_emi_asym.*(N_omega_antisym            +
1).*D_antisym.*temp3_emi_asym./(temp1_emi_asym.*temp2_emi_asym);
tau_inv_emi_asym = trapz(omega_antisym,TEMP_tau_inv_emi_asym,2);
TEMP_tau_inv_abs_sym                                                =
(m/aB)*(1/epsilon_r^2)*sigma_abs_sym.*(N_omega_sym).*D_sym.*temp3_abs
_sym./(temp1_abs_sym.*temp2_abs_sym);
tau_inv_abs_sym = trapz(omega_sym,TEMP_tau_inv_abs_sym,2);
TEMP_tau_inv_abs_asym                                               =
(m/aB)*(1/epsilon_r^2)*sigma_abs_asym.*(N_omega_antisym).*D_antisym.*
temp3_abs_asym./(temp1_abs_asym.*temp2_abs_asym);
```

```
tau_inv_abs_asym = trapz(omega_antisym,TEMP_tau_inv_abs_asym,2);

figure(4),semilogy(omega_antisym/(c0*2*pi*10^2),-
TEMP_tau_inv_emi_asym(4001,:),'b','Linewidth',2); hold on;
semilogy(omega_antisym/(c0*2*pi*10^2),-
TEMP_tau_inv_emi_asym(6001,:),'r--','Linewidth',2);
semilogy(omega_antisym/(c0*2*pi*10^2),-
TEMP_tau_inv_emi_asym(10001,:),'k:','Linewidth',2);
legend('E_{k}   =   0.2   eV','E_{k}   =   0.3   eV','E_{k}   =   0.5
eV','Location','southeast'); legend('autoupdate','off');
semilogy(omega_sym/(c0*2*pi*10^2),TEMP_tau_inv_emi_sym(4001,:),'b','L
inewidth',2);
semilogy(omega_sym/(c0*2*pi*10^2),TEMP_tau_inv_emi_sym(6001,:),'r--
','Linewidth',2);
semilogy(omega_sym/(c0*2*pi*10^2),TEMP_tau_inv_emi_sym(10001,:),'k:',
'Linewidth',2);
hold off; xlabel('Phonon Frequency \omega (cm^{-1})', 'FontWeight',
'normal');  ylabel('Scattering Rate (a.u.)', 'FontWeight', 'normal');
%line([omega_resonance omega_resonance],[1e0 1e+5],'LineStyle','-.');
str = '\omega_{res}'; text(omega_resonance + 0.1, 3e+0 ,str);

figure(5),semilogy(Ek_eV,tau_inv_emi_sym,'Linewidth',2);   hold   on;
semilogy(Ek_eV,tau_inv_emi_asym,'Linewidth',2);
semilogy(Ek_eV,tau_inv_abs_sym,'Linewidth',2);
semilogy(Ek_eV,tau_inv_abs_asym,'Linewidth',2); hold off;
xlabel('Hole Energy E_{k} (eV)', 'FontWeight', 'normal');
ylabel('Scattering Rate (s^{-1})', 'FontWeight', 'normal');
legend('\tau^{sym}_{emi}','\tau^{asym}_{emi}','\tau^{sym}_{abs}','\ta
u^{asym}_{abs}','Location','southeast','AutoUpdate','off');
%line([hbar*omega_resonance*c0*2*pi*10^2/e_h
hbar*omega_resonance*c0*2*pi*10^2/e_h],[1e9   1e14],'LineStyle','-.');
str  =  '\omega_{res}';  text(hbar*omega_resonance*c0*2*pi*10^2/e_h  +
0.005, 3e10 ,str);

tau_inv_emi = tau_inv_emi_sym + tau_inv_emi_asym;
tau_inv_abs = tau_inv_abs_sym + tau_inv_abs_asym;

figure(6), semilogy(Ek_eV,tau_inv_emi,'k','Linewidth',2); hold on;
semilogy(Ek_eV,tau_inv_abs,'r','Linewidth',2); hold off;
xlabel('Hole Energy E_{k} (eV)', 'FontWeight', 'normal');
ylabel('Scattering Rate (s^{-1})', 'FontWeight', 'normal');
%line([hbar*omega_resonance*c0*2*pi*10^2/e_h
hbar*omega_resonance*c0*2*pi*10^2/e_h],[1e9   1e14],'LineStyle','-.');
str  =  '\omega_{res}';  text(hbar*omega_resonance*c0*2*pi*10^2/e_h  +
0.005, 3e10 ,str);

tau_inv = tau_inv_emi + tau_inv_abs;
```

```
figure(7), semilogy(Ek_eV,tau_inv,'k','Linewidth',2);
xlabel('Hole Energy E_{k} (eV)', 'FontWeight', 'normal');
ylabel('Scattering Rate (s^{-1})', 'FontWeight', 'normal');
%line([hbar*omega_resonance*c0*2*pi*10^2/e_h
hbar*omega_resonance*c0*2*pi*10^2/e_h],[1e9   1e14],'LineStyle','-.');
str  =  '\omega_{res}';  text(hbar*omega_resonance*c0*2*pi*10^2/e_h  +
0.005, 3e10 ,str);

disp('Do you want to plot the mobility?');
disp('[1] Yes');
disp('[0] No');
sel =input('');
if sel==1
    mc = 0.4447*m0; %conduction mass [Li et Al 2018]
    mobility = (e_h/mc)*(1./(tau_inv)); %[m^2/(V s)]
    mobility = mobility*10^4; %[cm^2/(V s)];
    figure(8),            semilogy(Ek_eV,mobility,'k','Linewidth',2);
xlabel('Hole   Energy   E_{k}   (eV)',   'FontWeight',   'normal');
ylabel('\mu_{IF} [cm^2/(V s)]'); title('Mobility');
    %line([hbar*omega_resonance*c0*2*pi*10^2/e_h
hbar*omega_resonance*c0*2*pi*10^2/e_h],[1e2    1e6],'LineStyle','-.');
str  =  '\omega_{res}';  text(hbar*omega_resonance*c0*2*pi*10^2/e_h  +
0.005, 0.5e6 ,str);

    %% Comparison with Li (Temperature)
    temperatures = 1001;
    mobility_T       =       zeros(temperatures,1);       T_2       =
linspace(100,1000,temperatures);
    sigma_emi_sym_T   =   sigma_emi_sym(10001,:);   sigma_emi_asym_T   =
sigma_emi_asym(10001,:); %Ek=0.5 eV
    sigma_abs_sym_T   =   sigma_abs_sym(10001,:);   sigma_abs_asym_T   =
sigma_abs_asym(10001,:);
    D_sym_T = D_sym(10001,:); D_antisym_T = D_antisym(10001,:);
    temp3_emi_sym_T   =   temp3_emi_sym(10001,:);   temp2_emi_sym_T   =
temp2_emi_sym(10001,:); temp1_emi_sym_T = temp1_emi_sym(10001,:);
    temp3_emi_asym_T  =  temp3_emi_asym(10001,:);  temp2_emi_asym_T  =
temp2_emi_asym(10001,:); temp1_emi_asym_T = temp1_emi_asym(10001,:);
    temp3_abs_sym_T   =   temp3_abs_sym(10001,:);   temp2_abs_sym_T   =
temp2_abs_sym(10001,:); temp1_abs_sym_T = temp1_abs_sym(10001,:);
    temp3_abs_asym_T  =  temp3_abs_asym(10001,:);  temp2_abs_asym_T  =
temp2_abs_asym(10001,:); temp1_abs_asym_T = temp1_abs_asym(10001,:);

    for i=1:temperatures
        N_omega_sym_T    =    (1./(exp(hbar*omega_sym/(kB*T_2(i)))-1));
N_omega_antisym_T = (1./(exp(hbar*omega_antisym/(kB*T_2(i)))-1));
```

```
        TEMP_tau_inv_emi_sym_T                                          =
(m/aB)*(1/epsilon_r^2)*sigma_emi_sym_T.*(N_omega_sym_T                  +
1).*D_sym_T.*temp3_emi_sym_T./(temp1_emi_sym_T.*temp2_emi_sym_T);
        tau_inv_emi_sym_T = trapz(omega_sym,TEMP_tau_inv_emi_sym_T,2);
        TEMP_tau_inv_emi_asym_T
=(m/aB)*(1/epsilon_r^2)*sigma_emi_asym_T.*(N_omega_antisym_T            +
1).*D_antisym_T.*temp3_emi_asym_T./(temp1_emi_asym_T.*temp2_emi_asym_
T);
        tau_inv_emi_asym_T                                              =
trapz(omega_antisym,TEMP_tau_inv_emi_asym_T,2);
        TEMP_tau_inv_abs_sym_T                                          =
(m/aB)*(1/epsilon_r^2)*sigma_abs_sym_T.*(N_omega_sym_T).*D_sym_T.*tem
p3_abs_sym_T./(temp1_abs_sym_T.*temp2_abs_sym_T);
        tau_inv_abs_sym_T = trapz(omega_sym,TEMP_tau_inv_abs_sym_T,2);
        TEMP_tau_inv_abs_asym_T                                         =
(m/aB)*(1/epsilon_r^2)*sigma_abs_asym_T.*(N_omega_antisym_T).*D_antis
ym_T.*temp3_abs_asym_T./(temp1_abs_asym_T.*temp2_abs_asym_T);
        tau_inv_abs_asym_T                                              =
trapz(omega_antisym,TEMP_tau_inv_abs_asym_T,2);

        tau_inv_emi_T = tau_inv_emi_sym_T + tau_inv_emi_asym_T;
        tau_inv_abs_T = tau_inv_abs_sym_T + tau_inv_abs_asym_T;
        tau_inv_T = tau_inv_emi_T + tau_inv_abs_T;
        mobility_T(i) = (e_h/mc)*(1./(tau_inv_T))*10^4; %[cm^2/(V s)]
    end
    figure(9),              semilogy(T_2,mobility_T,'k','Linewidth',2);
xlabel('Temperature  (K)',  'FontWeight',  'normal');  ylabel('\mu_{IF}
[cm^2/(V s)]'); title('Mobility');


    %% Comparison with Li (Density of Charges)
    densities = 1001;
    N_h_2= linspace(10^15,10^18,densities); %[1/m^2]
    T = 300;
    mobility_den = zeros(densities,1);
    N_omega_sym_Nh        =        (1./(exp(hbar*omega_sym/(kB*T))-1));
N_omega_antisym_Nh = (1./(exp(hbar*omega_antisym/(kB*T))-1));
    for i=1:densities
        b                                                               =
(33*m*e_h^2*N_h_2(i)/(8*hbar^2*epsilon_0*epsilon_r))^(1/3);
        F = @(q)  ((b^3)/2)*exp(b*l)*((-L^2*exp(-(b  +  q)*L)./(b+q))  +
(l^2*exp(-(b+q)*l)./(b+q))   +   (2./(b+q)).*[((-L*exp(-(b   +   q)*L)   +
l*exp(-(b   +   q)*l))./(b+q))   -   ((exp(-(b   +   q)*L)   -   exp(-(b   +
q)*l))./(b+q).^2)] - 2*l*[((-L*exp(-(b + q)*L) + l*exp(-(b + q)*l))./(b
+ q)) - ((exp(-(b + q)*L) - exp(-(b + q)*l))./(b + q).^2)] + l^2*[(-
exp(-(b + q)*L) + exp(-(b + q)*l))./(b+q)];
        D_sym_Nh = abs(C_symm.^2.*(F(q_sym)).^2);
```

```
        D_antisym_Nh = abs(C_antisymm.^2.*(F(q_antisym)).^2);

        TEMP_tau_inv_emi_sym_Nh                                          =
(m/aB)*(1/epsilon_r^2)*sigma_emi_sym_T.*(N_omega_sym_Nh                  +
1).*D_sym_Nh.*temp3_emi_sym_T./(temp1_emi_sym_T.*temp2_emi_sym_T);
        tau_inv_emi_sym_Nh                                               =
trapz(omega_sym,TEMP_tau_inv_emi_sym_Nh,2);
        TEMP_tau_inv_emi_asym_Nh
=(m/aB)*(1/epsilon_r^2)*sigma_emi_asym_T.*(N_omega_antisym_Nh             +
1).*D_antisym_Nh.*temp3_emi_asym_T./(temp1_emi_asym_T.*temp2_emi_asym
_T);
        tau_inv_emi_asym_Nh                                              =
trapz(omega_antisym,TEMP_tau_inv_emi_asym_Nh,2);
        TEMP_tau_inv_abs_sym_Nh                                          =
(m/aB)*(1/epsilon_r^2)*sigma_abs_sym_T.*(N_omega_sym_Nh).*D_sym_Nh.*t
emp3_abs_sym_T./(temp1_abs_sym_T.*temp2_abs_sym_T);
        tau_inv_abs_sym_Nh                                               =
trapz(omega_sym,TEMP_tau_inv_abs_sym_Nh,2);
        TEMP_tau_inv_abs_asym_Nh                                         =
(m/aB)*(1/epsilon_r^2)*sigma_abs_asym_T.*(N_omega_antisym_Nh).*D_anti
sym_Nh.*temp3_abs_asym_T./(temp1_abs_asym_T.*temp2_abs_asym_T);
        tau_inv_abs_asym_Nh                                              =
trapz(omega_antisym,TEMP_tau_inv_abs_asym_Nh,2);

        tau_inv_emi_Nh = tau_inv_emi_sym_Nh + tau_inv_emi_asym_Nh;
        tau_inv_abs_Nh = tau_inv_abs_sym_Nh + tau_inv_abs_asym_Nh;
        tau_inv_Nh = tau_inv_emi_Nh + tau_inv_abs_Nh;
        mobility_den(i)  =  (e_h/mc)*(1./(tau_inv_Nh))*10^4;  %[cm^2/(V
s)]
    end

    figure(10),     loglog(N_h_2/10^4,mobility_den,'k','Linewidth',2);
xlabel('Hole    Density    (cm^{-2})',    'FontWeight',    'normal');
ylabel('\mu_{IF} [cm^2/(V s)]'); title('Mobility');
end

% if values==1
%     figure(1), export_fig dispersion_AlN.pdf
%     figure(2), export_fig phase_velocity_AlN.pdf
%     figure(3), export_fig group_velocity_AlN.pdf
%     figure(4), export_fig number_phonons_AlN.pdf
%     figure(5), export_fig scattering_4_AlN.pdf
%     figure(6), export_fig scattering_2_AlN.pdf
%     figure(7), export_fig scattering_AlN.pdf
%     figure(8), export_fig mobility_AlN.pdf
%     figure(9), export_fig mobility_T_AlN.pdf
%     figure(10), export_fig mobility_N_AlN.pdf
```

```
% elseif values==4
%     figure(1), export_fig dispersion_wBN.pdf
%     figure(2), export_fig phase_velocity_wBN.pdf
%     figure(3), export_fig group_velocity_wBN.pdf
%     figure(4), export_fig number_phonons_wBN.pdf
%     figure(5), export_fig scattering_4_wBN.pdf
%     figure(6), export_fig scattering_2_wBN.pdf
%     figure(7), export_fig scattering_wBN.pdf
%     figure(8), export_fig mobility_wBN.pdf
%     figure(9), export_fig mobility_T_wBN.pdf
%     figure(10), export_fig mobility_N_wBN.pdf
% end
```

Appendix D

SDE structure

```
(define nm 1e-3)
(define  L  150)
(define W 5)
(define H 5)
(define SEP 70)
(define Tox 0.8 )
(define Ratio 1 )
(define Radius 5)
(define Channel_Doping 1e16)
(define Bulk_Doping 1e15)
(define SD_Doping1 1e20)
(define SDE_Doping 1e20)
(define SD_Front_Doping 0)
(define Channel_Doping2 1.96e20)
(define Lsd 5)
(define SDlength 30)
(define RL1 1.5)
(define dopL 1)
(define dopBd 0.0)


;==============Geometry-===============;
;--- Metal gate
(sdegeo:create-cuboid (position 0 (* -1 10) 0)  (position L (+ (+ SEP (+ (* 2
W) (* 3 Tox))) 10) (+ 10 (+ H Tox))) "Titanium" "MG")

;--- Channel Oxide
"ABA"
(sdegeo:create-cuboid (position 0 (- 0 Tox) 0)  (position L (+ W Tox) (+ H
Tox)) "SiO2" "Gateoxide 1")
(sdegeo:create-cuboid (position 0 (- (+ SEP (+ W (* 2 Tox))) Tox) 0)  (position
L (+  (+ SEP (+ (* 2 W) (* 2 Tox)))  Tox) (+ H Tox)) "SiO2" "Gateoxide 2")

;--- Channel
"ABA"
(sdegeo:create-cuboid (position 0 0 0)  (position L W H) "Silicon" "Channel1")
(sdegeo:create-cuboid (position 0 (+ SEP (+ W (* 2 Tox))) 0)  (position L (+
SEP (+ (* 2 W) (* 2 Tox))) H)  "Silicon" "Channel2")



;--- Source
(sdegeo:create-cuboid (position (* -1 Lsd) W H)  (position 0 0 0) "Silicon"
"Source Extension 1")

(sdegeo:create-cuboid (position (* -1 Lsd) (+ SEP (+ W (* 2 Tox))) H)
(position 0 (+ SEP (+ (* 2 W) (* 2 Tox))) 0)  "Silicon" "Source Extensition 2")
```

```
(sdegeo:create-cuboid (position (- (* -1 Lsd) SDlength) (* -1 10) 0)  (position
(* -1 Lsd) (+ (+ SEP (+ (* 2 W) (* 3 Tox))) 10) (+ 10 (+ H Tox))) "Silicon"
"SC")


;--- Drain
(sdegeo:create-cuboid (position L 0 0)  (position (+ Lsd L) W H) "Silicon"
"Drain Extension 1")

(sdegeo:create-cuboid (position L (+ SEP (+ W (* 2 Tox))) 0)  (position (+ Lsd
L) (+ SEP (+ (* 2 W) (* 2 Tox))) H) "Silicon" "Drain Extention 2")

(sdegeo:create-cuboid (position (+  Lsd L) (* -1 10) 0)  (position (+ (+  Lsd
L) SDlength) (+ (+ SEP (+ (* 2 W) (* 3 Tox))) 10) (+ 10 (+ H Tox))) "Silicon"
"DC")


;---BOX
(sdegeo:create-cuboid (position (- (* -1 Lsd) SDlength) (* -1 10) 0) (position
(+ (+  Lsd L) SDlength) (+ (+ SEP (+ (* 2 W) (* 3 Tox))) 10) (* -1 20)) "SiO2"
"BOX")

;---Substrate
(sdegeo:create-cuboid (position (- (* -1 Lsd) SDlength) (* -1 10) (* -1 20))
(position (+ (+  Lsd L) SDlength) (+ (+ SEP (+ (* 2 W) (* 3 Tox))) 10) (* -1
40)) "Silicon" "Substrate")

;==============Geometry-===============;

;==============Contact-===============;
;--- Gate contact(1):
(sdegeo:define-contact-set "G" 4.0  (color:rgb 1.0 0.0 0.0 ) "||" )
(sdegeo:set-current-contact-set "G")
(sdegeo:set-contact-faces
 (find-face-id (position (* 0.5 L) 0 (+ 10 (+ Radius Tox)))))

;--- Assign drain contact
(sdegeo:define-contact-set "D" 4.0  (color:rgb 1.0 0.0 0.0 ) "##" )
(sdegeo:set-current-contact-set "D")
(sdegeo:set-contact-faces
 (find-face-id (position (+ (+  Lsd L) SDlength) 0 (+ 5 (+ Radius Tox))  )))

;--- Assign source contact
(sdegeo:define-contact-set "S" 4.0  (color:rgb 1.0 0.0 0.0 ) "##" )
(sdegeo:set-current-contact-set "S")
(sdegeo:set-contact-faces
 (find-face-id (position (- (* -1 Lsd) SDlength) 0 (+ 5 (+ Radius Tox))  )))

;--- Assign substrate contact
(sdegeo:define-contact-set "B" 4.0  (color:rgb 1.0 0.0 0.0 ) "##" )
(sdegeo:set-current-contact-set "B")
(sdegeo:set-contact-faces
 (find-face-id (position (* 0.5 L) 0 (* -1 40)  )))
```

```
;==============Contact-===============;



;==============Doping-===============;
;--- Constant BG doping in all of Si
(sdedr:define-constant-profile "Boron_Bulk" "BoronActiveConcentration"
Bulk_Doping)
(sdedr:define-constant-profile-material "Boron_bulk_PL" "Boron_Bulk" "Silicon")

;--- Constant doping is channel region
(sdedr:define-constant-profile "Channel" "BoronActiveConcentration"
Channel_Doping)
(sdedr:define-refinement-window "Channel_PlBox" "Cuboid"
   (position -1 (- 0 Tox) (- 0 Tox)) (position (+ 1 L) (+ SEP (+ (* 2 W) (* 3
Tox))) H))
(sdedr:define-constant-profile-placement "Channel_PL" "Channel" "Channel_PlBox"
0 )



;--- Constant doping SE/DE region
(sdedr:define-constant-profile "SDE" "ArsenicActiveConcentration" SDE_Doping)

(sdedr:define-refinement-window "DrainE_PlBox" "Cuboid" (position (+ 1 L) (* -1
Tox)  (- 0 Tox)) (position (+ Lsd L) (+ SEP (+ (* 2 W) (* 3 Tox))) H ))
(sdedr:define-constant-profile-placement "DrainE_PL" "SDE" "DrainE_PlBox" 0)

(sdedr:define-refinement-window "SourceE_PlBox" "Cuboid" (position -1 (* -1
Tox)  (- 0 Tox))  (position (* -1 Lsd) (+ SEP (+ (* 2 W) (* 3 Tox))) H ))
(sdedr:define-constant-profile-placement "SourceE_PL" "SDE" "SourceE_PlBox" 0)

;--- Constant doping is S/D region----SD_BOX
(sdedr:define-constant-profile "SD" "ArsenicActiveConcentration" SD_Doping1)

(sdedr:define-refinement-window "Drain_PlBox" "Cuboid"
  (position (- (* -1 Lsd) SDlength) (* -1 10)  0) (position (* -1 Lsd)  (+ (+
SEP (+ (* 2 W) (* 3 Tox))) 10) (+ 10 (+ H Tox)) ))
(sdedr:define-constant-profile-placement "Drain_PL" "SD" "Drain_PlBox" 0)

(sdedr:define-refinement-window "Source_PlBox" "Cuboid"
  (position (+  Lsd L) (* -1 10)  0) (position (+ (+  Lsd L) SDlength) (+ (+
SEP (+ (* 2 W) (* 3 Tox))) 10) (+ 10 (+ H Tox)) ))
(sdedr:define-constant-profile-placement "Source_PL" "SD" "Source_PlBox" 0)


;==============Mesh-===============;
(sdedr:define-refinement-size "Cha_Mesh2" 0.05 0.05 0.05 0.005 0.005 0.005 )
(sdedr:define-refinement-function "Cha_Mesh2" "DopingConcentration"
"MaxTransDiff" 1)
(sdedr:define-refinement-material "Cha_Mesh1n" "Cha_Mesh2" "Silicon" )

(sdedr:define-multibox-size "multibox_0" 0.04 0.04 0.04 0.002 0.002 0.002 1.2
1.2 1.2)
```

```
(sdedr:define-refinement-function "multibox_0" "DopingConcentration"
"MaxTransDiff" 1)
(sdedr:define-refinement-window "Region_1" "Cuboid" (position (- 0 1) (- 0 Tox)
0 )    (position  (+ L 1) (+ W Tox) (+ H Tox)))
(sdedr:define-multibox-placement "multibox0_PL1" "multibox_0" "Region_1")

(sdedr:define-multibox-size "multibox_1" 0.04 0.04 0.04 0.002 0.002 0.002 1.2
1.2 1.2)
(sdedr:define-refinement-function "multibox_1" "DopingConcentration"
"MaxTransDiff" 1)
(sdedr:define-refinement-window "Region_2" "Cuboid" (position (- 0 1) (- (+ SEP
(+ W (* 2 Tox))) Tox) 0)  (position (+ L 1) (+ SEP (+ (* 2 W) (* 3 Tox))) (+ H
Tox)))
(sdedr:define-multibox-placement "multibox0_PL2" "multibox_1" "Region_2")


;(sdedr:define-refinement-function "RefinementDefinition_1" "MaxLenInt"
"Silicon" "SiO2" 0.0002 1.4)

;==============Mesh-===============;



;==============Mesh-===============;
(sdegeo:scale "all" nm nm nm)

(sdeio:save-tdr-bnd (part:entities (filter:type "solid?"))"@boundary/o@")
(sdedr:write-cmd-file "@commands/o@")
(sde:build-mesh "snmesh" " " "n@node@_msh")
```

SDevice

```
Electrode{
   { name="S" voltage=0.0  }
   { name="D"  voltage=0.0  }
   { name="G"   voltage=0.0  }
   { name="B"   voltage=0.0  }


}

File{
   Grid        = "@tdr@"
   Doping = "@tdr@"
   Plot        = "@tdrdat@"
   Current = "@plot@"
   Output      = "@log@"
   parameter    = "@parameter@"
}

Physics {
   Mobility(  Enormal HighFieldsat DopingDep )
   Recombination( SRH(DopingDep) Auger )
```

```
        eQuantumPotential
        hQuantumPotential
}


Plot{
*--Density and Currents, etc
   eDensity hDensity
   TotalCurrent/Vector eCurrent/Vector hCurrent/Vector
   eMobility hMobility
   eVelocity hVelocity
   eQuasiFermi hQuasiFermi

*--Fields and charges
   ElectricField/Vector Potential SpaceCharge

*--Doping Profiles
   Doping DonorConcentration AcceptorConcentration

*--Generation/Recombination
   SRH Auger
   * AvalancheGeneration eAvalancheGeneration hAvalancheGeneration

*--Driving forces
   eGradQuasiFermi/Vector hGradQuasiFermi/Vector
   eEparallel hEparalllel

*--Band structure/Composition
   BandGap
   BandGapNarrowing
   Affinity
   ConductionBand ValenceBand
   eQuantumPotential
}

Math{

   Extrapolate
   Derivatives
   * Avalderivatives
   RelErrControl
   Digits=5
   ErRef(electron)=1.e10
   ErRef(hole)=1.e10
   Notdamped=50
   Iterations=20
   Directcurrent
   Method=ParDiSo
   Parallel= 2
   NaturalBoxMethod
}

Solve{
  #-initial solution:
```

```
  Coupled(Iterations=100 LineSearchDamping=1e-4){ Poisson }
  Coupled{ Poisson eQuantumPotential }
  Coupled{ Poisson eQuantumPotential Electron Hole }


  #-ramp gate
 Quasistationary(
    InitialStep=1e-3 Increment=1.2
    Minstep=1e-6 MaxStep=0.95
    Goal{ name="D" voltage=@VD@}
  ){
    Coupled { Poisson eQuantumPotential Electron Hole}
  }

  NewCurrentFile=""

  Quasistationary(
    InitialStep=1e-3 Increment=1.2
    Minstep=1e-6 MaxStep=0.02
    Goal{ name="G" voltage=@VG@ }
    DoZero
  ){
    Coupled { Poisson eQuantumPotential Electron Hole }
  }

}
```

Inspect

```
#-------------------------------------------------------------------------#
#        Script file designed to compute   :                              #
#         * The threshold voltage          :  VT                          #
#         * The transconductance           :  gm                          #
#-------------------------------------------------------------------------#

if { ! [catch {open n@previous@_ins.log w} log_file] } {
       set fileId stdout
}

puts $log_file " "
puts $log_file "             ------------------------------------ "
puts $log_file "             Values of the extracted Parameters : "
puts $log_file "             ------------------------------------ "
puts $log_file " "
puts $log_file " "
set  DATE   [ exec  date ]
set  WORK   [ exec pwd   ]
puts $log_file "      Date      : $DATE "
puts $log_file "      Directory : $WORK "
puts $log_file " "
puts $log_file " "

#                                                                        #
```

```
#                    idvgs=y(x) ;   vgsvgs=x(x) ;                          #
#                                                                        #

set out_file n@previous@_des
proj_load "${out_file}.plt"


# ------------------------------------------------------------------------ #
# I)  VT = Xintercept(maxslope(ID[VGS]))  or  VT = VGS( IDS= 0.1 ua/um ) #
# ------------------------------------------------------------------------ #
cv_create    idvgs   "${out_file} G OuterVoltage" "${out_file} D TotalCurrent"
cv_create    vdsvgs  "${out_file} G OuterVoltage" "${out_file} D OuterVoltage"

#..................................................................... #
# 1) VT extracted as the intersection point with the X axis at the point #
#    where the id(vgs) slope reaches its maxmimum :                     #
#..................................................................... #
set VT1 [ cv_compute "vecvalx(<idvgs>, 3.14e-7)" A A A A ]

#.....................................................................        #
# 2) Printing of the whole set of extracted values (std output) :        #
#.....................................................................        #
puts $log_file "Threshold   voltage VT1     = $VT1  Volts"
puts $log_file " "

#.....................................................................  #
# 3) Initialization and display of curves on the main Inspect screen  :  #
# ....................................................................  #
cv_display    idvgs
cv_lineStyle  idvgs  solid
cv_lineColor  idvgs  red


# ------------------------------------------------------------------------ #
# II)                 gm =  maxslope((ID[VGS])                          #
# ------------------------------------------------------------------------ #
set gm     [ f_gm idvgs ]
puts $log_file " "
puts $log_file "Transconductance gm                = $gm  A/V"
puts $log_file " "


set ioff  [ cv_compute "vecmin(<idvgs>)" A A A A ]
puts $log_file " "
puts $log_file "Current ioff        = $ioff  A"
puts $log_file " "

set isat  [ cv_compute "vecmax(<idvgs>)" A A A A ]
puts $log_file " "
puts $log_file "Current isat        = $isat  A"
puts $log_file " "


cv_createWithFormula logcurve "log10(<idvgs>)" A A A A
```

```
cv_createWithFormula difflog "diff(<logcurve>)" A A A A
set sslop [ cv_compute "1/vecmax(<difflog>)" A A A A ]
puts $log_file " "
puts $log_file "sub solp        = $sslop  A/V"
puts $log_file " "


### Puting into Family Table #####

ft_scalar VT $VT1
ft_scalar gmax $gm
ft_scalar ioff $ioff
ft_scalar isat $isat
ft_scalar sslop $sslop


close $log_file
```

Appendix E

Elsevier copyright

"Authors can use their articles, in full or in part, for a wide range of scholarly, non-commercial purposes as outlined below:

- Use by an author in the author's classroom teaching (including distribution of copies, paper or electronic)
- Distribution of copies (including through e-mail) to known research colleagues for their personal use (but not for Commercial Use)
- Inclusion in a thesis or dissertation (provided that this is not to be published commercially)
- Use in a subsequent compilation of the author's works
- Extending the Article to book-length form
- Preparation of other derivative works (but not for Commercial Use)
- Otherwise using or re-using portions or excerpts in other works

These rights apply for all Elsevier authors who publish their article as either a subscription article or an open access article. In all cases we require that all Elsevier authors always include a full acknowledgement and, if appropriate, a link to the final published version hosted on Science Direct."

Source: https://www.elsevier.com/about/policies/copyright/permissions

Nature permission requests

"Authors have the right to reuse their article's Version of Record, in whole or in part, in their own thesis. Additionally, they may reproduce and make available their thesis, including Springer Nature content, as required by their awarding academic institution."

Source: https://www.nature.com/nature-research/reprints-and-permissions/permissions-requests

PLOS One license and copyright

"PLOS applies the Creative Commons Attribution (CC BY) license to articles and other works we publish. If you submit your paper for publication by PLOS, you agree to have the CC BY license applied to your work. Under this Open Access license, you as the author agree that anyone can reuse your article in whole or part for any purpose, for free, even for commercial purposes. Anyone may copy, distribute, or reuse the content as long as the author and original source are properly cited. This facilitates freedom in re-use and also ensures that PLOS content can be mined without barriers for the needs of research."

Source: https://journals.plos.org/plosone/s/licenses-and-copyright

IEEE permissions

"In reference to IEEE copyrighted material which is used with permission in this thesis, the IEEE does not endorse any of [the University of Illinois at Chicago's] products or services. Internal or personal use of this material is permitted. If interested in reprinting/republishing IEEE copyrighted material for advertising or promotional purposes or for creating new collective works for resale or redistribution, please go to

http://www.ieee.org/publications_standards/publications/rights/rights_link.html

to learn how to obtain a License from RightsLink. If applicable, University Microfilms and/or ProQuest Library, or the Archives of Canada may supply single copies of the dissertation."

Source: https://journals.ieeeauthorcenter.ieee.org/choose-a-publishing-agreement/avoid-infringement-upon-ieee-copyright/

IOP current author rights policy

"Upon transfer of copyright, IOP and/or the copyright owner grants back to authors a number of rights. These include the right to copy the article for teaching purposes, and to include the article in research

theses or dissertations. Please include citation details and for online use, a link to the Version of Record. IOP's permission will be required for commercial use of an article published as part of your thesis."

Source: https://publishingsupport.iopscience.iop.org/questions/rp-use-of-a-subscription-article-in-your-thesis-or-dissertation-may-i-include-the-final-published-version-of-the-article-in-my-research-thesis-or-dissertation/

Vita

Name Ahmed Mohamed

Education

Ph.D., Electrical and Computer Engineering, University of Illinois at Chicago, Chicago, Illinois, USA, 2021

M.Sc., Electrical and Computer Engineering, University of Illinois at Chicago, Chicago, Illinois, USA, 2019

B.Sc., Electrical and Electronic Engineering, University of Khartoum, Khartoum, Sudan, 2014

Experience

Research Assistant, Nanoengineering Research Laboratory, University of Illinois at Chicago, 2016 – 2021

Teaching Assistant, Department of Electrical and Computer Engineering, University of Illinois at Chicago, 2016 – 2021

Publications

Mohamed A, Singh R, Dutta M, Stroscio MA. Anharmonic decay of high-frequency LA modes in quasi-isotropic III-nitrides. Journal of Physics: Condensed Matter. 2020 Nov 23;33(7):075501.

Singh R, Mohamed A, Dutta M, Stroscio MA. Fröhlich potential of the A2" phonon mode in MoS2. Solid State Communications. 2020 Oct 1;320:114015.

Mohamed A, Park K, Bayram C, Dutta M, Stroscio MA. Phonon-assisted reduction of hot spot temperature in AlInN ternaries. Journal of Physics D: Applied Physics. 2020 Jun 23;53(36):365102.

Bonomo G, Mohamed A, Farid S, Park K, Dutta M, Stroscio MA. Contribution of remote interface polar phonons in the hole mobility of diamond. Diamond and Related Materials. 2020 Jan 1;101:107650.

Mohamed A, Dutta M, Stroscio M. Phonon Engineering to Modify Acoustic Phonon Velocity in Hexagonal Layered Superlattices. IEEE Electron Device Letters. 2019 May 3;40(7):1175-7.

Mohamed A, Park K, Bayram C, Dutta M, Stroscio M. Confined and interface optical phonon emission in GaN/InGaN double barrier quantum well heterostructures. PLoS one. 2019 Apr 18;14(4):e0214971.

Park K, Mohamed A, Dutta M, Stroscio MA, Bayram C. Electron scattering via interface optical phonons with high group velocity in wurtzite GaN-based quantum well heterostructure. Scientific reports. 2018 Oct 29;8(1):1-0.

Mohamed A, Ghosh S, Araque M, Datta D, Mazouchi M, Rane V, Dutta M, Stroscio MA. Nanomechanical systems with normalized and coupled acoustic and electromagnetic modes in piezoelectric structures. Solid State Communications. 2018 Sep 1;277:1-6.